

Characterisation of Isidis Planitia and the Beagle 2 Landing Site on Mars

Ashley Mark Seabrook,
B.Sc. (Hons.) (Open), M.Sc. (Leicester)

A thesis submitted for the degree of Doctor of Philosophy
in the discipline of Planetary Science.

March 2005



Licensed under a Creative Commons 'Attribution
Non-commercial No Derivatives (by-nc-nd)' license.
<http://creativecommons.org/licenses/by-nc-nd/2.0/uk/>

Abstract

Isidis Planitia is a large impact basin on Mars. I have determined that the extensive numbers of sub-kilometre sized cones and cone chains in the basin are the result of deposition of sediments by retreating ice in a process analogous to terrestrial terminal moraine formation, along with the formation of pingos, mud- and cryovolcanoes by the expansion of freezing fronts into a subsurface containing liquid water. I have interpreted the sinuous ridges within the basin as analogous to terrestrial eskers. Much of the research I have carried out uses Mars Orbiter Laser Altimeter (MOLA) data to study the topography of the basin. I have interpolated and detrended the data in order to detect subtle variations in topography that are obscured by the the basin slope. I have analysed the large scale ridges within the basin, determining that they are the result of compressional tectonics forming normal faults, analogous to lunar wrinkle ridges. I have demonstrated that a model involving tectonic loading of the basin convincingly explains the division of ridges into an inner zone of concentric thrusting faults, and an outer zone of radially thrusting faults, and also provides an explanation for the gravitational anomaly found within the basin. I have analysed the larger impact craters in the basin, and determined that they show evidence of interaction with buried volatiles at the time of their formation. I have also identified a number of previously unknown buried craters within the basin, and calculated the age of the buried unit in which they formed to be Lower-to-mid-Hesperian. I have investigated thermal and other surface properties of the basin surface. Finally, I have drawn the available evidence together to determine a history of events that have shaped the surface and subsurface of the basin during the Hesperian and Amazonian Epochs.

Acknowledgments

Firstly, thanks to my supervisors, Prof. Ian Wright, Dr. Dave Rothery and Dr. John Bridges, who have been unstinting in their support. Without their expertise, cajoling, organisational abilities, understanding, advice, wisdom and commitment there simply would have been no thesis. My thanks must also go to those who took a chance on me at the interview stage, for allowing me the opportunity of going at least some of the way towards fulfilling my dream to do scientific research. Thanks also to the support staff at the university, particularly Ashea Tambe, Dick Carlton and John Taylor, who were always extremely helpful, and ready for a friendly chat. May I also extend my thanks to all the other staff and students in PSSRI and the Dept. of Earth Sciences generally, and in the Volcano Dynamics Group in particular, for being friendly and supportive at every opportunity. Thanks also to people at other institutions who helped me along my way, particularly Dr. Karl Mitchell. A final thanks must also go to the Open University as an institution. They've counted me as a student in one form or another for well over a decade, albeit discontinuously, and for nearly a third of my life in total. I think the most appropriate praise I can offer is that I hope there will be more to come!

Secondly, thanks to my friends and family. Obviously, as the cliché goes, without my Mum and Dad, I really wouldn't be here, but as a source of unwavering support throughout my life, I can honestly say I couldn't have got this far without them. They have been there every step of the way with emotional and financial support. I just hope I make them as proud of me as I am of them. Thanks also to my fiancée Hannah, who has shared the difficult times, and been, as she always is, a wonderful and eternally supportive person. Thanks to my brother for supplying me with his advice and helicopter-related factoids! Thanks to Reuben, Keshena and Shai, who have kept me sane by reminding

me there is life outside my thesis, and for just being themselves. You guys are the centre of my world. I don't have many friends, but those I do have have been very supportive. Thanks to Adrian and, in particular, Vix, for sticking with me through rough and smooth throughout the years.

Finally, thanks to some more esoteric allies in my quest to complete my thesis. Admittedly, it's not to everyone's taste, but music from some of the world's finest musical projects has kept me sane and focussed on long nights in front of a computer. Thanks guys – you'll never know how much you helped! Thanks must also go to the British countryside, which, although sadly neglected by me as thesis writing sucked up every available hour, has always been there to soothe my soul and calm my spirit.

Citations

Approximately 90% of Chapter 3 was presented in the following paper, which contained ~90% my own work:

Using MOLA data to investigate the topography of Isidis Planitia, Mars; Seabrook, A. M., Bridges, J. C., Rothery, D. A., and Wright, I. P.; Society of Cartographers Bulletin, Vol. 38 No. 1, 2005.

Approximately 5% of Chapter 2 was presented in the following paper, which contained ~5% my own work:

Selection of the landing site in Isidis Planitia of Mars probe Beagle 2; Bridges, J. C., Seabrook, A. M., Rothery, D. A., Kim, J. R., Pillinger, C. T., Sims, M. R., Golombek, M. P., Duxbury, T, Head, J. W., Haldemann, A. F. C., Mitchell, K. L., Muller, J.-P., Moncrieff, C., Wright, I. P., Grady, M. M., Morley, J. G.; Journal of Geophysical Research (Planets), Vol. 108 No. E1, 2003.

Contents

1	Introduction	1
1.1	Isidis Planitia	1
1.2	Previous study of Isidis Planitia	3
1.3	Thesis	4
2	Cones In Isidis Planitia	6
2.1	Introduction	6
2.2	Viewing the cones	6
2.3	Previous analyses of cones and cone chains	9
2.4	Analysis of cones and cone chains using MOC data	12
2.5	Analysis of cones and cone chains using THEMIS data	19
2.5.1	Comparison of daytime and nighttime THEMIS infrared images . .	21
2.5.2	Analysis of georectified THEMIS infrared images	25
2.5.3	Sinuuous ridges	30
2.6	Cone and cone chain formation	33

2.6.1	Cinder cones	33
2.6.2	Cones from magma/volatile interaction	35
2.6.3	Mud volcanism and cryovolcanism	36
2.6.4	Glacial/ice and depositional processes	38
2.6.5	Sinuuous ridges	39
2.7	Discussion	40
2.7.1	Sedimentation and a source of volatiles	40
2.7.2	Cinder cones	42
2.7.3	Cones from magma/volatile interaction	46
2.7.4	Mud volcanism and cryovolcanism	49
2.7.5	Glacial/ice and depositional processes	49
2.7.6	Sinuuous ridges	52
2.8	Conclusion	52
3	Topography using MOLA data	56
3.1	Introduction	56
3.2	Instrument and orbital characteristics	57
3.3	MOLA data	58
3.4	Processing, gridding and interpolation	59
3.5	Detrending MOLA topographic data	62
3.6	Conclusion	65

4	Ridges in Isidis Planitia	67
4.1	Introduction	67
4.2	Analysis of ridges	70
4.2.1	Wrinkle ridge morphology	70
4.2.2	Elevation offsets	78
4.2.3	Interaction with other features	79
4.3	Formation of the wrinkle ridges	82
4.3.1	Introduction to ridge formation	82
4.3.2	Stress origin for wrinkle ridge formation	85
4.4	Discussion	86
4.4.1	Nature of the Isidis Planitia subsurface	86
4.4.2	Mascon loading as a formation model	87
5	Craters in Isidis Planitia	93
5.1	Introduction	93
5.2	Crater morphology and morphometry	93
5.2.1	Crater morphology	93
5.2.2	Crater morphometry using IMPACT software	102
5.2.3	Discussion	108
5.3	Craters and stratigraphy	110
5.4	Stealth craters	113

5.4.1	Introduction	113
5.4.2	Stealth craters in Isidis Planitia	115
5.4.3	Discussion	123
5.5	Conclusion	125
6	Spectroscopy and Surface Features	127
6.1	Introduction	127
6.2	Thermal remote sensing	127
6.2.1	Thermal inertia	127
6.2.2	Particle size and rock abundance	129
6.2.3	Mineralogy	133
6.2.4	Discussion	135
6.3	Surface roughness and slope	138
6.3.1	Introduction	138
6.3.2	Surface roughness from MOLA data	138
6.3.3	Slopes	140
6.4	Geomorphology	141
6.4.1	Introduction	141
6.4.2	General features	141
7	Conclusion	150
7.1	Summary of conclusions	150

7.2	Synthesis of ideas	151
7.3	Future research	154
7.4	Final thoughts	157
A	Location of images	158
A.1	Images from Chapter 2	159
A.2	Images from Chapters 4, 5 and 6	161
B	Georectification of THEMIS data	163
C	MOLA PEDR volumes used	166
	References	169
	Production and Software Notes	190

List of Figures

1.1	Isidis Planitia	2
2.1	Cone chains in VOC MDIM 2 images	7
2.2	Cones and cone chains in a high-resolution MOC image	8
2.3	Cones and cone chains in THEMIS infrared images	9
2.4	Cones and cone chains in THEMIS visible images	10
2.5	Areal coverage of cones within Isidis Planitia	11
2.6	Cones in THEMIS image V06251019	13
2.7	Cones in MOC image ab103405	15
2.8	Cones in MOC image ab103405	17
2.9	Cones in MOC images	18
2.10	Cones and cone chains in THEMIS images	22
2.11	Cones and cone chains in THEMIS images	23
2.12	Cones and cone chains on MOLA data	27
2.13	Cones and cone chains on MOLA data	28
2.14	Cones and cone chains on MOLA data	29

2.15 Sinuous ridge in Isidis Planitia	31
2.16 Sinuous ridge in Isidis Planitia	32
2.17 Terrestrial cinder cone	34
2.18 My impression of tuff cones in Isidis Planitia	35
2.19 Possible igneous intrusions in MOC images	45
2.20 Ridges and cone in Isidis Planitia	47
2.21 Pseudocraters in Amazonis Planitia	48
2.22 Pingo and cryovolcano formation	54
3.1 Interpolation of MOLA data	61
3.2 Topography of Isidis Planitia using MOLA data	63
3.3 MOLA topography and interpolated detrended MOLA topography in Isidis Planitia	64
3.4 Detrending of MOLA data	65
4.1 Ridges in Isidis Planitia	68
4.2 Ridges in Isidis Planitia	69
4.3 Ridges in Isidis Planitia	71
4.4 MOLA tracks across ridges	72
4.5 Concentric ridges in Isidis Planitia	73
4.6 Radial ridges in Isidis Planitia	74
4.7 Ridges in Isidis Planitia	75

4.8	Ridge thrust directions in Isidis Planitia	76
4.9	Wrinkle ridges in Solis Planum	77
4.10	Detrended topography across ridges in Isidis Planitia	80
4.11	Ridges in Isidis Planitia using detrended data	81
4.12	Ridges and buried craters in Isidis Planitia using detrended data	83
4.13	Ridges in northeastern Isidis Planitia using detrended data	84
4.14	Lunar wrinkle ridges in Mare Serenitatis	86
4.15	The Isidis Planitia mascon	89
4.16	Nili Fossae	90
5.1	Craters types in Isidis Planitia	95
5.2	Rampart crater topography.	97
5.3	Rampart crater topography.	98
5.4	Rampart crater ejecta in Isidis Planitia	99
5.5	Rampart craters in Isidis Planitia	100
5.6	Pedestal craters	101
5.7	Craters in Isidis Planitia analysed using IMPACT software	103
5.8	The relationship of crater maximum depth plus mean rim height to diameter in Isidis Planitia	105
5.9	The relationship of crater maximum depth to diameter in Isidis Planitia . .	106
5.10	The relationship of crater mean rim height to diameter in Isidis Planitia . .	107

5.11	The relationship of crater morphology to latitude in Isidis Planitia	109
5.12	Impact craters within the Isidis Planitia inner ring	112
5.13	Crater count within the inner plains of Isidis Planitia	114
5.14	Stealth craters	115
5.15	Stealth craters in Isidis Planitia	116
5.16	Comparison between fresh and stealth craters in Isidis Planitia	118
5.17	Stealth and fresh crater topography in Isidis Planitia	119
5.18	Stealth crater in Isidis Planitia	120
5.19	Stealth crater in Isidis Planitia	121
5.20	Stealth crater in south east Isidis Planitia	122
5.21	Crater dunes in Isidis Planitia	126
6.1	Isidis Planitia thermal inertia	130
6.2	Isidis Planitia particle size	131
6.3	Isidis Planitia mineral maps	136
6.4	Isidis Planitia mineral maps	137
6.5	Surface roughness of Isidis Planitia	139
6.6	Gradients in Isidis Planitia	140
6.7	High resolution THEMIS visible images of central Isidis Planitia	143
6.8	High resolution THEMIS visible images of southern Isidis Planitia	144
6.9	High resolution MOC images of southern Isidis Planitia	146

6.10	High resolution MOC images of southern Isidis Planitia	148
6.11	High resolution MOC images of southern Isidis Planitia	149
A.1	Images from Chapter 2	160
A.2	Images from Chapters 4, 5 and 6	162

List of Tables

5.1	Crater-density boundaries and absolute ages for martian stratigraphic series	111
5.2	Crater-density results for Isidis Planitia surface and buried units	117
A.1	List of images used in figures from Chapter 2	159
A.2	List of images used in figures from Chapters 4, 5 and 6	161
C.1	MOLA PEDR Primary Mission volumes used, part 1.	166
C.2	MOLA PEDR Primary Mission volumes used, part 2.	167
C.3	MOLA PEDR Extended Mission volumes used.	168

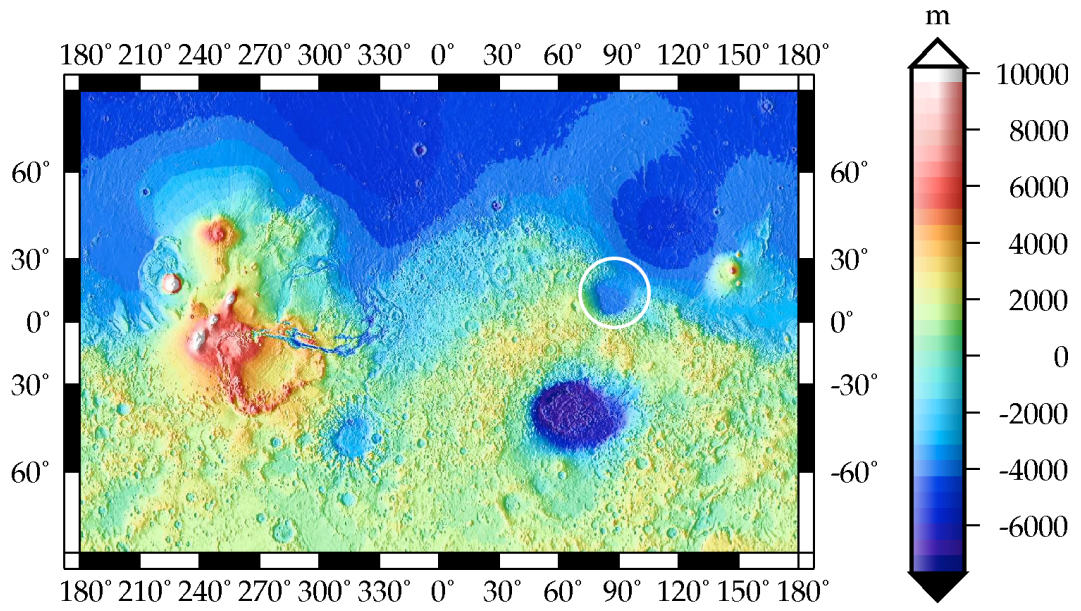
Chapter 1

Introduction

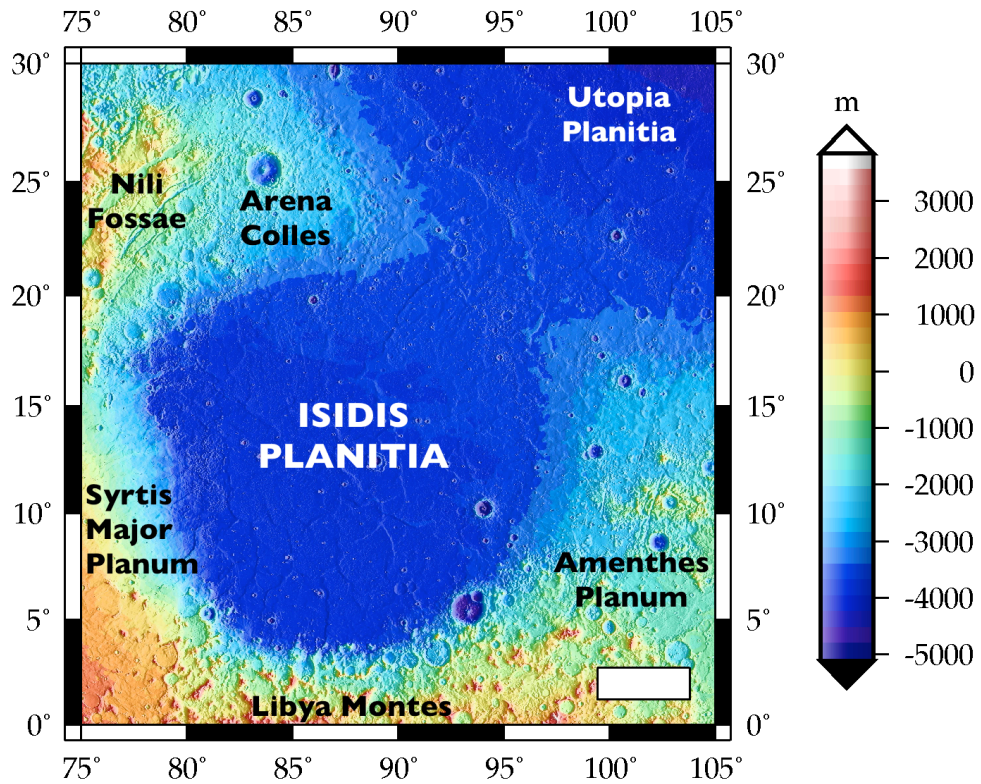
1.1 Isidis Planitia

Isidis Planitia is a large impact basin that straddles the boundary between the ancient heavily-cratered southern highlands and the younger smooth lowland plains of Mars. Figure 1.1 shows its location. It lies in the eastern hemisphere of Mars, east of Syrtis Major Planum - one of the earliest features of Mars to be identified during telescopic observations of the planet. A region named Isidis Regio was first identified on the 1877 map of Mars by Giovanni Schiaparelli, famous for his observations of *canali*. The name Isidis Planitia was officially adopted for the region by the International Astronomical Union General Assembly in 1973. The term ‘Isidis’ is believed to originate from the ancient Egyptian goddess Isis, and ‘Planitia’ denotes a low plain or basin.

Forming the southern contact to the basin are the highlands of Libya Montes, and further south the major highland region of Tyrrhena Terra. A small strip of the Amenthes Planum plains unit lie to the southeast, and to the northeast lies the contact with Utopia Planitia and the wider northern lowland plains. To the northwest lies Arena Colles. There are regions of extensive fracturing around the basin (Nili Fossae to the northwest and Amenthes Fossae to the southeast).



(a)



(b)

Figure 1.1: Isidis Planitia. (a) shows the location (circled) of Isidis Planitia on a Mars Orbiter Laser Altimeter (MOLA) topography map of Mars (see Chapter 3 for further details of the MOLA instrument, data and data processing). (b) shows important locations in the Isidis Planitia basin. Bar is ~ 250 km.

1.2 Previous study of Isidis Planitia

Mariner and Earth-based missions provided early information about the nature of the Isidis Planitia basin. It soon became apparent that Isidis Planitia, along with features such as Hellas Planitia and Argyre Planitia, were comparable to the giant impact basins previously identified on the Moon (e.g. Wilhelms, 1973). The Viking Orbiter Cameras (VOC, Viking Orbiter 1 launched in 1975 and powered down in 1980; Viking Orbiter 2 launched in 1975 and powered down in 1978) provided a more detailed view of structures within the basin itself (e.g. Carr, 1981), as did multispectral data from the Thermal Emission Spectrometer (TES). Further missions, such as Mars Global Surveyor (MGS, launched in 1996, mission ongoing) and Mars Odyssey (MO, launched in 2001, mission ongoing) with their wide range of instrumentation, have added enormously to our understanding of Mars, and data from these missions are used extensively in this thesis to analyse the Isidis Planitia basin.

Study of Isidis Planitia moved into a new phase when it was selected to be the landing site for the Beagle 2 Mars lander (Bridges et al., 2003a). Isidis Planitia was deemed to be the most feasible site for landing once engineering limitations (e.g. near to the equator for maximum sunlight, flat and level terrain, a small number of large rocks, low elevation to allow for sufficient retardation of atmospheric entry velocity) were coupled with scientific considerations. Identification of a number of channels leading into Isidis Planitia from the Libya Montes highlands, together with speculation about outburst floods and possible oceans within the northern lowlands (e.g. Carr, 1996) made landing in Isidis Planitia an exciting prospect. Similar reasoning led Isidis Planitia also to be considered as one of the four final candidate target sites for the Mars Exploration Rover (MER) landers (Golombek et al., 2003a), although sites in Terra Meridiani and Gusev Crater were eventually selected on the basis of combined science and safety evaluations.

One of the foremost questions about Mars is whether it once supported, even temporarily, stable bodies of water on its surface (e.g. Carr, 1996). As part of the northern lowlands, with an altitude well below the planetary datum, and with evidence of channels leading into it from higher ground, Isidis Planitia is a prime candidate for finding evidence of such oceans if they existed. The Isidis Planitia basin is bounded to the west by the large Hesperian volcanic complex of Syrtis Major Planum, and evidence suggests

a possible history involving volcanic deposition within the basin, so there is interest for planetary volcanologists. Isidis Planitia also shows evidence of aeolian activity, possible effects of ice deposition and removal, possible igneous intrusions, resurfacing of the basin by material from the highlands, large fluidised ejecta craters, and many more fascinating features.

1.3 Thesis

In this thesis I examine the geomorphology of many of the features found within the basin, and attempt to identify their nature and mechanisms of origin, in order to derive a broader picture of the evolution of the Isidis Planitia basin, and to understand why it looks the way it does today. In Chapter 2 I investigate the sub-kilometre-sized cones that are found extensively across Isidis Planitia in arcuate chains, clusters and singly, and discuss possible mechanisms of formation and the environments in which these mechanisms could occur.

In Chapter 3 I discuss the Mars Orbiter Laser Altimeter (MOLA) mission and data, and methods I have used to process the data in order to make use of its potential in identifying and characterising martian landforms. Detrended topography maps constructed using techniques from this chapter are used in many of the following chapters of this thesis.

In Chapter 4 I discuss the extensive basin-wide network of ridges that is apparent in detrended topography maps of the area, their mechanism of formation, and their relationship to tectonic events within the basin.

In Chapter 5 I analyse impact craters in Isidis Planitia. This includes the investigation of the ages of the surface and sub-surface units in the basin using crater-counting techniques, the identification of a large number of circular features with subdued topography identifiable in detrended maps of the basin that resemble impact craters, and the gathering of information about surface and subsurface conditions that the geomorphology of impact craters can provide.

In Chapter 6 I collect together information on various aspects of the basin using a variety of data, including using thermal infrared data to identify the size of material

covering the Isidis Planitia basin, the abundance of rocks, and the mineralogy of the basin. I include information on miscellaneous surface features within the basin and their relationship to features discussed earlier in this thesis, and a discussion about dunes and other surface features.

Finally, Chapter 7 summarises some of the most important points made within the thesis, and brings together many of these threads to discuss how, if at all, the features investigated relate to one another in order to identify a coherent history for the basin that explains how the basin looks today. Additionally, I also discuss further research that is needed to support and extend hypotheses developed within this thesis, and some of the prospective missions that may provide exciting new data related to this investigation.

Additionally, there are three appendices that clarify discussions in the main chapters. Appendix A lists all the images used in figures within this thesis, and plots their location within the Isidis Planitia basin on a chapter-by-chapter basis. Appendix B details the georectification of Thermal Emission Imaging System (THEMIS) images and is relevant to the discussion in Chapter 2. Appendix C lists the MOLA data volumes used in Chapter 3.

Chapter 2

Cones In Isidis Planitia

2.1 Introduction

With the availability of high-resolution data of the martian surface, attention has been drawn to the large numbers of small cones found across the planet. These may or may not be of volcanic origin, but may also be as important an indicator of the geological processes at work on Mars as the larger and more famous volcanic constructs found elsewhere on the planet. Small, kilometer- and sub-kilometer scale cones and domes have been observed at several places on the martian surface, including Cydonia/Eastern Acidalia (e.g. Frey et al., 1979), a region near Hellas (e.g. Frey et al., 1981), Chryse Planitia (e.g. Greeley and Theilig, 1978), Deuteronilus Mensae (e.g. Lucchita, 1978), Marte Valles, Cerberus and Amazonis Planitia (e.g. Lanagan et al., 2001) and the Utopia-Isidis-Elysium region (e.g. Frey and Jarosewich, 1982). In this chapter I will consider the cones in Isidis Planitia, their origin, and their use as indicators of past and present surface and subsurface conditions in the basin.

2.2 Viewing the cones

The two Viking Orbiter missions which operated between 1975 and 1980 were, in some respects, overshadowed by the associated Lander missions. However, the Orbiters com-

bined provided more than 2100 orbits worth of imagery data, which involved the imaging of the entire martian surface with their Viking Orbiter Cameras (VOC) at pixel sizes of between 150 and 300 metres, and a few areas down to a pixel size of 8 metres.

Plescia (1980) noted features within Isidis Planitia and Elysium Planitia in several VOC images with pixel sizes of between approximately 20 to 30 metres that resembled terrestrial cinder cones in morphology. It was also noted that these features were circular, capped with a depression, and, in Isidis, could be found individually and in chains. Further observations of the cones also used VOC high- and medium-resolution data, and the global Mars Digital Image Model 2 (MDIM 2) produced from a mosaic of medium-resolution VOC images (see Figure 2.1). Grizzaffi and Schultz (1989) mapped the cones and cone chains in detail, producing a map of the cone chains, which they described as curvilinear ridges, throughout the Isidis Planitia basin.

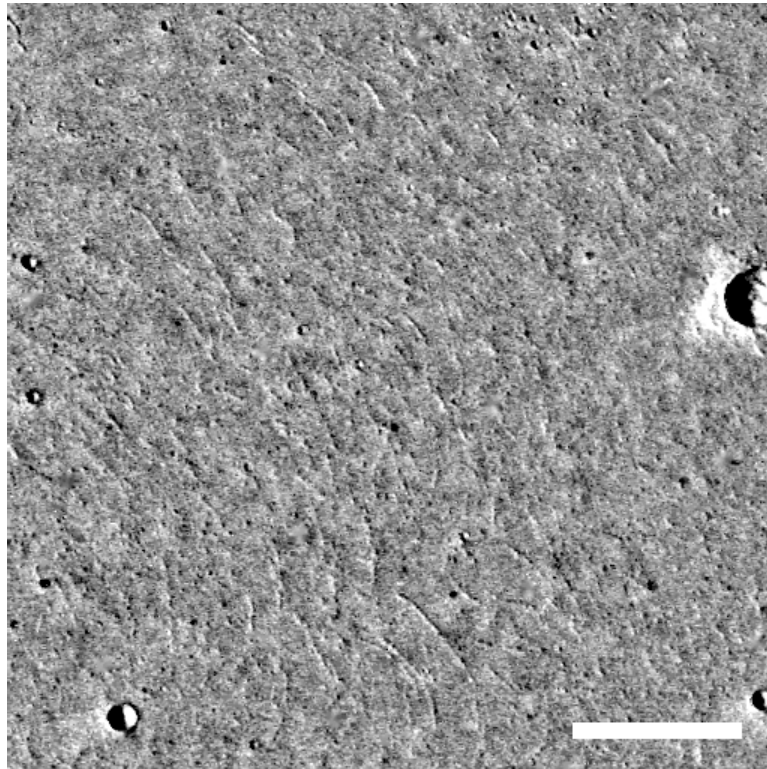


Figure 2.1: Cone chains seen in an VOC MDIM 2 image. This MDIM 2 image mosaic shows the area between 85° to 87° East and 16° to 18° North, located in the north-west part of Isidis Planitia. Bar is 25 kilometers. Extensive fields of cone chains can be seen within this image.

The Mars Global Surveyor (MGS) mission, which was launched in 1996, carried the Mars Orbiter Camera (MOC) (Malin et al., 1992), as well as numerous other instruments. MOC consists of three optical sub-assemblies which provide a single narrow angle and two

wide angle cameras (Malin et al., 1991). Full resolution images from the narrow angle component in the mapping orbit have pixel sizes of 1.4–1.6 metres per pixel, although over a relatively limited area of up to approximately 73 square kilometers. Pixel summing can provide narrow angle camera assembly images of a larger surface area at the expense of resolution. MOC, with its higher resolution than VOC, offers the potential for a more detailed understanding of the nature of the Isidis cones. MOC, along with many of the other instruments on board MGS, has greatly exceeded its mission lifetime, and continues to return valuable data from Mars. Figure 2.2 shows examples of cones and cone chains in MOC images.

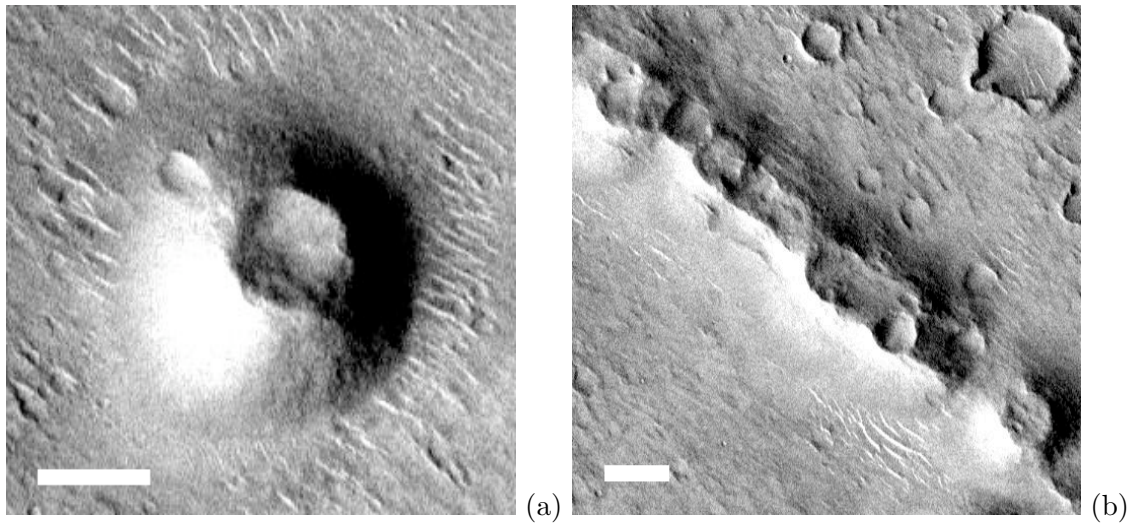


Figure 2.2: Cones and cone chains in a section of MOC image ab103405. (a) shows a single cone in detail. (b) shows a series of cones in a cone chain. The complete original image is centred at 85.96° East, 16.80° North, in the north-west part of Isidis Planitia. Bars in both images are 250 metres.

The Mars Orbiter Laser Altimeter (MOLA) (Zuber et al., 1992) aboard MGS is unfortunately less useful for imaging and interpreting the Isidis cones. Although topographic data for the cones would be very useful, a relatively large footprint size of approximately 150 metres, and an across-track spacing of the MOLA laser shots often of the order of kilometres, mean that the results for features as small as the Isidis cones can be rather inaccurate. However, MOLA data have been used to support investigations into cones which primarily use other data (e.g. Fagents et al., 2002), and are used extensively in this thesis to investigate other features in Isidis Planitia which could be relevant to cone formation in the basin (see Chapter 3).

The Mars Odyssey (MO) mission, launched in 2001, has provided another view of the

Isidis Planitia cones with the Thermal Emission Imaging System (THEMIS) (Christensen et al., 1999), which comprises a ten-band thermal infrared imager with a resolution of 100 metres per pixel (see Figure 2.3), and a five-band visible wavelength imager with a resolution of 18 metres per pixel (see Figure 2.4). At the present time, global coverage for the infrared images is extensive, although less than complete, whereas the visible image coverage is relatively low. However, continuing releases of THEMIS data provide increasing coverage of the martian surface.

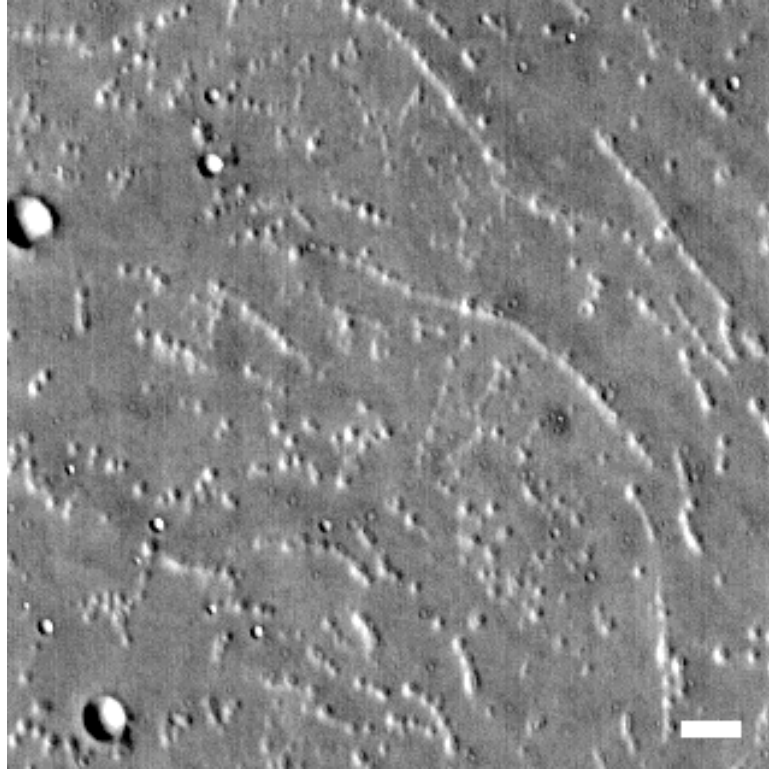


Figure 2.3: Cones and cone chains seen in a section of THEMIS infrared image I01832002. The complete original image is centered at 83.096° East, 14.661° North, in the north-west part of Isidis Planitia. Bar is 2.5 kilometers.

2.3 Previous analyses of cones and cone chains

Extensive analyses of the morphology and distribution of the cones and cone chains throughout the Isidis Planitia basin have taken place. Plescia (1980) described 371 cones with summit craters in Isidis Planitia, grouped into 5 areas with image coverage, along with a further 77 similar features in Elysium Planitia. Plescia (1980) obtained basal diameters and crater/cone diameter ratios for the cones he identified. These measurements are useful for terrestrial cones in assisting the classification of morphologically similar

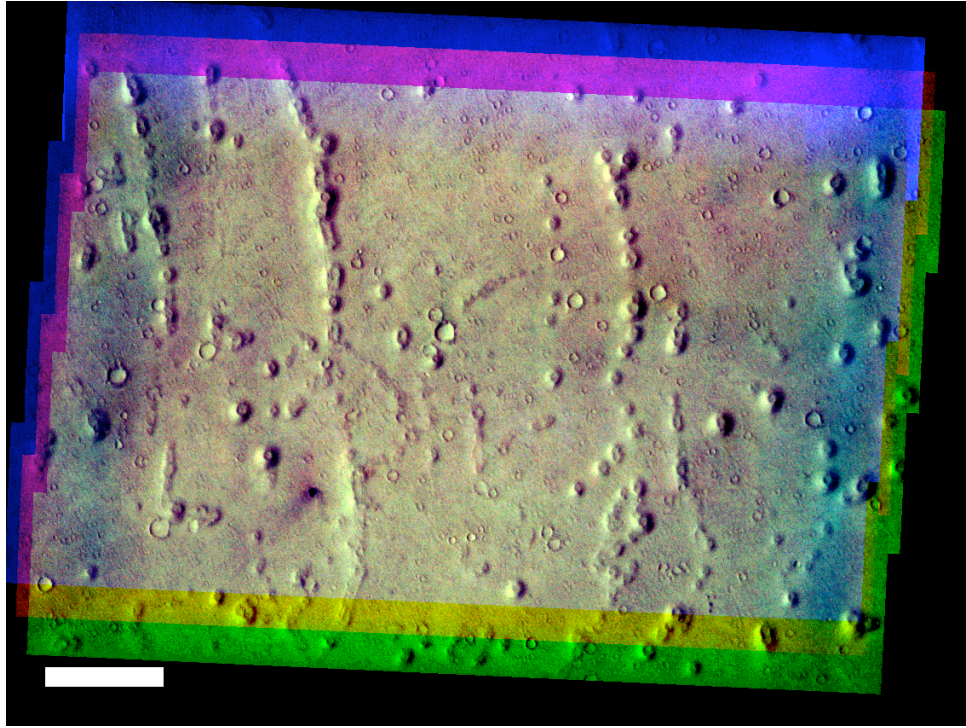


Figure 2.4: Cones and cone chains seen in a colour composite of THEMIS visible image V01807007. I created this false colour composite with the GRASS GIS software using band 2 as blue, band 3 as green and band 4 as red. The image is centered at 84.264° East, 15.946° North, in the north-west part of Isidis Planitia. Bar is 2.5 kilometers.

features such as pseudocraters and cinder cones. The Isidis Planitia cones had a mean basal diameter of between 467 and 578 metres, and mean crater/cone diameter ratios of between 0.415 and 0.465. However, only cones that could be positively identified as having summit craters were included in the study. This may have skewed the results towards showing larger average basal diameters by excluding smaller cones that may have undetected summit craters.

Frey and Jarosewich (1982) identified 666 cones in the Utopia-Isidis-Elysium region that they believed were similar morphologically, although the majority of these cones were in Utopia Planitia. In an analysis of the ratio between summit crater and cone base diameters, they found a sharp peak in the 0.45-0.54 bin, with the 0.35-0.44 bin being the next most common. They also found that the Isidis cones were generally between 300 and 600 metres in diameter – slightly smaller than those in neighbouring areas, but similar enough for their study to group the cones in Isidis together with those in Utopia and Elysium. A tendency for the cones to group in chains was noted.

Grizzaffi and Schultz (1989) identified in Isidis Planitia an inner basin region that

comprised hillocky terrain with many isolated cones and cones often collecting into chains that have a disordered relationship, and a surrounding ridged terrain, composed of a system of parallel curvilinear ridges often formed of individual cones. Ridges were measured to be between 500 and 1000 metres wide, 10 to 40 kilometers long, and 150 to 300 metres high. Mapping of the cone chains revealed the occurrence of the chains throughout the basin except for regions near the basin rim, and near to very large impact craters, and that the chains in the ridged terrain showed a marked degree of non-random orientation. Figure 2.5 shows the approximate distribution of cones within Isidis Planitia by analysing the percentage ground cover of cones in many of the high resolution MOC images of the basin.

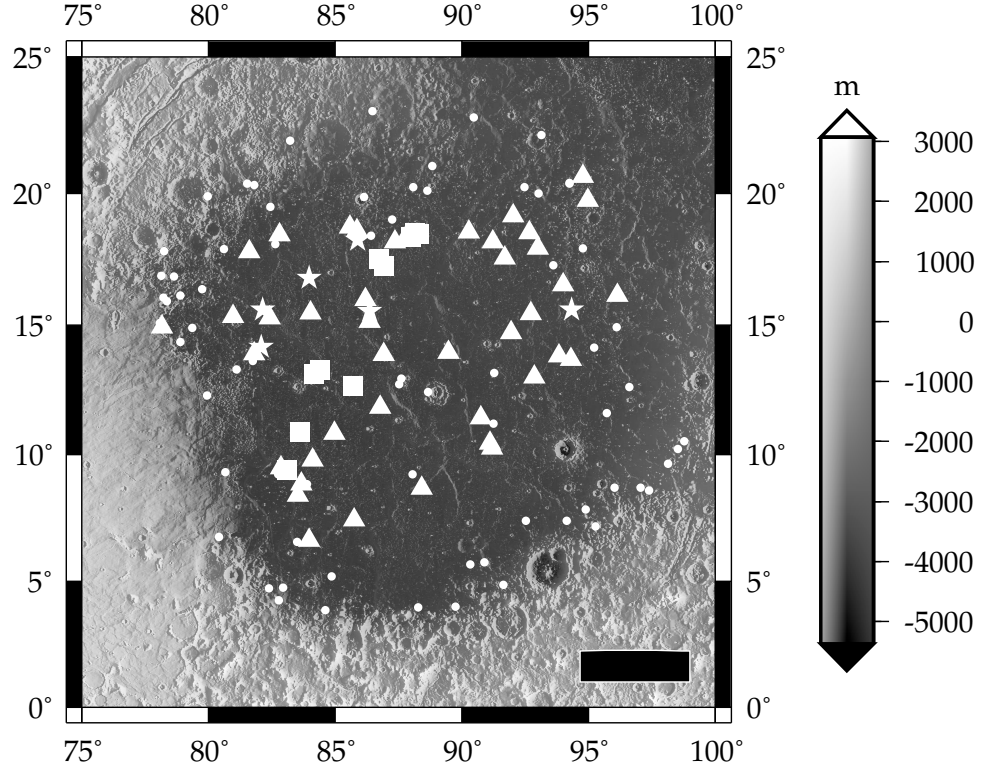


Figure 2.5: Areal coverage of cones within Isidis Planitia. Dots refer to percentage areal extent of cones within high resolution MOC images. Small dots represent images with no cones. Triangles represent 0–5% coverage. Squares represent 5–10% coverage. Stars represent >10% coverage. Bar is ~250 km.

High-resolution MOC images provide very incomplete coverage of the martian surface, although they are very useful in providing closer views of individual cones and cone chains. An analysis of cones using MOC by Fagents et al. (2002) found that the Isidis cones studied have basal diameters of between 200 and 1000 metres, with a peak in the 350 to 399 metre

bin. Cone heights, determined from MOLA altimetry, were found to exceed 25 to 60 metres, although the large footprint of the MOLA laser pulse makes such results inaccurate as the return from a single MOLA laser pulse is likely to include a high proportion of terrain below cone summit height integrated within its 150 metre footprint. The Isidis cones were also identified as being more degraded than similar features analysed in Amazonis Planitia in the same study. Bridges et al. (2003a) also looked at the Isidis cones and deduced from MOC images that the cones could cover up to 13% of the surface area in MOC images, and that higher areal coverages of the cones are found in the western-central part of the basin, with much lower areal coverage in the basin margins (<5%).

Bruno et al. (2004) used a THEMIS image of some of the cones in Isidis Planitia in their study of the mathematical distribution of candidate rootless cone groups on Mars and their comparison with rootless cone fields in Iceland. Figure 2.6 shows part of the THEMIS image used. It should be noted that this image does not show as many of the cone chains as other images of cones within the basin display (compare Figure 2.4). Bruno et al. (2004) used nearest neighbour analysis to determine the ratio of the mean actual distance between a cone and its nearest neighbour, and the confidence estimate in the departure from randomness for the Isidis Planitia cones suggested that the cones were strongly aggregated with a significant departure from randomness, and show some degree of linear cone alignment. A study of impact craters using the same techniques for control purposes showed that these display no evidence of aggregation and are randomly distributed, as expected.

2.4 Analysis of cones and cone chains using MOC data

There are several dozen high resolution MOC images of cones and cone chains within Isidis Planitia. One of the best, and one that clearly demonstrates several typical features of the cones, is image ab103405, obtained on 4th November 1997 during the Aerobraking and Science Phasing Orbits subphase of the mission. Details from this image appear in Figures 2.7, and 2.8, as well as in Figure 2.2.

Figure 2.7(a) shows two of the larger and more pristine cones to be found in high-

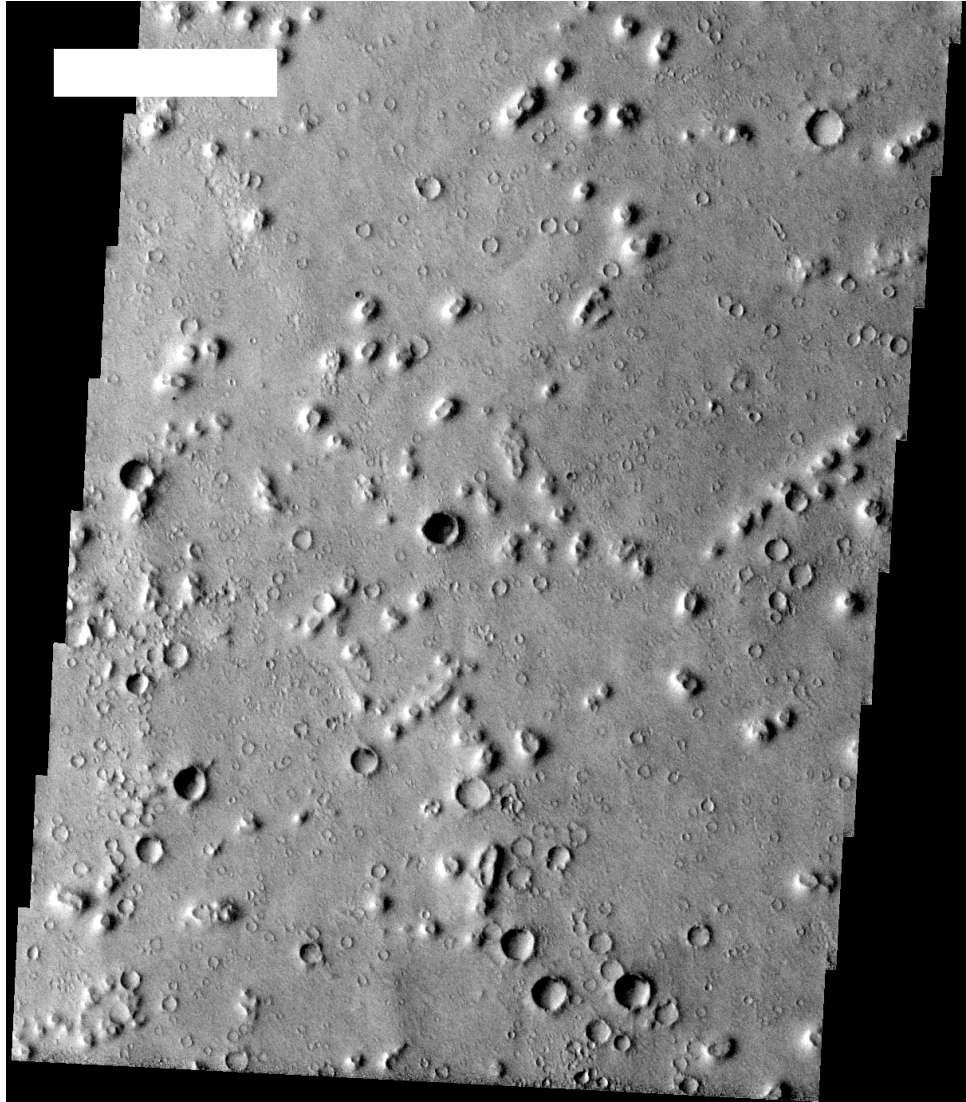


Figure 2.6: Cones in THEMIS image V06251019. Part of a THEMIS visible image used by Bruno et al. (2004) to study the mathematical distribution of candidate rootless cones fields on Mars. The complete original image is centred at 84.8° East, 11.6° North. Bar is 5 kilometres.

resolution MOC images of Isidis Planitia. To give some indication of the dimensions, the larger cone has a basal diameter of 684 metres, and a bowl-shaped summit pit 272 metres wide, with a crater-cone ratio (diameter of the summit pit/diameter of the cone base) of 0.40. The summit crater does not appear perfectly centered on the cone, and the cone is not perfectly circular, appearing elongated towards the bottom-left of the image. This could be distortion caused by viewing the cones at an oblique angle. However, the emission angle of this particular image is 0.51° – very close to a perfect nadir view. Calculating the height of the rim of the cone from the shadow length and solar incidence angle (72.03° for this image) gives a result of approximately 49 metres, and a resulting slope angle for the right hand side of this cone of approximately 13° . The smaller cone has a basal diameter of approximately 482 metres, a shallower-appearing summit crater of approximately 195 metres diameter, with crater-cone ratio of approximately 0.40. The smaller cone's summit crater does appear centred and the cone itself is more circular than the larger example. The rim height of the cone is approximately 47 metres, with a steeper slope angle of approximately 18° . However, estimating dimensions from shadow lengths has several potential problems. These include the difficulty of identifying the edge of the shadow by taking into account the effects of the umbral and penumbral components of the shadow, and the effect of sloping terrain on apparent shadow length.

The cones themselves sit on relatively smooth, flat and fairly sparsely cratered terrain. Those craters easily visible are in the tens to hundreds of metres diameter range and appear fairly eroded and perhaps mantled by dust. Smaller impact craters are visible, but are generally very subdued, particularly in the area between the two cones, which appears very smooth. A very small (~ 20 metres), fresh looking impact crater appears on this surface, just south of the larger cone, illustrating the likely erosional or depositional nature of the surface. The area around the bases of the cones appears to be smoother still, and there are noticeable dunes around the larger cone, and to a much lesser extent the smaller cone. These could be the result of aeolian mobilisation of smaller diameter material produced by the formation of the cones (see Chapter 6, Section 6.4 for further discussion of aeolian features within Isidis Planitia), or by drifting of dust and/or sand against a positive relief feature.

Figure 2.7(b) shows parts of two cone chains. The one to the right of the image

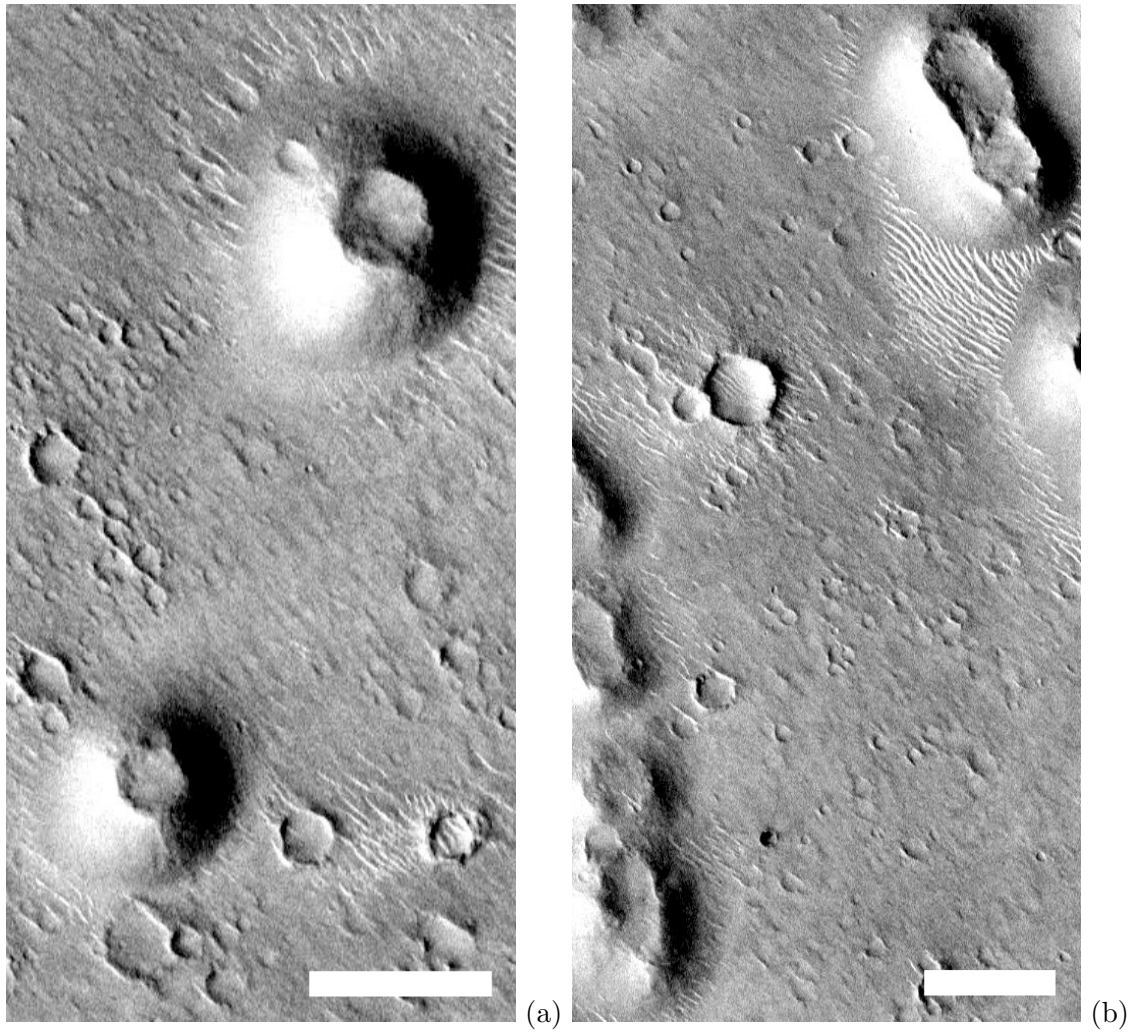


Figure 2.7: Cones in MOC image ab103405. Two areas in detail from MOC image ab103405 showing cones and cone chains. The complete original image is centred at 85.96° East, 16.80° North, in the north-west part of Isidis Planitia. Bars in both images are 500 metres – note the slightly different scales of the two images.

is as pristine as the cones in Figure 2.7(a), with a distinct ‘double cone’ nature. The components of this ‘mini chain’ have dimensions that are harder to quantify due to their orientation, but they are of a comparable size to the cones in Figure 2.7(b). The shadow cast by the cones indicates a height of approximately 25 metres, and the summit crater has a noticeably raised rim profile. There are extensive dunes surrounding the components of this chain, particularly between the ‘double cone’ and the off-image continuation of the chain.

The second cone chain in Figure 2.7(b) lies at the left of the image and despite lying within 2 kilometres of the first is very different in morphology. The cones here appear more eroded, and do not have the pristine slopes that those elsewhere in the image do. The flanks and rims of the cones appear eroded, and the summit craters appear irregular.

Figure 2.8(a) shows a section of a cone chain that traverses the image. This chain appears in a less degraded state than that in Figure 2.7(b), and the elements making up the chain are generally closer together. The cones appear to all have fairly distinct summit pits that converge to some extent, but the cones themselves have shapes that merge to a greater extent. Again, there are areas of dunes surrounding the cones. Note also the separate, larger, cone near the chain.

Figure 2.8(b) shows an interesting cone chain that forms an inverted ‘Y’ shape. The ends of the cone chains nearer the bottom of the image appears slightly more eroded than that in Figure 2.8(a), and perhaps more so even than the eroded chain in Figure 2.7(b), but still shows distinct cone shapes with summit craters. Further towards the top of the image, after the two arms of the ‘Y’ have joined, the cones appear less well formed, to the extent where they barely resemble cones – appearing as mound-like hillocks, and do not have such obvious summit craters. They are also spread out, although still obviously aligned as a chain. It is possible that the cones in this image are the result of two generations of cone formation.

Figure 2.9 shows some detail from two other MOC images. Figure 2.9(a) shows a single cone near a cluster of considerably more degraded cones, asking questions about the relationship between cones of different degradational states. Figure 2.9(b) shows another situation similar to that in Figure 2.7(b), with cones of differing apparent degradational

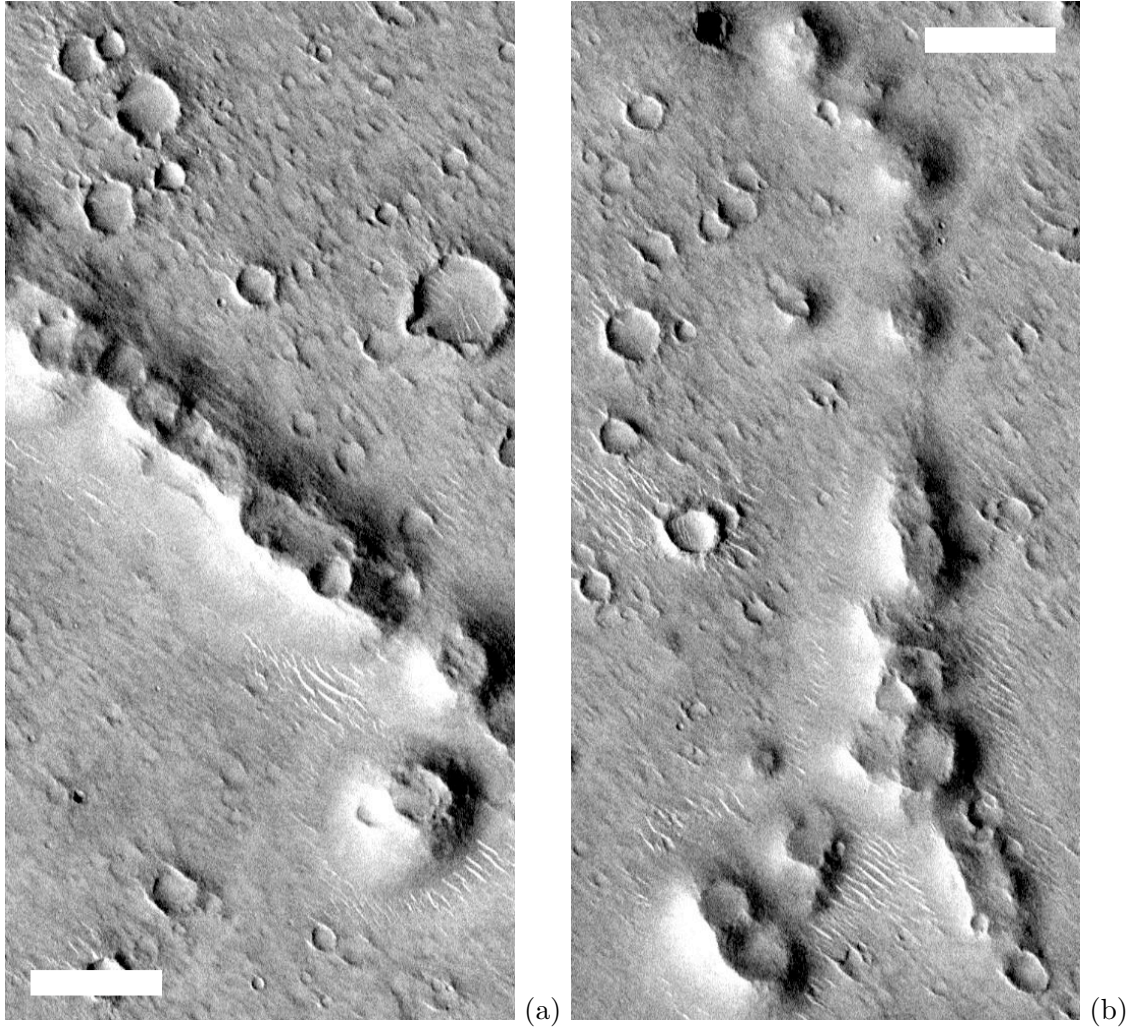


Figure 2.8: Cones in MOC image ab103405. Two areas in detail from MOC image ab103405 showing cones and cone chains. The complete original image is centred at 85.96° East, 16.80° North, in the north-west part of Isidis Planitia. Bars in both images are 500 metres.

states appearing in close proximity to one another. In this case three relatively pristine individual cones are within a few kilometers of a cone chain that appears very degraded and subdued.

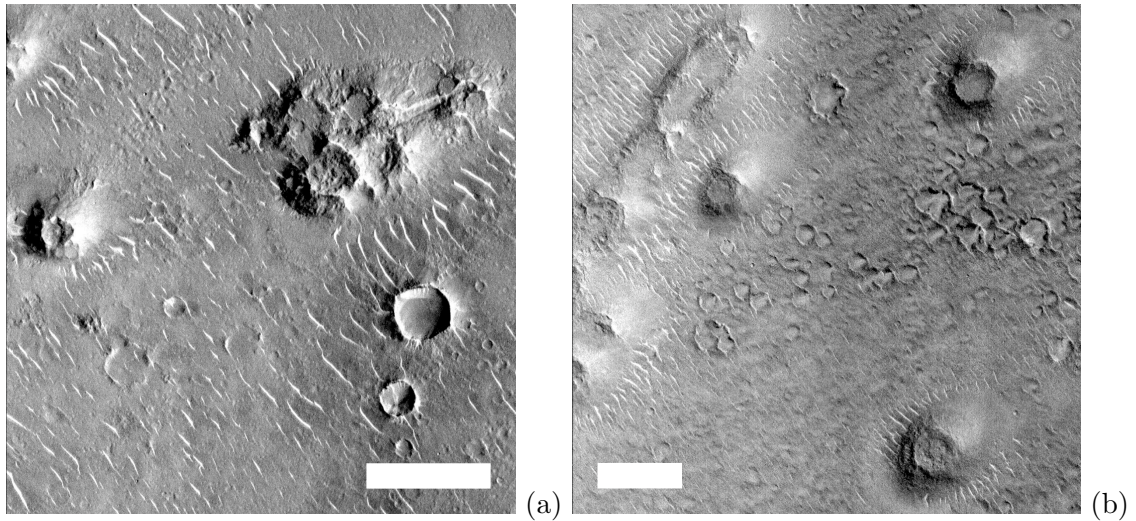


Figure 2.9: Cones in MOC images. (a) shows detail from MOC image m0302859 showing a single cone and eroded cone cluster. The complete original image is centred at 91.12° East, 10.43° North, in central south-west Isidis Planitia. (b) shows detail from MOC image m0901055 showing several cones near an eroded cone chain. The complete original image is centred at 85.71° East, 12.65° North in central west Isidis Planitia. Bars in both images are 500 metres.

Visual analysis of just these few MOC images show a wide variety of morphologies of cones, occurring both singly, in clusters and in chains. Given the close proximity of different types of cone (e.g. those appearing pristine and those degraded or unformed), and the mixture of types even within the same chain, I believe it is reasonable to conclude that the differences in morphologies, at least over small areas, are unlikely to be due to differences in degradational rates over similar timescales, and are therefore most likely to be the result of differences in the method of formation – producing different morphologies of cones, or differences in the age of formation – which implies a history of cone forming events.

Additionally, MOC images may be used in estimating ages of the cones by crater counting (see Chapter 5, Sections 5.2 and 5.3 for further details of cratering in the basin and using crater counts to identify surface ages respectively). From an initial visual inspection of the cones in the MOC images, it is apparent that they are less heavily cratered than the terrain they sit upon (Bridges et al., 2001), which implies a younger age for the cones than the surrounding terrain. However movement of poorly consolidated

material could obscure craters and make the slopes appear younger than they actually are.

2.5 Analysis of cones and cone chains using THEMIS data

THEMIS data complement the MOC coverage of the basin. Coverage by the 18 metres per pixel visible THEMIS images is sparse but, where available, these provide a useful multi-spectral view of the cones (e.g. Figure 2.4). The ~ 100 metre per pixel infrared THEMIS images provide comparable resolution and coverage to VOC images, although are subjectively sharper, and have a greater dynamic range (VOC returned 7-bit data, giving 128 grey levels, and THEMIS returns 8-bit data, giving 256 grey levels). In addition, many of the infrared THEMIS images are multi-spectral, and THEMIS infrared images are returned from both daytime and nighttime passes.

THEMIS data are distributed to scientists and the public at the Planetary Data System website (<http://pds.jpl.nasa.gov>) and at the Arizona State University THEMIS website (<http://themis-data.asu.edu>). The data are provided as raw images, radiometrically calibrated images, and derived brightness temperature images, with the multi-spectral datasets distributed in a three-dimensional format (samples, lines and spectral bands) (Murray et al., 2003). The data are also distributed as simple image files derived from brightness temperature data and provided in a standard image file format.

With its almost complete ~ 100 metres per pixel coverage of the basin, the THEMIS data archive provides a good basis for an overview of the distribution of the cones and cone chains with the basin. Cones and cone chains are distributed unevenly across the basin, with regions of the basin showing no cones at all, and others exhibiting very dense coverage. The most densely covered areas are generally in the western half of the centre of the basin. Generally there are lower densities of cones towards the basin rim, with areas containing no cones at all in parts of the rim next to the highlands in the south and amid the knobby terrain near Syrtis Major.

The areas near the southern rim are also high thermal inertia areas (see Chapter 6, Section 6.2 for further discussion about the thermal remote sensing of Isidis Planitia),

and are interpreted as areas where deposition of material from the highlands has taken place (Crumpler et al., 2002). Cones are rare in the southern rim of the basin and this could be due to a variety of reasons. The cones could have been buried, perhaps by material from highland areas surrounding the basin entering the basin and covering the terrain nearest the basin edge. Another possibility is that material deposited in this region of the Isidis Planitia basin could have prevented cone formation. If the cones were formed by near-surface processes, significant burial of the surface could conceivably prevent the cones from forming. Finally, it is possible that subsurface conditions in this region of the basin may not be conducive to cone formation.

The chaotic terrain found in western Isidis Planitia has been interpreted as a region where Upper Hesperian volcanism from Syrtis Major Planum covered an area of the western Isidis Basin, and the superposition of volcanic material upon the postulated volatile-rich deposits of the Vastitas Borealis formation within the basin led to the formation of the present terrain of mesas, and removed the volatile component of the pre-volcanic surface (Ivanov and Head, 2003). Therefore if the cones post-date the Upper Hesperian and are formed by a process or processes involving volatiles, then this could explain their absence in this region.

I have also used individual THEMIS images for simple photogeologic investigation, complementing the high-resolution MOC images. For example, both day- and night-time infrared THEMIS images are available of the area surrounding the footprint of MOC image ab103405 (see Figures 2.7 and 2.8) – enabling the image to be put into a wider context, albeit at a lower resolution. Figure 2.10(a) shows the daytime image covering this area. Features visible in the higher resolution MOC image ab103405 are easily identifiable. This broader view of the cones and cone chains seen in MOC image ab103405 shows that the cones are located upon terrain that is very smooth at the resolution of the THEMIS images (~100 metres per pixel), with very few visible impact craters. There are clusters of cones visible, but many of the cones are aligned in broad arcuate chains, many of which appear to be oriented in similar directions and with similar degrees of curvature. This is the ‘thumbprint’ terrain described by many researchers (e.g. Kargel et al., 1995). Figure 2.10(b) shows the nighttime image covering a similar area. This has less dynamic range than the daytime image, and features are more difficult to identify, but it does show

the major chains visible in Figure 2.10(a) clearly. A more detailed discussion about the comparison of day- and nighttime THEMIS images can be found later in this chapter in Subsection 2.5.1.

Figure 2.11(a) shows the area surrounding a large infilled impact crater. Further discussion of such buried impact craters takes place in Chapter 5, Section 5.4. However, this THEMIS image shows that the cones do not appear affected by the presence of such a large filled impact crater. On closer inspection, some of the cones at the edge of the crater appear to be split by the fractures found along the rim, but the distribution and orientation of the cones within the crater and in the surrounding area appear similar. The cones in Figure 2.11(a) are similar to those in Figure 2.10(a), although there are far fewer cone chains. Figure 2.11(b) shows an area further to the south where the cones and cone chains exhibit a slightly different morphology. Here, they appear on raised platforms in terrain that appears more undulating. This could be an erosional feature – the material between the chains being preferentially eroded, or it could be a result of the formation style of the cones here – subsurface activity causing bulging of the terrain, with the cones forming on top of the ‘bulges’.

2.5.1 Comparison of daytime and nighttime THEMIS infrared images

The THEMIS instrument is used to take nighttime as well as daytime images. The daytime infrared images are dominated by the albedo of the surface (Wyatt et al., 2003b) and lighting effects caused by the solar illumination angle, whereas the nighttime images can be used as a estimate of thermal inertia (Mustard, 2003). For an accurate qualitative measure of true thermal inertia, a thermal model incorporating latitude, albedo, solar angle, and elevation must be created (Ferguson and Christensen, 2003), but for a first-order analysis of the surface’s thermophysical characteristics, interpreting the nighttime THEMIS images alone, and comparing them with daytime THEMIS infrared images, and high-resolution MOC visible images can be useful (e.g. Farrand and Gaddis, 2003).

The analysis of a nighttime infrared THEMIS image – in this case I06732011 (see Figure 2.10(b)) – may contribute some useful clues as to the nature of the Isidis cones. The cones and cone chains appear bright in the equivalent daytime infrared THEMIS image

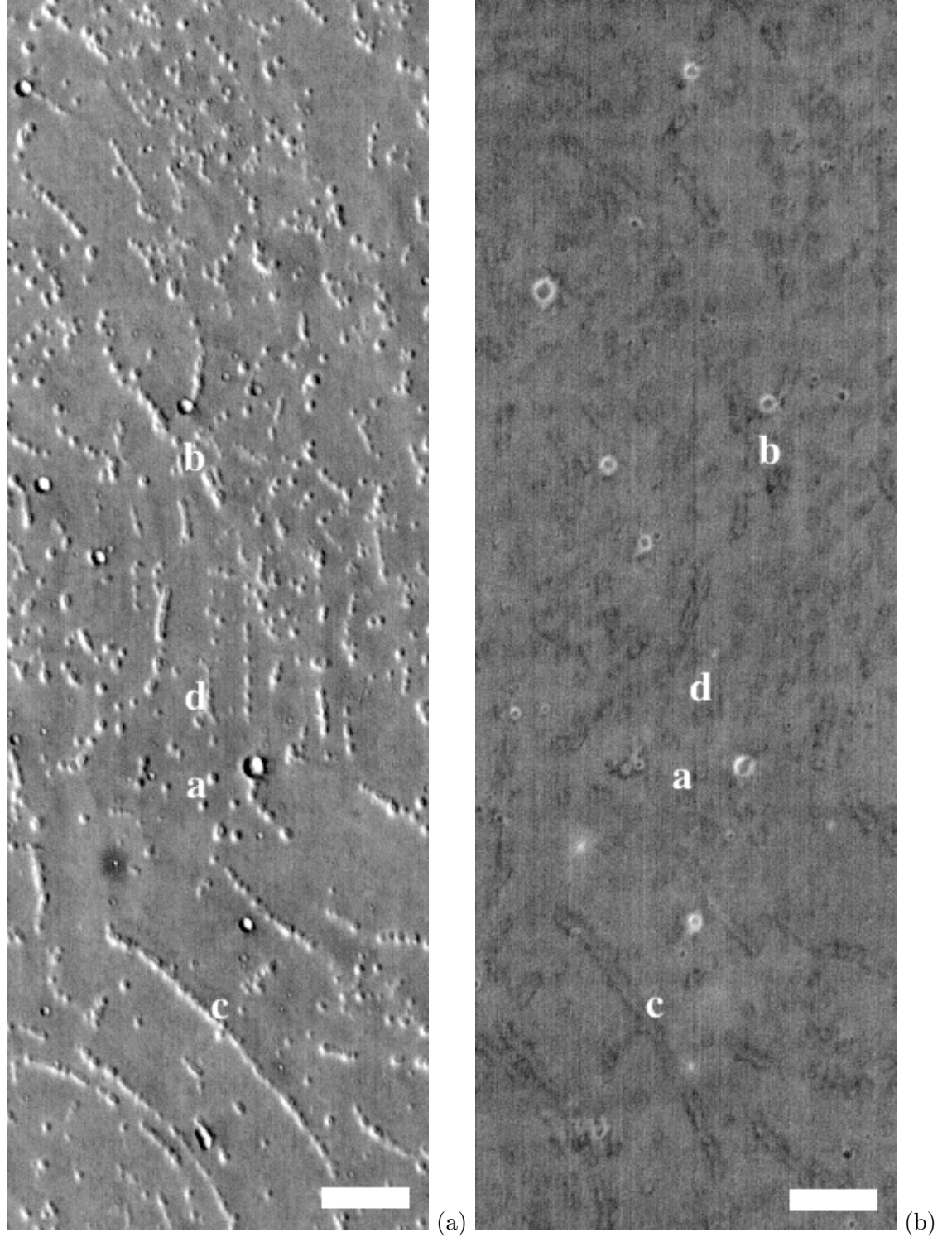


Figure 2.10: Cones and cone chains in THEMIS images. (a) shows detail from THEMIS daytime infrared image I01807006. (b) shows detail from THEMIS nighttime infrared image I06732011. Both images cover the area of MOC image ab103405 used earlier in the chapter, and the surrounding area. Note that the images are not georectified and are oriented slightly differently. Letters on the images refer to sections of MOC image ab103405 used elsewhere in this chapter – ‘a’ refers to Figure 2.7(a), ‘b’ refers to Figure 2.7(b), ‘c’ refers to Figure 2.8(a), and ‘d’ refers to Figure 2.8(b). Bars in both images are 5 kilometres.

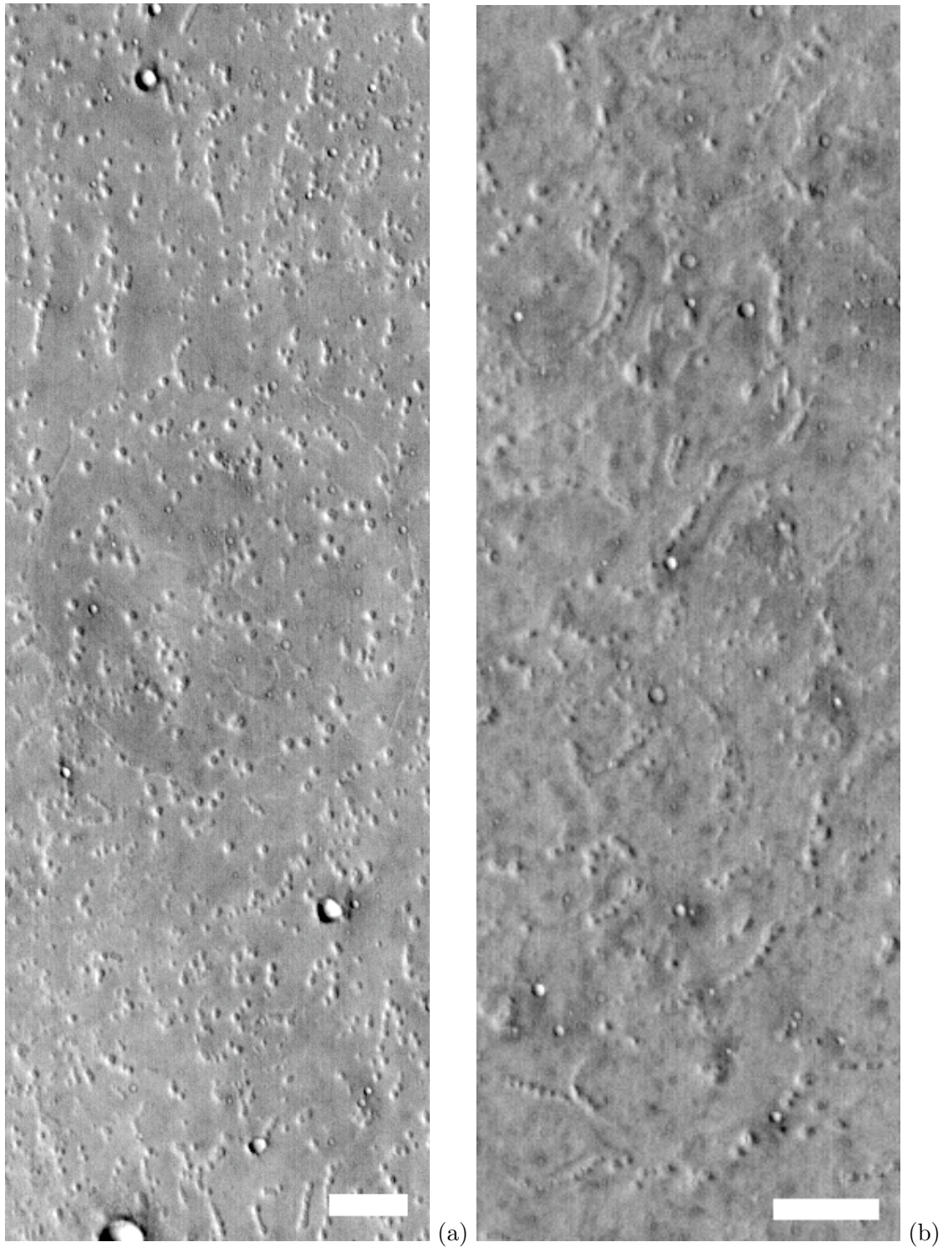


Figure 2.11: Cones and cone chains in THEMIS images. Both images show detail from THEMIS daytime infrared image I01782005. (a) shows the area surrounding a large buried impact crater. The crater is the large circular area in the centre of the image, occupying most of its width, and edged by thin fractures. (b) shows an area of cones and cone chains that appear on raised terrain. Bars in both images are 5 kilometres.

(see Figure 2.10(a)) mainly as a result of their positive relief and the subsequent heating of slopes facing the sun. In the nighttime images the cones and chains appear to have summit pits of approximately similar brightness temperature to the surfaces surrounding the cones, but with noticeably darker, and therefore lower brightness temperature, flanks. This contrasts with the impact craters of comparable size in the image, which have very bright (and therefore higher brightness temperature) inner slopes, and interiors that appear to be the same temperature as the surrounding surface, or much colder.

Given the first-order relationship between brightness temperature and thermal inertia for the nighttime images, the lower brightness temperature flanks suggests that the cone flanks are composed of, or mantled by, material with a lower thermal inertia, such as finer-grained dust or sand. This fits with the idea of the cones being constructed explosively, and suggests that the grains their flanks are composed of, or mantled by, are finer, or less well cemented, than the grains comprising the surface the cones sit upon. The bright inner slopes and darker bowls of the impact craters in the images suggest high thermal inertia inner slopes – most likely bedrock, and bowls with a similar thermal inertia to the surrounding plains, or in the case of deeper craters, lower thermal inertia, suggesting infilling with fine, uncemented aeolian material. Unlike similar investigations into pitted cones in Acidalia Planitia and Cydonia Mensae (Farrand and Gaddis, 2003), my study shows no sign of bright, irregularly shaped, flow-like features on the surface of the nighttime THEMIS images in Isidis Planitia.

A quantitative approach to determining thermal inertia from nighttime THEMIS images in the absence of a comprehensive thermal model has been suggested by Farrand et al. (2004). This involves determining a thermal inertia value for the plains areas surrounding a feature using thermal inertia derived from TES data (Mellon et al., 2002). Identification of an average grey value for the plains area surrounding cones and impact craters on a THEMIS image of the same area gives a point of reference. Assuming that the nighttime images show a linear response to emissivity, one can make an estimate of the likely thermal inertia of features with a differing greyscale. This is an inaccurate method, but nevertheless may be useful in providing supporting evidence for various theories of cone formation.

My results from analysing the features in the area of THEMIS image I06732011 show

the average thermal inertia of the plains in this area to be approximately 240 to 290 $\text{J m}^{-2} \text{s}^{1/2} \text{K}^{-1}$. The thermal inertias of the flanks of the cones and cone chains were estimated to be substantially lower at between 120 and 220 $\text{J m}^{-2} \text{s}^{1/2} \text{K}^{-1}$, although there are isolated areas where thermal inertia appears to be as low as 50 $\text{J m}^{-2} \text{s}^{1/2} \text{K}^{-1}$. Thermal inertia for the tops of the cones and cones chains were estimated to be between 160 and 250 $\text{J m}^{-2} \text{s}^{1/2} \text{K}^{-1}$. These results are consistent with the plains surfaces having a thermal inertia approaching coarse sand, and the cone flanks having thermal inertias approximating fine sand, and in some locations approaching that of dust (Mellon, 2001). However, these results do not take in consideration the effect of induration, which will increase the thermal inertia of a surface substantially. It is therefore entirely possible that the cone flanks are composed of material that is simply a loosened, and less indurated version, of that forming the surface of the surrounding plains.

2.5.2 Analysis of georectified THEMIS infrared images

Given the good coverage of the THEMIS instrument at medium resolutions using the infrared imager, the instrument is ideal for investigating the cone chains. At the time of conducting my research using THEMIS images, no geometric information for THEMIS images was available, other than a simple centre coordinate, which made any comparison between THEMIS data and data from other instruments awkward. In order to prepare a meaningful comparison between data sets I georectified the THEMIS images using interpolated MOLA topography data I had prepared previously (see Chapter 3 for further information on the retrieval and processing of the MOLA topographic data). The combination of THEMIS infrared and MOLA topographic data was carried out using the powerful open source geographic information systems (GIS) package GRASS (Neteler and Mitasova, 2002). Details of the processing are given in Appendix B.

Figures 2.12, 2.13 and 2.14 show the results of this processing – cones and cone chains identified from two daytime infrared THEMIS images, and overlain upon an interpolated MOLA map which has been detrended to remove the regional slope (see Chapter 3 for further information on detrending the MOLA topographic data). These figures can be used to identify any correlation between topography – particularly the wrinkle ridges, which after impact craters and the basin tilt probably represent the most important large-

scale morphological features within Isidis Planitia – and the cone and cone chains (see Chapter 4 for further details regarding the nature and origin of the wrinkle ridges).

An important factor to note in these figures is that the larger cone chains may make a significant contribution to the returned height of a MOLA pulse, and so some of the topography shown in the Figures, particularly that of smaller extent, may be a result of the cones and cone chains themselves rather than simply the terrain they sit upon. Obviously in this instance a correlation between topography and cone chains will be apparent with the cones appearing on an elevated ridge. However, the larger-scale wrinkle ridge features shown are much broader than the cone chains, and any correlation between the wrinkle ridges and cone chains may be significant.

Figure 2.12 shows the northernmost extent of the cones in this region. The two THEMIS images actually extend northwards, beyond the northern edge of this image, and indeed beyond the boundary of Isidis Planitia itself, but cones and cone chains are not found north of approximately 19° North. Additionally, some of the chains found at the basin rim may be sinuous ridges rather than cone chains. These features are discussed later in this chapter in Subsection 2.5.3, but appear broadly similar to cone chains at lower resolutions. Further south, the cones and chains in both THEMIS images present a fairly disordered appearance, until in the left hand THEMIS image the chains appear to form roughly concentric curved chains oriented with their outer concave curved surface towards the north-east. This is in contrast to the underlying ridge which runs north-south. Further south in Figure 2.13, the orientations of the right-hand THEMIS image in the northernmost 25 kilometers of this image show more concentric curved chains, this time oriented with their outer concave curved surfaces towards the east, and an underlying ridge oriented northwest-southeast. Another east-west ridge further south shows more apparent parallel orientation of chains, and there also appears to be some parallel orientation of ridges in the northern part of the left hand THEMIS image. Figure 2.14 probably yields the most interesting information. For both of the THEMIS images here, the cone chains seem to be aligned in concentric patterns oriented with their convex surfaces facing southwest in the left-hand THEMIS image and south-east in the right-hand THEMIS image, with detail in the MOLA topographic map between the two images suggesting that chains here were oriented southwards, completing a broad sweep of chains oriented in an almost

semi-circular pattern. This pattern is broken where it meets the north-south ridge at the western edge of the left-hand THEMIS image.

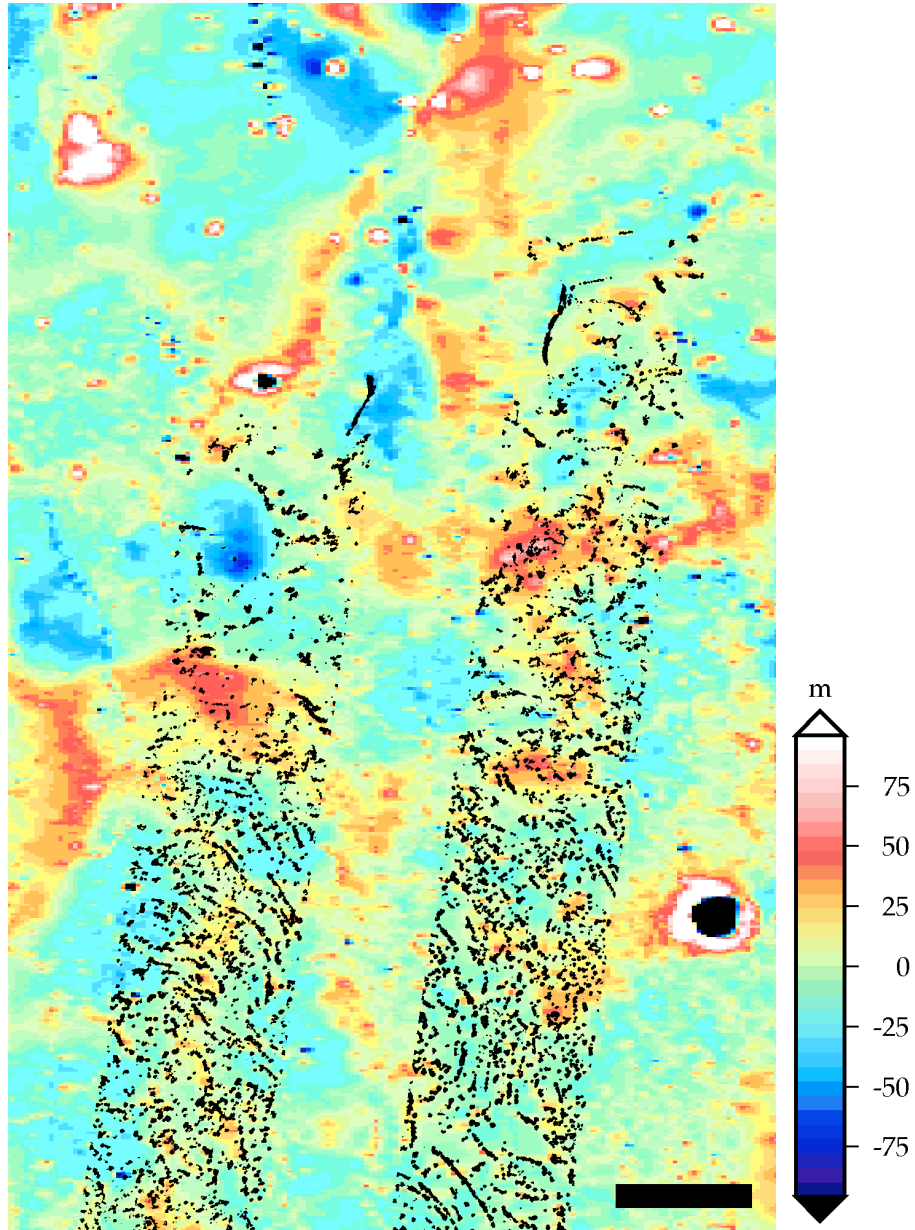


Figure 2.12: Cones and cone chains on MOLA data. Image shows cones and cone chains identified from THEMIS daytime infrared images I0101832002 (left) and I01807006 (right) superimposed on detrended interpolated MOLA data showing wrinkle ridges. Area shown is from 82.5° East to 85° East, and 16° North to 20° North. Bar is 25 kilometers.

Although not obviously aligned with the ridges in most places, the ‘thumbprint’ or almost concentric appearance of many of the cones chains suggests a large scale orientation of the cones. This may reflect the pattern of flatter areas bordered by the major wrinkle ridges rather than the ridges themselves. For example, given the situation at 10° to 11° North, there is an obvious area of terrain bordered to the south and southwest by a

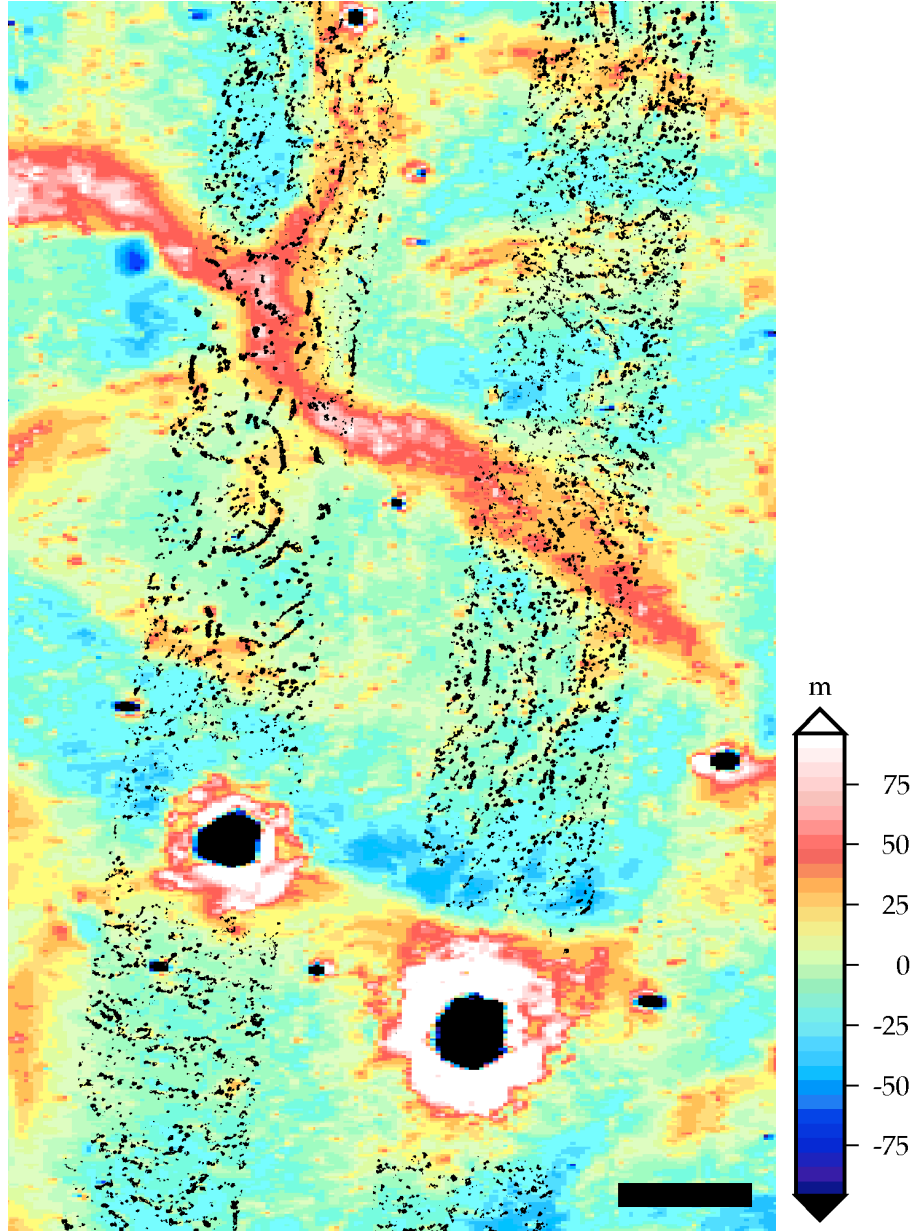


Figure 2.13: Cones and cone chains on MOLA data. Image shows cones and cone chains identified from THEMIS daytime infrared images I0101832002 (left) and I01807006 (right) superimposed on detrended interpolated MOLA data showing wrinkle ridges. Area shown is from 82° East to 84.5° East, and 12° North to 16° North. Bar is 25 kilometers.

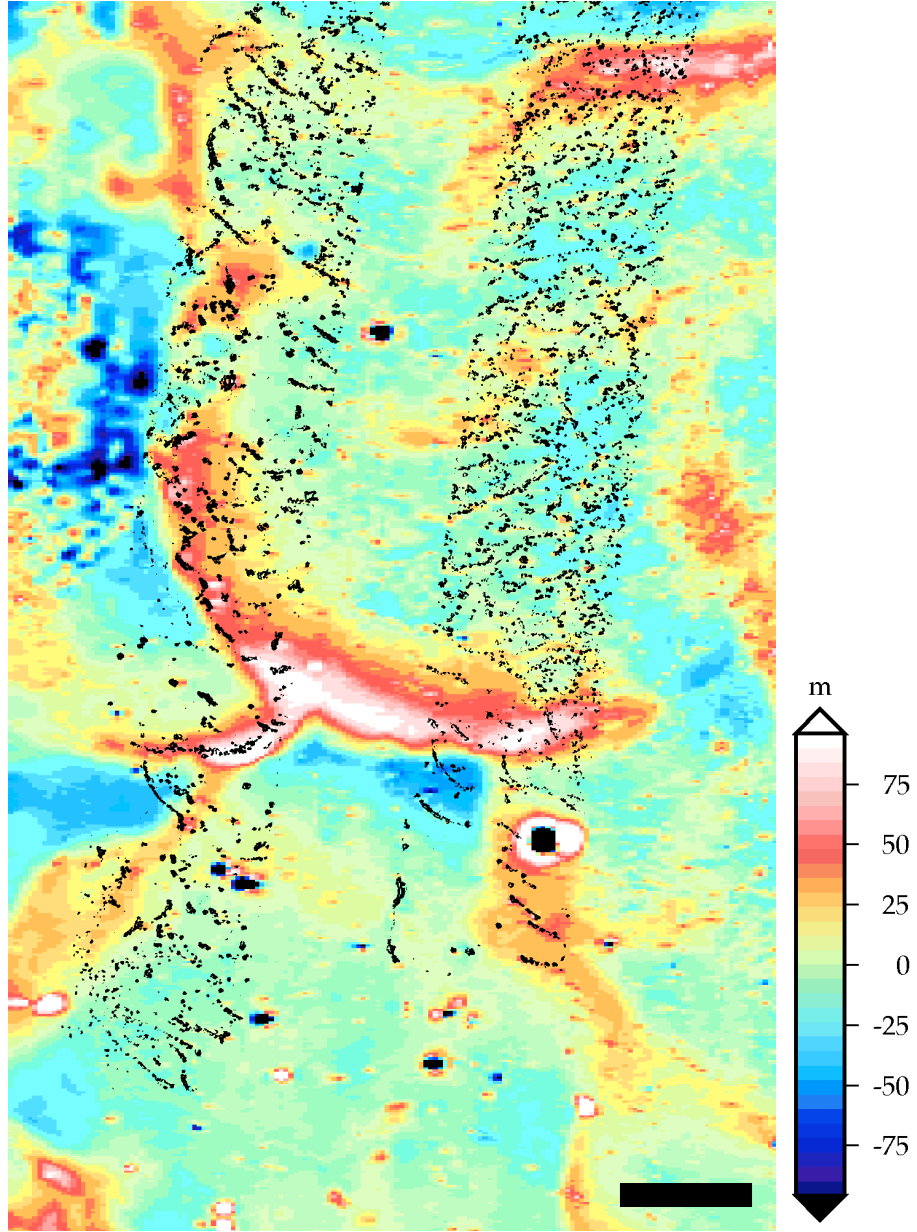


Figure 2.14: Cones and cone chains on MOLA data. Image shows cones and cone chains identified from THEMIS daytime infrared images I0101832002 (left) and I01807006 (right) superimposed on detrended interpolated MOLA data showing wrinkle ridges. Area shown is from 81.5° East to 84° East, and 8° North to 12° North. Bar is 25 kilometers.

curved wrinkle ridge which has an inferred direction of thrusting towards the south and southwest (see Chapter 4, Subsection 4.2.1 for further discussion of the wrinkle ridges thrust directions). However, the pattern of cone chain orientation within this area reflects a similar orientation. Unfortunately, the wrinkle ridges and their enclosed flatter areas form very complex overlapping patterns, and identifying the wrinkle ridges as a mechanism involved in controlling the orientation of the cone chains is fraught with difficulty. The wrinkle ridges are interpreted as being Early Hesperian in age, and stratigraphically pre-dating the surface upon which the cones themselves sit (see Chapter 5, Section 5.4 for a discussion about dating the buried unit). This implies that any influence that the wrinkle ridges may have on cone chain orientation is as a result either of the effect of the ridges on subsurface composition or on surface topography, rather than as active fault-generating thrusts. However, it is possible that faulting in the buried unit as a result of the compressional forces that formed the wrinkle ridges could allow fluid seep to take place if there were suitable reservoirs of volatiles (Okubo et al., 2003). Overall, it appears that there is no clear control on cone chain formation by the ridges, although a connection between the ‘thrust direction’ of the ‘lobate’ areas of terrain between wrinkle ridges and cone chain orientation cannot be entirely ruled out.

2.5.3 Sinuous ridges

There are other positive relief features in Isidis Planitia which may relate to the cones in the basin, or may have origins that can contribute to the discussion regarding cone formation. Features described by researchers as sinuous ridges are found in Isidis Planitia, and also elsewhere on Mars, such as in Dorsa Argentea near the martian South Pole (e.g. Head, 2000; Head and Hallet, 2001b). In Isidis Planitia these features are found mainly at the northern, western and southern rims of the basin, usually in areas without significant numbers of cones or cone chains. Figures 2.15 and 2.16 show a sinuous ridge in Isidis Planitia. Sinuous ridges broadly resemble the curvilinear ridges of cones in the basin, but where multiple sinuous ridges exist they are not usually oriented parallel to each other, they tend to form narrow medial ridges that form in a trough, they are far more symmetrical about the long axis of the ridge, show no sign of being composed of individual structures, and they tend to have a more ‘winding’ appearance than the cone chains, which generally

only have a simple curve.

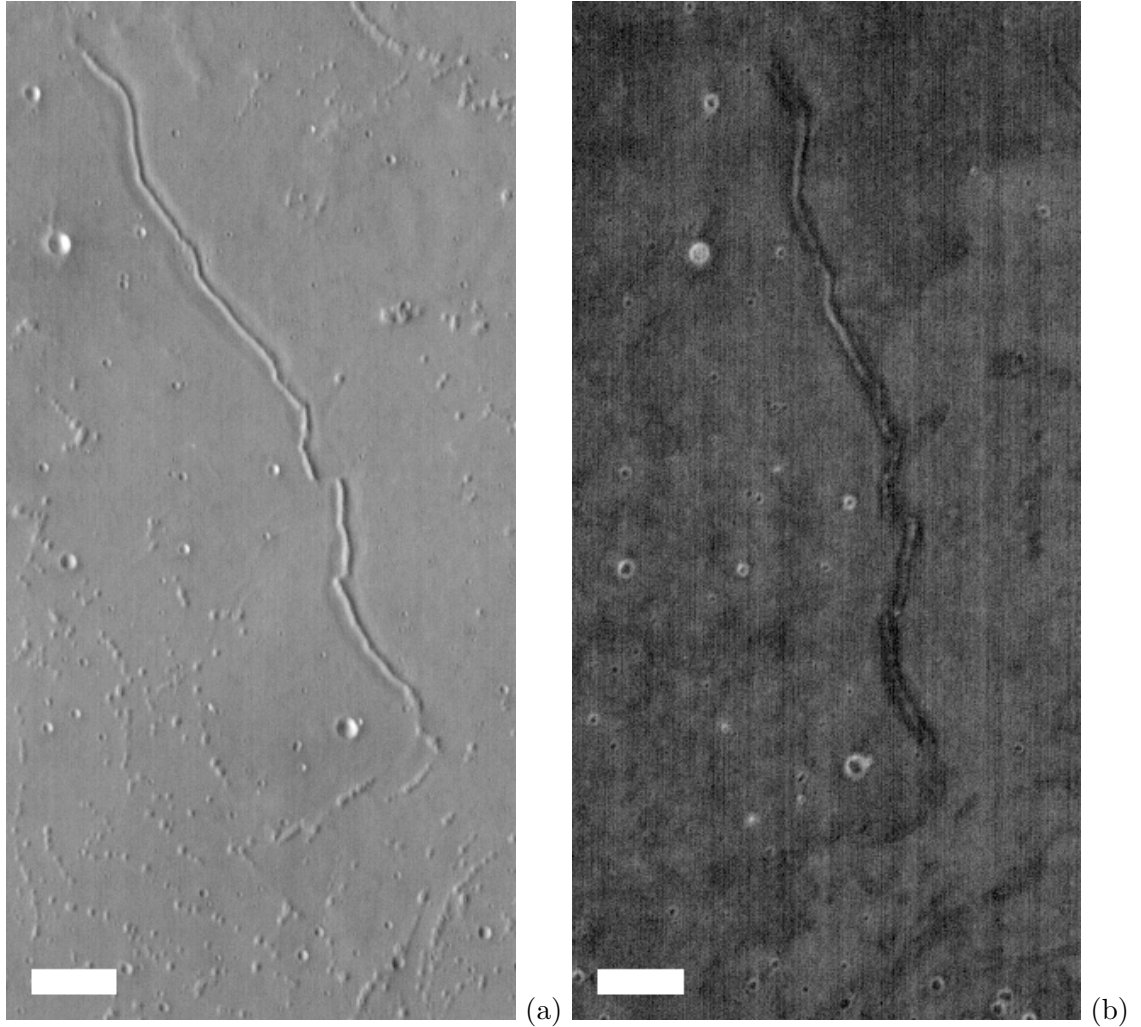


Figure 2.15: Sinuous ridge in Isidis Planitia. (a) shows detail from THEMIS daytime infrared image I05215009 showing an example of a sinuous ridge in north-western Isidis Planitia. Note the possible discontinuities along its length, and compare to the short cone chains in the bottom-right of the image. (b) shows detail from THEMIS nighttime infrared image I06757009 showing the same sinuous ridge as in (a). Bars in both images are 5 kilometres.

Some of the sinuous ridges in Isidis Planitia are branching, although the one in Figures 2.15 and 2.16 is not, although interestingly this ridge appears displaced at least once, and possibly twice. There is little other sign of faulting visible in relation to this displacement of the ridge. The trough that the ridge sits in is best seen in Figure 2.16(a). Small numbers of cones and cone clusters are visible in Figures 2.15 and 2.16(a), approaching to within a few kilometres of the ridge itself.

The infrared view of the sinuous ridge implies that the ridge flanks are composed of very low thermal inertia material compared with the plains it sits upon, and lower than that

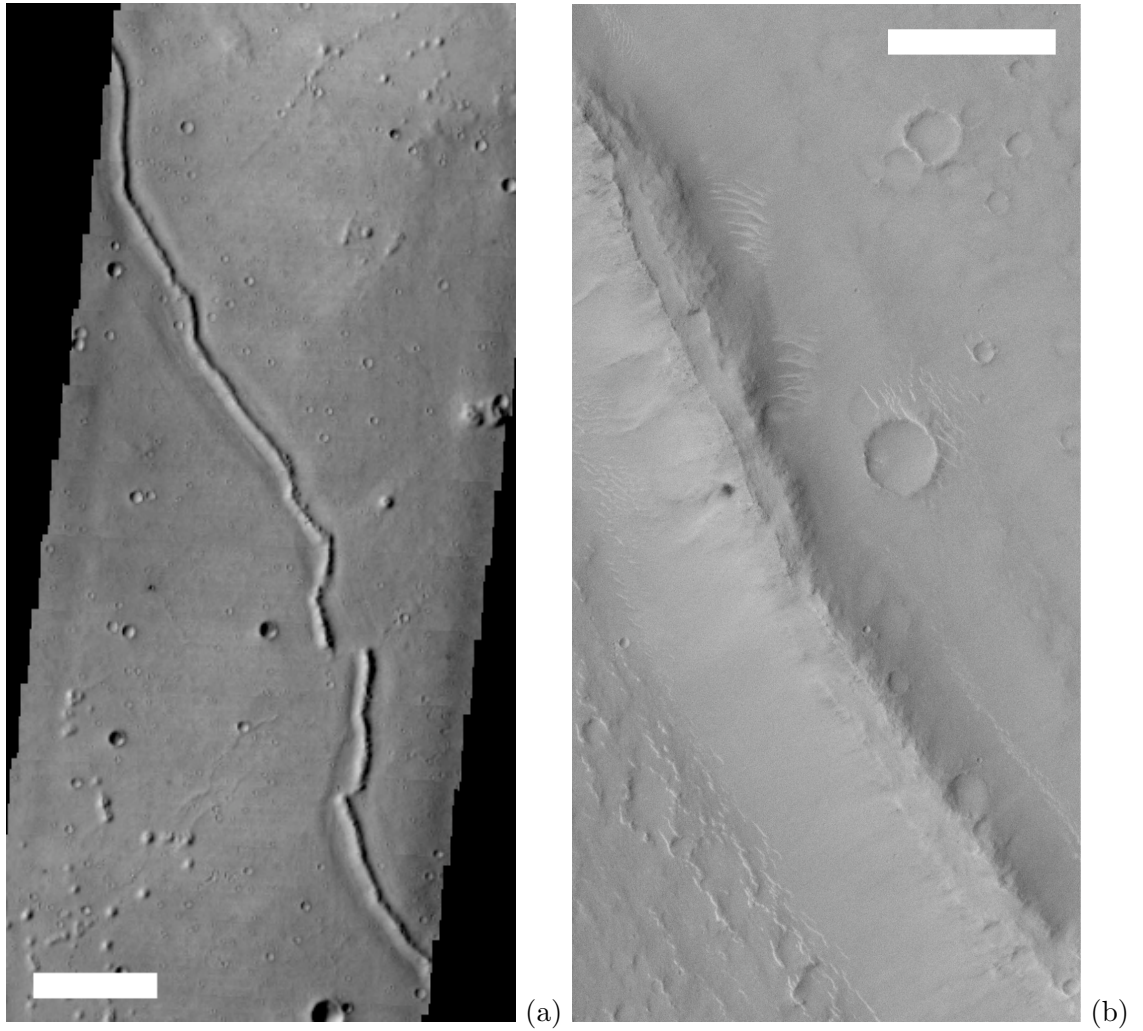


Figure 2.16: Sinuous ridge in Isidis Planitia. (a) shows detail from band 4 ($0.749 \mu\text{m}$) of the THEMIS visible image V05215010 showing the same sinuous ridge in north-western Isidis Planitia as Figure 2.15. Bar in this image is 5 kilometres. (b) shows detail from MOC image fha00994, showing a section across the same sinuous ridge. The complete original image is centred at 82.69° East, 18.35° North in the north-west of Isidis Planitia. Bar in this image is 500 metres.

found on the flanks of nearby cone chains. The ridge crest, at least in part, is composed of much higher thermal inertia material than the surrounding plains, unlike the thermal inertia of the centre of cone chains, which appears generally higher than the cone chain flanks, but lower than the surrounding plains. This implies the crest of the sinuous ridge comprises material that either has a larger grain size, or is more welded than is found in most cone chains. The trough generally appears to have slightly lower thermal inertia than the surrounding plains, which is perhaps to be expected for a feature with negative topography in a region where aeolian activity is expected.

2.6 Cone and cone chain formation

There are several different hypotheses describing the processes that lead to the formation of the cones in Isidis Planitia. Chiefly, these fall into four broad categories – that the cones are formed by the explosive eruption of magma resulting in the build up of a scoria, or cinder, cone (e.g. Plescia, 1980); that the cones are formed by an interaction between water, or another volatile, and magma or lava, or magmatic heat, resulting in either a rootless feature such as a pseudocrater, or a rooted feature such as a tuff cone (e.g. Frey and Jarosewich, 1982); that the cones are formed by a ‘sedimentary’ eruption resulting from buried subsurface volatiles, analogous to terrestrial mud volcanoes and similar processes not necessarily requiring magmatic heat (e.g. Davis and Tanaka, 1995); or finally, that the cones are formed by a non-eruptive process of ice and/or debris accumulation and modification or an intrusive process involving ice, resulting in features analogous to moraines and/or pingos (e.g. Grizzaffi and Schultz, 1989). There is also the possibility that more than one of these mechanisms is responsible for the formation of the cones across such a large area as Isidis Planitia.

2.6.1 Cinder cones

On Earth, cinder cones (see Figure 2.17) are formed by fragmented gas-charged lava being erupted from a single vent, with the pyroclastic fragments, or scoria, falling around the vent to form a cone. Most have a summit crater. Cinder cones on Earth are typically

relatively small, rarely being more than a few hundred metres to their summit. Spatter cones, commonly found in chains or ridges, are also features formed by explosive volcanism in the same way.



Figure 2.17: The terrestrial cinder cone Pu'u ka Pele, Hawaii, USA. This cone is located on the flank of the volcano Mauna Kea volcano, and is 95 metres high with a crater diameter of 400 metres. Credit: Photograph by J.P. Lockwood on 1 December 1975, USGS.

One of the first comparative studies of monogenetic volcanism on Mars and other terrestrial planets (Wood, 1979) did not specifically identify any cinder cones in Isidis Planitia, although martian cones in other areas were identified within the broader category of pyroclastic cones (which include spattercones, pseudocraters and maars). In an associated paper, Wood (1980) identified an average cone basal diameter of 800 metres, and an average crater/cone ratio of 0.40 for 910 terrestrial cinder cones. In comparison, the results from Fagents et al. (2002) show that the Isidis Planitia cones have, on average, only half the basal diameter of terrestrial cinder cones. However, work by Wood suggested that crater/cone ratios should be similar in terrestrial and martian cones, which is borne out in these studies, if indeed these are the product of explosive volcanism. However, Wilson and Head (1994) suggest that strombolian eruption styles such as these would form broader and lower cones than on the Earth, resulting in a lower crater/cone ratio if the crater is assumed to be of comparable size.

One of the first specific references to possible cinder cones in Isidis Planitia was by Plescia (1980), who identified 371 cones with summit craters in several high-resolution VOC images. This study also suggested that the arrangement of the cones in chains may be a result of the concentration of cones along fractures or subsurface faults. Subsequently,

investigation of explosive volcanism on Mars has concentrated on different locations, and not much work has been carried out relating the Isidis cones to terrestrial cinder cones.

2.6.2 Cones from magma/volatile interaction

Several types of terrestrial geological features are formed by the interaction of lava, or magmatic heat, and volatiles (in the terrestrial case, water or ice – with a resulting phreatic, or steam-driven, explosion). Pseudocraters are rootless volcanic cones formed by lava flowing over water, or a surface containing water such as a marsh. Examples of terrestrial pseudocraters include the structures found at Lake Mývatn, Iceland, which were formed when lava flowed into a shallow lake. The resulting steam explosions formed several conical structures of varying sizes (Thorarinsson, 1953; Greeley and Fagents, 2001). Tuff cones, tuff rings and maars are another series of hydrovolcanic constructs found on Earth. They are formed when surface water interacts with a volcanic vent to produce a steam explosion. Maars are very shallow cones, with crater floors below the original ground level, and may appear to be large craters with very little rim or cone shape. Tuff rings have a crater floor above the original ground level, and more built-up rims. Tuff cones are tuff rings with a further buildup of the cone structure to form a feature more resembling a cinder cone (Sheridan and Wohletz, 1983). The differences in morphology of these features are a result of differences in eruption conditions (Sohn, 1996), such as availability of water (e.g. Sheridan and Wohletz, 1983; Wohletz, 1986). Figure 2.18 shows how tuff cones would have looked if they formed in a martian environment with shallow water present.

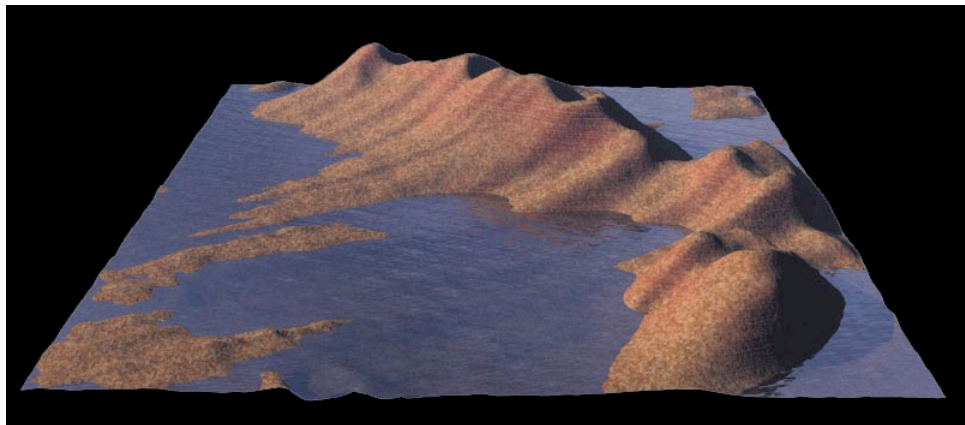


Figure 2.18: Artists impression of tuff cones in Isidis Planitia. Image created using shape from shading on cones from MOC image ab103405 (see Figure 2.8(a)).

Interpretation of some of the small cone-like features as being the result of interaction between magma and volatiles was briefly suggested by Wood (1979) in his study of features generated by monogenetic volcanic activity on terrestrial planets, but it was Frey et al. (1979) who carried out the first major study of features analogous to terrestrial pseudocraters found in Cydonia Mensae. Frey and Jarosewich (1982) expanded this research and looked at small martian cones found in several locations, including Isidis Planitia, and on the basis of their crater/cone ratio determined that they were most likely pseudocraters. A pseudocrater origin has also been suggested for cones found in Elysium Planitia (Mouginis-Mark, 1985). No maars have been positively identified on the martian surface, although differences in martian environmental conditions may have resulted in the martian analogues of terrestrial maars being difficult to differentiate from non-volcanic features such as impact craters (Mitchell and Wilson, 1998). More recent work on the Isidis Planitia cones by Rothery et al. (2001) suggested that the cones may be tuff rings. Greeley and Fagents (2001) compared cones on Mars with pseudocraters in Iceland, Fagents et al. (2002) compared the Isidis Planitia cones with similar structures interpreted to be pseudocraters in Amazonis Planitia, and Bridges et al. (2003a) favoured a tuff cone explanation. The analysis of the spatial distribution of cones within cone fields on Mars, including those in Isidis Planitia, carried out by Bruno et al. (2004) showed that the distribution of cones was statistically indistinguishable from that of Icelandic pseudocrater groups.

2.6.3 Mud volcanism and cryovolcanism

Mud, or sedimentary, volcanism is the intrusion and extrusion of fluid-rich sediments as a result of their relative buoyancy compared to the surrounding lithology (Kopf, 2002). Mud volcanism is widely distributed on Earth, with mud volcanoes found in many varying environments, both onshore and offshore. Terrestrial mud volcanoes show a number of features in common regardless of their location – these include the presence of rapidly deposited, overpressured sediments and the presence or introduction of fluids. On Earth, many mud volcanoes occur at convergent plate margins, where conditions are favourable to the rapid deposition of fluid-rich sediments. However, as far as is known comparable conditions do not exist on Mars, and are unlikely to have done so during the timescale of

cone formation in Isidis Planitia.

Mud volcanism has only relatively recently been suggested as a means of formation of cone-like features on Mars. Davis and Tanaka (1995) suggested that the curvilinear ridges were analogous to terrestrial mud volcanoes, and formed as a result of the rapid filling of Isidis Planitia with volatile-rich sediments, and the resulting overpressuring of the sediments and the forcing of fluidised sediments up along fractures produced by the basin formation. Their study was carried out before the availability of data from MGS, and incorrectly determined that a low percentage of the cones within chains had summit craters, using this to support their assertion that the cones chains were mud volcanoes. Higher resolution MOC images suggest that this is not the case.

Terrestrial mud volcanoes, as opposed to more slowly emplaced sedimentary intrusive and extrusive features, are associated with the confinement and subsequent release of fluid pressure within the ascending sediment (Kopf, 2002). This mechanism requires a seal, which ultimately fails and results in an explosive phase which produces the volcanic edifice shape (Ori et al., 2000). Work by Ori et al. (2001) looked at the possibility that the mud volcanic formation model for the Isidis Planitia cones may involve the presence of reservoirs of subsurface gas and/or gas bearing water driving the eruptive process, with a possible seal being gas hydrates, which may be stable in the martian subsurface (e.g. Kargel et al., 2000).

Hoffman et al. (2001) also suggested a mechanism for formation for the Isidis cones based upon the rapid infill of the basin by fluidised sediments, resulting in overpressure and subsequent fluid escape through fissures. As well as comparing the cones to terrestrial mud volcanoes, this study also suggested CO₂, rather than water, as the fluidising agent, which when confined by an impermeable seal is stable in the martian subsurface. The removal of this seal would result in the explosive eruption of the decompressed CO₂ and associated crustal materials in a form of ‘cryoslurry’ (Bradak and Kereszturi, 2003), a form of volcanism known as cryovolcanism. Gaidos (2001) also proposed confined aquifers at depths of several kilometres as being potentially responsible for cryovolcanism at the martian surface, suggesting planetary cooling, volcanism, climate change and tectonics as possible mechanisms that could result in ascent of water to the surface.

Crumpler (2003) suggested that the Isidis cones could be analogous to terrestrial spring deposits, where a highly fractured upper crust would allow fluid flow and aquifer development. Spring deposits, perhaps in the form of pitted mounds or cones, could form where faulting or less permeable rocks enable an aquifer to release to the surface. Kreslavsky and Head (2002) suggested that the overpressure necessary for the ascent of material to be erupted at the surface could be generated by weight of ice and/or an expanding freezing front causing overpressure in a sediment-rich liquid water layer in the near subsurface, or by extrusion of brine-rich melts during the subliming of an ice sheet. Tanaka and Skinner (2003) put forward the notion of water- and steam-charged clastic discharges driven by near-surface concentrations of volatiles. Gas dominated mud volcanism taking place along tectonic arcs is suggested to have formed the cone chains in Isidis Planitia.

2.6.4 Glacial/ice and depositional processes

The terrestrial glacial or ice-related depositional features thought to be particularly analogous to those found on Mars include moraines – a wide range of features which are the result of debris deposition by glaciers, eskers – long ridges resulting from the deposition of material from sub-glacial streams, pingos – ice-cored hills, and other related forms. These are common in previously glaciated or periglacial conditions on Earth (e.g. Bennett and Glasser, 1996). Jöns (1987) suggested that the depositional environment for the cones and cone chains results from mud lakes or mud sheet flows emerging from Syrtis Major. Grizzaffi and Schultz (1989) discussed the cones and cone chains as being the result of the deposition and subsequent removal of a thick layer of volatile-rich transient air-fall deposit. In their model, the curvilinear cone ridges are terminal moraines – sediment deposited at the margin of a glacier – and which are subsequently modified by ice movement, forming push moraines, or by the downwastage of debris from subliming ice forming ice-cored ridges (Rossbacher and Judson, 1981). The ice-cores would sublime to leave craters. Backwasting of the ice would produce more or less parallel sets of recessional moraines, with increasing backwasting likely to produce more random distributions of deposited sediment as the glacier shrank. A similar origin for the cones, but from a different source, is put forward by several researchers who also suggest a moraine mechanism of formation for the cone chains, but point to a glacial paleolake being the source of the ice and debris (e.g.

Lockwood and Kargel, 1994; Kargel et al., 1995; Kreslavsky and Head, 2002), possibly as the result of the freezing of a postulated ocean in part or all of the northern lowlands of Mars (e.g. Carr and Head, 2003).

Pingos have been suggested as mechanisms of formation for mounds found elsewhere on Mars, such as those in Gusev (Cabrol et al., 1997) and Utopia Planitia (Soare and Peloquin, 2003). Pingos form when an expanding freezing front pressurises subsurface liquid water, forcing it towards the surface, causing the formation of a mound, which, if the pingo continues to grow, may breach to form an ice-cored hill (Wood, 1982). Terrestrial pingos have two types – hydraulic, or open system, and hydrostatic, or closed system. Hydrostatic pingos form from locally derived water, whereas hydraulic pingos require a more extensive region of groundwater but are more likely to form in clusters. Terrestrial pingo bases average approximately 200 metres in diameter, but can be up to 600 metres across.

2.6.5 Sinuous ridges

As with the cones, the sinuous ridge features have several different methods of formation proposed for them. The majority of these are depositional mechanisms and involve ice. The sinuous ridges have been found in several locations on Mars, and have often been interpreted as eskers, which result from glacial meltwater streams depositing sediment as elevated ridges (e.g. Kargel and Strom, 1991; Lockwood and Kargel, 1994; Bennett and Glasser, 1996), with the troughs they sit upon representing subglacially eroded fluvial channels (Kargel et al., 1995), although other possible mechanisms for their formation have been proposed (Metzger, 1995), including linear dunes formed by aeolian action (Ruff, 1992, 1994), or plastic flow and uplift by a mechanism involving subsurface volatiles (Tanaka and Skinner, 2003).

2.7 Discussion

2.7.1 Sedimentation and a source of volatiles

All of the discussed explanations of cone formation require the presence of volatiles in some form – entrained within magma for cinder cones, at or near the surface for pseudocraters and tuff rings/cones, deeper, buried volatiles in the case of mud volcanism, or in the form of a frozen lake or glaciation for the ice/depositional processes. The volatiles in question may be water, as a liquid or solid, another substance such as frozen carbon dioxide, or possibly a combination of several substances, such as a clathrate. Where the volatile in question originated may also have implications for the cone forming processes.

The current surface of Isidis Planitia is generally considered to be sedimentary in nature (e.g. Tanaka, 1997). There are several strong lines of evidence for the deposition of a relatively thick layer of sedimentary material within the basin (see also Chapters 5 and 6 for further discussion about the deposition of a sedimentary unit). With a suitable volatile content this depositional layer can be used to support the glacial/ice depositional hypothesis of cone formation, and also to some extent the tuff ring/cone mechanism of cone formation by providing surface volatiles that could interact with magma or magmatic heat from below. Alternatively, or additionally, volatiles may have been made available in the basin subsurface by processes such as the accumulation of ground ice (e.g. Sueyoshi and Hamano, 2002), or the formation of more exotic volatile deposits (e.g. Kargel et al., 2000). Recent research has suggested that such ground ice may exist as little as 1.5 metres below the surface in parts of the Isidis Planitia basin (Helbert and Benkhoff, 2003). However, lower-bound estimates of the water abundance within the upper 1 metre of the martian surface using the Gamma Ray Spectrometer (GRS) aboard MO suggest very low levels of water content in Isidis Planitia compared with other region of Mars (Feldman et al., 2003). This does not necessarily preclude deeper reservoirs of water being present.

Grizzaffi and Schultz (1989) theorised an air-fall origin for the sedimentary deposit whereas Hoffman (2000) suggested gas-supported cryoclastic flows as the deposition mechanism. Tanaka et al. (2000) suggested catastrophic breakup of volatile-rich material from Syrtis Major, although Bridges et al. (2003a) showed that thermal inertia data from the

basin implies sedimentation proceeding from the south and southeast of the basin rather than the west, although this does not preclude multiple episodes of sedimentation within the basin (see also Chapter 6, Section 6.2 for further discussion about the evidence for sedimentation of the basin taking place from the south). Much recent work has concentrated on possible Upper Hesperian-era massive floods forming sediment-rich oceans in the northern lowlands which may have resulted in freezing, subliming and retreat and deposition of sediment (e.g. Kreslavsky and Head, 2002; Carr and Head, 2003). It is also suggested that the flooding was episodic (Fairén et al., 2003). However, Tanaka et al. (2002) and Tanaka and Skinner (2003) suggest that the current sedimentary surface may be the result of resurfacing by subsurface H_2O and CO_2 rather than emplaced sediments from water or ice, and Janhunen (2002) hypothesises that the northern plains may currently be a frozen ocean covered in a thick enough layer of debris to prevent the ice from subliming.

Although Grizzaffi and Schultz (1989) suggest a deposited sedimentary layer of 0.4 to 2 kilometres thick in Isidis Planitia, it is generally considered by more recent researchers that the deposited sedimentary layer is likely to have been relatively thin – at the lower end of their estimate at most (see Chapter 5, Subsection 5.4.3 for further discussion about the thickness of this sedimentary layer), to allow for the easy detection of overlain features such as wrinkle ridges (see Chapter 4) and buried craters (see Chapter 5, Subsection 5.4). Several of the larger buried craters have modified depths that would require much greater amounts of infill, and Kreslavsky and Head (2002) suggested that erosion of the crater rim and ejecta, and subsequent deposition in the crater itself by the sediment-carrying floods filled these craters, with the possibility that some of the ice that sublimed away on the surface could be buried in these craters within a sediment trap protected by the layer of debris found on the surface. However, the evidence found in this study suggests that cone activity above buried craters is similar to that in surrounding areas (see Figure 2.11(a)), which implies that the mechanism of formation is most likely restricted to the surface layer, or at least is not affected by the greater depth of sedimentation found in the craters or by any possible buried ice within these features.

The presence of layered ejecta surrounding impact craters larger than a certain size in Isidis Planitia, and elsewhere on Mars, has been interpreted as impacts taking place into

subsurface strata containing liquid water or ice (e.g. Barlow and Bradley, 1990; Barlow and Perez, 2003) (see 5, Section 5.2 for further discussion of layered ejecta craters). Smaller craters (less than approximately 5 kilometres in diameter in Isidis Planitia) either do not excavate deeply enough to reach a subsurface water or ice layer, or do not excavate enough buried water or ice to modify the ejecta to form a layered morphology. The discontinuity in morphology between conventional and layered ejecta (i.e. with no obvious intermediate stages) perhaps suggests that the volatiles are located in specific strata rather than relatively evenly distributed throughout the upper layers. A 5 kilometre diameter crater would excavate a crater that is nearly 800 metres deep (Garvin et al., 2003). This is deeper than the likely depth of the sediments laid down to form the current basin surface, suggesting that the volatile layer or layers responsible for impact crater ejecta modification lie beneath the pre-sedimentation surface. However, this evidence does not necessarily rule out subsurface volatiles as a source for the Isidis Planitia cones and cone chains, as there could potentially be a region of buried volatiles nearer the surface which is not extensive enough to strongly modify impact crater ejecta, but which is available for cone formation.

2.7.2 Cinder cones

One of the biggest problems with using terrestrial cinder cones as an analogy for the Isidis cones is that, despite careful examination of the many cones across the basin, I could not find any that exhibit any kind of flow features, whether these be lava flows breaching the cone wall, or clastogenic flows formed by pyroclastic material accumulating at a high enough rate and temperature to form a flow (Hoffman et al., 2001). Although it is not unusual for individual terrestrial cinder cones to not exhibit such flows, it would be unlikely that a large population of cinder cones would show no such features. One possible explanation for this could be that explosive volcanism would generally be more explosive under martian environmental conditions than terrestrial ones, given a similar magmatic volatile content (Wilson and Head, 1994; Mitchell and Wilson, 2002). The enhanced adiabatic cooling of magmas on Mars would result in finer-grained non-welded volcanic products (Mitchell et al., 1999; Mitchell, 2001). However, this does result in the problem that larger explosions and smaller pyroclast sizes, coupled with lower gravity would result in eruption products being dispersed over large areas, and perhaps forming

features less directly analogous to terrestrial cones in terms of morphology (Fagents and Wilson, 1996; Mitchell and Wilson, 2001). Similarly, the increased likelihood for pyroclastic flow production (Wilson and Head, 1994) does not tally with a region where such flow features appear to be absent at any scale, although the relative lack of welding, and smaller size of eruption products would result in flows that were more mobile and prone to erosion. Indeed, the rough thermal inertia measurements of the cones and cone chains made earlier in this chapter (see Subsection 2.5.1) confirm that the cone flanks at least are composed of material with a much lower thermal inertia than the surrounding terrain, implying material which is less welded and/or finer grained. However, no sign is found of large (hundreds of metres) areas of lower thermal inertia extending beyond the cone structures which could represent the remnants of large-scale pyroclastic flows.

Terrestrial cinder cone fields form on either the flanks of a major volcano (a volcano cone field), or in flat volcanic provinces not associated with a major volcano (a platform cone field). Syrtis Major, to the west of Isidis Planitia, is generally considered to be the site of a large ancient shield volcano, and flows from Syrtis Major are thought to have entered the basin, possibly as part of the deposition of the basin's volcanic basement during the Early Hesperian, and more probably as a more limited Upper Hesperian deposit (Ivanov and Head, 2003). However, the Isidis Basin does not appear to form part of the Syrtis Major volcanic construct, and therefore is not likely to contain a volcanic cone field. The San Francisco Volcanic Field, Arizona, USA, a terrestrial platform cone field, contains over 600 volcanoes in an approximately 4,700 square kilometre area. Most of these features are cinder cones, although there is a single stratovolcano, and several lava domes (Priest et al., 2001). This gives a volcanic edifice density for the cones in this field of approximately 130 per 1000 km², which is relatively dense for a terrestrial cinder cone field (Kortz and Head, 2001). As an Isidis Planitia example, Figure 2.11(a) shows an area of approximately 2100 square kilometres, and has more than 750 cones – probably more, given the difficulty in determining the number of ‘individual’ cone features in the short cone chains in the image. This gives a volcanic edifice density of more than 350 per 1000 km² – more than twice the density of the San Francisco field, and more than four times the density of an average terrestrial cone field (Kortz and Head, 2001). This area of Isidis Planitia is relatively densely populated with cones compared with the basin average, although there are areas of the basin with higher cone densities. Although a cinder cone hypothesis

remains a plausible mechanism for the generation of the Isidis Planitia cones, such a high number of cones over such a large area as the Isidis Planitia basin, and such a high density of cones compared with a terrestrial cone field, combined with the apparent absence of larger volcanic constructs, and relative paucity of other volcanic features such as domes or dykes, means that if the Isidis Planitia cones are indeed cinder cones then the origin of their magma and subsurface ‘plumbing’ must differ substantially from cinder cone fields on Earth. Fields of small volcanic edifices also exist on Venus (e.g. Kortz and Head, 2001), but are believed to have significantly mechanisms of formation due to different atmospheric, surface, and subsurface environments on that planet.

However, some possible evidence for structures relating to magmatism in the basin have been found, possibly helping support a cinder cone or magma/volatile interaction hypothesis for the cone formation. Although there is the suggestion of intrusive volcanic activity at the basin rim, such as possible exhumed laccoliths (Albin and King, 2002), there exists much less evidence to support the existence of the extensive network of intrusive volcanism within the basin itself that would be required to support either the cinder cone mechanism, or some of the magma/ice interaction methods, of cone formation. Bridges et al. (2003a) identified what may be an example of an exhumed dyke in the Isidis Planitia basin (see Figure 2.19(a)), and during this study I have found several other examples of possible igneous intrusions in Isidis Planitia, some of which are shown in Figure 2.19. These include other potential exhumed dykes, and a possible laccolith (see Figure 2.19(c)) – a dome of magma fed by a dyke and formed beneath the surface, which after cooling may become exposed by erosion of the overlying surface. The widths of the dyke-like features are reasonable when compared to terrestrial examples, and allowing for the likelihood that martian dykes may be wider than those on Earth as a result of lower gravity (Wilson and Head, 1994). However, in all examples there is a lack of further evidence of diagnostic volcanic features, so their interpretation as having a magmatic origin is speculative.

In some instances cones appear associated with possible exhumed dykes, or in one case, a possible sinuous ridge. Figure 2.20(a) clearly shows some kind of ridge with a single cone nearby. It is not clear from the morphology of the ridge in this MOC image what its origin is. It appears similar to the sinuous ridges discussed earlier in this chapter (see Subsection 2.5.3), and a similar ridge is found elsewhere in the full image which is

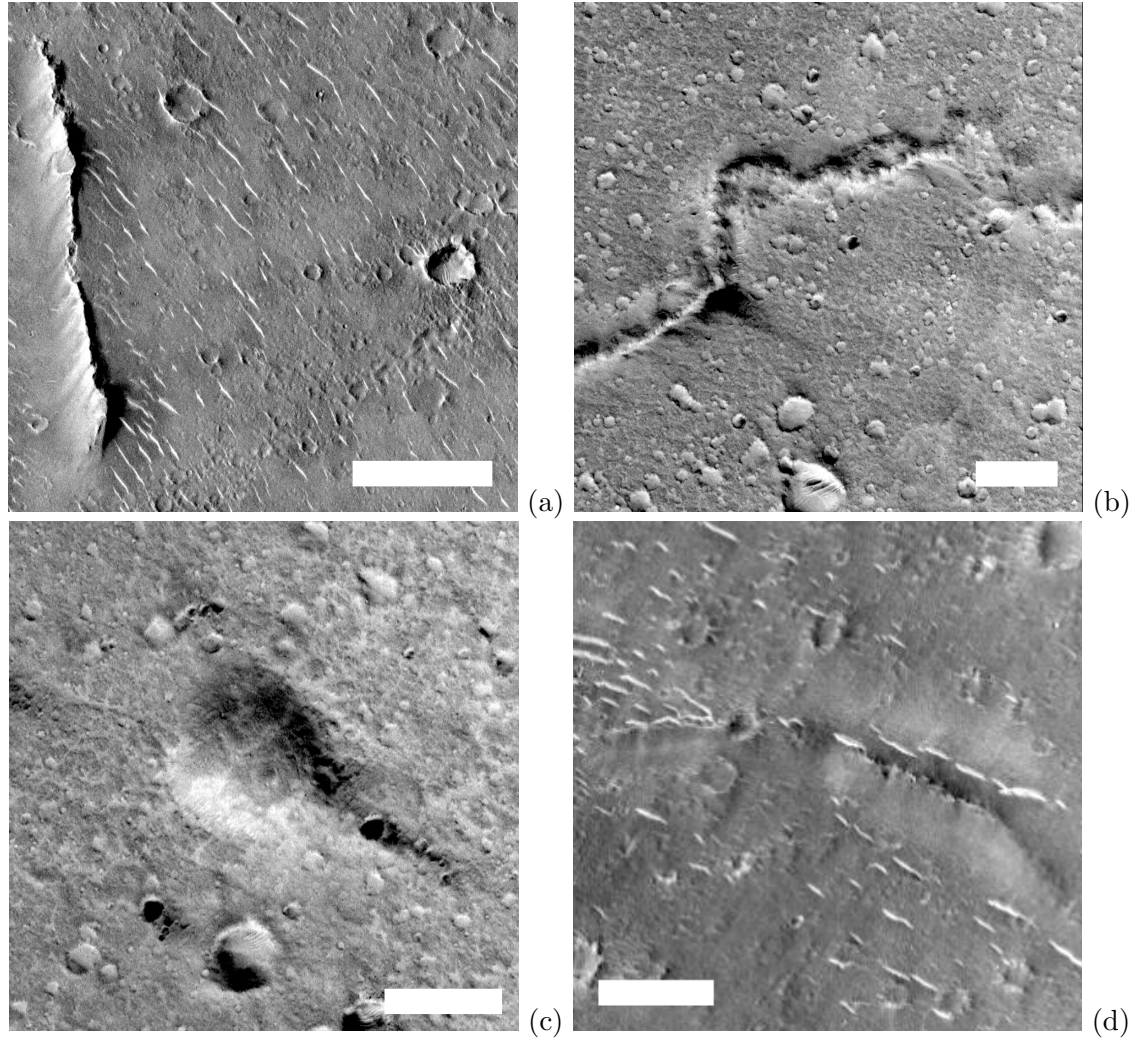


Figure 2.19: Possible igneous intrusions in MOC images. (a) shows detail from MOC image m0302859 showing a narrow ridge interpreted by Bridges et al. (2003a) as a exhumed dyke. The complete original image is centred at 91.12° East, 10.43° North, in central south-west Isidis Planitia. (b) shows detail from MOC image e1004377, showing a sinuous ridge which may be an exhumed igneous feature. The complete original image is centred at 89.01° East, 4.46° North in the far south of Isidis Planitia. (c) also shows detail from MOC image e1004377, showing a dome which may be an exposed laccolith. (d) shows detail from MOC image e05018656, showing a curvilinear ridge which may be an exhumed dyke. The complete original image is centered at 84.33° East, 7.23° North in the southwest of Isidis Planitia. Bars in all four images are 500 metres.

located in an obvious wide trough, in a similar way to many other sinuous ridges in the basin. However, these ridges are much narrower than many of the sinuous ridges found elsewhere in the basin (compare Figure 2.20(a) with Figure 2.16(b)). The ridge does not appear to be composed of cones as many in the basin interior are, and indeed is much narrower than a typical cone chain (compare with Figure 2.8(a)). The ridge could be an exhumed dyke, although the morphology expressed is more subdued and smoother than would perhaps be expected from such an intrusive igneous feature, and not very similar to features described as possible exhumed dykes in Figure 2.19. The ridge in Figure 2.20(b) can be more plausibly interpreted as a dyke. The associations between the cones and the ridge structures in these images can not be conclusively used to prove a connection between either dykes or sinuous ridges and mechanisms of cone formation, as with so few examples to support any particular hypothesis their association may well be just coincidental. Certainly, if the ridge in Figure 2.20(a) is indeed a sinuous ridge, then the association between cone and ridge would seem most likely coincidental, given that sinuous ridges are generally interpreted to be formed by a process analogous to those of terrestrial eskers (see discussion later in this chapter in Subsection 2.7.6), which would not have an obvious contribution to cone formation given its composition and formation process. Also, if the ridge is a exhumed dyke then it seems unlikely that erosional processes have exposed the dyke but not affected the nearby cones which, if related to the dyke, must be younger.

2.7.3 Cones from magma/volatile interaction

A pseudocrater formation mechanism for the cones seems initially quite plausible on the basis of morphology – the cones in Isidis Planitia being very similar in terms of crater/cone ratio (Frey and Jarosewich, 1982) and in spatial distribution (Bruno et al., 2004) to those found in terrestrial pseudocrater fields. Linear arrangements have been found in terrestrial and candidate martian pseudocrater fields (Bruno et al., 2004), although not in the chains of linked cones found in Isidis Planitia. However, while terrestrial pseudocraters are formed by the interaction between lava and surface water, Isidis Planitia shows no signs of lava flows over the vast majority of its area. One area in Isidis Planitia where lava has been suggested to have modified the basin surface is in the chaotic terrain in the west of the

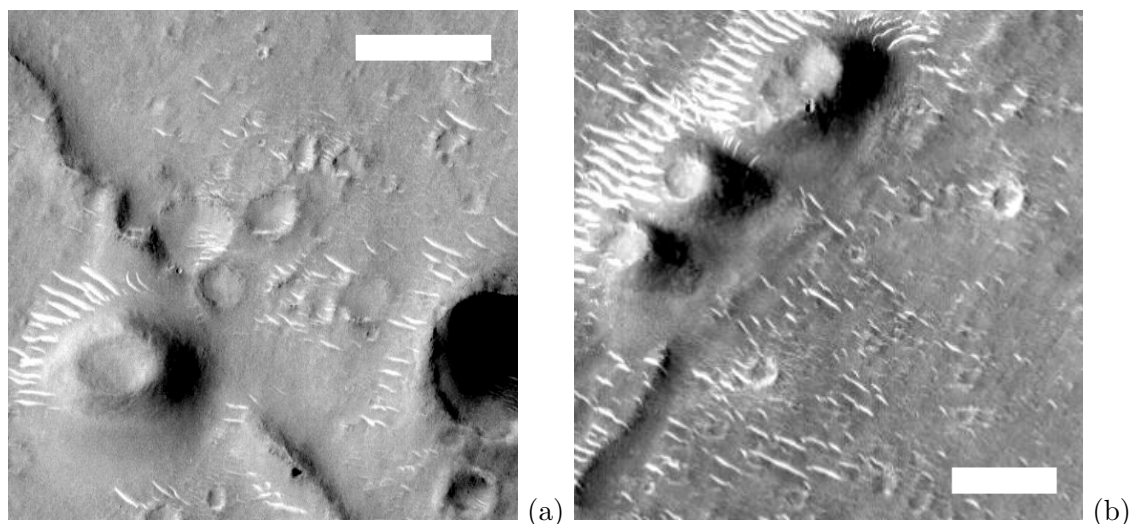


Figure 2.20: Ridges and cone in Isidis Planitia. (a) shows detail from MOC image m0203053 showing an example of a sinuous ridge or possible exhumed dyke associated with a single cone. The complete original image is centred at 83.97° East, 6.61° North in the south-west of Isidis Planitia. (b) shows detail from MOC image e0501865, showing a chain of cones associated with a possible exhumed dyke. The complete original image is centred at 84.33° East, 7.23° North in the south-west of Isidis Planitia. Bar in both images are 500 metres.

basin, where lava flows from Syrtis Major Planum are suggested to have postdated the emplacement of the Vastitas Borealis plains unit (Ivanov and Head, 2003). This is also an area devoid of cones. Although Isidis Planitia is a region of heavy modification by aeolian, and possibly fluvial, burial and erosional processes, it seems unlikely that no trace of a lava flow responsible for the Isidis Planitia cones, which are found over an extensive area, would be found. More plausible candidates for martian pseudocraters are located in Amazonis Planitia (Greeley and Fagents, 2001). These are located on what appear to be relatively fresh and young lava flows, are significantly smaller than the cones found in Isidis Planitia (Fagents et al., 2002), and are not found in chains (see Figure 2.21).

A tuff ring/cone hypothesis has many of the same problems associated with it as the cinder cones hypothesis, and there is somewhat less support for this mechanism in the scientific literature. A tuff ring/cone hypothesis would require volcanic activity within the basin to be at or near the level required for the cinder cone hypothesis, and would additionally require the presence of significant amount of volatiles. Terrestrial tuff ring/cone fields are also generally found associated with lava flows (e.g. Hoffman et al., 2001). In the absence of volatiles in sufficient quantities across the entire area of cone formation it is likely that other volcanic features would be generated as magma reached the surface. The

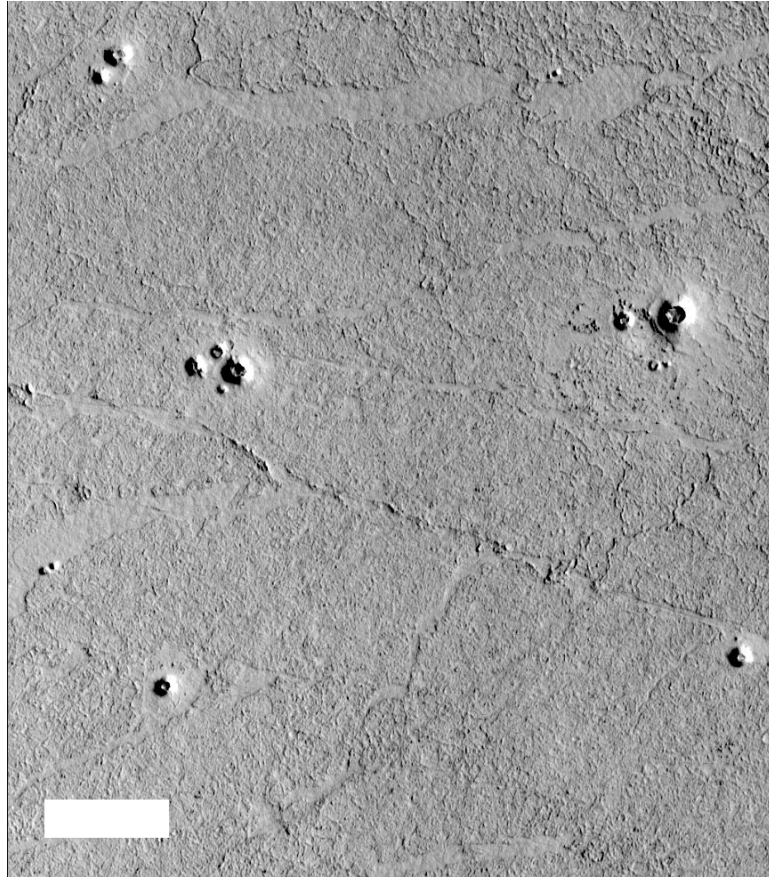


Figure 2.21: Pseudocraters in Amazonis Planitia. Detail from MOC image m0303958 showing examples of cones interpreted to be pseudocraters on a young surface interpreted as being formed from recent lava flows. The complete original image is centred at 188.33° East, 24.84° North in Amazonia Planitia. Bar is 500 metres.

volatiles could be present as water but, although there is some support for the previous existence of surface water in the northern lowlands (e.g. Carr, 1996), there is no evidence of lacustrine activity associated directly with the cones, and the cones themselves do not resemble submarine volcanoes, suggesting a thin layer of water at the time of eruption at most. However, the required volatiles could also form a solid or liquid layer beneath the surface, although current evidence suggests there is little or no near-surface water or ice in Isidis Planitia (Feldman et al., 2003).

2.7.4 Mud volcanism and cryovolcanism

The presence of a relatively thin sedimentary layer in Isidis Planitia suggests that if mud volcanism is the appropriate hypothesis for describing the Isidis Planitia cones, it is not generated as a result of the rapid deposition of a great depth of volatile-bearing sediments, which is a common terrestrial mechanism for the production of these features. In the absence of overpressure caused by rapid sedimentation, it is left to mechanisms such as heating or freezing to generate the required overpressure in the subsurface to produce mud volcanism. These are plausible mechanisms that could be expected to occur in conjunction with the glacial/ice and depositional processes of formation, which could perhaps usefully explain the variety of cone and cone chain morphologies seen in the basin. Mud volcanism driven by subsurface volatiles could also be responsible for the formation of cones on raised platforms shown in Figure 2.11. These platforms could be the result of doming above areas where volatiles are moving towards the surface, although it remains to be seen why these features are restricted to one area in the basin whereas the cones and cone chains are found across the majority of it.

2.7.5 Glacial/ice and depositional processes

From data available before the MGS mission, the glacial/ice depositional hypothesis appeared a strong candidate for cone and cone chain formation. Data from this mission and the MO mission have permitted a reevaluation of earlier hypotheses. Certainly, the idea of ice-cored moraines would appear to suit the cone chain landforms in the basin. Variations in ice/debris ratios could form features with different sized craters and, in cases

where large quantities of ice are mixed with debris, the subliming of the ice would form more hummocky and irregular chains (Grizzaffi and Schultz, 1989). Problems with the orientation of the cones could perhaps be due to particular environmental conditions on the martian surface and their influence on the backwasting mechanisms that would affect subliming glaciers. However, theories regarding the formation of the ‘thumbprint terrain’ and sinuous ridges within the Isidis Planitia basin have tended to overlook the widespread prevalence of single cones and cone clusters, although these features did not show up as well as the more obvious cone chains in pre-MGS era images. In some areas of the basin the cone chains are absent, and most cones are found singly (see Figure 2.11(a)). In many other areas, single cones are found surrounding cone chains. These features in many cases appear fully rounded and smooth and therefore do not resemble individual deposits of ice-cored debris, or hummocky hillocks.

Individual cones could perhaps be formed by processes analogous to terrestrial pingos. The ice core of pingos could sublime away under martian environmental conditions, which would result in a crater. In some cases this may collapse and the resulting structure could resemble some of the more ‘degraded’ examples of cones in the basin. If this is the case, the ‘degraded’ cones and cone chains may in fact simply be cones where the subliming of an ice core has resulted in collapse, rather than being features with a different origin, age, or erosional history. Terrestrial pingos often display dilation cracking, as the ice core splits the top of the mound; however, none of the martian examples show such cracking. The more pristine looking cones appear particularly smooth. It is possible this could relate to the mechanical properties of the surface. In an environment where the surface layer is formed by recently deposited sediments from a ocean which subsequently froze, the surface may be relatively unconsolidated when compared with terrestrial periglacial environments, and cracking may be less common.

Formation of moraines and pingos would require surface ice retreat (forming parallel rows of terminal moraines), but including expanding freezing fronts (forming pingos). The combination of glacial shrinkage and expansion of the zone of frozen ground water seems to be counter-intuitive to some extent, at least when related to terrestrial examples. However, a possible mechanism in which this could occur may involve the enhanced subliming of glaciers due to the low atmospheric pressure on Mars, rather than their shrinkage due to

warming, and which could be coupled with the freezing of water-containing near-surface layers in which the water is protected from subliming by a layer of sediment. It is uncertain whether, under martian conditions, a freeze-thaw cycle would be needed to drive the growth of periglacial features, or whether oscillations in temperature below freezing would be sufficient. Mellon and Phillips (2001) suggest that the growth of pingos could be driven by orbital-driven thermal changes at the martian surface.

If the nature of the cone chains is that they are moraines left behind due to glacial retreat, this could explain some of the features of their orientation – e.g. parallel or near-parallel sets of chains. If the ice cover in the basin were the result of a frozen ocean, it is likely that in the event of melting of this ice cover ice would retreat from areas of higher topography, such as wrinkle ridges – where the ice layer would be thinner – and towards thicker regions of ice in the lower topography areas in the flatter areas away from the wrinkle ridges. Other localised effects may influence glacial retreat to the extent that this mechanism would provide only a proportion of the control over ice cover shrinkage and subsequent moraine deposition, which could explain why the resulting cone chains are often not strongly oriented parallel to the wrinkle ridges in any systematic way.

Problems with the absence of features commonly associated with terrestrial glacial environments also have to be overcome before a glacial deposition hypothesis can be further considered. Kargel et al. (1995) notes the lack of drumlins – elongate hills produced by glacial action – in the northern lowlands, although it was suggested this was due to the ice in the basin being static. This in turn supports the suggestion that the ice in the basin was the result of a frozen ocean (Carr and Head, 2003). Another possible explanation for the lack of drumlins is that the Viking-era images used at the time were perhaps unable to identify drumlins due to insufficient resolution. However, Pomerantz and Head (2003) note that MGS-era data also do not show evidence of drumlins either, and suggest that the glaciers shaping the local terrain had frozen bases, and therefore did not generate these features. Areas on Earth previously covered with cold-based glaciers can show little evidence of glacial erosion, or even occupation (Lee, 2000). Terrestrial cold-based glaciation may deposit landforms such as drop moraines, which can be ice-cored and may resemble the cone chains, although terrestrial drop moraines contain relatively coarse material as cold-based glaciers do not significantly erode their underlying surfaces (Marchant and

Head, 2003). This is not, however, reflected in the thermal inertia measurements of the cone chains, which suggest relatively fine material, although this perhaps does not preclude the glaciers themselves being the source for the debris in the event of the deposition of sediment-rich water in the basin. Another problem is that cold-based glaciers would not form features such as eskers, which are generally thought to be analogous to the sinuous ridges found in the basin, implying that the ice in the basin was wet-based and therefore most likely static and in the form of a frozen ocean.

2.7.6 Sinuous ridges

The estimates of relative thermal inertia determined earlier in this chapter (see Subsection 2.5.1) for the sinuous ridges suggest an esker hypothesis to be the most plausible (unless the dunes material has become strongly indurated since its deposition). The ridge crests were predicted to exhibit high thermal inertia by Kargel et al. (1995). However, the particularly low thermal inertia of the ridge flanks were perhaps less expected. In the light of data from later Mars missions, reinterpretations of sinuous ridges on Mars have concluded that a mechanism analogous to the formation of terrestrial eskers is indeed the most plausible (e.g. Head and Hallet, 2001b; Metzger, 2001). The ridge shown in Figures 2.15 and 2.16 is much larger than most eskers in relatively recently glaciated terrain on Earth, which have ridges that are generally less than 150 metres in width, although the giant paleoeskers found in Mauretania are 1–1.5 km in width (Mangold, 2000). The sinuous ridges in Dorsa Argentea are generally between 2–4 km wide, but can be up to 6 km in width (Head, 2000). The evidence that the sinuous ridges in Isidis Planitia may be glacial in nature perhaps acts to strengthen the idea that the Isidis Planitia cones and cone chains may also be glacier-related depositional features, although the presence of glacial features in the basin does not preclude a non-glacial origin for the cones and cone chains.

2.8 Conclusion

In summary, it appears that most of the major proposed mechanisms for the formation of the cones and cone chains in Isidis Planitia are plausible, but all have some difficulties.

Perhaps the least likely from the available evidence is the pseudocrater hypothesis. Given the huge numbers of cones across the basin, it seems highly unlikely that no trace of the extensive lava flows that would be required to generate this many pseudocraters are apparent. Cinder cone and tuff ring/cone origins are both plausible, but require significant volcanic activity to have taken place across the basin, for which there is scant other evidence. The involvement of mud volcanism of some type seems more likely, although this is unlikely to be due to overpressure generated by rapid and deep sedimentation. I suggest that the most likely mechanism for the formation of the cones, cone chains, and indeed sinuous ridges, in Isidis Planitia is as a result of sediment deposition and modification by an subliming ice sheet, with the possible addition of a form of mud- or cryo-volcanism driven by the expansion of freezing fronts into subsurface layers charged with volatiles by flooding events.

It seems likely that a major flooding event emplaced a sediment-rich basin-wide ocean in Isidis Planitia (and probably also the wider northern lowlands) at some point in the Hesperian (see Chapter 5, Section 5.4 for further discussion of the buried unit in Isidis Planitia, and Chapter 6, Section 6.2 for further evidence of sedimentary deposition in the basin). Sediment brought in by the water and unconsolidated material from the pre-existing surface were redistributed across the basin, and preferentially deposited in topographic lows such as impact craters (see Chapter 5, Section 5.4). A thin layer (approximately 300–400 metres depth) of material was deposited across the basin floor. The emplaced ocean then froze relatively rapidly (over hundreds, thousands, or perhaps tens of thousands, of years, depending on depth of water and other factors (Kreslavsky and Head, 2002)). This ice cover then sublimed away, most likely over a longer timescale than its emplacement (e.g. Moore et al., 1995; Kreslavsky and Head, 2002). The subliming ice retreated from areas where it was thinnest first – the basin edges (where in some locations, and wet-based, it left eskers where water channels between the ice and surface deposited material to form sinuous ridges), and the wrinkle ridges. The retreating ice deposited a series of ice-cored recessional moraines (e.g Kargel et al., 1995) that can be seen today as degraded chains of ‘cones’ containing pits left by sublimed ice. The more ‘eruptive’-appearing cones may have been formed as a result of the extrusion of buried areas of liquid water in the near-surface being overpressured and erupted at the surface. This may have formed features analogous to pingos, or perhaps more analogous to mud- (Kreslavsky and Head, 2002) or

cryovolcanoes (Gaidos, 2001). Figure 2.22 shows a simple cartoon showing how overpressuring of a volume of subsurface water by expanding freezing fronts can drive the ascent of water to the surface. If the water freezes it forms the ice core of a pingo. Initially this may not break the surface and the surface expression of the ice core is simply a mound. Pingo growth is driven by a freeze-thaw cycle, resulting in ice-core growth. It is unclear whether martian environmental conditions would support such a cycle. If the ice core breaks the surface it will rapidly sublime, leaving a pit, which may collapse. If the water reaches the surface before freezing it would produce a mud- or cryo-volcano, with cone formation driven by entrained sediment. As mentioned before with other explanations of cone formation in the basin, there are no signs of flows from any of the cones. This could be explained in this instance by the rapid boiling away of erupted water under martian surface conditions, quickly leaving a dry sediment residue before flow features form.

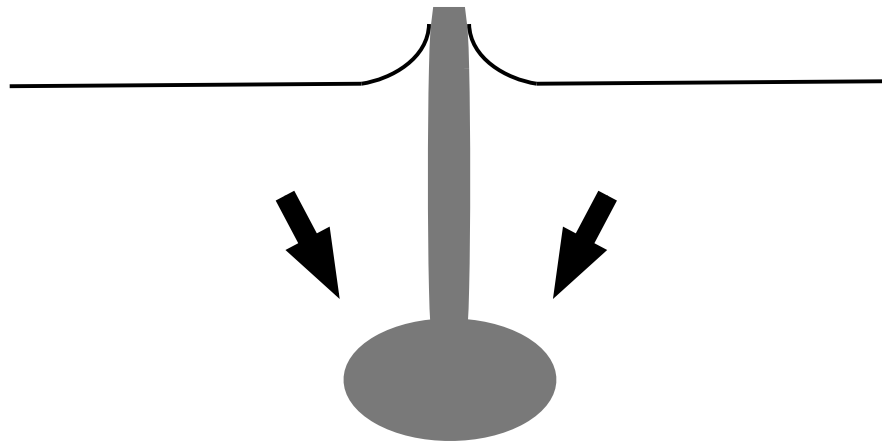


Figure 2.22: Pingo and cryovolcano formation. Simple cartoon showing overpressure from expanding freezing fronts drives the ascent of water to the surface. If the water freezes to form an ice core, a pingo is formed. If the water erupts on the surface it becomes a mud- or cryo-volcano. See text for further discussion.

The freezing out of the emplaced ocean, which would have proceeded from the surface downwards, would have resulted in an increased concentration of dissolved salts at the bottom of the ocean. These may have become entrained within, or seeped into, sediment layers, and may have prevented the volatiles in the subsurface from freezing (e.g. Bodnar, 2001; Madden and Bodnar, 2002; Kargel and Marion, 2004). If the subsurface volatile reservoir is a brine, this would also favour a mud- or cryo-volcanic formation mechanism for some of the cones, as the liquid would be more likely to reach the surface before

freezing. However, it would still evaporate on reaching the surface, and this may leave detectable traces of deposited salts at the basin surface. The region of subsurface volatiles may have formed from the charging of the near surface layers by water from the emplaced ocean, by the deposition of mixed sediment and water, or may have been preexisting and possibly even the remnants of a previous flood in the basin. It is possible that some of the cones in the basin are tuff cones/rings, formed by the interaction of magma or magmatic heat and the subsurface volatiles in the basin. However, given the lack of strong evidence for igneous features within the basin, few of the cones are likely to be related to igneous intrusive activity.

Further research will be necessary in order to fully understand the nature of the complex formation processes involved, and the availability of new data from the MO and Mars Express (MEX) missions, as well as the lander missions, will play an important part in this investigation. Work is already being carried out on analysing the spectra of candidate features in order to look for signatures of possible interaction with water (e.g. Farrand, 2000; Bishop et al., 2002), and to also determine differences between material formed in sub-glacial and liquid water environments (Farrand and Lane, 2002). Detection of such signatures would significantly strengthen formation hypotheses involving interaction between water and magma. Instruments onboard Mars Express will give a better understanding of the subsurface of Mars, including the possible detection of subsurface water, an important component in several of the mechanisms described.

Chapter 3

Topography using MOLA data

3.1 Introduction

Before the arrival in Mars orbit of the Mars Global Surveyor (MGS) spacecraft, investigation of martian topography was performed using several Earth- and spacecraft-based techniques (e.g. Esposito et al., 1992; Davies et al., 1992). Radar time-delay measurements, or altimetry, obtained from Earth-based equipment have been used since the late 1960s, taking place primarily at planetary oppositions in order to maximise the scientific return. However, these observations were limited in their coverage and resolution of the martian surface. Observations from the Mariner (1964 to 1972) and Viking (1975 to 1980) series of missions included radio occultation measurements and the use of various spectral and optical instruments to determine topography from variations in local pressure and temperature. The Viking Orbiters also contributed significantly to mapping the topography of Mars by providing tens of thousands of pictures of the surface that could be used to map topographic features stereoscopically.

The MGS spacecraft was launched on the 7th of November 1996, and marked the first successful return to Mars for NASA after a 20-year absence of Mars missions since the highly successful Viking series of lander/orbiters. Aboard MGS was the Mars Orbiter Laser Altimeter (MOLA, or, more accurately, MOLA-2 as it is descended from a similar instrument carried aboard the ill-fated earlier Mars Observer spacecraft) instrument (Zu-

ber et al., 1992), which was specifically designed with mapping the topography of Mars in mind. It was designed by the Laser Remote Sensing Branch of the Laboratory for Terrestrial Physics of NASA/GSFC, with support from Goddard’s Engineering Systems Analysis Branch.

3.2 Instrument and orbital characteristics

At its heart, the MOLA instrument uses a diode laser pumped Q-switched Nd:YAG laser transmitter (Afzal, 1994) which fires 8 ns bursts of 1064 nm wavelength infrared light ten times a second, and a receiver which measures the time taken for reflected energy to return from the martian surface in order to make its range determination (Abshire et al., 2000). This is achieved by diverting a portion of the output laser energy to start a precision clock counter. Returning photons generate a voltage in the instrument detector that is proportional of the rate of photon returns, and when the voltage exceeds a noise threshold, which is dynamically set by software to maximise the chances of a scientifically useful return, a time interval is determined. Additionally, four parallel channels filter the detector’s output to detect returns that have been spread out by rough terrain or clouds, and increase the probability of returned pulse detection as well as providing information about within-footprint roughness or cloud characteristics.

After its launch in November 1996, MGS achieved martian orbital insertion on the 17th September 1997, and proceeded to aerobrake into the correct orbit for mapping, which was achieved by the 28th of February 1997, although pre-mapping orbit data had been collected and relayed to Earth since arrival. MGS’s mapping orbit has an inclination of 92.869° , and an eccentricity of 0.00405, with an altitude of between 375 km and 445 km above the martian surface. An orbit is completed approximately every 177 minutes, and repeats approximately once every 7 martian days (89 revs). MOLA data were collected continuously until the end of the primary mission on the 1st June 2000. However, the mission was so successful that an extended mission plan was drawn up, and after a solar conjunction during which time no data were collected, the MOLA mission continued, transmitting a total of over 671 million individual laser shots, until failure of the instrument oscillator prevented the transmitter from receiving any further fire commands on 30th June

2001. However, despite its mission as an altimeter being curtailed, albeit after a mission life that was greatly extended beyond original plans, the MOLA instrument continues to function as a passive 1064 nm infrared radiometer (Sun et al., 2001).

As a result of its orbital and instrument characteristics, MOLA data have a vertical shot-to-shot precision of 0.375 metres, and an absolute vertical accuracy, depending on an accurate reconstruction of the spacecraft’s orbital parameters, of less than 10 metres. Along the highly-inclined (i.e. near pole-to-pole) orbital tracks, shot spacing is 330 metres, whilst across-track shot spacing depends on orbit and latitude, and, even after completion of the primary mission, along with the extra data from the extended mission, may be on the order of kilometres. The footprint size of the MOLA pulse on the martian surface is approximately 150 metres in diameter.

3.3 MOLA data

MOLA data are made available to the scientific community via the Planetary Data System (PDS), both online (<http://pds.jpl.nasa.gov>) and on CD-ROM (Arvidson et al., 1999). Data are published after a delay for calibration and processing. PDS distribute four types of MOLA altimetry products – Aggregated Experiment Data Records (AEDR), which are raw altimetry profiles, Precision Experiment Data Records (PEDR), which are processed AEDR records, Experiment Gridded Data Records (EGDR), which are global maps of martian topography produced by taking the median topography within a specified area from PEDRs, and Spherical Harmonics ASCII Data Records (SHADR), which is a spherical harmonics model derived from EGDRs.

PEDRs were used for this research. At the time this work was carried out the EGDRs provided topographic maps with a limited resolution (Smith et al., 2001), and more advanced data interpolation of PEDRs provided more control over interpolation and a higher resolution from the resulting topographic maps than available from EGDRs. Processing of PEDRs from the original AEDRs is repeated when better orbital information becomes available as the mission progresses, and so the PEDR set is revised regularly. The data used in this research were the latest available at the time of utilisation. However a final

processing revision, L, is due for public release (Neumann et al., 2003b). This will incorporate changes to the rotation model and cartographic frame, as well as a change to the topographic reference datum and recalibration of the pulse width returns. Thus research based on this later revision may have a slight quantitative difference from this work.

The PEDR data are distributed in volumes, each containing binary data files and associated documentation and labels. Tables C.1, C.1, and C.3 in Appendix C list the MOLA PEDR volumes used in this research. Note that volumes MGSL_0001 and MGSL_0002 contain pre-mapping orbit data and were not used, and volumes MGSL_2001 to MGSL_2009 are older revisions of volumes MGSL_2010 to MGSL_2016.

3.4 Processing, gridding and interpolation

PDS provide a software specification interface document (Neumann et al., 2000), which is useful in understanding the format of the binary data files. PDS also make several small data processing software packages for several computer platforms freely available on their web site. In this study, after downloading the relevant freely available binary PEDR files they were processed into ASCII tables with one line for each altimetry shot detected, and limited to the geographic area of interest. These data files were then further processed with the text-processing language **gawk** (<http://www.gnu.org/software/gawk/>) in order to specify fields of interest – e.g. a file with longitudes, latitudes, topography and orbit numbers for each shot. Individual MOLA tracks can also be extracted at this stage if required, again using a **gawk** program.

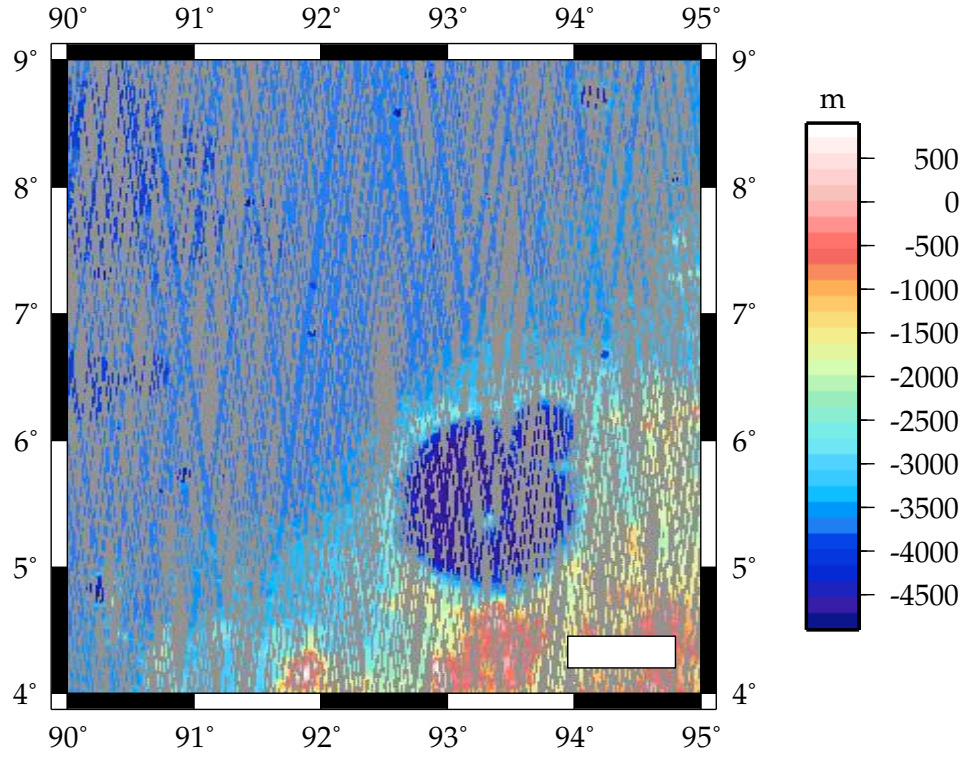
MOLA data points are not evenly distributed across the surface of Mars, and in order to produce usable topographic maps the data must be gridded into regular bins, and then interpolated in order to fill any bins that do not contain data. For this task I chose to use the Generic Mapping Tools (GMT) (Wessel and Smith, 1991, 1995, 1998), a suite of powerful open source UNIX tools that allow users to manipulate and plot 2- and 3-d data sets in many ways. The software is made freely available on the GMT web site (<http://gmt.soest.hawaii.edu/>) along with extensive documentation.

Abramov and McEwan (2004) investigated four interpolation methods – Delaunay-

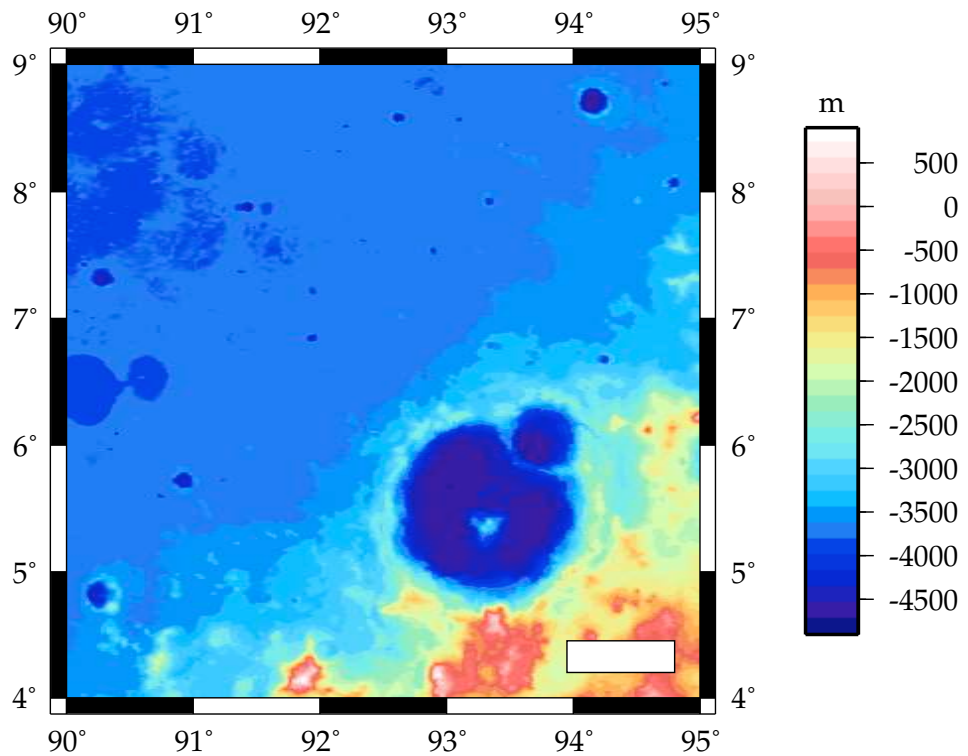
based linear interpolation, splining, nearest neighbour, and natural neighbour – and suggested that at lower data resolutions there was little difference in their qualitative and quantitative performance, but that natural neighbour interpolation, followed by splining, were the more accurate methods for higher resolution studies. GMT does not provide natural-neighbour interpolation software, and the relatively low density of MOLA data does not require very high resolutions anyway, but it does have tools to use the other three methods, including the spline interpolation-based **surface** (Smith and Wessel, 1990) program, which provides variable tension continuous curvature interpolation.

Initial binning of the data was provided by the GMT program **blockmedian**, which reads the arbitrarily located MOLA data and generates a median position and value for every non-empty bin. As with the similar **blockmean** and **blockmode** it also acts as a pre-processor for data destined for the **surface** program, but is preferred over the other two for topographical work. The grid spacing chosen for the MOLA data was important. If the resolution were made too low, information would be lost, whereas too high a resolution would result in a greater amount of the resulting map being interpolated data, putting a strain on the effectiveness of the interpolation routines (e.g. Okubo et al., 2004). I chose a non-square bin size to reflect the difference between across-track (predominately longitudinal) and along-track (predominately latitudinal) spacing in the MOLA data, and make best use of the available resolution where possible. For longitude, 64 pixels per degree resolution was chosen, and 128 pixels per degree for latitude – equivalent to a bin size of approximately 920 metres by 460 metres at the equator (Kieffer et al., 1992). Figure 3.1 shows the results of interpolation using the **surface** program compared to the simple binning of the MOLA data.

At this stage, the resulting maps were visually inspected for any bad data. Several MOLA tracks with spurious topography values showed up, and were manually removed from the original shot data tables, and the process of binning and interpolation repeated in order to produce interpolated grid files with reduced errors from bad orbits. The maps produced by this method were projected using a Mercator projection, and use a standard martian ellipsoid (Duxbury et al., 2001). Additionally, the interpretation of the resulting maps can be made easier, and their appearance improved, by using GMT programs such as **grdcontour** to add contour lines, and by adding illumination by generating an



(a)



(b)

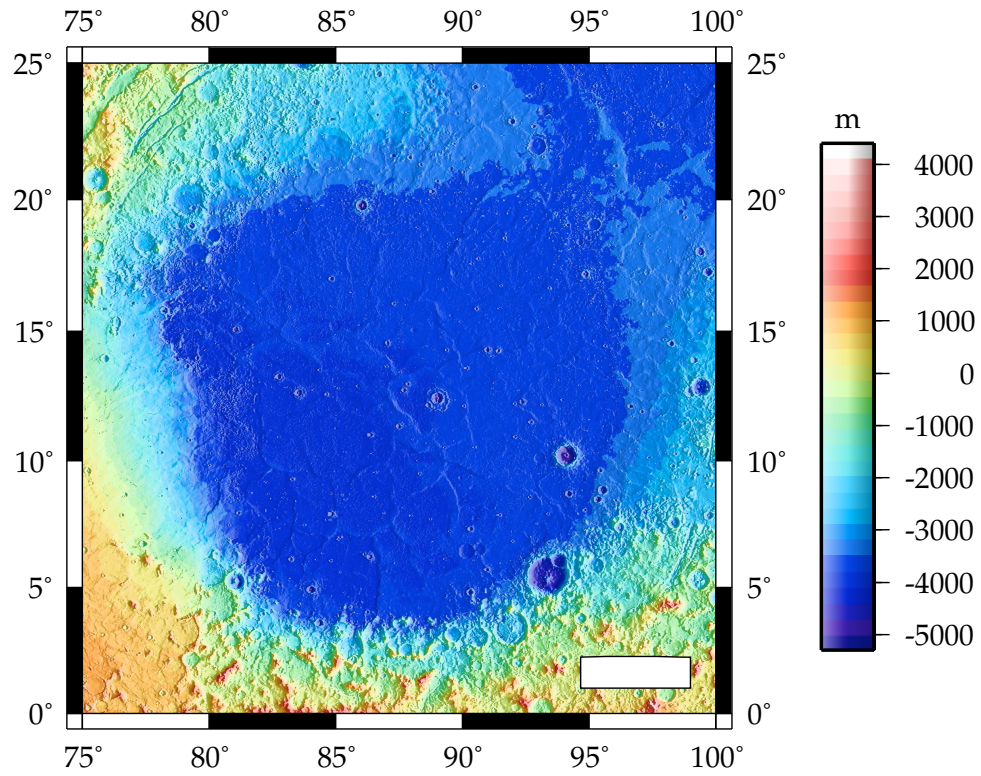
Figure 3.1: Interpolation of MOLA data. (a) shows simple binning of MOLA topography data for a small area of south east Isidis Planitia using the `blockmedian` program. (b) shows the same data interpolated using the `surface` program. Bars in both images are ~ 50 km.

accompanying file of gradients for each data point using `grdgradient`. Non-topographic MOLA data such as returned pulse width information was also used during my research and processed using `GMT` software into useful maps. Individual tracks of MOLA topography data were also extracted from the processed data files using `gawk` and superimposed on `GMT` maps, along with accompanying profiles, for some of this research.

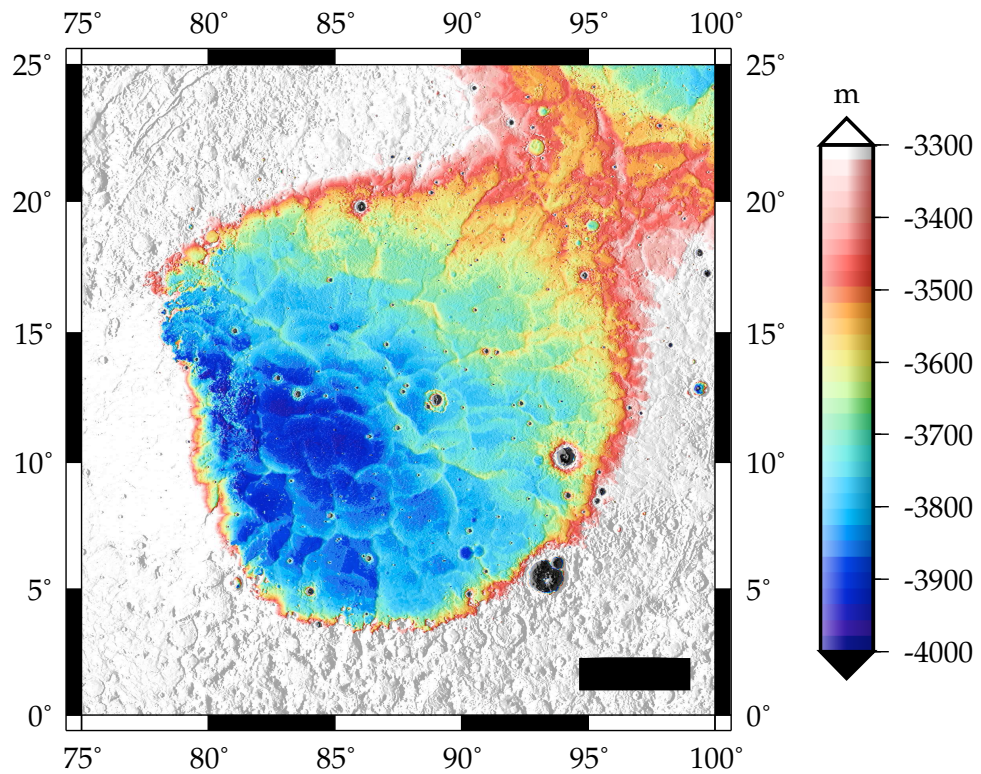
3.5 Detrending MOLA topographic data

One problem with investigating features within the Isidis Planitia basin is that although generally the basin is very flat (e.g. Bridges et al., 2003a), and many features on it have only metres or tens of metres of topography, it is adjoined on three sides by terrain with topographical ranges spanning several thousands of metres, and contains many impact craters with large ranges of topography. A topographical map generated with a set colour table may have, for example, 256 levels, and these levels are spread across the selected topography – e.g. for a topography range of 10,000 metres (not atypical for a map including both lowland and highland areas), each colour table level will represent nearly 40 metres. Features exhibiting less topographic variation than this will therefore be invisible. A solution to this problem is to clip higher and lower topographies so that they are not shown, which can be carried out simply by restricting the range of the colour table used, or by using the `GMT` program `grdclip` to replace topography above or below a certain point in a `grdfile` by NaN, indicating a non-numeric value. These techniques lead to perhaps less visually attractive maps, but reduce the topography range for each colour table level, with a resulting increase in z-axis topographic detail visible, thereby potentially increasing their scientific content (see Figure 3.2). Another, related, problem that becomes visible with this increase in detail is that the Isidis Planitia basin is tilted from higher in the northeast at its contact with Utopia Planitia, to lower in the southwest (Frey et al., 2000), which is apparent in 3.2(b). This tilt is approximately 0.02 degrees (Frey et al., 1998; Hiesinger and Head, 2003), and is postulated to be the result of the loading of the northern lowlands by kilometre-thick deposits, and the resulting tectonic tilting of the adjacent southern highlands and Isidis Planitia region (Tanaka et al., 2000; Watters, 2003).

Across the basin the slope results in a larger topographic variation than that of many of



(a)



(b)

Figure 3.2: Topography of Isidis Planitia using MOLA data. (a) a full range of topography, with detail enhanced using illumination. (b) shows a limited range of topography, with a resulting increase in detail. Bar in both images is ~ 250 km.

the individual features on the basin floor. Hence when viewing topographic maps that have a large extent, the increased topographic variation caused by the basin tilt can obscure features with low topographic variation, again as a result of giving each colour table level too large a topography range. A solution to this problem is to detrend the data, which is a technique that has also been used by other researchers in Isidis Planitia and elsewhere (e.g. Head and Bridges, 2001; Head et al., 2002). This can be done either by representing the regional slope by a mathematical function, and then removing this from the data, or by using a moving average technique to remove the average value surrounding each point from each point. The latter is the method chosen for this research, and was carried out by filtering the gridded, interpolated topography data using a 1-degree radius median filter using the GMT program `grdfilter` and subtracting the result from the gridded, interpolated topography using the GMT program `grdmath`. The results of this technique on the topographic slope across Isidis are shown in Figure 3.3. This technique was then used to produce a map of topography variation about a regional median value (see Figure 3.4).

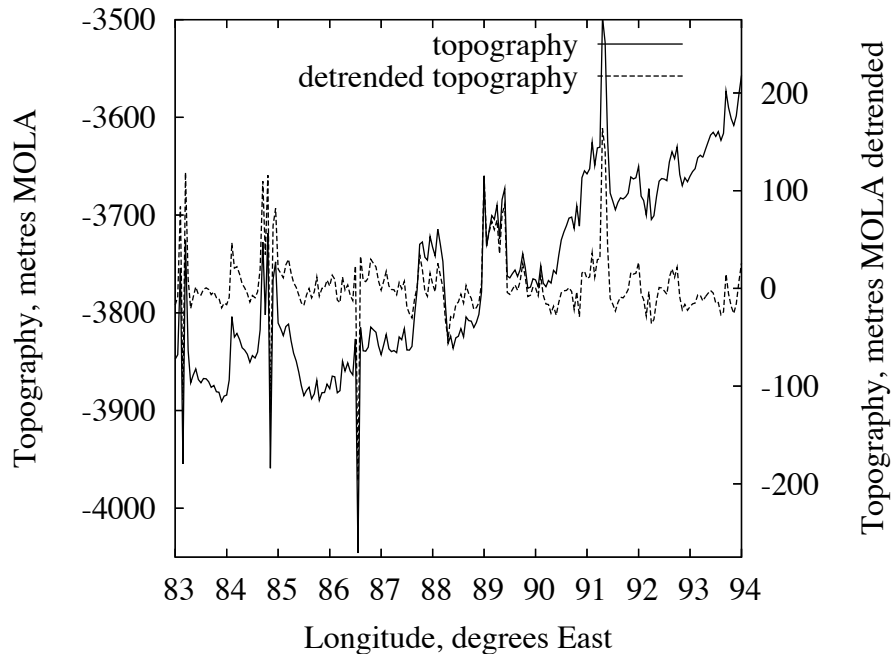


Figure 3.3: MOLA topography and interpolated detrended MOLA topography in Isidis Planitia. Transect taken across Isidis Planitia is from 83° East, 6° North, diagonally across basin to 94° East, 17° North, approximating the direction of the slope across the basin.

For some of the research for this thesis using single tracks of MOLA data has been useful

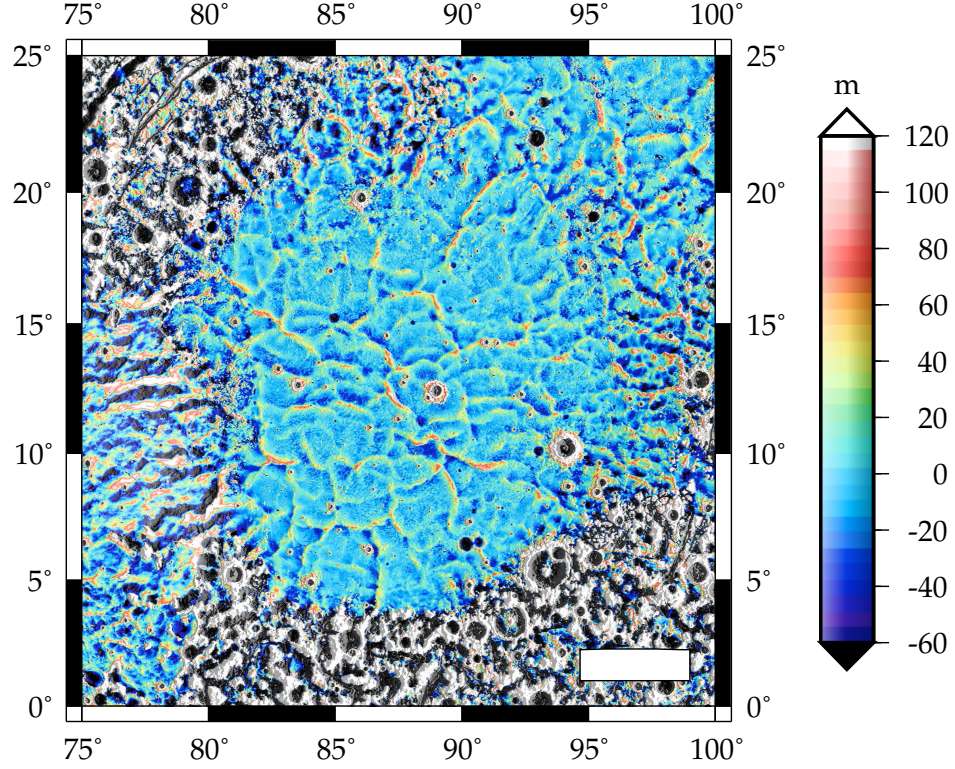


Figure 3.4: The results of detrending MOLA data from the Isidis Planitia basin, showing greater detail in the basin lowlands than either map from Figure 3.2. Bar is ~ 250 km.

in order to make use of their superior shot-to-shot resolution, for example in obtaining a simple profile across a topographic feature. Over short distances these can be used without detrending, but the regional slope may become a problem for longer profiles. Detrending these single tracks cannot be carried out using `GMT`. Instead, I wrote a program using the `python` programming language (<http://www.python.org/>) together with the `Numeric` multidimensional array module (<http://www.pfdubois.com/numpy/> – now surpassed by `Numerical Python` at the same web address) that detrends MOLA data along a single track, but using the same principles as the `GMT` detrending.

3.6 Conclusion

MOLA data have been essential to the research presented in this thesis. Processed MOLA topography has been used in Chapter 2 and the associated Appendix B, but is more extensively used, particularly after being detrended using the techniques described in

this chapter, in Chapter 4 and Chapter 5. Detrended single MOLA tracks are used in Chapter 4. Roughness data derived from returned MOLA pulsewidth, and slope data derived from MOLA topography are used in Chapter 6, Section 6.3.

Chapter 4

Ridges in Isidis Planitia

4.1 Introduction

Wrinkle ridges are generally linear and asymmetric topographic features exhibiting positive relief (Banerdt and Golombek, 1992). They have been identified and investigated on several planetary surfaces, including those of Mercury, Venus, Earth and the Moon, as well as Mars (e.g. Watters, 1988). These features were identified on the martian surface in the high-resolution images sent back by orbiter missions. Wrinkle ridges have been identified in many highland plains areas of Mars (Chicarro et al., 1985), where such ridges are often found extensively, and where they are easily visible using Viking Orbiter Camera (VOC) or Mars Orbiter Camera (MOC) images. Mars Orbiter Laser Altimeter (MOLA) data can also be used to accurately map these features using GIS techniques (e.g. Frigeri et al., 2002). However, such easily identifiable ridges are absent from the Isidis Planitia basin.

Analysis of detrended interpolated MOLA data (see Chapter 3 for details of the MOLA instruments and the MOLA data processing) has revealed many subtle features within the Isidis Planitia basin. Isidis Planitia has an extremely flat and smooth surface, and using detrended topography data enables features with a relatively small amount of topographic range to be identified. Among these features is a network of large ridges found throughout the basin (Withers and Neumann, 2001; Head et al., 2002) (see Figure 4.1). Unlike ridges

found in the highland plains, the Isidis Planitia ridges are often very difficult to identify from visual or infrared data sets such as VOC, MOC or THEMIS. This can be seen in Figure 4.2 where some evidence can be seen for some, but not all, of the ridges exhibiting a relatively large topographic range (e.g. towards the right of Figure 4.2(a)); those with a smaller topographic range are not seen, and all the ridges that are visible show a subdued nature with little structural detail.

At first, planetary wrinkle ridges were considered to have a volcanic origin, the result of the intrusion and extrusion of magma (e.g. Quaide, 1965). However, these features are now generally considered to be formed as the result of tectonic compression causing faulting and folding (e.g. Golombek et al., 1991).

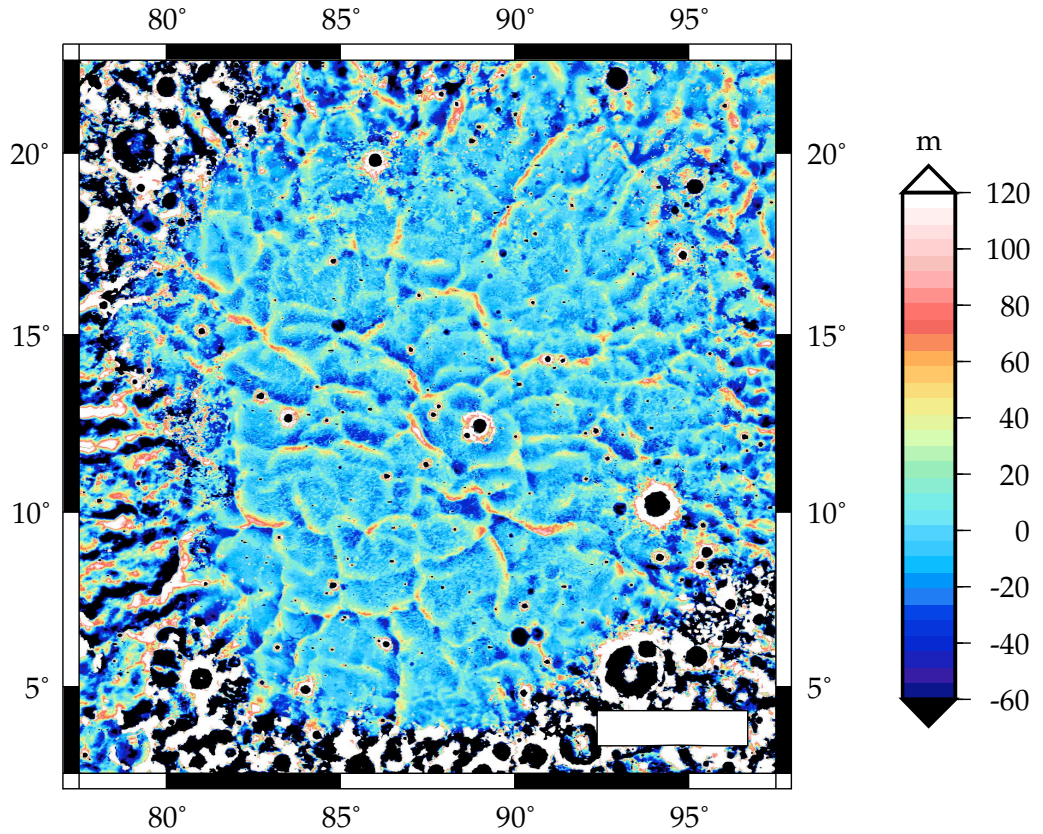


Figure 4.1: Ridges in Isidis Planitia. Ridges in a detrended MOLA map of the basin. Bar is ~ 250 km.

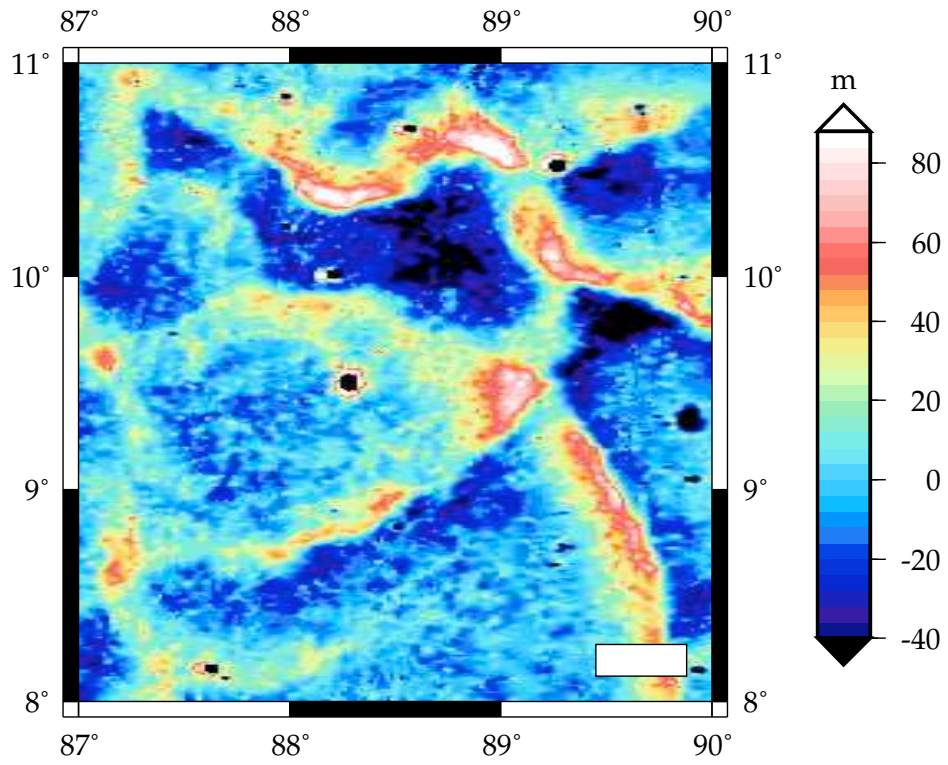
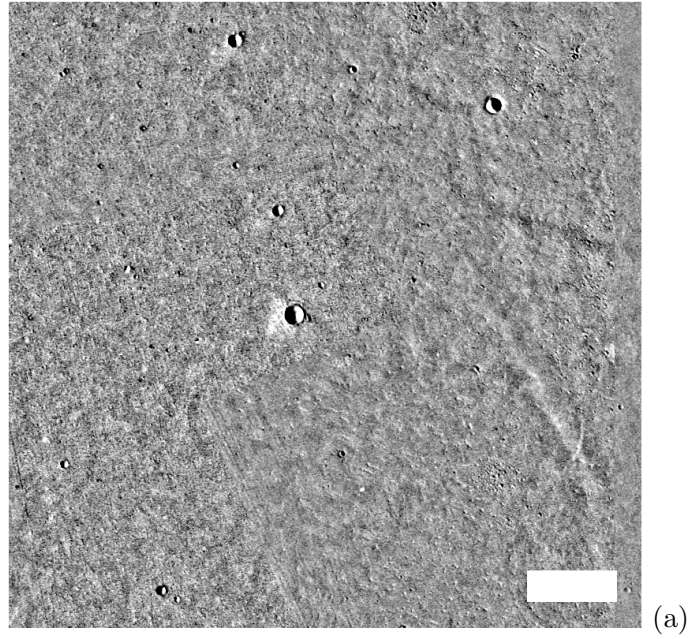


Figure 4.2: Ridges in Isidis Planitia. (a) part of the VOC Mars Digital Image Mosaic (MDIM) mosaic. (b) detrended topography from MOLA track for approximately the same geographical region. Compare visibility of major and minor wrinkle ridges in the two images. Bars in both images are ~ 25 km.

4.2 Analysis of ridges

4.2.1 Wrinkle ridge morphology

Figure 4.1 clearly shows that the the ridge structure in Isidis Planitia is quite complex. Immediately obvious is that the ridges are broadly divided into two orientations – curved or curvilinear ridges forming a concentric pattern apparently centred west of the basin’s geographical centre, and generally linear ridges forming a radial pattern nearer to the basin rim. The latter pattern is more obvious towards the east of the basin as a result of the non-central position of the curvilinear ridge pattern. Also apparent is that larger and smaller ridges combine to form a somewhat polygonal structure, although with many of the concentric ridges being curved, many of the polygons have few straight sides. These polygons are roughly of similar size, although there is much variation in shape, and some of the ridges have topography that is so subdued that even when using detrended data it is difficult to identify all ridge structures in the basin.

Figure 4.3 shows more detail than Figure 4.1, and illustrates further some of the points already made. Many possible ridges are so subdued topographically that it is difficult to make a determination about the polygonal nature of the terrain. Figure 4.3 also shows that some of the ridges may overlap each other. In particular, the ridge running in a semicircle from approximately $87.5^{\circ}\text{E } 10^{\circ}\text{N}$ clockwise to approximately $88^{\circ}\text{E } 6.5^{\circ}\text{N}$ may be a single ridge structure, in which case it crosses at least one other major ridge. This point, at approximately $89^{\circ}\text{E } 9.5^{\circ}\text{N}$, shows a large raised area, although it is very difficult from these data to determine the sequence in which these ridges operated on each other. Elsewhere, for example in the west of this figure, many of the ridges appear to run into each other with no noticeable morphological changes.

Another feature noticeable in Figure 4.3 is the asymmetry across the short dimension of many of the ridges. This is a characteristic feature of ridges produced by compressional tectonics (Banerdt and Golombek, 1992). Obvious asymmetry is found in the ridges that show greater ranges of topography, although this may be due to the limited horizontal and vertical resolution of the displayed detrended data precluding easy identification of this feature in more topographically subdued ridges. Figures 4.5 and 4.6 show MOLA

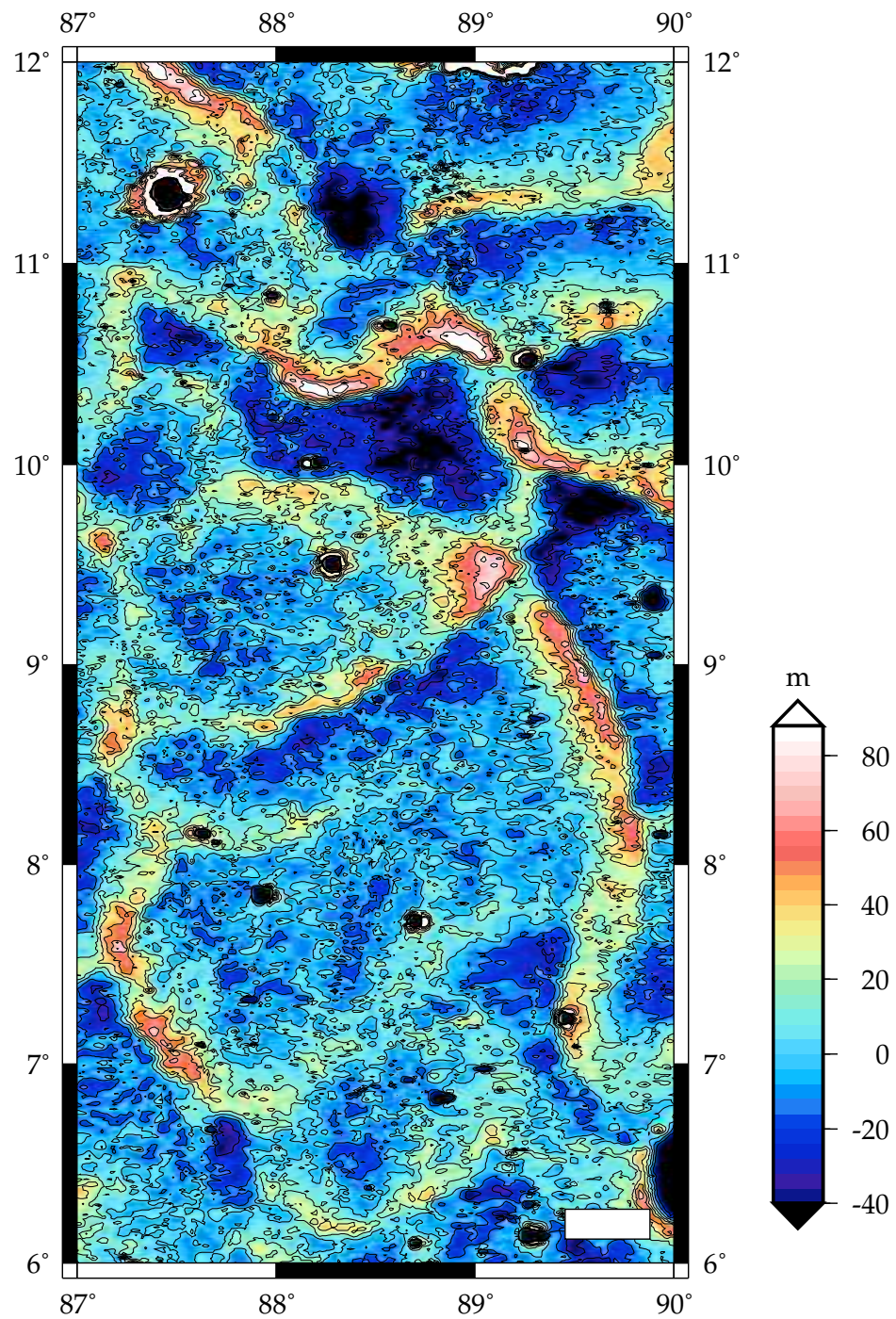


Figure 4.3: Ridges in Isidis Planitia, showing the ridges in central southern Isidis Planitia in a detrended MOLA map of the basin with contours showing the asymmetry of many of the ridges. Bar is ~ 25 km.

tracks across concentric and radial ridges respectively (and their general locations in the basin are illustrated by Figure 4.4). Many of the ridges in these profiles are distinctly asymmetric.

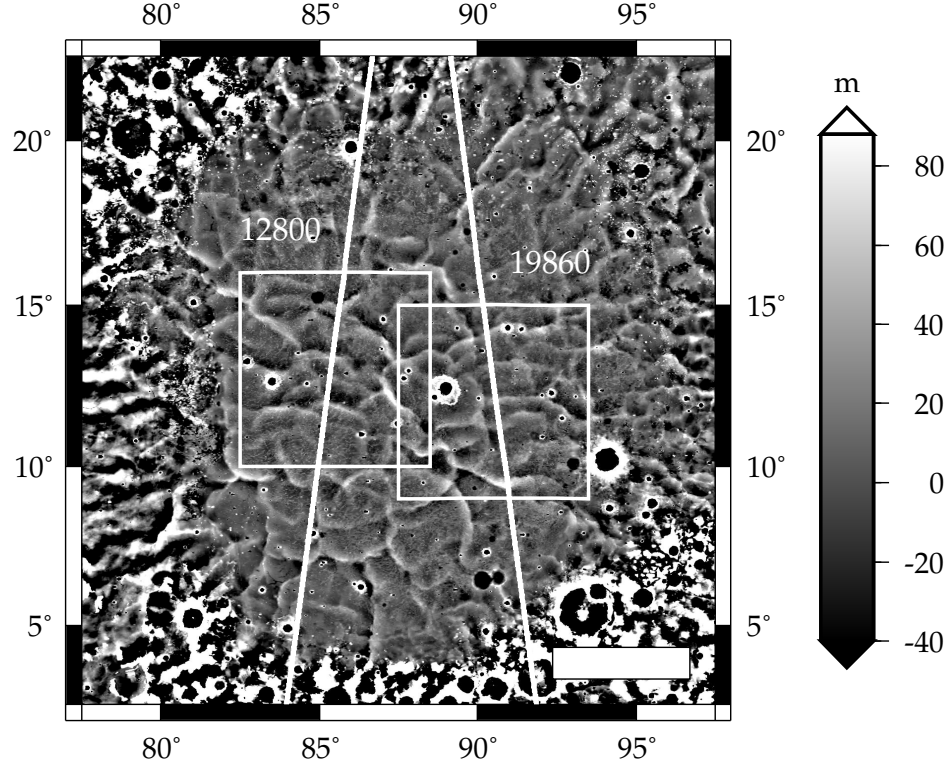
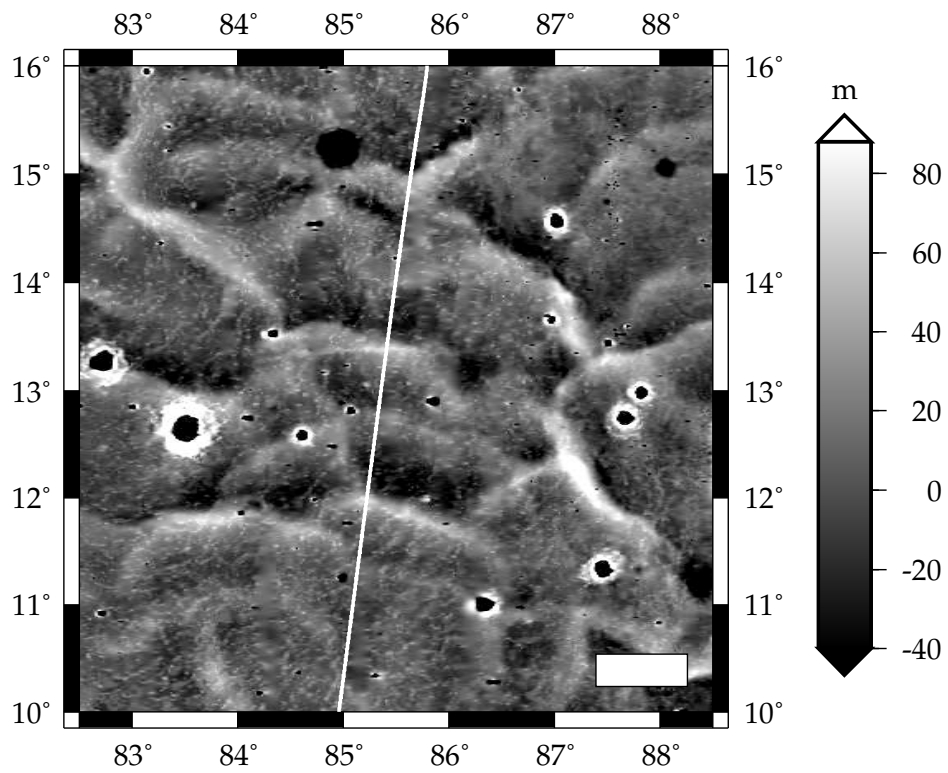


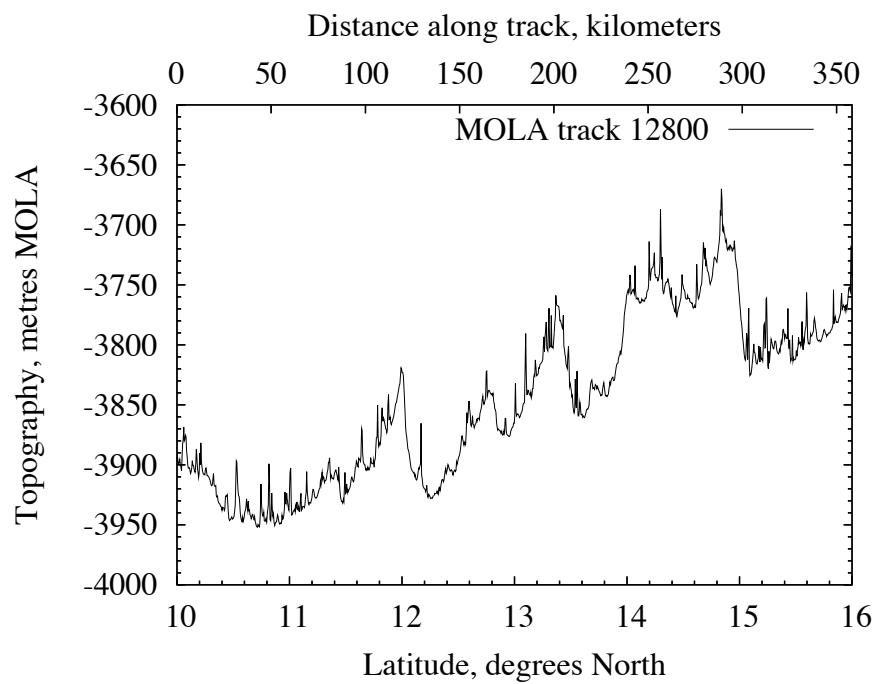
Figure 4.4: MOLA tracks across ridges. MOLA tracks 12800 and 19860 as they pass across Isidis Planitia. Boxes indicate the extent of the area shown in Figures 4.5 (left) and 4.6 (right). Bar is ~ 250 km.

For a closer view of the profile of individual ridges, Figure 4.7 shows two ridges in profile using non-detrended and ungridded MOLA data from individual orbits. Both ridges illustrated show distinct asymmetry. Figure 4.7(a) shows a concentric ridge which displays approximately 70 metres of topography, and a width of approximately 30 kilometres. Figure 4.7(b) shows a radial ridge which displays approximately 130 metres of topography, and a width of also approximately 30 kilometres. These figures appear typical of many of the ridges in the basin. As can be seen in both Figures 4.1 and 4.3 is that there is variation in topographic range within both concentric and radial ridges, with prominent and subdued examples of each.

If the asymmetry of the ridges is due to the uplift above thrust faults due to tectonic compression (e.g. Plescia and Golombek, 1986), this can be used to infer the dip direction

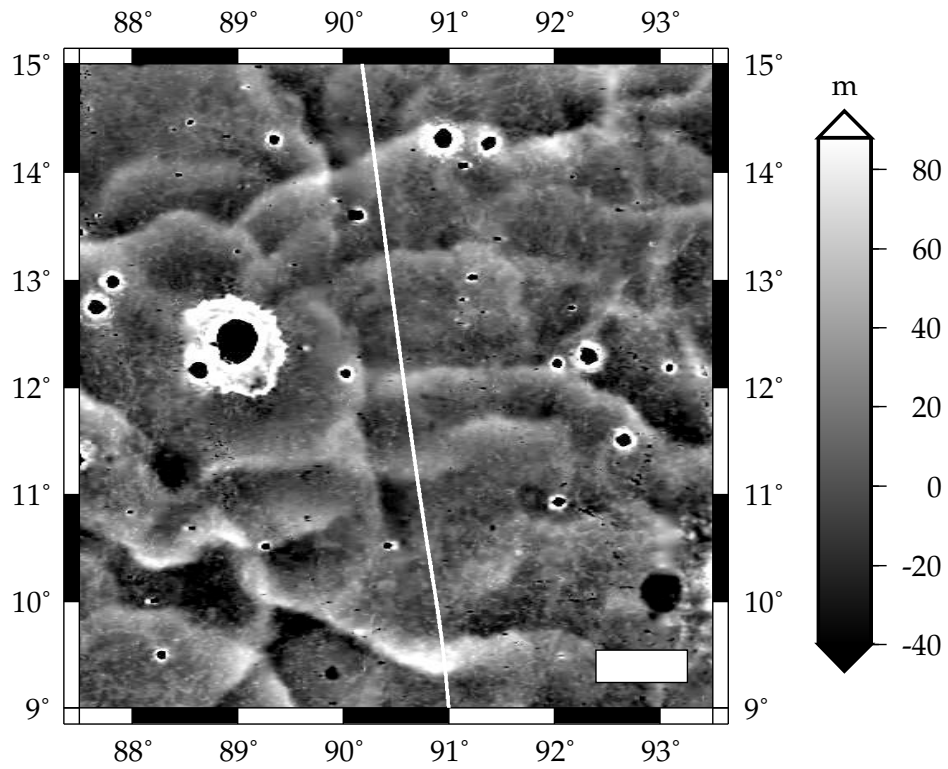


(a)

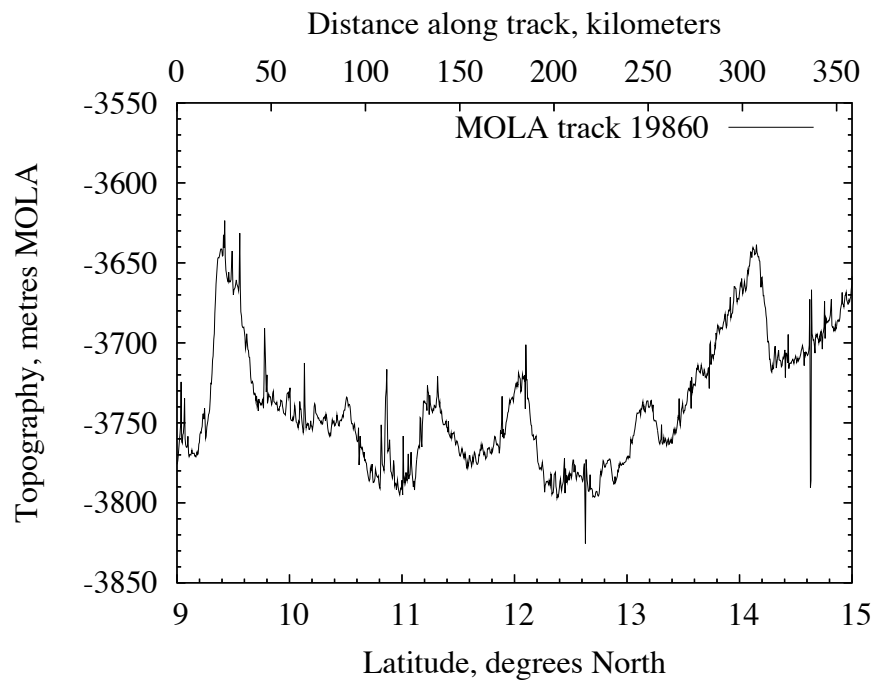


(b)

Figure 4.5: Concentric ridges in Isidis Planitia. (a) section of MOLA track 12800 and the surrounding area. Bar is ~ 50 km. (b) topography of MOLA track 12800 for the same geographical region

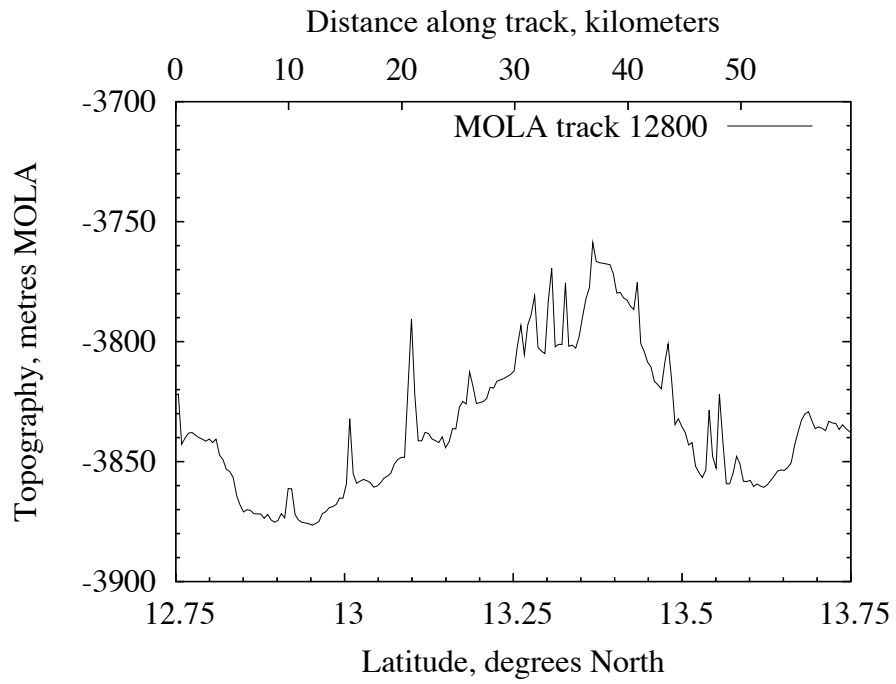


(a)

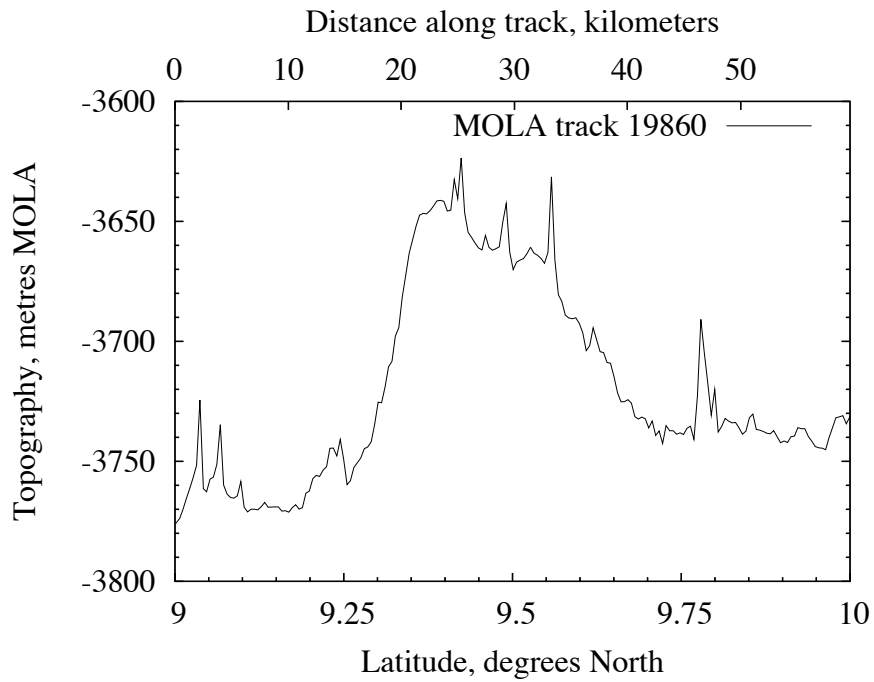


(b)

Figure 4.6: Radial ridges in Isidis Planitia. (a) section of MOLA track 19860 and the surrounding area. Bar is ~ 50 km. (b) topography of MOLA track 19860 for the same geographical region



(a)



(b)

Figure 4.7: Ridges in Isidis Planitia. (a) shows a profile of a single ridge in from MOLA track 12800. This is an example of a concentric ridge. (b) shows a profile of a single ridge from MOLA track 19860. This is an example of a radial ridge. Note the asymmetry of the ridges, implying a thrust direction, and the fairly simple morphology of the ridge.

of thrust of the fault. Variation in asymmetry may also provide information about the degree of subsurface fault dip (Okubo and Schultz, 2002). Figure 4.8 shows a map of these thrust directions for those wrinkle ridges which show enough topographic prominence to have an identifiable asymmetry. This shows that the concentric ridges generally have a thrust direction that is outwards from the centre of the area of concentric ridges (the centre-west of the basin), whereas the radial ridges generally have a thrust direction that appears anticlockwise in the northern half of the basin, and clockwise in the southern half of the basin. The complexity of the pattern of wrinkle ridges in Isidis Planitia, along with their relatively subdued topography, makes it difficult to identify secondary faults which may result from local stress changes due to slip along a primary thrust (Okubo and Schultz, 2002).

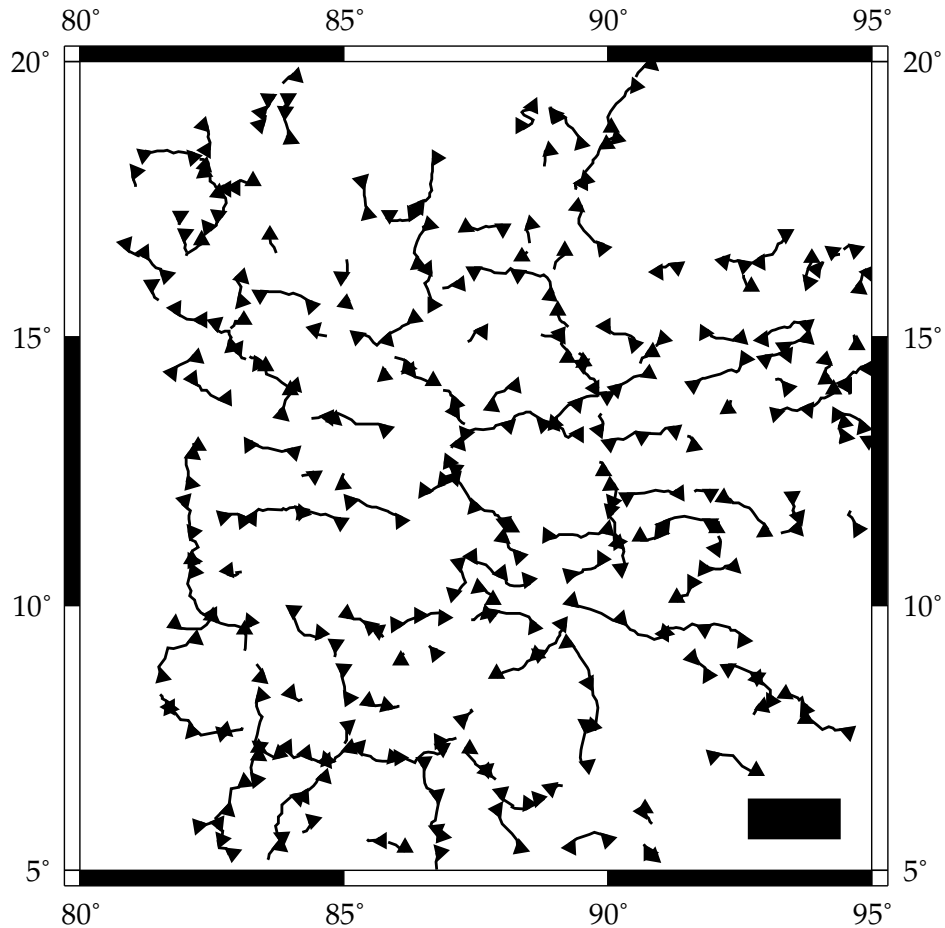


Figure 4.8: Ridge thrust directions in Isidis Planitia. Showing the same area with the most prominent ridges from Figure 4.1 and their thrust direction. Triangles point in the down-dip direction. Bar is ~ 100 km.

Assessment of the spacing between ridges is difficult in Isidis Planitia, due to the curvilinear nature of the concentric ridges, and the radial, rather than parallel, nature of the more linear radial ridges. However, generally the ridges appear to be between 30 and 60 kilometres apart, although the difficulty in identifying many of the more subdued ridges makes any estimate of ridge spacing problematic.

Figure 4.7 also shows that the ridges have a fairly simple morphology. Wrinkle ridges on terrestrial planets usually show a broad and gentle slope, sometimes with associated scarps, and with a superposed ridge (Banerdt and Golombek, 1992; Schultz, 2000a). The wrinkle ridge shown in Figure 4.7(a) shows only the broad topographic rise, although the ridge in Figure 4.7(b) may show a superposed ridge. However, the relatively broad and subdued nature of the topography of these particular ridges may play a part in the difficulty of identifying such features in the Isidis Planitia ridges. In particular the ‘wrinkle’ or crenulation typical of such ridges found elsewhere on Mars (e.g. see Figure 4.9) is not apparent in the Isidis Planitia features.

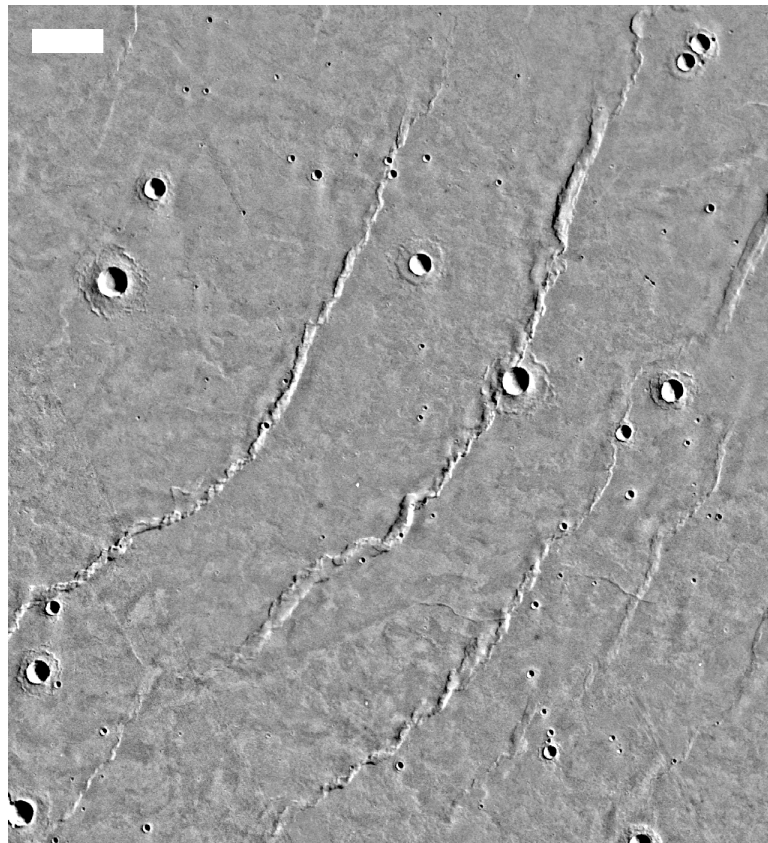


Figure 4.9: Wrinkle ridges in Solis Planum. VOC MDIM showing part of the western hemisphere highland plain Solis Planum. Bar is 25 kilometres. Mercator projection. Note distinct crenulations apparent as knotted and sinuous sharp relief features.

It must also be noted that the Isidis Planitia basin has been subject to significant amounts of sedimentary deposition (for further discussion about sedimentary deposition in the basin, see Chapter 2, Subsection 2.7.1, Chapter 5, Section 5.4, and Chapter 6, Section 6.2), so the morphology apparent at the basin surface may be somewhat misleading when compared with regions of Mars where such substantial deposition has not taken place. Certainly it appears that although the general morphology of ridges in Isidis Planitia is similar to that of those in highland plains areas, the northern plains ridges do have a more subdued appearance consistent with burial by sediments (Kreslavsky and Head, 2001; Thomson and Head, 2001; Head et al., 2002). Figure 4.9 shows ridges in a highlands plains region, and when compared with Figure 4.2(a), the highland ridges do show more detailed relief features, such as crenulations. Despite these differences, the ridges in Isidis Planitia have a similar topographic range to that of highland ridges, suggesting that their relatively low observability in comparison may be due to their shallower slopes, an absence of significant crenulations, or, probably less importantly, greater atmospheric scattering in images of the topographically low northern plains terrain (Tanaka et al., 2003), rather than necessarily by burial.

4.2.2 Elevation offsets

Elevation offsets are differences in surface height on either side of a wrinkle ridge. Elevation offsets were initially determined for the highland plains wrinkle ridges using photoclinometry and ascribed to faulting (Golombek et al., 1991), although Watters and Robinson (1997) suggested that photoclinometry alone was not sufficient to determine an accurate profile, and combined the photoclinometric data with radar altimetry, finding little evidence of offsets between structural blocks of ridges, and suggesting that any offsets could be the result of lava ponding or the deposition of aeolian material. Subsequently, accurate topography data from MOLA enabled more detailed investigation of elevation offsets to take place.

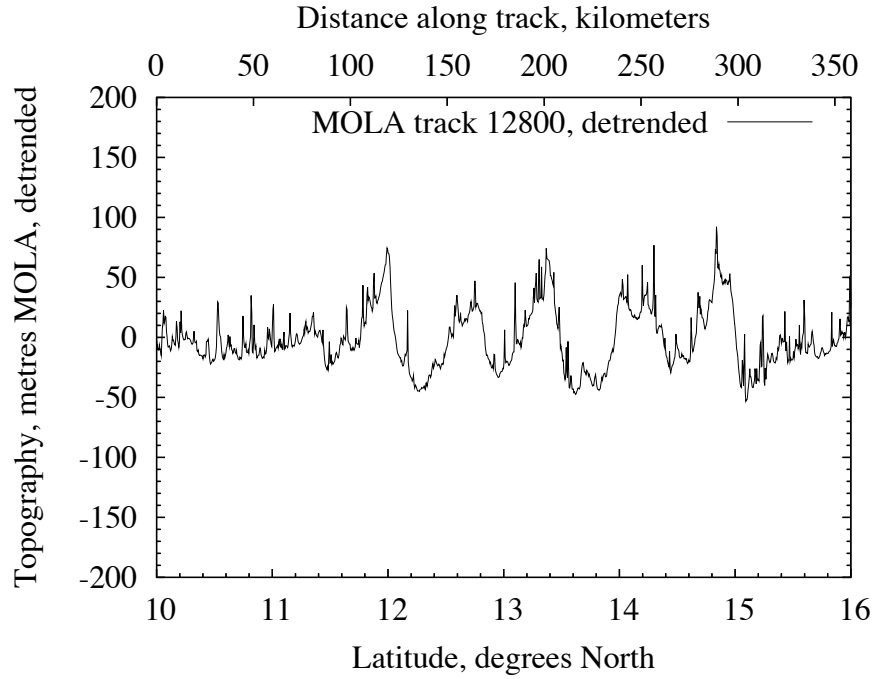
Determining the presence and extent of elevation offsets across the Isidis Planitia wrinkle ridges is made more difficult by the relative proximity of the ridges caused by their great width. Figures 4.5 and 4.6 show the close proximity of both concentric and radial ridges, and in many cases the plains between them are significantly narrower than

the ridges themselves. However, in both the profiles in Figure 4.7 it can be seen that there exists an elevation offset – approximately 15 metres in Figure 4.7(a) and 30 metres in Figure 4.7(b). Offsets can also be seen in other ridges from these MOLA tracks, as shown in Figures 4.5 and 4.6. However, many elevation offsets found elsewhere on Mars have been found to disappear when the regional slope from the area in which they are found is removed (Watters and Robinson, 2000; Watters, 2001). As noted previously in this chapter, and discussed more fully in Chapter 3, there is a small ($< 0.02^\circ$), but statistically important, slope across the Isidis Planitia basin (Frey et al., 1998; Hiesinger and Head, 2003).

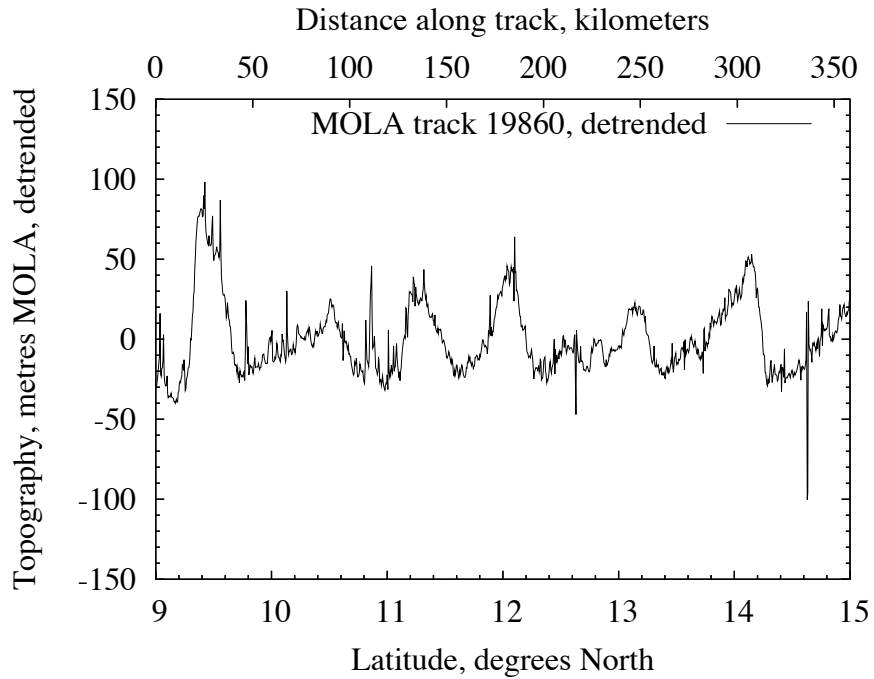
Removing the regional slope from a MOLA track by detrending the data is discussed in Chapter 3. Removal of the regional slope from the profiles shown in Figures 4.5, 4.6 and 4.7 is shown in Figures 4.10 and 4.11. In comparison, there appears to be a significant reduction, or even elimination, of the elevation offset across the wrinkle ridges shown in these profiles. This is particularly noticeable in Figure 4.10. In Figure 4.11(a) the elevation does not appear to have decreased significantly in magnitude, but detrending the data has resulted in the plain in ‘front’ of the ridge (to the right of the figure) having a lower altitude than that ‘behind’ the ridge in contrast to the original data. In Figure 4.11(b) the elevation offset is approximately 10 metres, which is significantly less than in the corresponding non-detrended profiles, suggesting that it is the regional slope that is primarily responsible for the elevation offset across wrinkle ridges in Isidis Planitia. This may have far-reaching consequences for the nature of the subsurface, and the mechanism of formation of these features.

4.2.3 Interaction with other features

The wrinkle ridges’ interaction with other physical features, such as impact craters, in the basin may provide clues about their nature and time of formation (Mest and Crown, 1996). Isidis Planitia contains two ‘levels’ of impact craters – fresh craters that appear on the basin surface, and buried craters that appear to have impacted into a previous basin surface and subsequently been covered (for further discussion of the fresh and buried impact craters in the basin, see Chapter 5). Analysis of MOLA gridded and interpolated data suggests that the fresh craters are superposed upon the wrinkle ridges – i.e. the

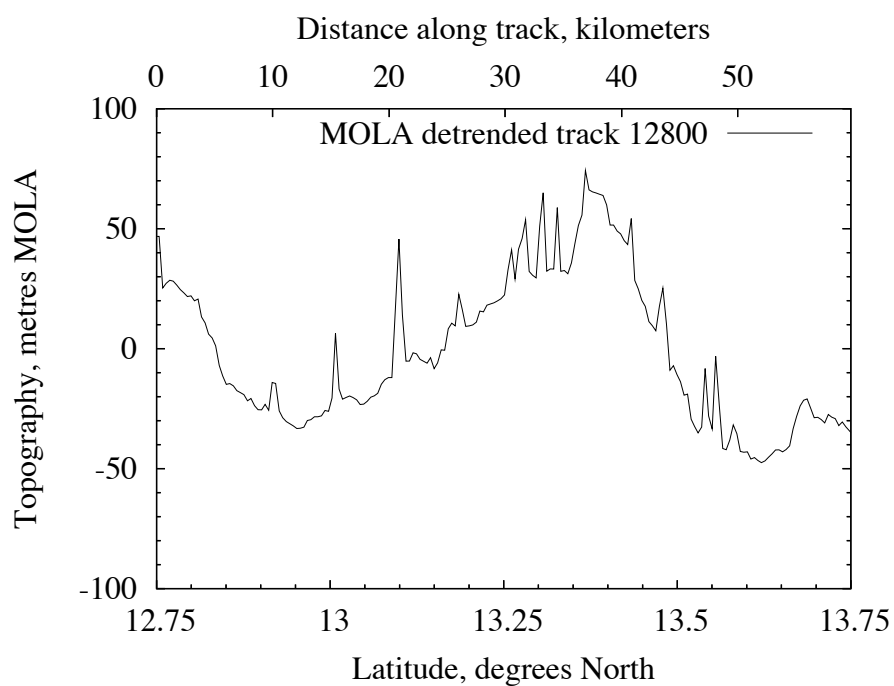


(a)

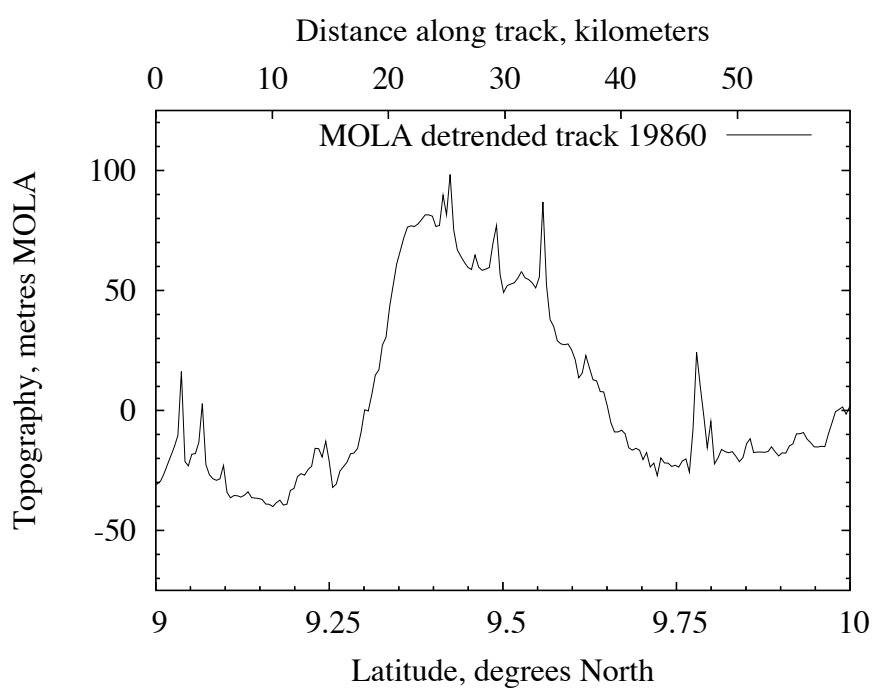


(b)

Figure 4.10: Detrended topography across ridges in Isidis Planitia. (a) detrended topography of MOLA track 12800. Compare to Figure 4.5(b). (b) detrended topography of MOLA track 19860. Compare to Figure 4.6(b). Note that the topography is detrended linearly along the MOLA track, and not taking into account adjacent MOLA tracks and may therefore differ to a small extent to that from a more complete detrending of a gridded MOLA dataset. See Chapter 3 for further details.



(a)



(b)

Figure 4.11: Ridges in Isidis Planitia using detrended data. (a) profile of a single ridge in from MOLA track 12800 using detrended data. (b) profile of a single ridge from MOLA track 19860 using detrended data. Compare with Figure 4.7.

wrinkle ridges predate the craters. It is difficult to identify the buried craters in the basin due to their subdued topography in gridded data with a relatively coarse resolution, but the ones that are easily visible all appear to superpose the wrinkle ridges, in much the same way as the fresh craters (e.g. see Figure 4.12(a)). One particular example is the pair of buried craters centred at approximately $90.5^{\circ}\text{E } 6.5^{\circ}\text{N}$ which appears to superpose a wrinkle ridge, with no evidence of faulting and/or thrusting in the crater floor, again implying that ridge formation predates this impact (see Figure 4.12(b)).

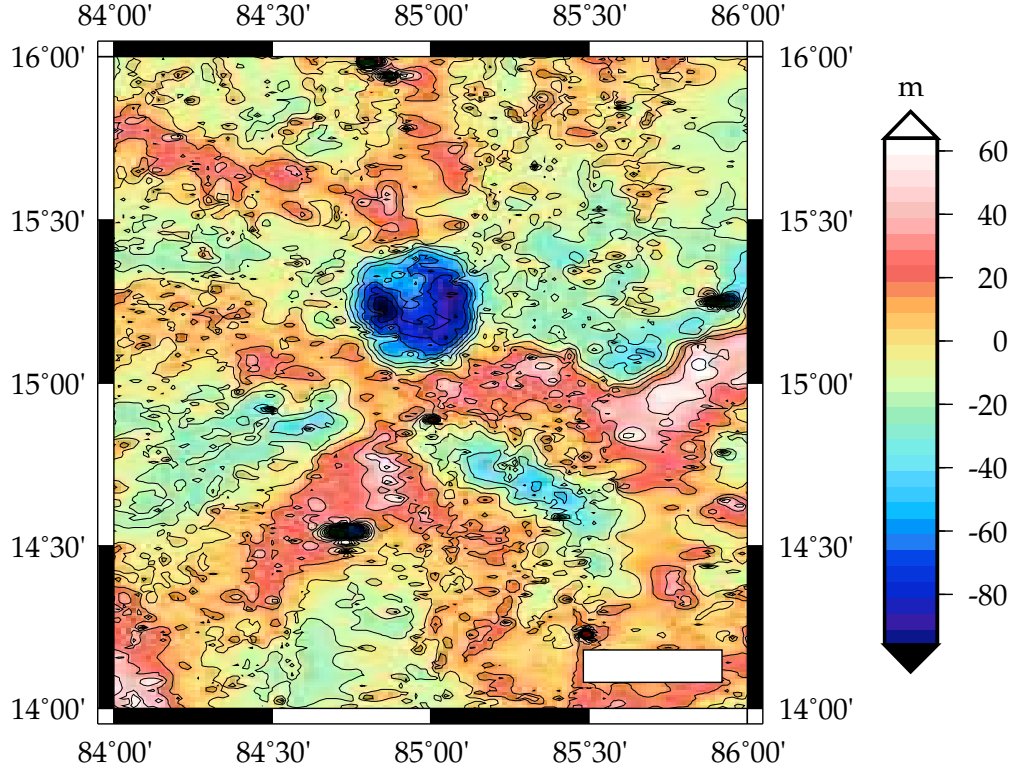
The older highland terrain surrounding the Isidis Planitia basin to the northwest, west and south is topographically much more complex than the basin itself. It is much more mountainous and densely cratered. In a very few places, particularly in the southwest of the basin, it appears that there may be some correlation between wrinkle ridges in the basin and topographic features in the highland terrain. However, I believe this is most likely to be coincidental.

To the northeast of the Isidis Planitia basin lie the plains of Utopia Planitia, which are separated from Isidis Planitia by a broad, generally raised, area of terrain. Utopia Planitia also exhibits a network of wrinkle ridges (Head et al., 2002), as does the raised transition area between the two basins. However, there is little evidence of continuity of ridges across the boundary between the Isidis Planitia basin and the raised transition area. In fact the two areas appear to show a discontinuity at a relatively distinct boundary in detrended MOLA maps of the region, with the ridges in the transition area appearing less subdued topographically, and more chaotic (see Figure 4.13).

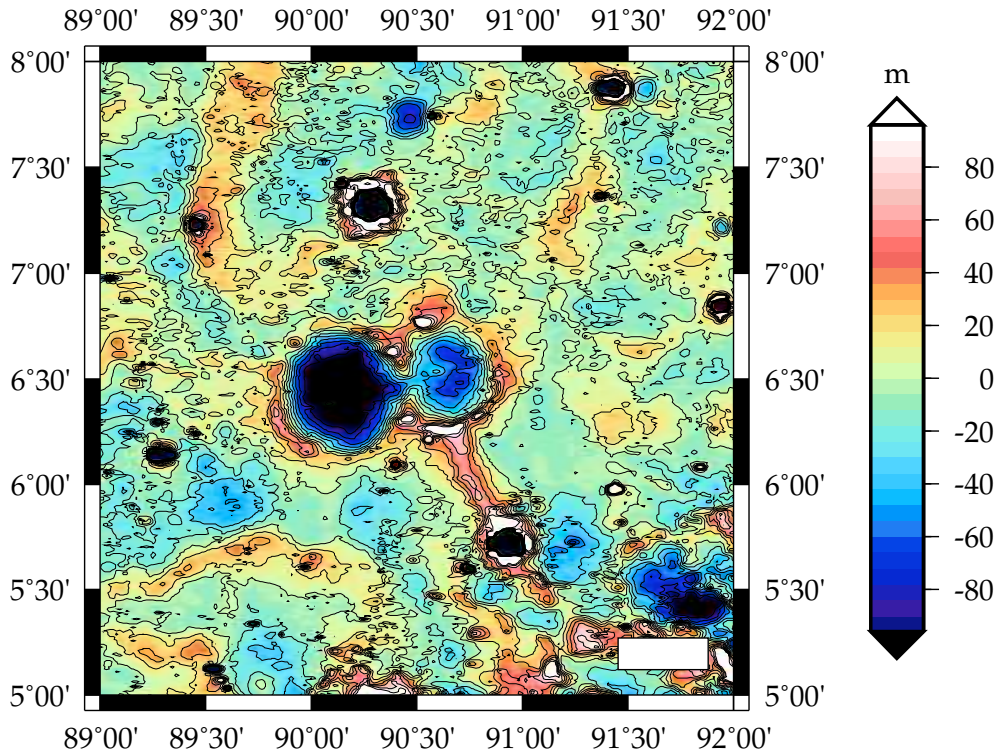
4.3 Formation of the wrinkle ridges

4.3.1 Introduction to ridge formation

Wrinkle ridges on Mars are considered by most current researchers to be compressional structures (e.g. Mueller and Golombek, 2004). Plescia and Golombek (1986) determined that the martian structures were analogous to certain terrestrial features caused by thrust faults reaching the surface and forming asymmetric ridges in a compressional environment. Many structural models have been proposed for the formation of wrinkle ridges



(a)



(b)

Figure 4.12: Ridges and buried craters in Isidis Planitia using detrended data. (a) wrinkle ridges surrounding a buried crater in central-west Isidis Planitia. (b) wrinkle ridges surrounding a pair of buried craters at the southeastern rim of the basin. Bars in both images are ~ 25 km.

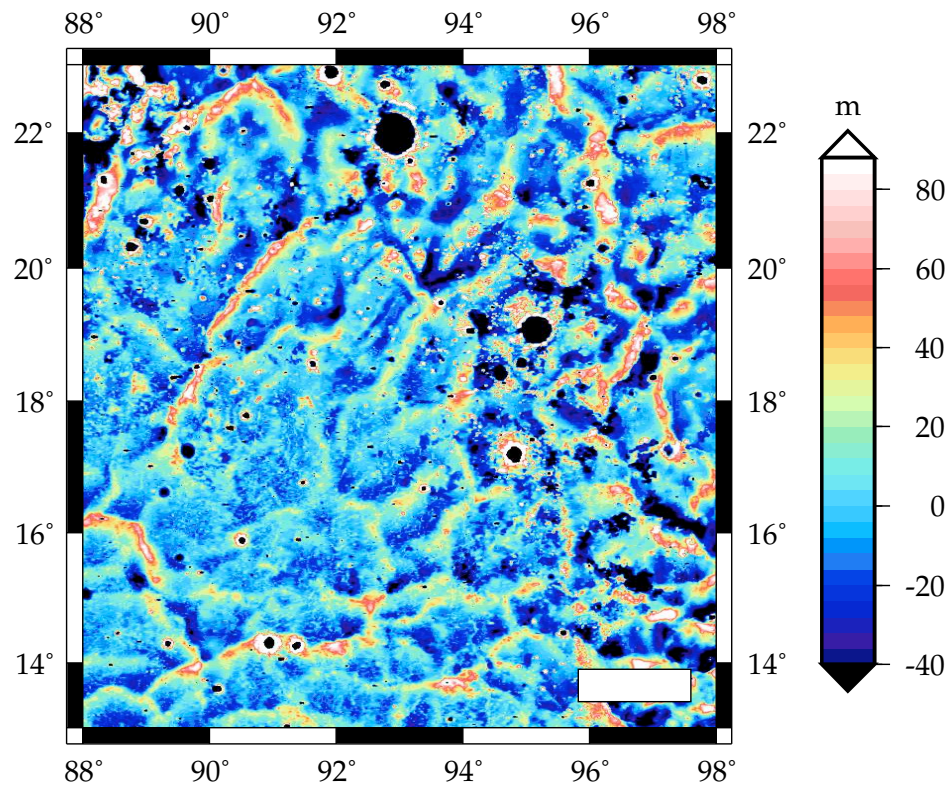


Figure 4.13: Ridges in northeastern Isidis Planitia using detrended data. Shows the discontinuity in wrinkle ridges and general terrain between Isidis Planitia (bottom-left), and the unit that separates it from Utopia and Elysium Planitiae (top-right). The discontinuity exists as an irregular curve from top-left to bottom-right. Bar is $\sim 100\text{km}$.

on Mars, and elsewhere on terrestrial planets. These include buckle folds (e.g. Watters, 1988), simple thrust faults (e.g. Plescia and Golombek, 1986), conjugate thrust faults (e.g. Mangold et al., 1998), fault-bend folds, fault-propagation folds, foreland basin uplifts (e.g. Golombek et al., 2001), and blind thrust faults (Schultz, 2000b). The subdued nature of the ridge topography makes the photogeological or topographic analysis of features that would favour a particular model of subsurface ridge formation very difficult. Significant work has been done by several researchers in using models of the subsurface mechanisms responsible for wrinkle ridge formation to make inferences about the nature of the surface layers of Mars (e.g. Zuber, 1995; Schultz, 2000a).

4.3.2 Stress origin for wrinkle ridge formation

Many of the wrinkle ridge populations on Mars are thought to have been generated by compressional tectonic forces from the development of the Tharsis rise (Banerdt and Golombek, 1992; Golombek and Banerdt, 1999). Flexural loading by Tharsis is thought to be the main mechanism for producing the radial compressive stress concentrations that generated wrinkle ridge populations (Banerdt and Golombek, 2000). Wrinkle ridges generated by the stresses from the development of Tharsis are found throughout the western hemisphere of Mars, and this mechanism may also have influenced wrinkle ridge development and orientation in the eastern hemisphere (Hall et al., 1986), perhaps forming a global circum-Tharsis ridge system (Head et al., 2002). However, many ridge systems in the eastern hemisphere may be primarily generated by stresses from non-Tharsis related sources. These may include impact cratering (Raitala and Kauhanen, 1992), lithospheric loading by mare basalt accumulation (Head et al., 2002), and other local and global mechanisms (e.g. Hauck et al., 2003).

The discovery of extensive wrinkle ridge populations within the northern hemisphere lowlands (Withers and Neumann, 2001; Head et al., 2002) added new populations of martian ridges to the highland plains ridges mapped by Chicarro et al. (1985). The Isidis Planitia wrinkle ridges, along with those in Utopia Planitia, show individual ridge patterns unrelated to those influenced by Tharsis (Head et al., 2002). The Isidis Planitia ridge system has been interpreted as forming as a result of stress from lithospheric loading by the accumulation of basalts within the basin, in a process similar to lunar mare exam-

ples (Solomon and Head, 1980) (see Figure 4.14), and possibly combined with contraction caused by global thermal stress (Head et al., 2002).

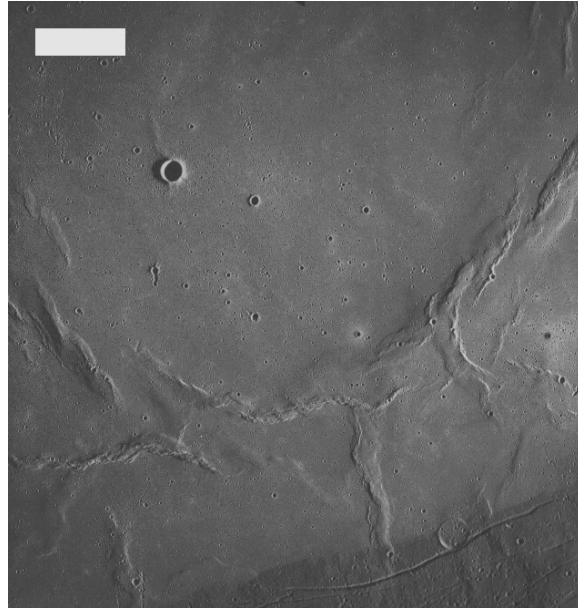


Figure 4.14: Lunar wrinkle ridges in Mare Serenitatis. Apollo 17 Metric photograph AS17-602. Bar is 25 kilometres.

4.4 Discussion

4.4.1 Nature of the Isidis Planitia subsurface

The subsurface nature of the Isidis Planitia wrinkle ridges is difficult to determine from photogeology of the surface, given the difficulty in identifying even the most basic components of the ridge structure in images of the basin. The lack of distinct crenulations found in northern plains wrinkle ridges (Tanaka et al., 2003) could suggest that northern plains ridges form in a mechanically homogenous material that inhibits the secondary faulting that may be the cause of crenulation formation in ridges found elsewhere (Okubo and Schultz, 2002; Tanaka et al., 2003). Alternatively, the lack of crenulations could perhaps be the result of the softening of topography by erosion or burial, which seems quite likely given that Isidis Planitia is considered to be a site of significant deposition of material.

Ridge spacing has been used in other wrinkle ridge populations to infer details of the vertical strength of the martian lithosphere (e.g. Banerdt and Golombek, 1992). In the ridged highland plains wrinkle ridge spacing is ~ 40 kilometres, whereas across the northern

lowlands generally, ridge spacing is ~ 80 kilometres. This was interpreted by Head et al. (2002) as being due to sediment burial obscuring alternate ridges. However, Montési and Zuber (2003) pointed out that the necessary bimodal distribution of ridge heights is not seen in ridge populations in the highland plains, and is mechanically unlikely, suggesting instead that a greater depth of faulting may be the explanation for the spacing. In highland areas the crust is thicker and the brittle-ductile transition may lie within the crust, whereas in lowland areas the thinner crust may be completely brittle and faulting may occur in the mantle, which has a much deeper brittle-ductile transition region than the crust. The situation may not be so clear in Isidis Planitia as with relatively few parallel ridges ridge spacing is hard to accurately assess. Where ridge spacing in Isidis Planitia can be estimated it does appear to be generally nearer to the typical value for the northern lowlands than that of the highlands.

The presence of significant numbers of strongly curved ridges within the Isidis Planitia basin may argue against a formation model involving deep rooted thrust faults. Variation of local stress along the length of a deep thrust fault would seem unlikely to produce such large rotations of principal stress as can be found in some of the Isidis Planitia ridges. One alternative model could involve conjugate thrust faults rooted on a décollement level and initiated at the boundary of a filled crater (Mangold et al., 1998). However, this perhaps does not adequately explain the relatively similar radii of curvature of the concentric ridges in the basin, their overlapping nature, and their localisation to one specific part of the basin floor. However, a thin-skinned model of formation is perhaps also supported by one model of wrinkle ridge formation in Isidis Planitia that suggests that ridge formation is due, at least in part, to internal contraction of the basin (Head et al., 2002) as ridges in this environment are unlikely to have formed above blind thrusts that are deep-seated in the lithosphere (Mueller and Golombek, 2004). The lack of significant elevation offsets across the ridges also favours a thin-skinned model of formation.

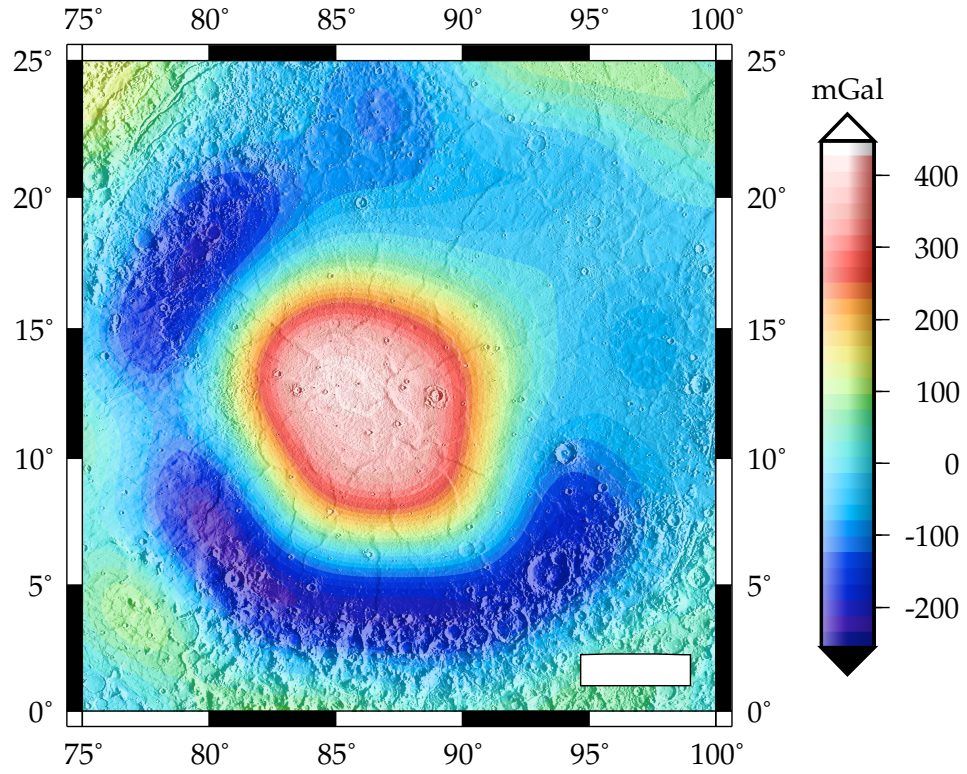
4.4.2 Mascon loading as a formation model

Isidis Planitia has the thinnest crust on Mars – perhaps as thin as 3 kilometres (Zuber et al., 2000), which is much thinner than is generally found beneath the northern lowlands – and is the site of a lunar-like mascon (Solomon et al., 1983). Mascons are positive

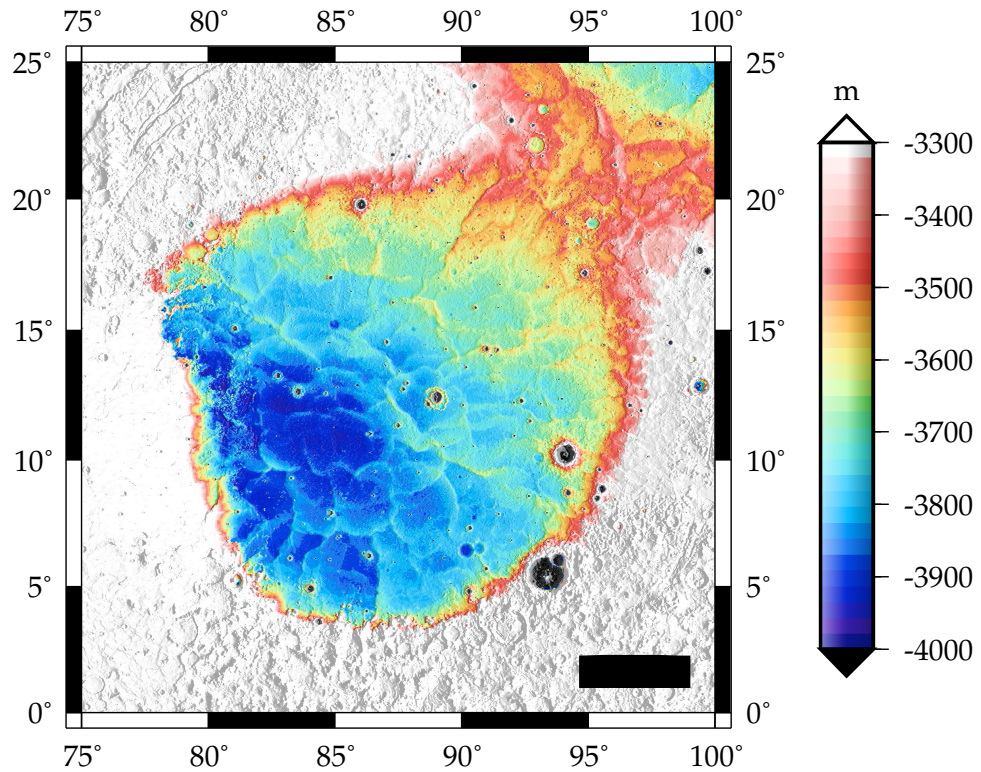
gravity anomalies. Two main models have been proposed to explain the mascon gravity high (Kiefer, 1999). The first model involves an uncompensated load present close to the surface – often considered to be dense basaltic fill. In the second model, the excess mass is a result of super-isostatic relief at the crust-mantle boundary (note that in this case the Isidis Planitia crust is so thin that this may occur very near to the basin surface). It may be the case that both mechanisms play a part in the formation of mascons.

In many respects the Isidis Planitia tectonic environment seems very similar to that of a lunar mascon, and such sites on the Moon are also the location of wrinkle ridge populations. As a means of generating the compressive stresses required to form the series of ridges found in the Isidis Planitia basin, the loading of a mascon basin would seem to be a mechanism supported by much of the evidence. Melosh (1978) derived a model for an idealised lunar mascon based upon Anderson’s criterion for faulting styles (Anderson, 1951). This determined that at the centre of the mascon is a region of thrust faults resulting from the hoop (concentric) stress and radial stress both being compressive. At the centre the hoop and radial stresses would be equal so thrust orientation would not be controlled, but away from the centre of this region the thrusts would be radial thrust faults due to the hoop stress being more compressive than the radial stress. Surrounding this region is an annulus of strike slip faults resulting from a compressive hoop stress and an extensional radial stress. Beyond this is a region of concentric normal faults, or grabens, formed by extensional hoop and radial stresses.

Isidis Planitia is partially surrounded by features considered to be concentric grabens as predicted by the Melosh (1978) model (e.g. Head and Bridges, 2001). The Nili Fossae series of grabens lie northwest of the basin (see Figure 4.16). To the southeast are the Amenthes Fossae grabens, which appear infilled in places by the material forming the Amenthes Planum. However, the wrinkle ridge patterns in Isidis Planitia show a controlled orientation towards a concentric thrust direction near the basin centre, and a radial thrust direction only nearer the basin margin. There is no obvious sign of a region of strike-slip faulting between the radial thrusts and the grabens. A revised and expanded version of the Melosh (1978) model addressed the lack of strike-slip faulting (Freed et al., 2001), which is also missing from lunar examples. Freed et al. (2001) suggested that the Melosh (1978) model was too simple, and included the effects of lunar curvatures, heterogenous crustal



(a)



(b)

Figure 4.15: The Isidis Planitia mascon. (a) free-air gravity anomaly characteristic of a mascon within the Isidis Planitia basin. Gravity anomaly data from MGS75D (Tyler et al., 2000). Data have been illuminated using MOLA topography for reference. (b) MOLA topography of the same geographical region for comparison. Bars in both images are ~ 250 km.

strength, initial stress conditions and multistage loading histories in their model with the result that the zone of strike-slip faulting is much reduced in size. Additionally, the thrust fault region towards the centre of the basin becomes more complex, with the central region of the mascon having compressive radial stress of a greater magnitude than compressive hoop stress, resulting in concentric thrust faults, with the region of radial thrust faults predicted by Melosh (1978) forming an annulus between the central concentric thrust fault region and the now much reduced region of strike-slip faulting. Further away from the centre, there is again a region of concentric normal thrusts or grabens, followed by zones of radial normal and strike-slip faulting, although with an increasingly lower stress state presumably resulting in less obvious tectonic features.

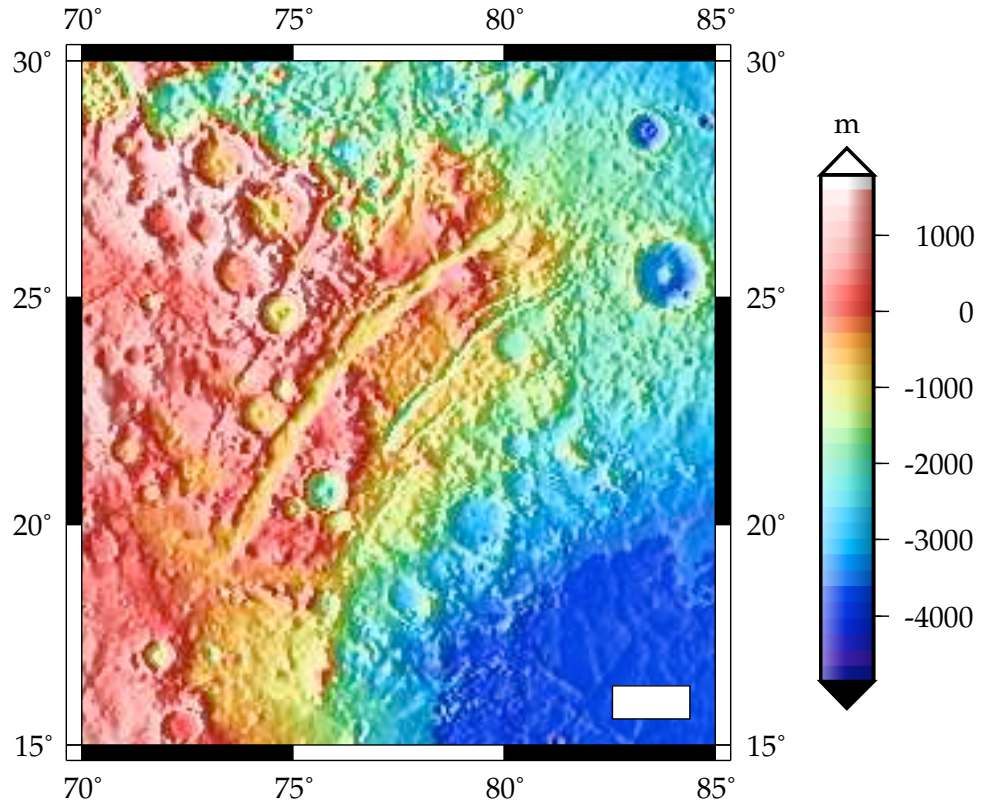


Figure 4.16: Nili Fossae. The Nili Fossae series of grabens to the northwest of the Isidis Planitia basin (which is visible at the bottom-right of the image). Bar is ~ 100 km.

The Freed et al. (2001) revised model is a reasonable explanation of the origin of many of the tectonic features associated with the Isidis Planitia basin. A region of concentric thrusts surrounded by an annulus of radial thrusts, with concentric normal faulting occurring further from the basin, is predicted by the model and is seen in Isidis Planitia. No strike-slip faults are visible in the expected region in Isidis Planitia, but this region is

predicted to be small, and given that the detectable concentric normal faulting around the basin is incomplete it is not unreasonable to suppose that either local conditions prevented strike-slip faulting from taking place, or there is limited strike-slip faulting that has either been obscured or not yet detected from photogeological or topographical investigations. The Freed et al. (2001) model incorporates surface curvature as a parameter, and determines that the annulus of strike-slip faulting decreases in width with decreasing planetary radius. This suggests that the region of strike-slip faulting on Mars would be larger than for lunar examples, but still relatively small. The width of the strike-slip zone in this model is also affected by the lithospheric thickness at the time of basin loading, with a decrease in the width of the strike-slip region with decreasing lithospheric thickness. The lithospheric thickness beneath Isidis Planitia is estimated to be approximately 120 kilometres (Comer et al., 1985; Solomon et al., 1998), which is thicker than in lunar examples. Lithospheric thickness also determines the location of the region of normal faulting, with decreasing lithospheric thickness being reflected in decreasing distance of the normal faulting zone from the basin centre.

The off-centre orientation of the concentric ridges in the basin noted could perhaps be the result of a non axially-symmetric load. The gravity anomaly identifying the Isidis Planitia mascon (see Figure 4.15) suggests that the mascon is neither axially symmetric itself, nor lying centrally within the Isidis Planitia basin. The mascon lies towards the southwest of the basin, near the region of the basin that is lowest lying, although these regions are not entirely superimposed – the topographic low being further southwest than the gravity anomaly high. If the topographic low and the gravity anomaly high are related, it may suggest that rather than the tilt in Isidis Planitia being due to external tectonics (e.g. Tanaka et al., 2000), it may be due, at least in part, to tectonics within the basin itself caused by non axially symmetric loading.

The origin of the volcanic fill in lunar mascons is debated, with emplacement of basalts suggested as being a result of either the basin-forming impact or due to post-impact mechanisms (e.g. Werner and Loper, 2000). The current Isidis Planitia basin surface is considered to be upper-Hesperian or Amazonian in age (Greeley and Guest, 1987; Tanaka et al., 2003) (for further discussion on the age of the basin surface, see Chapter 5, Section 5.3), although the basin is generally believed to have been formed early in the Noachian epoch.

However, there is significant evidence for a buried unit beneath the current surface layer of the basin (Head et al., 2002) (for further discussion about the nature and age of the buried unit, see Chapter 5, Section 5.4). Ivanov and Head (2003) suggested a sequence of events where lavas from Syrtis Major filled the Isidis Planitia basin and were subsequently deformed to form the wrinkle ridges. Vastitas Borealis materials then filled the basin, covering the volcanic layer and softening the topography of the wrinkle ridges. Later lava flows from Syrtis Major were then emplaced upon this surface, resulting in the knobby terrain found in western Isidis Planitia. Ivanov and Head (2003) suggest a lower- to mid-Hesperian age for the emplacement of the lavas, which is most likely significantly later than any impact unloading event which might have formed basalts as a result of mantle decompression. The emplaced lava flows would then subsequently deform to produce the wrinkle ridges, and this is generally consistent with the suggested age for the formation of the concentric normal faults around the Isidis Planitia basin (Greeley and Guest, 1987), which would have formed as a response to the loading of the basin by the volcanic infill.

Chapter 5

Craters in Isidis Planitia

5.1 Introduction

Mars has a great diversity of crater morphology, modification and density compared with other planets and moons in the Solar System. This is the result of a unique combination of factors such as the influence of an atmosphere, the likely presence of subsurface volatiles, and the wide range in age of surface material (Strom et al., 1992). Crater morphology can also indicate the environment in which the craters exist after formation, and subsequent modification by geophysical processes. Study of these aspects of the martian cratering record can shed light on many of the processes and environments that are involved in the formation and modification of martian impact craters.

5.2 Crater morphology and morphometry

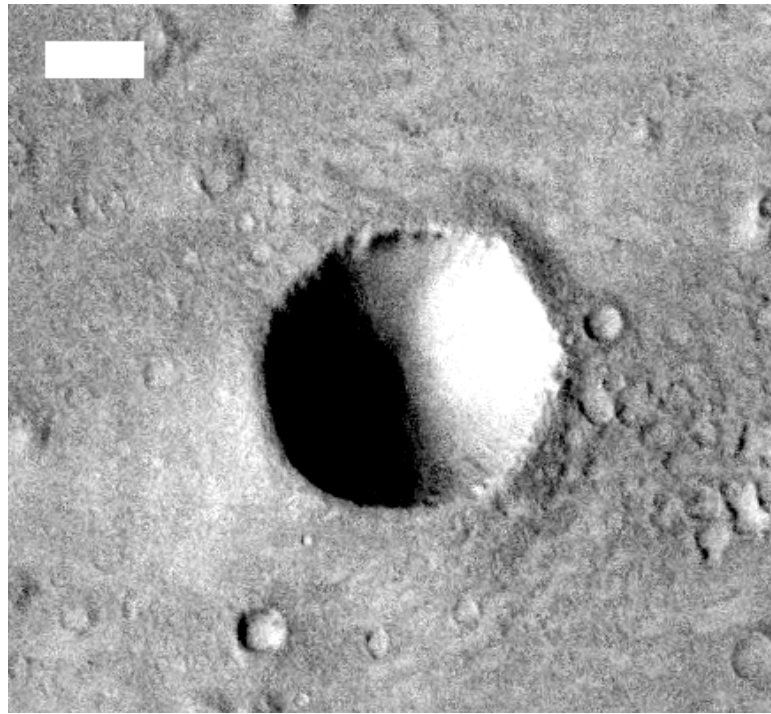
5.2.1 Crater morphology

Along with the rest of the northern lowland plains, Isidis Planitia is relatively lightly cratered. This is due to its relatively young age (see discussion later in this chapter, in Section 5.3). However, there are plenty of craters to study in Isidis Planitia, with sizes from as small as can be identified in remotely sensed images of the region (a few

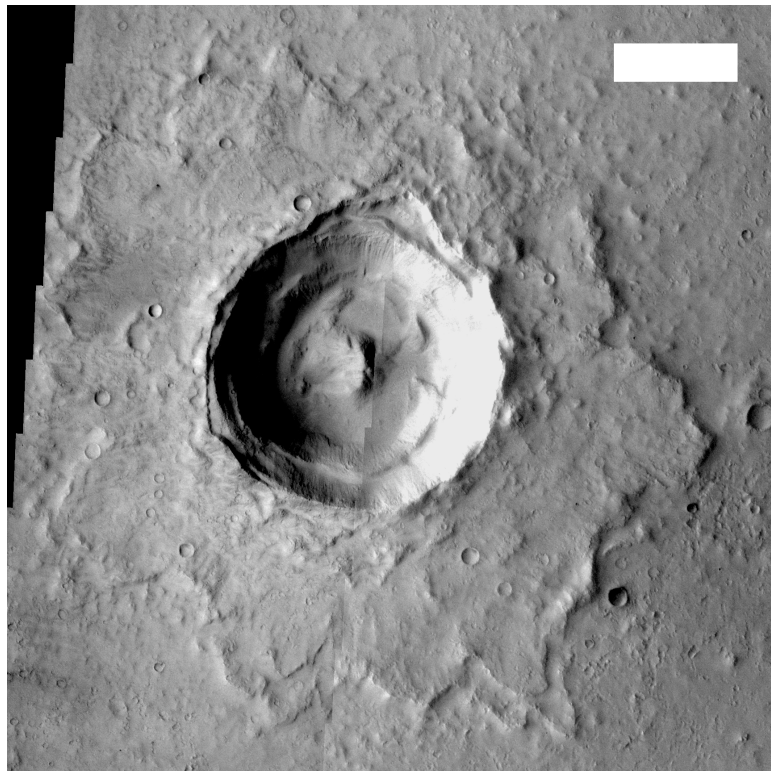
metres), through to a crater with a diameter of nearly 50 km – large enough to encompass Greater London. Isidis Planitia also contains a variety of crater forms, from simple bowl-like depressions to complex craters with central peaks, terraced walls, and layered ejecta. Analysing these crater morphologies plays an important role in understanding the basin itself.

Simple craters are small, less than ~ 7 km in diameter on Mars (Garvin et al., 2003), and have a simple bowl shaped depression, smooth walls, and a raised rim (see Figure 5.1(a)). Complex craters are larger – approximately 7 to 100 km on Mars, and have a central peak caused by rebound of the target material after impact, with terracing and landslides in the internal wall resulting in shallower walls than a simple crater (see Figure 5.1(b)). The layered ‘rampart’ ejecta of the crater in Figure 5.1(b) is not necessarily a feature of complex craters, although most craters in Isidis Planitia larger than a few kilometres in diameter show some degree of layered ejecta. Craters near the size boundary between simple and complex often show features of both and are known as transitional craters. Craters larger than the complex type are not found within the Isidis Planitia basin, although Isidis Planitia itself is an impact basin – a feature on a much larger scale. Secondary craters may be formed from the material ejected from a impact. These may be non-circular as a result of a relatively low angle of impact, although many appear morphologically similar to primary craters (see discussion later in this chapter, in Section 5.3, about the problems secondary craters pose in determining the age of the martian surface).

All the larger craters in Isidis Planitia exhibit layered ejecta to some extent (e.g. Figure 5.1(b)). Although the term ‘fluidised’ is often used in publications when referring to these craters – reflecting the fluidised appearance of their ejecta – the description ‘layered’ is more properly used in order to remove the potential for confusion regarding origin, which may, or may not, involve a fluid (Barlow et al., 2000). Figure 5.2 shows the topography of two layered ejecta craters in Isidis Planitia which show ramparts and moats, and are usually simply referred to as a rampart craters. The ‘rampart’ refers to the distal ridge at the edge of the ejecta, and ‘moat’ to the dip in the topography between the rampart and crater rim. All layered ejecta craters show a rampart of some kind (Barlow et al., 2000). Differences between the two examples shown include the more subdued topography of the ejecta, including a less prominent distal ridge and moat, in Figure 5.2(a). This example



(a)



(b)

Figure 5.1: Craters types in Isidis Planitia. (a) Simple crater from Thermal Emission Imaging System (THEMIS) visible image V09334009. Bar is 1 km. Crater is 3.15 km in diameter. (b) Complex crater showing central peak, terracing, and rampart ejecta. From a mosaic of THEMIS visible images V01832003 and V06301020. Bar is 5 km. Crater is 12.4 km in diameter.

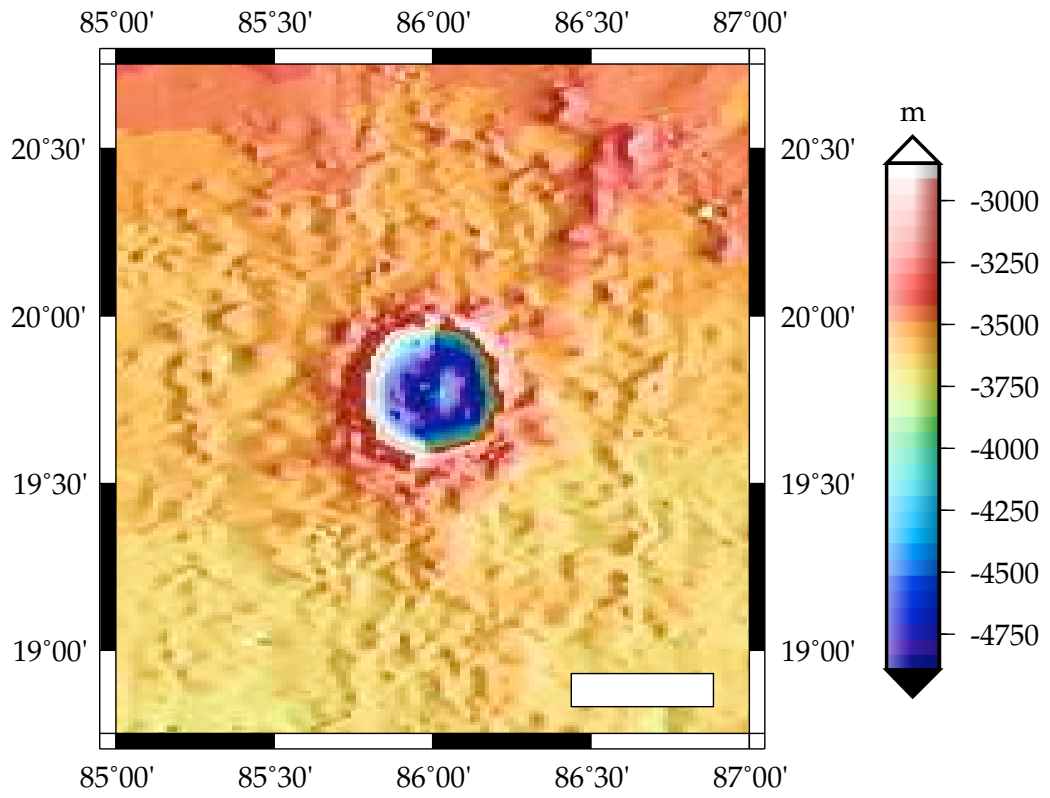
also has a greater ejecta runout distance than that in Figure 5.2(b). Figure 5.3 shows the topography of the craters along the Mars Orbiter Laser Altimeter (MOLA) tracks shown in Figure 5.2, showing that the crater in Figure 5.2(a) (MOLA track 14523) is deeper than the crater in Figure 5.2(b) (MOLA track 17981), but with a slightly smaller diameter, and confirms the greater ejecta runout distance.

Figure 5.4 shows a higher resolution view of part of the ejecta from the crater shown in Figure 5.2(b) using the Thermal Emission Imaging System (THEMIS). This shows the strong discontinuity between the edge of the distal ridge and the surrounding terrain. Also visible are faint radial streaks and some evidence of layering within the ejecta.

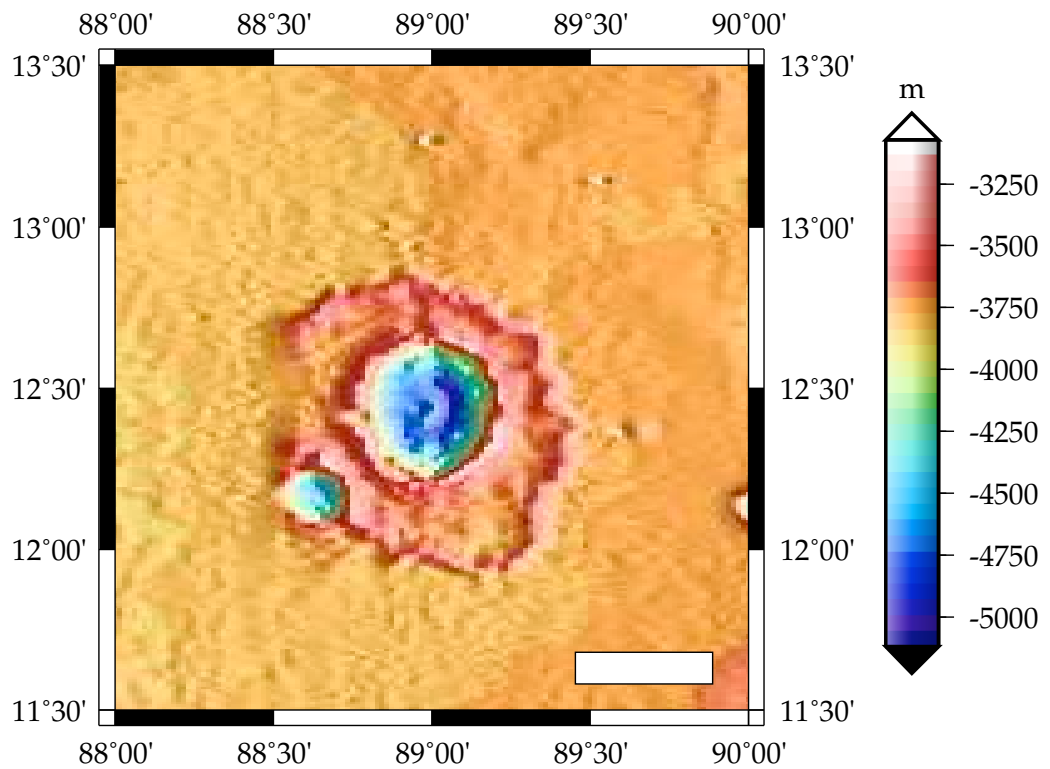
Figure 5.5(a) shows the distribution of rampart craters and possible rampart craters in Isidis Planitia as determined by an analysis of a Viking Orbiter Camera (VOC) Mars Digital Image Mosaic 2 (MDIM 2) image of the basin. Figure 5.5(b) shows a linear relationship between rampart crater diameter and the maximum ejecta runout distance from the centre of the crater. Rampart crater formation has been attributed to the vapourisation and fluidisation of subsurface ice during impact (e.g. Carr et al., 1977; Boyce and Roddy, 1997), or the effects of an atmosphere on ballistic ejecta (e.g. Schultz and Gault, 1979; Barnouin-Jha and Schultz, 1998), or possibly a combination of the two. This currently remains a controversial issue with researchers, although the majority favour a formation process involving subsurface volatiles.

Layered ejecta craters have been classified by many researchers into various groups depending on morphology (e.g. Mouginis-Mark, 1979). The main groupings currently used are single layer ejecta (SLE), where craters have one continuous layer of ejecta surrounding the crater; double layer ejecta (DLE), where craters have two layers of ejecta, usually with one layer upon the other; and multiple layered ejecta (MLE), which have three or more layers of ejecta surrounding the crater (e.g. Barlow and Perez, 2003). Isidis Planitia rampart craters are mostly of the SLE type (e.g. Barlow and Perez, 2003), although close analysis of high-resolution data does show there to be some added complexity in the layering of ejecta of craters identified as SLE in older data – e.g. see Figure 5.1(b) where there appears to be a double layer in the extreme southern area of the ejecta.

The distribution of SLE-, DLE- and MLE-type craters is strongly dependant on lati-



(a)



(b)

Figure 5.2: Rampart crater topography. (a) large rampart crater in northern Isidis Planitia, and the track of MOLA orbit 14523. (b) large rampart crater in central Isidis Planitia, and the track of MOLA orbit 17981. See Figure 5.3 for MOLA vertical topography along tracks. Bars in both images are ~ 25 km.

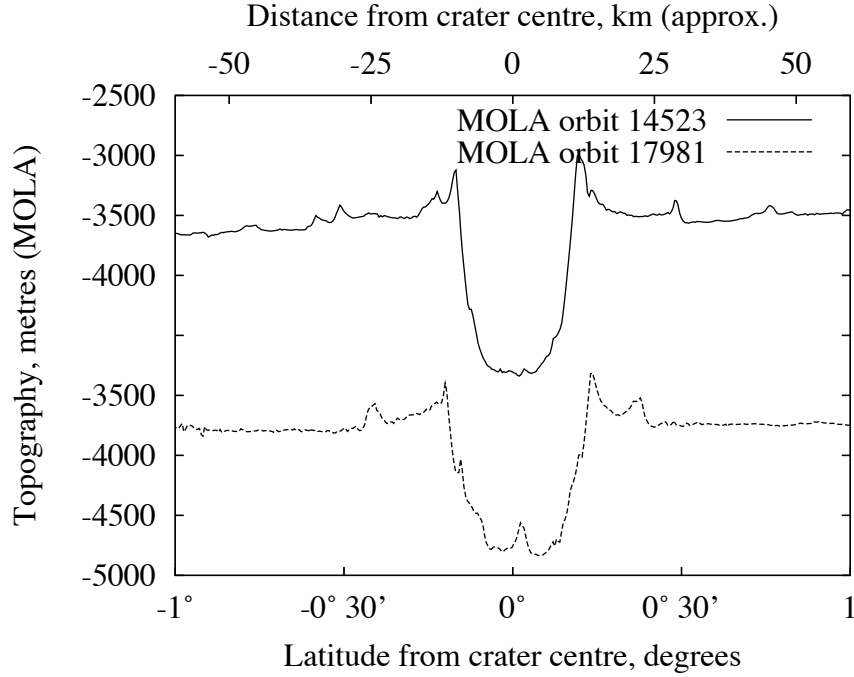


Figure 5.3: Rampart crater topography. MOLA vertical topography along orbits 14523 and 17981 across the rampart craters shown in Figure 5.2.

tude and crater depth-diameter relationships. The latitude of Isidis Planitia is dominated by SLE craters for diameters less than approximately 20 km, and MLE craters for larger diameters. Only four impact craters in Isidis Planitia have diameters greater than 20 km, and only one is larger than 27 km and this shows an incomplete annulus of topographically very subdued layered ejecta, making it hard to identify its type. When excavation depths and hydrologic models (e.g. Clifford, 1993) are taken into account, Barlow and Bradley (1990) suggest that SLE craters may excavate into ice-bearing subsurface layers and MLE craters into liquid water containing strata, accounting for their morphological differences. Later research by Barlow and Perez (2003) agrees with the mechanism of formation for SLE craters, and also points to a positive correlation between distribution of DLE and MLE morphologies and the distribution of near-surface water identified by the Gamma-Ray Spectrometer (GRS) instrument (Boynton et al., 2002), also suggesting that these ejecta morphologies are dependent on subsurface water. The presence of regional variations in morphology of some of the layered ejecta types also supports the idea that subsurface volatiles rather than atmospheric interaction is the dominant process involved (e.g. Barlow and Perez, 2003).

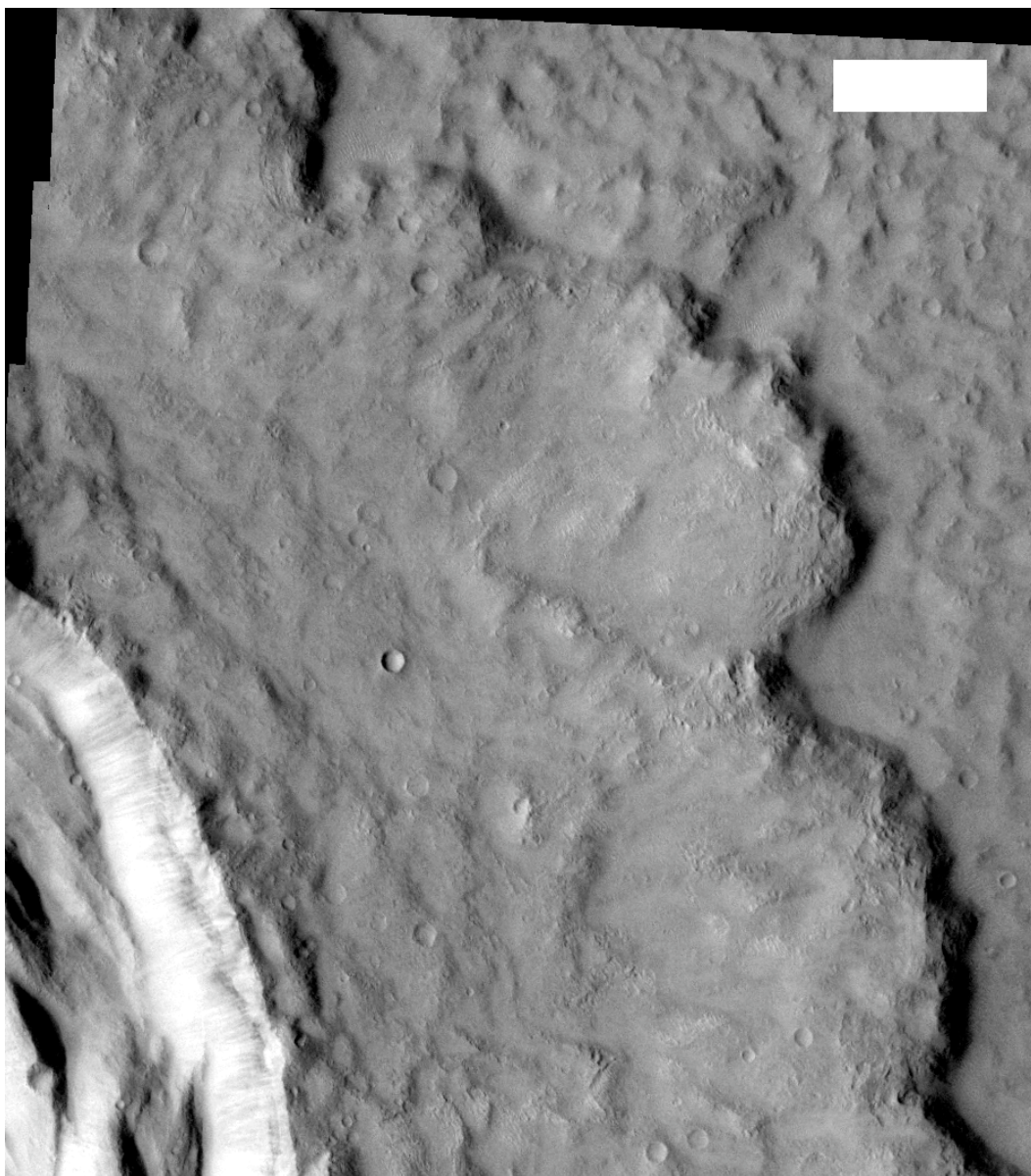
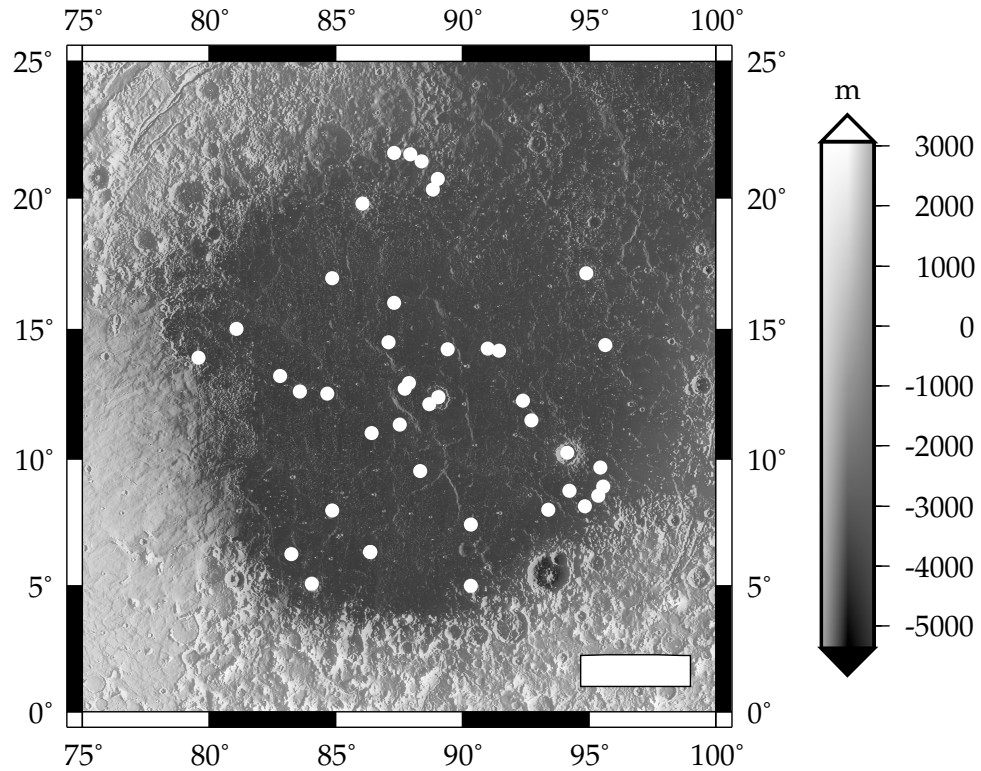
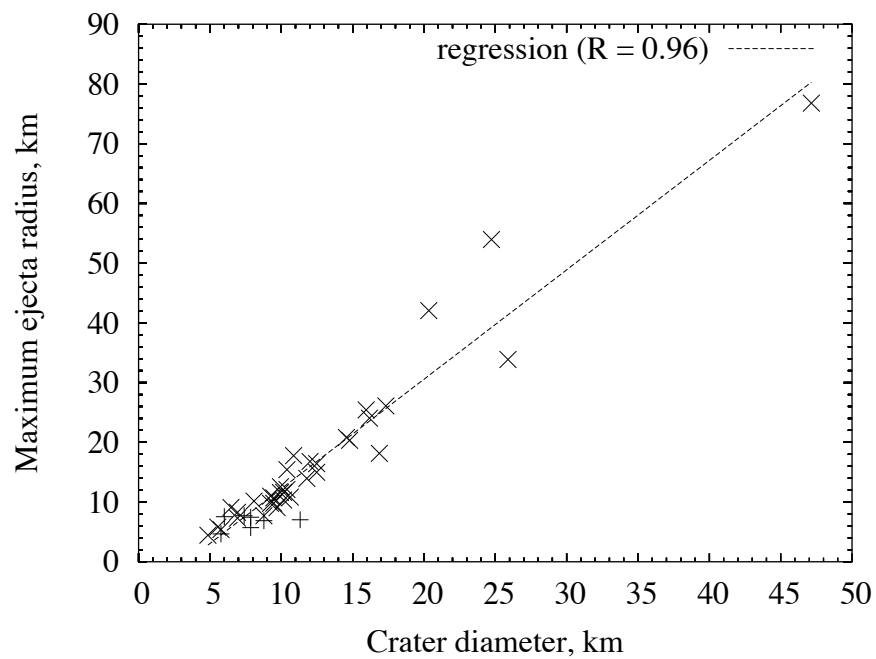


Figure 5.4: Rampart crater ejecta in Isidis Planitia. Part of the rampart and moat ejecta from the crater shown in Figure 5.2(b). Part of band 3 of the THEMIS visible image V09933014. Bar is 2.5 km.



(a)



(b)

Figure 5.5: Rampart craters in Isidis Planitia. (a) Distribution of rampart and possible rampart craters in Isidis Planitia. Bar is ~ 250 km. (b) Crater diameter plotted against maximum ejecta runout distance from centre of crater for rampart craters in Isidis Planitia. Possible rampart craters plotted as '+'. Regression line shown with $R = 0.96$.

Smaller craters in Isidis Planitia, and elsewhere, do not show layered ejecta. The implication is that these smaller craters, with shallower depths, may not excavate to a depth where enough subsurface volatiles are available to alter morphology towards a layered style are. Figure 5.5 suggests that the onset diameter of craters showing layered ejecta morphologies is approximately 5 km, which represents a typical value for craters at the approximate latitude of Isidis Planitia, although some areas of Mars, such as Solis Planum, may have lower onset diameter (Barlow et al., 2001). This is interpreted as being due to the concentration or depth of burial of subsurface volatiles due to modification of the regional hydrosphere by Tharsis-related uplift (Barlow et al., 2001).

Another type of feature known as pancake or, more commonly, pedestal craters, which are believed to form by the armouring of surface materials by ejecta and subsequent deflation of the surrounding surface, is completely absent in Isidis Planitia. Figure 5.6 shows pedestal craters elsewhere in the northern lowland plains of Mars. Analysis of crater rim height/diameter ratios, which show a distinct difference between pedestal and non-pedestal forms (Mitchell et al., 2002), also confirms that none of the larger Isidis Planitia craters studied here show pedestal morphologies.

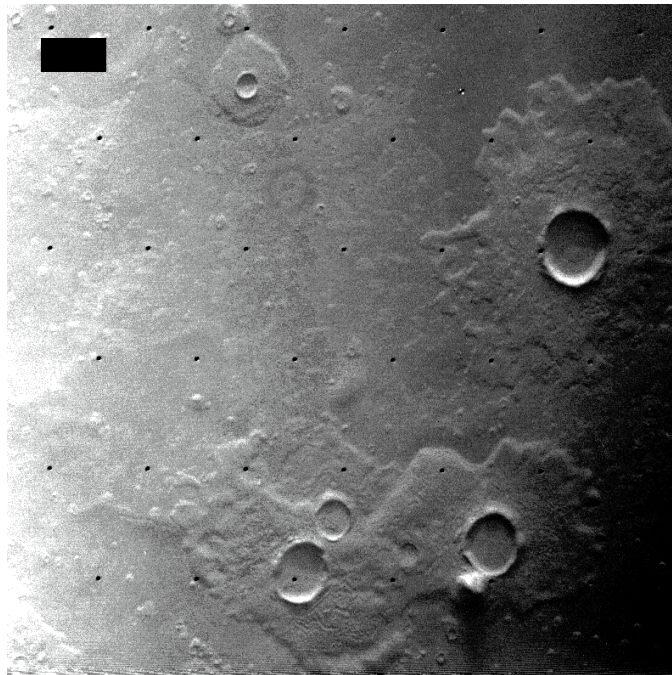


Figure 5.6: Pedestal craters. Several pedestal craters in the northern lowland plains of Mars in part of VOC image 043A04 from Viking Orbiter 1. Bar is 5 km.

5.2.2 Crater morphometry using IMPACT software

The availability of relatively high-resolution topographic data from MOLA has greatly expanded the understanding of martian impact craters (see Chapter 3 for further information about MOLA and its data). As well as using individual MOLA tracks across individual features (e.g. Figure 5.3), gridded MOLA data have been used to investigate the complete geometry of craters (e.g. Garvin et al., 2000a,b; Mouginis-Mark et al., 2004). The main shortcoming of this method in the appraisal of craters in Isidis Planitia is that, at the latitudes concerned, the grid resolutions involved are relatively coarse, making analysis of smaller craters difficult (e.g. Garvin et al., 2003) (see Chapter 3 for further information on MOLA processing and gridding).

However, using the freely available Interactive Measurement Profiling and Analysis of Crater Topography (IMPACT) software developed by Mouginis-Mark et al. (2004) it is still possible to obtain substantial information on the geometry of craters in Isidis Planitia, with most craters greater than 10 km diameter providing useful results. Some parameters for craters smaller than this cannot be reliably analysed using these methods due to the limitations of the digital elevation model (DEM) resolution. However, restricting analysis of craters to larger craters also avoids any problem with differences between the parameter relationships for simple (generally <7 kilometres in diameter) and complex crater (generally 7 to 100 kilometres in diameter) types (Garvin et al., 2003). The craters analysed are shown in Figure 5.7.

Using the IMPACT program for crater analysis involves preparing a set of reference files for the area of interest. These include a DEM, illuminated DEMs to aid feature recognition, and a ‘hits’ file to indicate how many MOLA hits have occurred within each bin in order to determine whether a topographical height is ‘real’ or the result of software interpolation. The IMPACT program then allows the manual selection of points relating to crater bowl, rim and ejecta features on the DEM and produces a set of statistics based upon the selected points that can then be analysed further.

Figures 5.8, 5.9, 5.10 and 5.11 show some of the results obtained for impact craters in Isidis Planitia using the IMPACT software. Figure 5.8 plots crater maximum depth below the level of the surrounding plains surface plus mean crater rim height above the

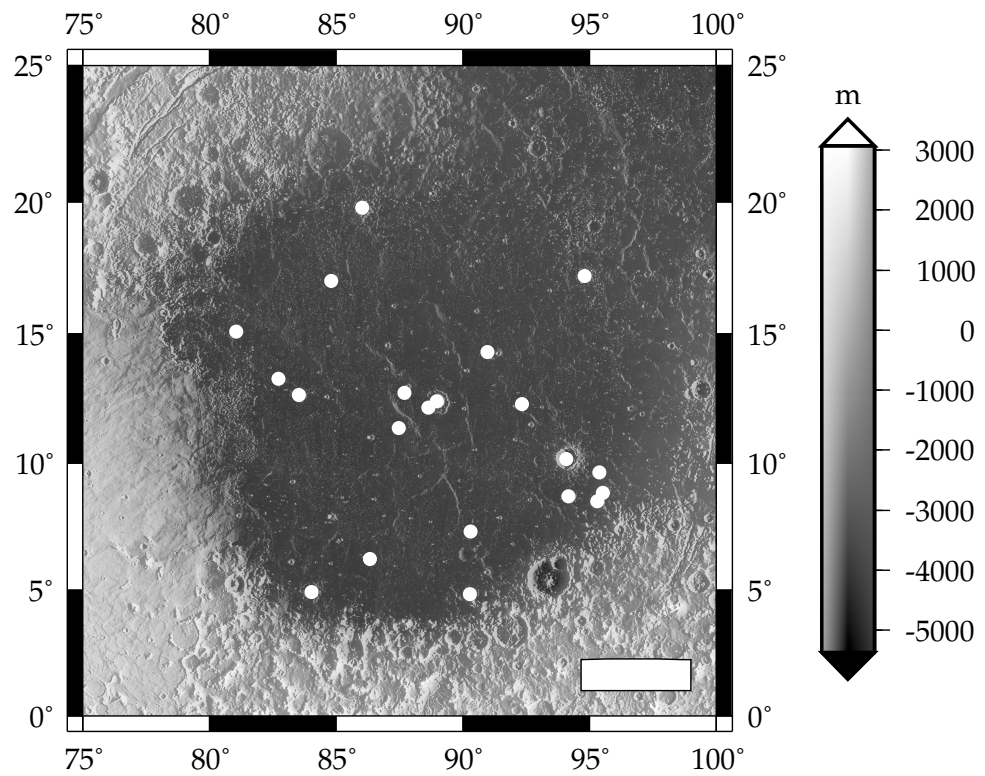


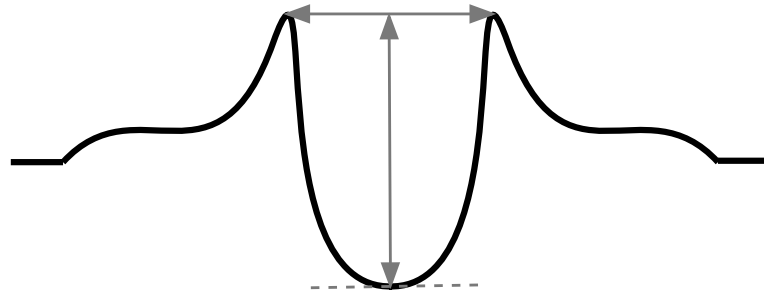
Figure 5.7: Craters in Isidis Planitia analysed using IMPACT software. The craters, all greater than 10 km in diameter, analysed using the IMPACT software (Mouginis-Mark et al., 2004) to investigate crater, rim and ejecta statistics. Bar is ~ 250 km.

level of the surrounding surface (a measure of the depth of a crater relative to the mean rim height) against crater diameter for lowland plains craters with diameters greater than 10 km within the inner tectonic ring in Isidis Planitia. It also shows the diameter-depth from rim relationship for all martian complex craters derived by Garvin et al. (2003) for comparison. This figure shows that although there is an obvious relationship between diameter and depth from rim for the larger craters in Isidis Planitia, they generally appear to be shallower for a given diameter than those elsewhere on Mars. This could be related to the basin subsurface composition, or result from deposition of material within the craters subsequent to their formation.

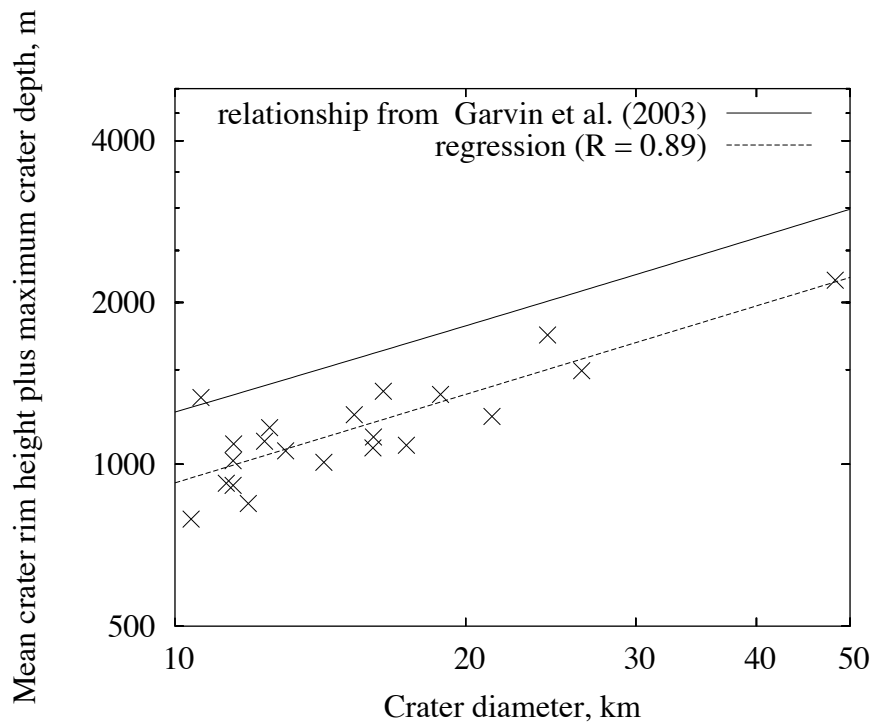
Figure 5.9 plots crater maximum depth below the level of the surrounding plains surface against crater diameter for lowland plains craters with diameters greater than 10 km within the inner tectonic ring in Isidis Planitia. The diameter-depth relationship for all martian complex craters derived by Garvin et al. (2003) is overlain for comparison. When compared with Figure 5.8 this figure shows that although there is an obvious relationship between diameter and depth for the larger craters in Isidis Planitia, they generally appear to be shallower for a given diameter than those elsewhere on Mars.

Figure 5.10 plots crater mean rim height above the level of the surrounding plains surface against crater diameter for the same population of impact craters. It also shows the diameter-rim height relationship for all martian complex craters derived by Garvin et al. (2003) for comparison. The regression line for these data shows a slightly greater rim height for a given crater diameter than the theorised relationship, although given the spread of data this is within acceptable error. However, when compared with Figures 5.8 and 5.9 this figure shows that it is the mean rim height of the Isidis Planitia craters that is the measurement closest to that predicted using the model by Garvin et al. (2003).

Figure 5.11(a) shows the maximum measured depth of each crater divided by the depth of the crater derived by Garvin et al. (2003), and Figure 5.11(b) shows the mean measured height of the rim of each crater divided by the rim height of the crater derived by Garvin et al. (2003) for all martian complex craters plotted against the latitude of the crater centre. This shows the variation in crater morphology according to location within the basin. The figures show that there is no conclusive difference between the infill or erosion of craters at different latitudes within the basin, although there is some indication that

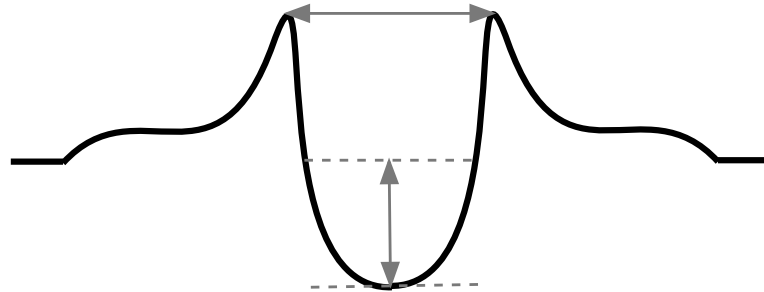


(a)

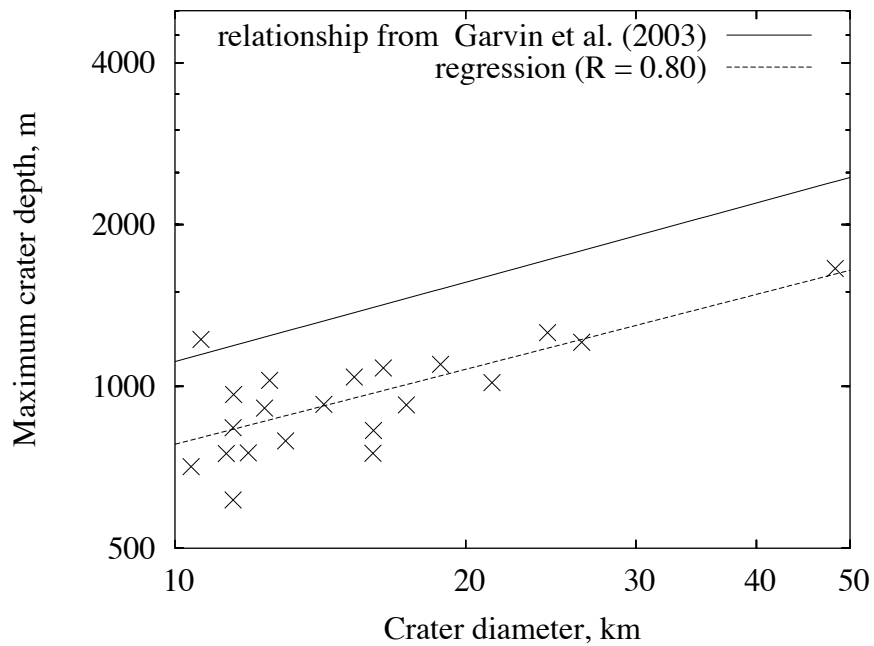


(b)

Figure 5.8: The relationship of crater maximum depth plus mean rim height to diameter in Isidis Planitia. (a) Details of parameters measured. (b) Maximum depth below the surface surrounding the crater plus mean rim height above surface surrounding crater plotted against diameter for craters in Isidis Planitia with a diameter greater than 10 kilometres. The solid line represents the crater depth-diameter relationship for all complex craters on Mars (Garvin et al., 2003). The dashed line is the regression. Both axes are logarithmic. Crater data generated using IMPACT software (Mouginis-Mark et al., 2004).

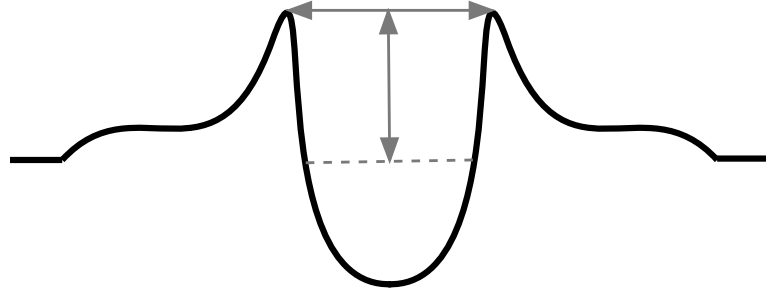


(a)

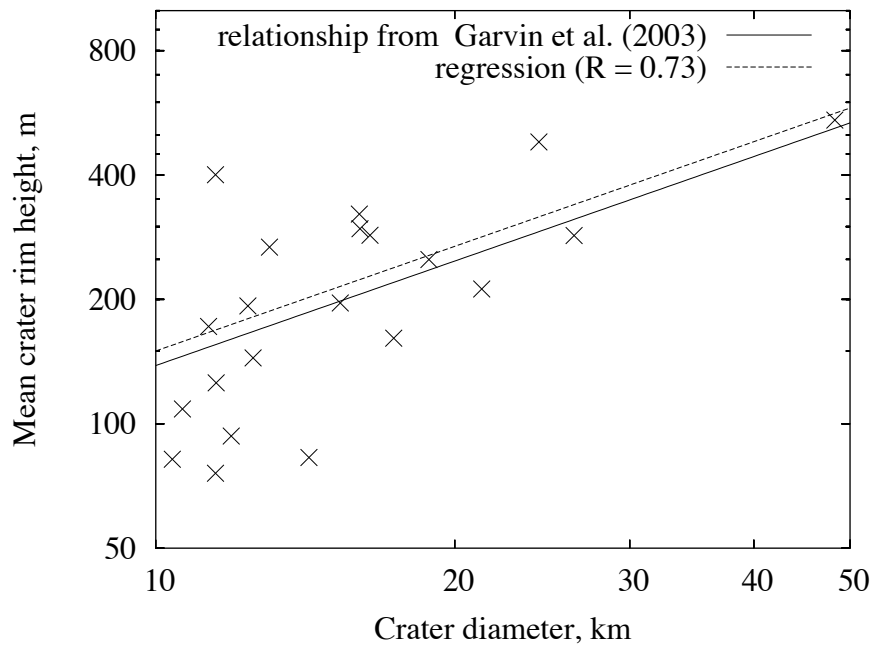


(b)

Figure 5.9: The relationship of crater maximum depth to diameter in Isidis Planitia. (a) Details of parameters measured. (b) Maximum depth below the surface surrounding the crater plotted against diameter for craters in Isidis Planitia with a diameter greater than 10 kilometres. The solid line represents the crater depth-diameter relationship for all complex craters on Mars (Garvin et al., 2003). The dashed line is the regression. Both axes are logarithmic. Crater data generated using IMPACT software (Mouginis-Mark et al., 2004).



(a)



(b)

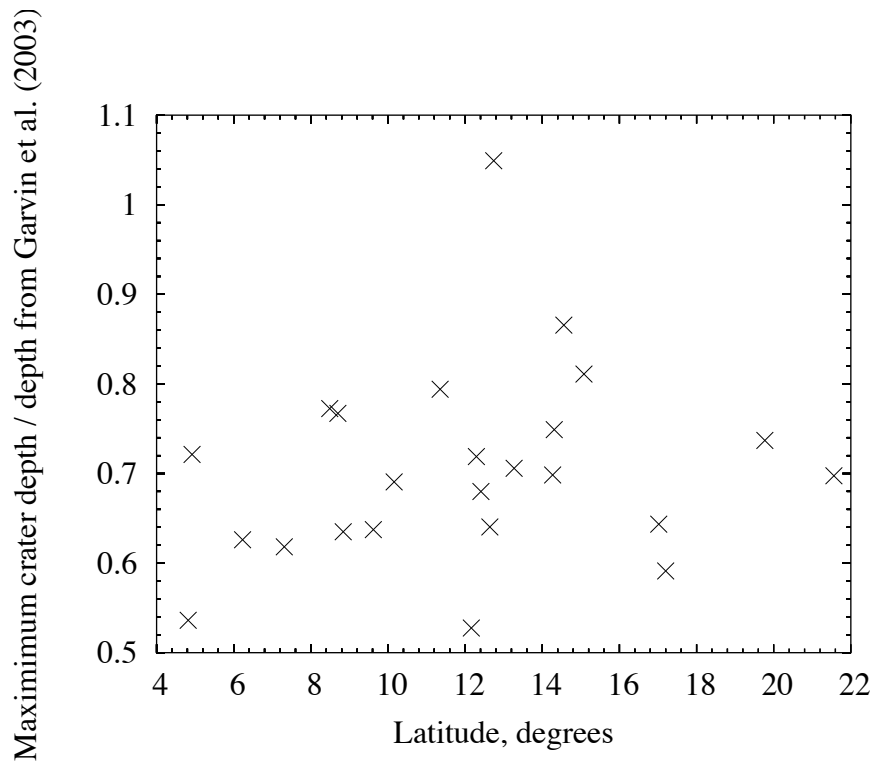
Figure 5.10: The relationship of crater mean rim height to diameter in Isidis Planitia. (a) Details of parameters measured. (b) Mean rim height above the surface surrounding the crater plotted against diameter for craters in Isidis Planitia with a diameter greater than 10 kilometres. The solid line represents the crater depth-diameter relationship for all complex craters on Mars (Garvin et al., 2003). The dashed line is the regression. Both axes are logarithmic. Crater data generated using IMPACT software (Mouginis-Mark et al., 2004).

craters nearer to the middle latitudes of the basin may be deeper than those further north and south, but also may have higher rims for a given diameter. It is possible that the unusually high value for the crater near the middle latitude of the basin could be because the feature is particularly fresh and unmodified.

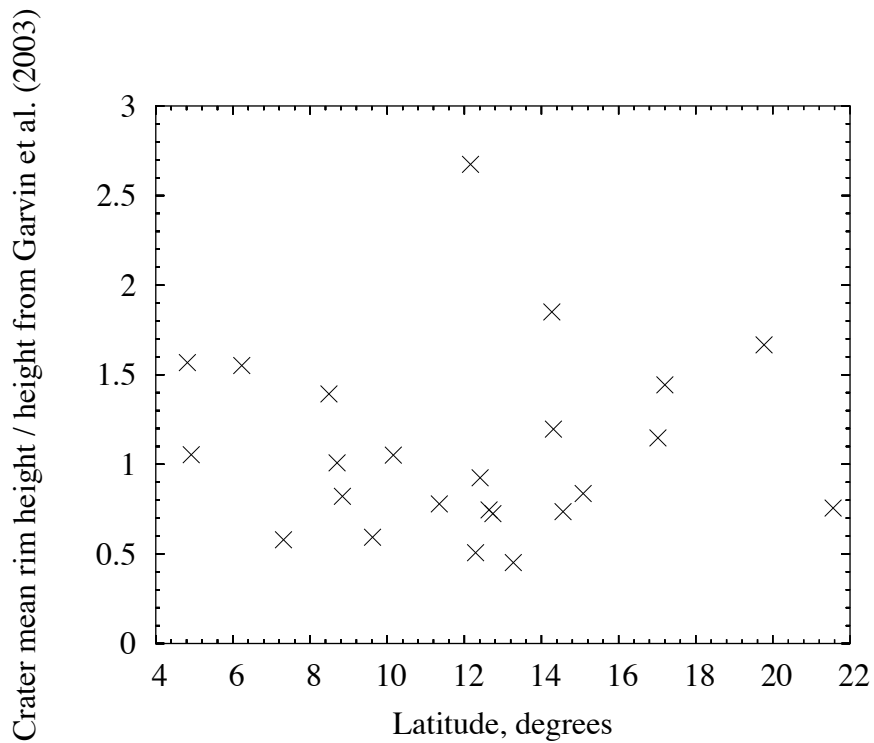
Analysis of crater parameters obtained using the IMPACT software has been used by other researchers to investigate the geologic history of martian impact craters – e.g. in the lowland plains of Mars north of 45° (Boyce et al., 2003a), and in polar regions (Boyce et al., 2003b). Boyce et al. (2003a) determined that crater depths relative to the surrounding surface in parts of the northern lowland plains were relatively constant across a range of crater diameters (i.e. the regression line for the data is approximately horizontal), and that many craters had depths that were negative in relation to the surrounding surface (i.e. the lowest point of the crater was above the level of the surrounding surface). Crater depths relative to rim height followed the expected relationship, and increased with increasing crater diameter. Figures 5.8, 5.9 and 5.10 show that in Isidis Planitia crater depths increase in a similar way to that expected with increasing crater diameter, as do mean rim heights. This suggests that the mantling that may have taken place in the lowland plains north of 45° North has not taken place in Isidis Planitia. It should be noted that these studies also analysed craters with diameters at the smaller end of, and less than, the range analysed in my own work in order to maximise the statistical accuracy of the study. This was possible as only diameter, depth and rim statistics obtained by IMPACT were used, whereas I also wanted to obtain reliable statistics about ejecta. It was noted by Boyce et al. (2003a) that there may be a slight increase in depth with increasing diameter for craters more than ~ 13 km in diameter, although the implication is that the regression is still closer to horizontal than expected. This may be due to the increasing depth of craters greater than a certain diameter being proportionally more important than the effects of the mantle of material.

5.2.3 Discussion

Crater morphology can be used to indicate the atmospheric, surface, and subsurface conditions in which an impact crater was formed. The prevalence of SLE-type ejecta morphologies suggests that, typically for its latitude, Isidis Planitia is underlain by ice-bearing



(a)



(b)

Figure 5.11: The relationship of crater morphology to latitude in Isidis Planitia. Measured maximum crater depth (a), or measured crater mean rim height (b), divided by the appropriate value derived by Garvin et al. (2003) and plotted against latitude for craters in Isidis Planitia with a diameter greater than 10 kilometres. Crater data generated using IMPACT software (Mouginis-Mark et al., 2004).

strata, and that given the typical layered ejecta onset diameter for the latitude, these ice-bearing layers are at a depth that is also typical for the latitude.

Results from the IMPACT software show that crater mean rim height is fairly close to the expected global average, suggesting that crater rims have not been buried to any great extent by deposition, or exposed further by significant erosion. Crater maximum depths are shallower than expected when compared with the global average. This could relate to deposition of material within the crater cavity, but this seems unlikely to be the result of significant episodes of deposition in the basin as a whole as this would also affect rim heights.

5.3 Craters and stratigraphy

In the absence of extensive in-situ measurements that could provide absolute ages for the martian rocks, cratering statistics are essential for assessing the relative ages of different parts of the martian surface (Strom et al., 1992). In brief, a heavily cratered region is evidence for an older surface. In contrast, a relatively recent surface, such as a fresh lava flow, would not have had the chance to become heavily scarred by impact events. Crater counting involves recording the number density and diameter of craters on a surface. Dating of older surfaces may be affected by saturation – where the whole surface has been modified by the effects of impacts, and further impacts cannot take place into unmodified surface material, obscuring the true relative age of the surface. Table 5.1 shows the established cratering densities for the stratigraphic series used on Mars determined by Tanaka (1986) in relation to stratigraphic units on the martian surface.

The absolute ages of the stratigraphic series shown in Table 5.1 are a subject of much debate amongst researchers. A chronology for the martian surface (e.g. Neukum and Wise, 1976; Hartmann and Neukum, 2001) is obtained by combining studies of crater counts on Mars with an estimated Mars/Moon cratering rate (e.g. Hartmann, 1977; Ivanov, 2001), and the size-frequency distribution for lunar craters and the resulting estimation of the same distribution for Mars (e.g. Neukum et al., 2001). The Moon is a well known reference body in cratering studies, for which we have fairly extensive absolute dating evidence from

Stratigraphic Series	Crater density			Absolute dating	
	N(2)	N(5)	N(16)	Start	End
Upper Amazonian	<40			0.3–0.6 Ga	present
Middle Amazonian	40–150	<25		1.4–2.1 Ga	0.3–0.6 Ga
Lower Amazonian	150–400	25–67		2.9–3.3 Ga	1.4–2.1 Ga
Upper Hesperian	400–750	67–125		3.6 Ga	2.9–3.3 Ga
Lower Hesperian	750–1200	125–200		3.7 Ga	3.6 Ga
Upper Noachian		200–400	<25	3.8 Ga	3.7 Ga
Middle Noachian		>400	100–200	3.9 Ga	3.8 Ga
Lower Noachian			>200	formation	3.9 Ga

Table 5.1: Crater-density boundaries and absolute ages for martian stratigraphic series from Tanaka (1986). $N(n)$ is the number of craters of (n) kilometers diameter or greater per million square kilometers area. Approximate absolute dating of series from Hartmann and Neukum (2001).

analysing rock samples. Results from the limited sampling of Mars material in the form of martian meteorites found on the Earth is also used to help constrain absolute ages (e.g. Nyquist et al., 2001). Table 5.1 also shows approximate absolute ages (Hartmann and Neukum, 2001) for the stratigraphic series derived by Tanaka (1986).

The Beagle 2 lander would have carried out absolute dating of surface rocks in Isidis Planitia by determining the abundance ratio between potassium-40, identified by the X-ray spectrometer, and argon-40, measured by the Gas Analysis Package, providing the first absolute and in-situ frame of reference for the martian dating system. Unfortunately, due to the loss of the lander, such measurements will have to wait for another lander mission to the region.

The mapping of the eastern hemisphere of Mars by Greeley and Guest (1987) interpreted the Isidis Planitia lowlands to be broadly divided into an upper-Hesperian ridged plains (Hvr) component in the west and an Amazonian smooth plains (Aps) unit in the east. Later analysis of the stratigraphy of northern lowlands using data from Mars Global Surveyor reinterpreted these units as a single unit of an Amazonian/Hesperian Vastitas Borealis hummocky member (AHvh) which formed during the Hesperian-Amazonian boundary (Tanaka et al., 2003). There is clearly little difference in age between the different lowland areas of the basin based upon the crater counts carried out herein (see Figure 5.12). I have measured that the surface of Isidis Planitia within the 1,100 kilome-

the diameter inner ring (Schultz and Frey, 1990; Frey et al., 1998) has a crater density for $N(2)$ of 443, $N(5)$ of 78, and $N(16)$ of 7 – where $N(n)$ is the number of craters of (n) kilometers diameter or greater per million square kilometers area – which when compared to the series in Table 5.1 gives a relative age that is in the Upper Hesperian, near the Hesperian-Amazonian boundary.

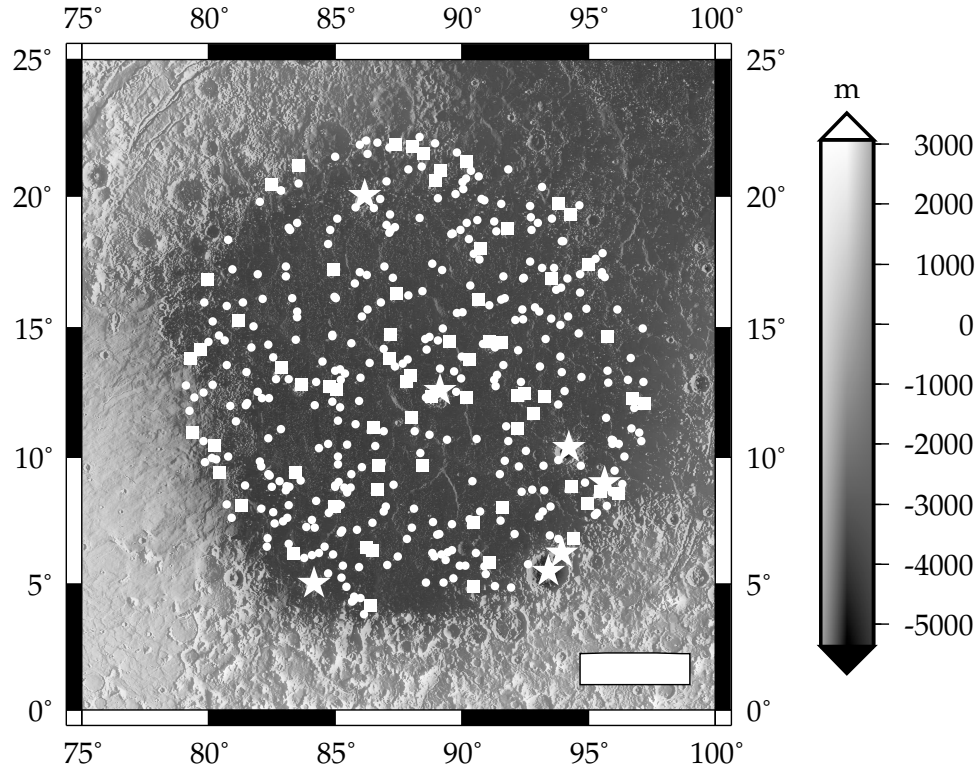


Figure 5.12: Impact craters within the Isidis Planitia inner ring. Small dots show the location of impact craters of 2–5 km diameter; medium squares show impact craters of 5–16 km diameter, and large stars show impact craters of greater than 16 km diameter. Background map shows MOLA topography. Bar is ~ 250 km.

Figure 5.13 shows the results of another series of crater counts of Isidis Planitia impact craters, using the system devised by Hartmann and Neukum (e.g. 2001). These counts by Bridges et al. (2003a), including some undertaken by myself, show the age for the plains within the inner ring of the basin to be between Hesperian and Amazonian, or Lower Amazonian, based upon VOC MDIM 2 image mosaics. The age is less quantifiable, but probably younger when based upon the counting of the three high-resolution MOC narrow angle images in Figure 5.13. Further analysis of sub-kilometre craters in MOC narrow angle images of the Mars Exploration Rover (MER) proposed landing site in southern Isidis Planitia undertaken by Gilmore and Tanaka (2003) also suggest an age of between

Upper Hesperian and Upper Amazonian.

Also notable in Figure 5.13 are the number densities of the smaller craters from the latter count, which cut across rather than run parallel to the isochrons in the graph, demonstrating a deficit of smaller (less than 250 metre diameter) craters. This has been interpreted as being due to infilling by aeolian deposition or erosion (Bridges et al., 2003a). This is also supported by Gilmore and Tanaka (2003) who suggest a change in the crater-density distribution at diameters of less than 100 metres, and the following of a production slope at crater diameters of greater than 300 metres.

As with all crater counting exercises it is important to consider the effect of secondary craters for counts of features less than 1 kilometre in diameter. There is some evidence that the proportion of secondary craters in a crater population is larger than is currently being assumed, which may result in surface ages being incorrectly assessed as older than their actual age (e.g. McEwen, 2003; Hurst et al., 2004), or possibly younger if the production function itself is affected. However, any resulting errors in the dating of the surface should not affect the order in which geological events take place within the basin.

5.4 Stealth craters

5.4.1 Introduction

Analysis of the detailed high-resolution topographic data obtained by MOLA has shown that as well as the established population of relatively fresh impact craters, the northern lowlands of Mars also contain numerous shallow circular depressions that are referred to as ‘stealth’ craters (Kreslavsky and Head, 2001; Head et al., 2002) or ‘ghost’ craters (Tanaka et al., 2003). These are interpreted to be impact craters that have been buried or eroded until they are topographically very subdued. These craters are often very difficult, or even impossible, to identify in, for example, Viking Orbiter images of the northern lowlands, and are best seen in detrended MOLA topographic data (see Chapter 3 for further information on this process), or in MOLA topographic data that have been strongly artificially ‘illuminated’ by a light source at a large angle to the normal. Using such data the stealth craters appear as circular features with significantly shallower bowls than fresh impact

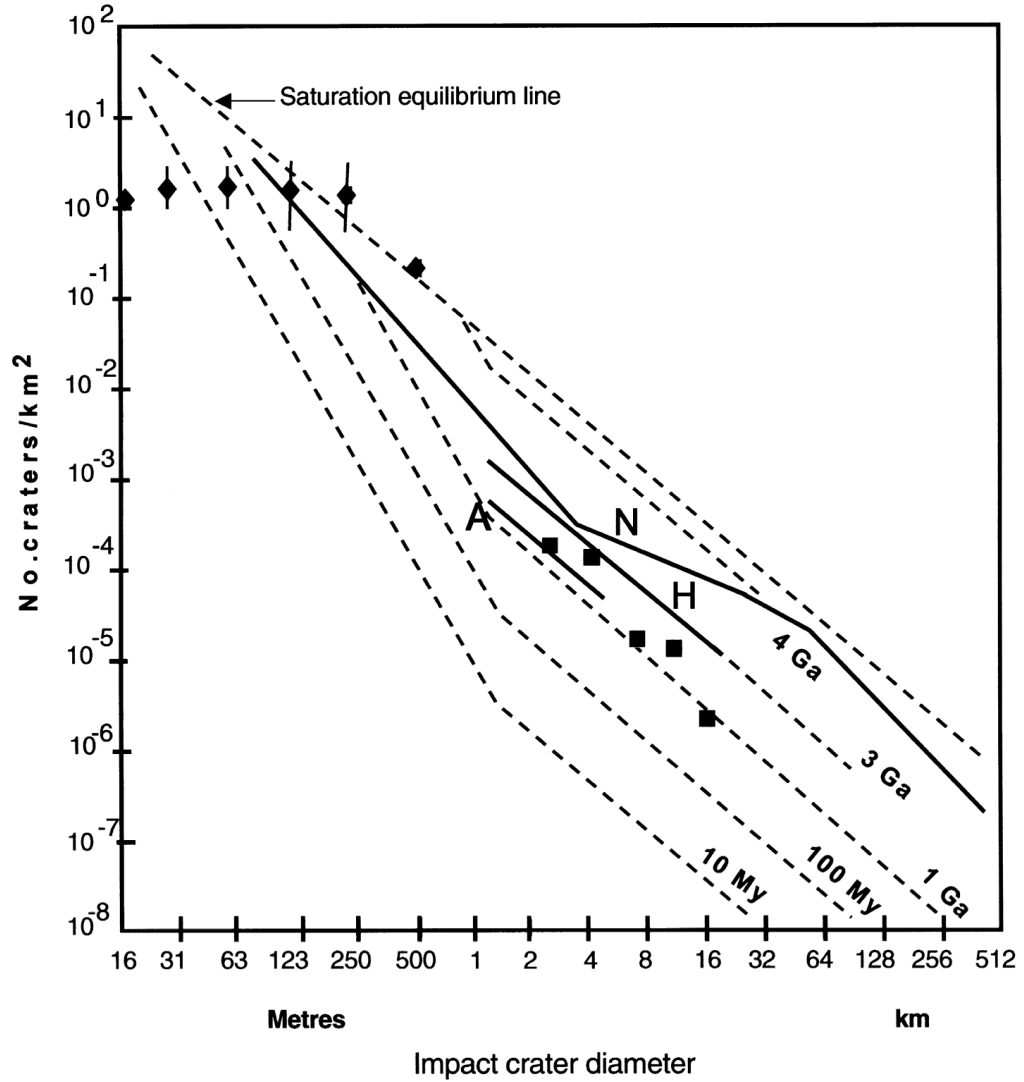


Figure 5.13: Crater count within the inner plains of Isidis Planitia. Diamonds are data from crater counts of 3 narrow angle MOC images (M0903399, M2001670, M0202490), squares are crater counts of VOC MDIM 2 photomosaic. A, H, and N are the Amazonian, Hesperian, and Noachian isochrons respectively. Saturation Equilibrium Line shows the maximum possible crater densities. Vertical bars show ± 2 standard deviation errors, where calculated. Crater counts by Dr. J. C. Bridges and myself (Bridges et al., 2003a). Original diagram with isochrons from Hartmann and Neukum (2001).

craters of similar diameter, and with little or no evidence of a rim or ejecta. In nighttime infrared THEMIS images there appears to be no, or virtually no, surface expression of the actual crater rim or ejecta, which would be indicated by elevated brightness temperatures, as seen in images of fresh impacts. This indicates that the stealth craters are entirely buried. The circular features in Isidis Planitia are significantly smaller than the buried impact basins identified by Frey (2003) across the martian surface. Figure 5.14 shows several stealth craters in northern Isidis Planitia, illustrating their morphological differences from nearby fresh impact craters.

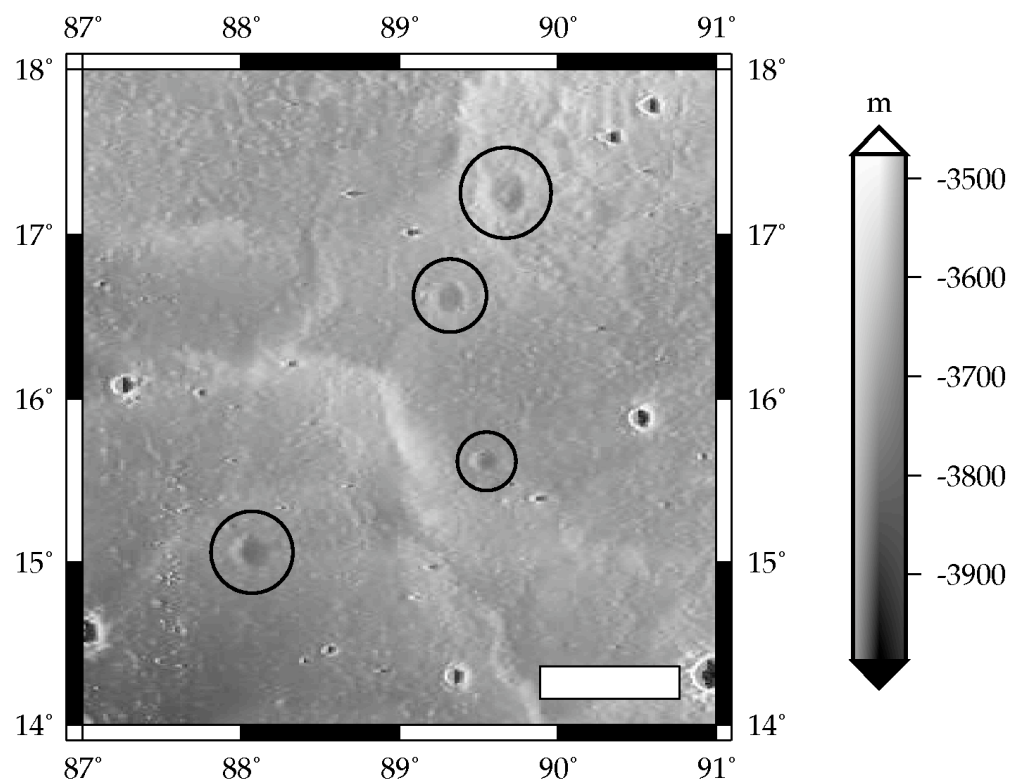


Figure 5.14: Stealth craters. Examples of stealth craters (circled) in northern Isidis Planitia from illuminated MOLA topography data. Compare stealth crater morphology with that of fresh craters elsewhere in the image. Bar is ~ 50 km.

5.4.2 Stealth craters in Isidis Planitia

Tanaka et al. (2003) identified approximately 15 stealth craters within Isidis Planitia, along with many others throughout the northern lowlands. Using a combination of VOC MDIM 2 and MOLA data I have determined that there are in fact more than 30 such features within Isidis Planitia (see Figure 5.15). In this study I identified stealth craters by

eye, although Salamunićar and Selar-Glavočić (2003) suggest a method for the automation of stealth crater detection using MOLA data. A few stealth craters less than 5 kilometres in diameter were also identified during this survey, but have not been included in the results as I consider that they do not reflect the real number of such features in that size range. The remainder of the craters this size are assumed to be obscured to the extent that they are not detectable either in VOC or MOLA data. In total, I identified 25 stealth craters of between 5 and 16 kilometres diameter, and 6 stealth craters of more than 16 kilometres diameter.

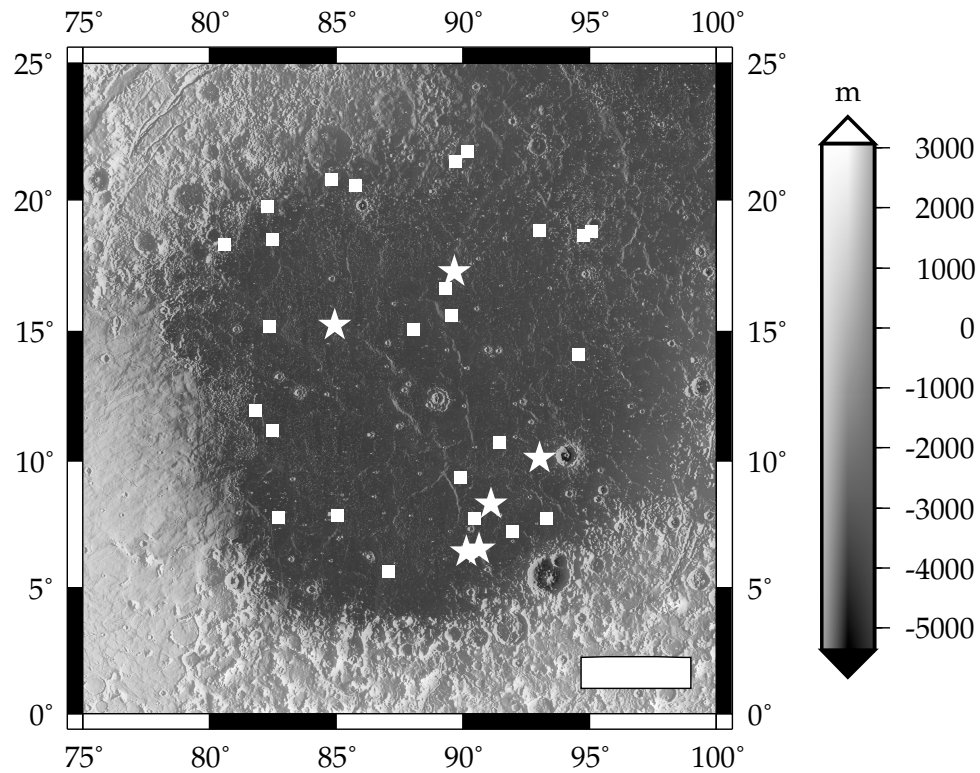


Figure 5.15: Stealth craters in Isidis Planitia. Showing stealth craters of 5–16 kilometers diameter (squares), and over 16 kilometers diameter (stars) identified within the Isidis Basin inner ring (diameter 1100 kilometers). Background map shows MOLA topography. Bar is ~ 250 km.

If it is assumed that the stealth craters lie upon a stratigraphic unit older than the current surface, and were subsequently buried by the material that forms the surface today, the crater count of stealth craters within the basin can be used to estimate the age of the buried unit, in the same way as counts of fresh craters can estimate the age of the basin surface, as documented earlier in this chapter (see Section 5.3). The addition of the stealth craters to the fresh craters counted in Figure 5.12 gives crater densities for the

Layer	Crater density		
	N(2)	N(5)	N(16)
Surface	443	78	7
Buried	-	110	14

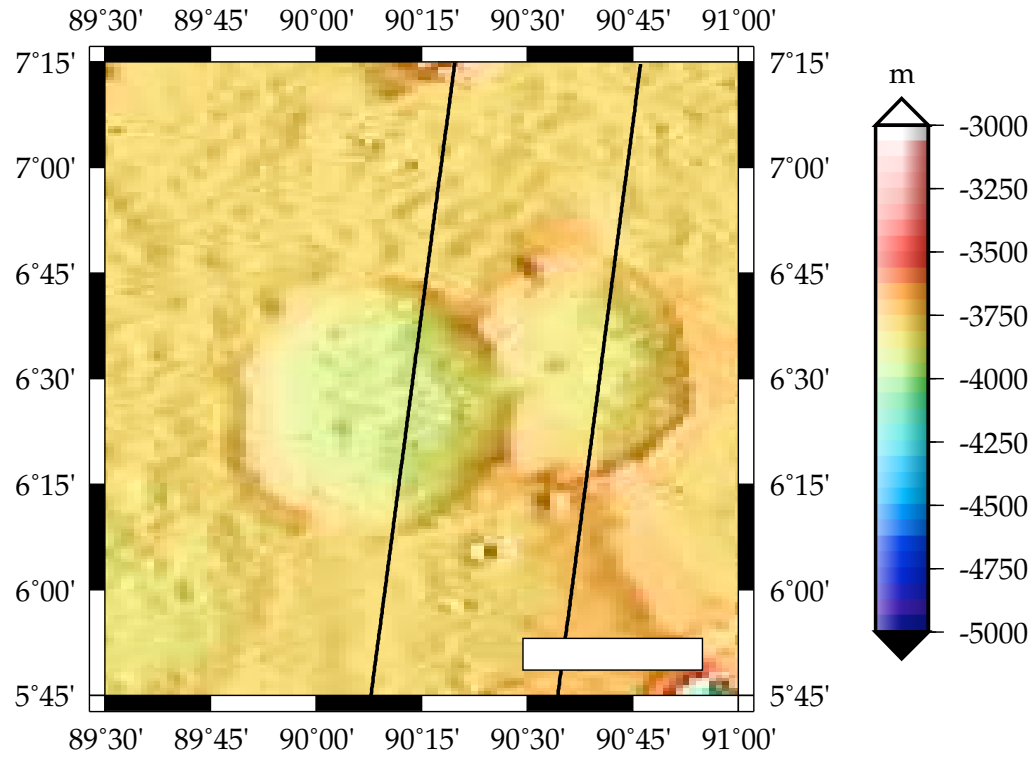
Table 5.2: Crater-density results for Isidis Planitia surface and buried units. N is the number of craters of (n) kilometers diameter per million square kilometers area. See Table 5.1 for absolute ages.

buried unit for N(5) as 110 and N(16) as 14 (see Table 5.2). N(2) for the buried unit is not calculated as stealth craters smaller than 5 km in diameter are not counted. Table 5.1 gives an age for the buried unit that is close to the boundary between Upper and Lower Hesperian. It is likely that the age of this surface is actually older than this, because some craters of between 5 and 16 kilometres may be undetected. Note that there are nearly as many stealth craters of more than 16 kilometres diameter as there are fresh craters of the same size – if this proportion were reflected in the craters of between 5 and 16 kilometres diameter the age of the buried unit would be within the Lower Hesperian.

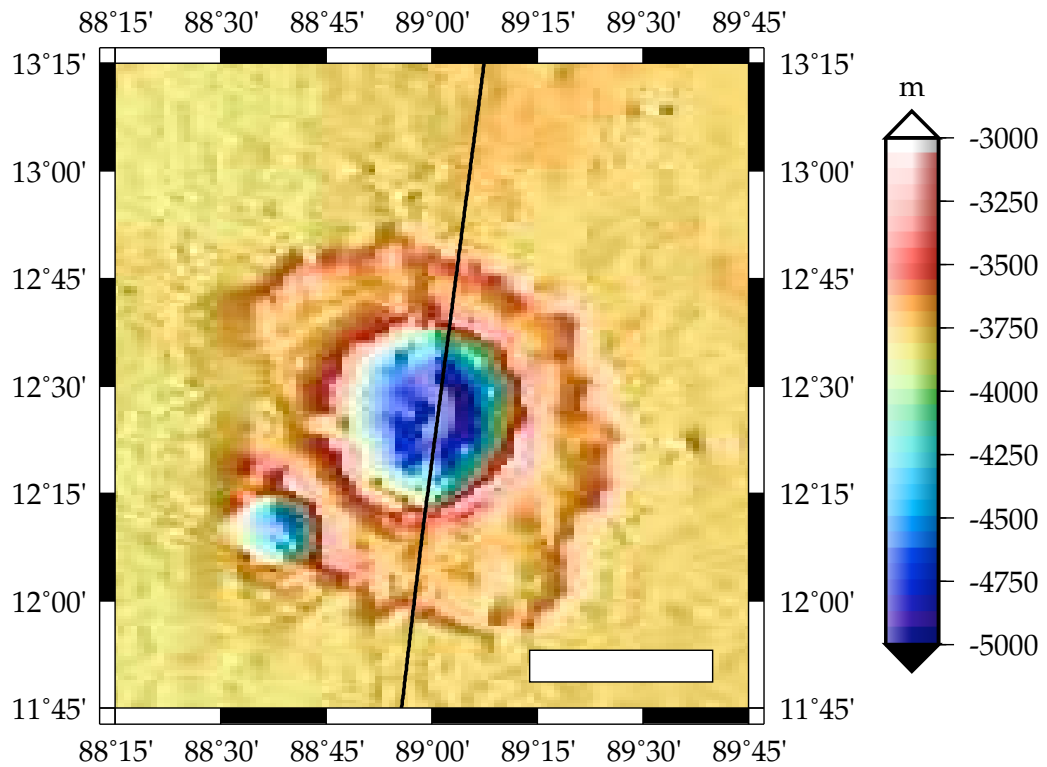
Figures 5.16 and 5.17 show the difference in topography between two of the largest stealth craters in the basin and a fresh crater of comparable size. The two stealth craters show only a tenth of the topographic height from rim to floor, with minimal rim and no obvious central peak or ejecta pattern, at least in the topography track. The more obvious rim at the south of MOLA orbit 18534 in Figure 5.17 may be due to interaction with the prominent ridge that can be seen in Figure 5.16(a). The fresh crater shows a range of topography from rim to floor of nearly 2000 metres, with a well defined rim approximately 600 metres high, and a central peak about 300 metres high. The crater is surrounded by ejecta.

Figures 5.18 and 5.19 show a large stealth crater in another part of the Isidis Planitia basin. This shows even more subdued topography than the stealth craters in Figure 5.16(a), showing less than 100 metres of topography from the supposed rim to floor, with no evidence of a raised rim. This is typical of stealth craters of this size and smaller within Isidis Planitia. There is evidence of a discontinuous graben at the rim of the crater.

There appears to be a small number of slightly different stealth craters in the south east of the basin. Figure 5.20(a) shows one of these. It is ~ 3 kilometres in diameter, making it



(a)



(b)

Figure 5.16: Comparison between fresh and stealth craters in Isidis Planitia. (a) two stealth impact craters and the tracks of MOLA orbits 19891 (west) and 18534. (b) fresh impact crater and the track of MOLA orbit 17981. Topography along the MOLA tracks is shown in Figure 5.17. Bars in both images are ~ 25 km.

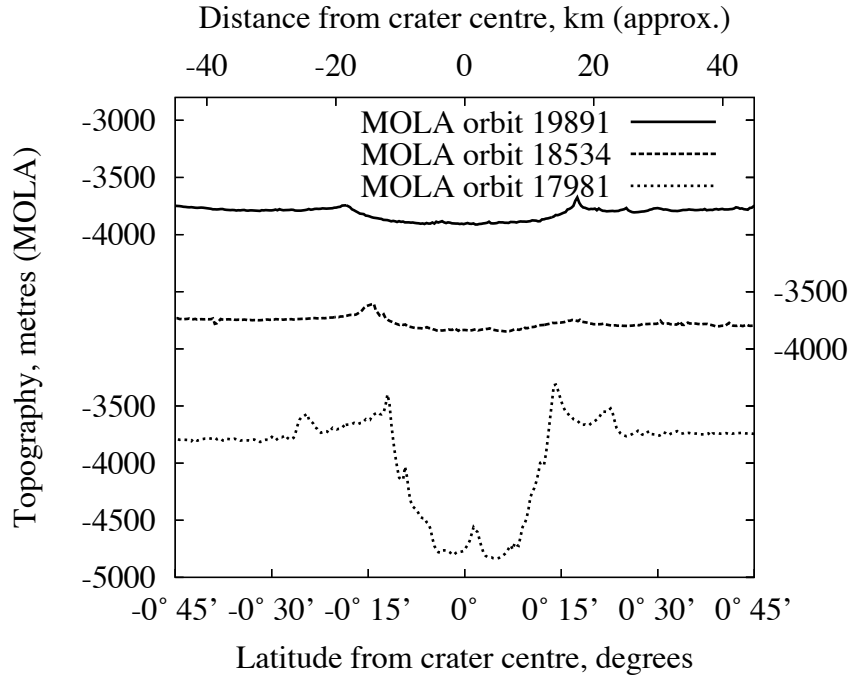


Figure 5.17: Stealth and fresh crater topography in Isidis Planitia. Topography along the MOLA tracks from Figure 5.16.

much smaller than nearly all the stealth craters identified elsewhere in the basin. It also appears to clearly show its actual rim, rather than a more subdued surface expression of a buried rim as is believed to be the case with stealth craters elsewhere. Figure 5.20(b) shows the same crater in a nighttime THEMIS image, where the high brightness temperature of the crater rim is obvious. This is typical of fresh craters, but fresh impacts also show elevated brightness temperatures within the crater bowl, whereas this stealth crater does not. In the absence of useful topographic data for this crater – it is too small to be clearly seen in MOLA gridded data – it is difficult to determine how much infilling has taken place. However, comparison with a similar sized fresh crater (see Figure 5.20(c)) shows that the stealth crater has been substantially infilled – note the lack of shadows from the crater rim compared with the fresh example. These small stealth craters are found in an area of very high thermal inertia (for further discussion of the basin’s thermal inertia see Chapter 6, Section 6.2).

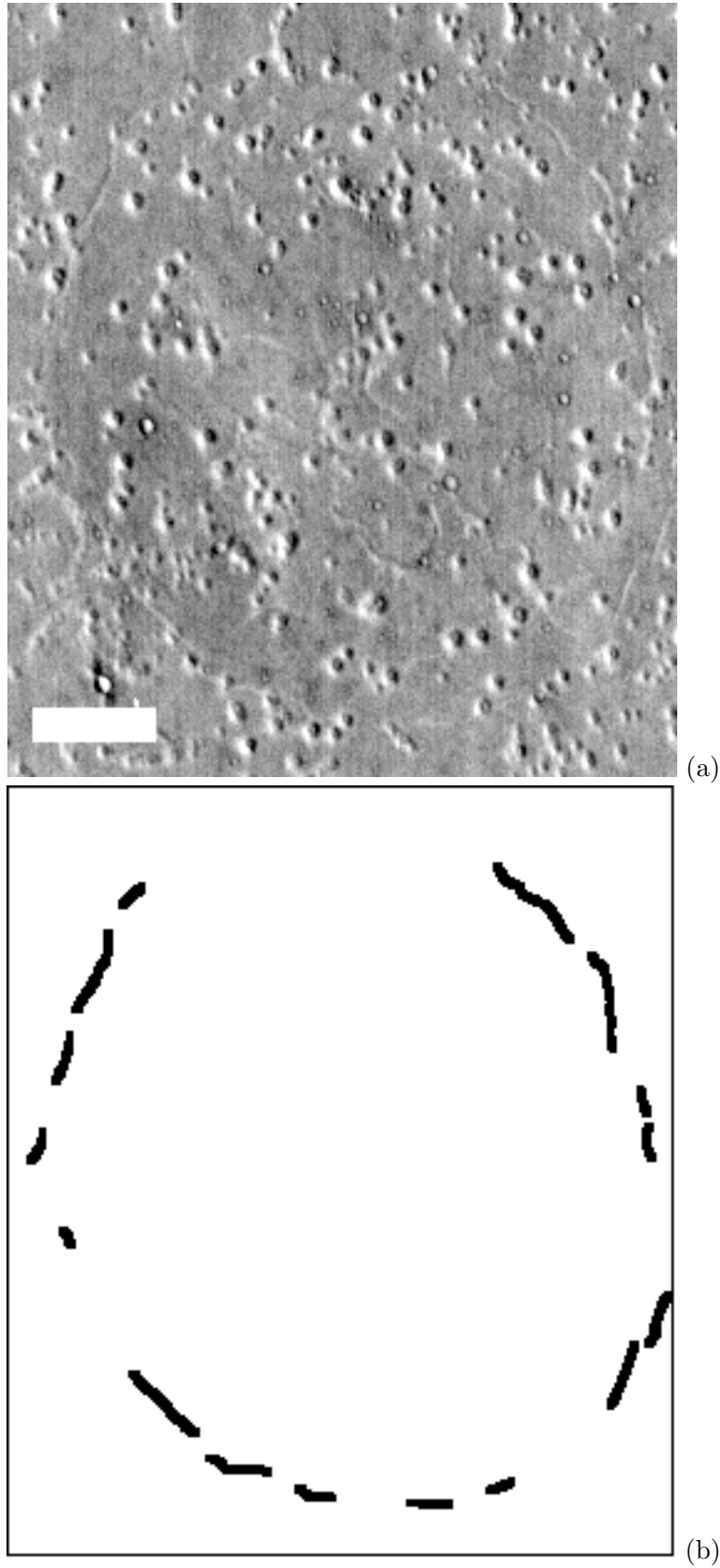


Figure 5.18: Stealth crater in Isidis Planitia. (a) a large stealth crater in Isidis Planitia from THEMIS infrared daytime image I01782005. Bar is 5 kilometres. (b) cartoon showing the extent of the discontinuous graben around the edge of the stealth crater in (a).

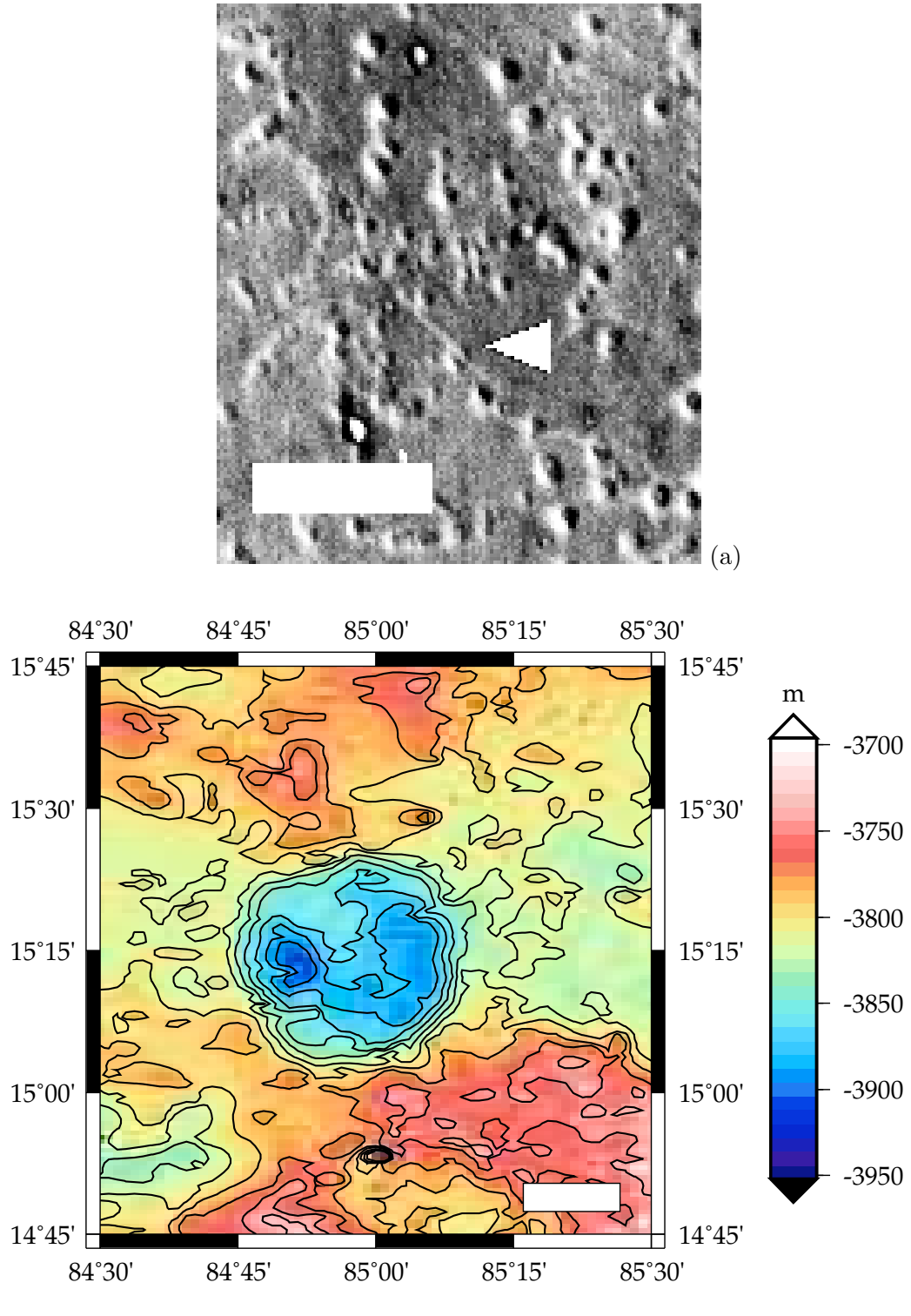


Figure 5.19: Stealth crater in Isidis Planitia. (a) 2 x magnification of the lower-left region of the large stealth crater in Isidis Planitia from THEMIS infrared daytime image I01782005 depicted in 5.18, showing a closer view of parts of the discontinuous graben, including a small cone that appears to be bisected by the graben (arrowed). Image has been contrast stretched for clarity. Bar is 5 kilometres. (b) the MOLA topography of the area surrounding the stealth crater shown in Figure 5.18. Contours have a 16 metre interval. Bar is ~10 km.

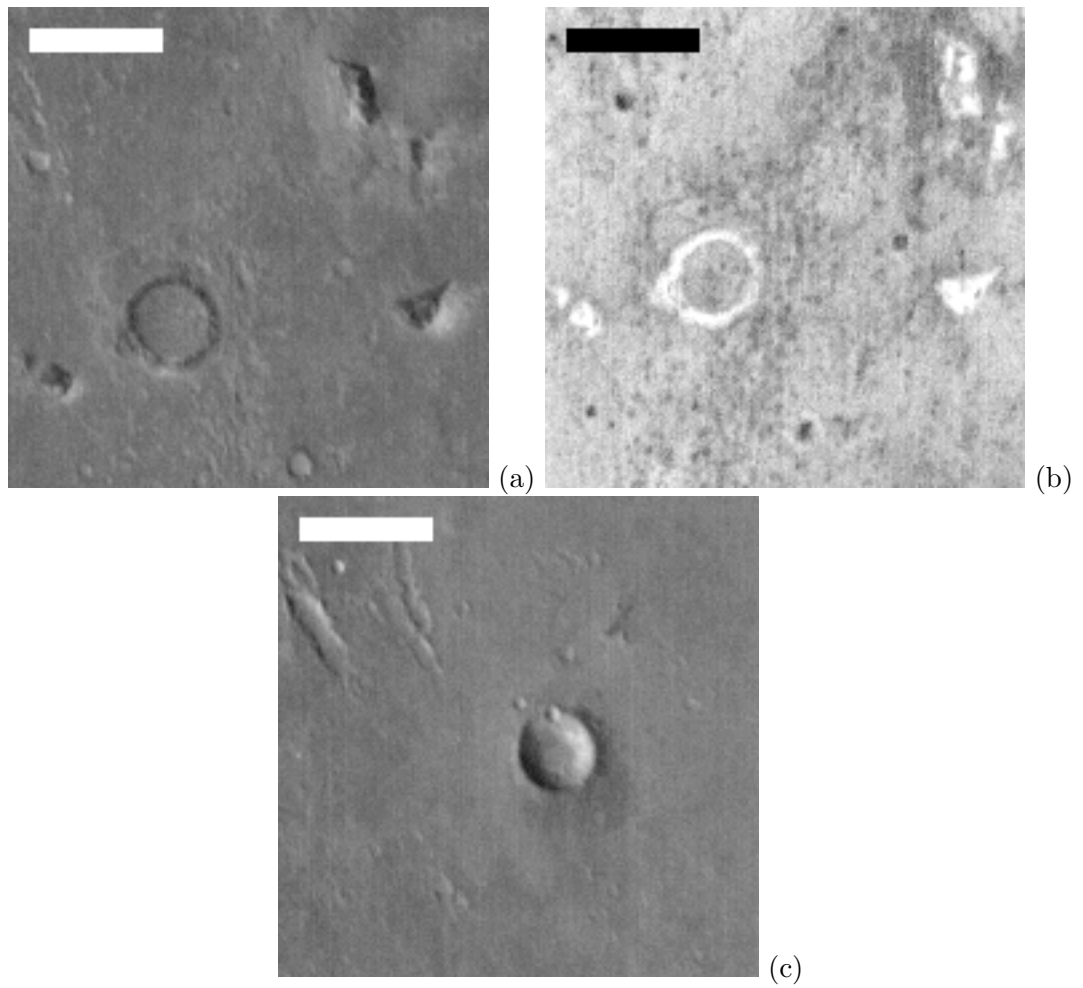


Figure 5.20: Stealth crater in south east Isidis Planitia. (a) Stealth crater in THEMIS infrared daytime image I09808025. (b) the same stealth crater in THEMIS infrared night-time image I02013005. (c) a nearby similarly-sized fresh impact crater from the same THEMIS image as (a) for comparison. Bars in all images are 5 kilometres.

5.4.3 Discussion

The evidence presented in this section strongly suggests that Isidis Planitia is the site of sedimentary deposition burying a pre-existing cratered surface, possibly involving episodic sedimentation. It is possible that the stealth craters in the basin have been exposed by the erosion of a layer of deposited material, as has been suggested for other regions on Mars (Schultz, 2002). However, evidence of features such as sediment fans in the southern part of the basin (e.g. Crumpler and Tanaka, 2003) tends to suggest that, although erosion is probably a component in the processes taking place in the basin, deposition of sediment upon a relict basin floor is most likely responsible for the stealth crater features (for a further discussion of the evidence for sediment fans and basin sedimentation, see Chapter 6, Section 6.2). This scenario is also supported by the lack of erosional features such as pedestal craters, and the confinement of mesas and relict plateaus primarily to the chaotic terrain near Syrtis Major Planum.

The method of by which the sediment was carried and deposited would also have had a strong bearing on the resulting stealth crater features. Sediment carried by water shallower than a crater rim would have been deposited evenly around a crater, but not within its bowl. Sediment deposited by air-fall would be relatively evenly spread over both the surrounding terrain, the crater rims and within the crater bowl. Sediment deposited from water deeper than a crater rim would be similarly distributed, although it is possible that some preferential accumulation of sediment within crater bowls could occur if they act as sediment traps. Aeolian deposition of sediment would result in a greater thickness of deposit on the windward side of a crater. In this scenario the greatest depth of deposition within the crater itself would be towards the opposite side of the bowl as the windward rim acted to shadow the adjacent part of the crater bowl from sedimentary deposition. The evidence in this chapter generally points to a waterbourne origin for the sediments, and given that none of the larger stealth craters show exposed rims, it would seem that the water depth was greater than the craters rim depth.

The thickness of the sedimentary deposit may be estimated from the morphology of the stealth craters. The stealth crater shown in Figure 5.18 shows no evidence for a raised rim, suggesting that the depth of sediment must be at least the height of the rim.

The presence of a discontinuous graben around much of the crater rim implies that the thickness of deposited sediment is greater than the crater rim height (Buczkowski and McGill, 2003). The diameter of the crater in Figure 5.18 is approximately 27.4 kilometres, which should result in a rim height of approximately 320 metres (Garvin et al., 2003). However, the craters in Figure 5.16(a) show obvious rims, which are most likely the surface expressions of crater rims buried at a relatively shallow depth given the lack of evidence for exposed rims in THEMIS images of these craters. The western crater is approximately 36.8 kilometres across, and should have a rim height of approximately 410 metres, and the eastern crater is approximately 30.7 kilometres across, and should have a rim height of approximately 350 metres. The results from the craters described here therefore suggest that the sediment layer thickness is greater than 320 metres, but probably not significantly more than 410 metres. There is also the possibility that different parts of the basin experienced differing depths of sedimentation. It is also possible that the crater rims may be extensively eroded (e.g. Head et al., 2002), perhaps by the flooding which may have carried the sediment into the basin, which would therefore require a thinner layer of sediment to obscure them.

The small population of small partially-buried stealth craters found in the south east of the basin (see Figure 5.20) may have been buried by a smaller, and most likely more localised, episode of sediment deposition that occurred after the event which completely covered much larger craters across the basin. The burial that took place here must have involved deposition of less than approximately 60 metres of sediment (Garvin et al., 2003) for the rims to still be visible. The stealth craters in question appear to have infilled bowls, which suggests sediment carried in water deep enough to spill over the crater rims. However, this form of deposition would most likely cover the rims with sediment, which is clearly not the case here.

The graben noted in Figure 5.18 and 5.19(a) is unlike the distinct continuous double-ring circular grabens found in Utopia Planitia which are interpreted as being due to volumetric compaction of material over buried craters (Buczkowski and Cooke, 2004). Instead, the Isidis Planitia example appears as a simple single graben formed in a discontinuous ring around the presumed crater rim. This may be as a result of simple drape folding of sediment over the crater rim producing a bending stress resulting in graben formation just

inside the crater rim (e.g. Buczkowski et al., 2003). The lack of a double graben means that models involving horizontal extension caused by compaction and shrinkage of the crater infill (Buczkowski and Cooke, 2004) are not necessary. This does not then necessarily require the deposited material in the Isidis Planitia crater to be wet, as is suggested for the Utopia Planitia features (Buczkowski and Cooke, 2004).

5.5 Conclusion

Drawing together the information from the different sections of this chapter – Isidis Planitia impact crater morphology and morphometry, stratigraphy and stealth cratering – helps to provide a relative timeline of events within the basin, and perhaps information about the basin’s subsurface composition. Evidence from crater morphology suggests the presence of ice in the subsurface, and at a depth that would be excavated in sufficient quantities to modify ejecta morphology by impacts forming craters larger than approximately 5 km in diameter. This suggests that in this regard Isidis Planitia is similar to other locations at the same approximate latitudes, as this is a typical onset diameter for layered ejecta at these locations.

Results from the investigation of the morphometry of fresh impact craters within the Isidis Planitia basin tend to suggest that little sedimentation has taken place since the formation of the fresh impact features, with none of the mantling that is suggested to have taken place in parts of Utopia Planitia and elsewhere (Boyce et al., 2003a). Rim heights are approximately as expected, implying minimal erosion of these features or deposition to reduce their height above the surrounding surface. Crater depths are slightly shallower than expected, which is most likely the result of preferential aeolian deposition within craters. Some larger craters in Isidis Planitia show dune fields in their interiors (see Figure 5.21).

Crater counts within the basin suggest an age for the current basin surface within the Upper Hesperian, near the boundary with the Lower Amazonian. There seems to be little difference in the age of the surface across the basin, in line with recent research which places the majority of the Isidis Planitia basin surface in one geological unit at the

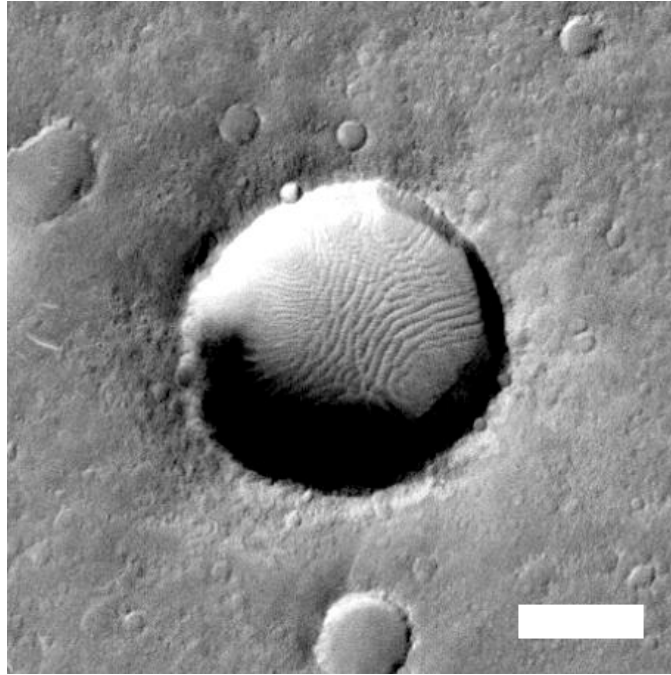


Figure 5.21: Crater dunes in Isidis Planitia. Impact crater containing dunes in a section of MOC image m2101624. The complete original image is centred at 88.56° East, 6.92° North, in the central-southern part of Isidis Planitia. Bar is 250 metres.

Amazonian/Hesperian boundary (Tanaka et al., 2003).

The presence of stealth craters in Isidis Planitia suggests an older surface that has been buried by sediment, most likely carried by deep water, to form the surface we see today. Crater counts of the stealth craters suggest that the buried unit is at youngest the age of the Upper/Lower Hesperian boundary, and is more likely to be Lower Hesperian. The depth of burial of this unit is difficult to estimate, and may vary across the basin, but is likely to be approximately 300–400 metres. An important point to note is that even a 2.5 km diameter impact crater will excavate the surface down to beyond this depth, with a 5 km diameter crater (the approximate cut-off for layered ejecta formation) excavating down to nearly 800 m (Garvin et al., 2003). This suggests that entrained volatiles – the most likely explanation for formation of layered ejecta surrounding larger craters – are not present in the layer or layers of sediment deposited upon the stealth crater bearing buried unit, at least not in sufficient quantities to significantly alter the onset diameter of layered ejecta craters in Isidis Planitia.

Chapter 6

Spectroscopy and Surface Features

6.1 Introduction

There is more to the current surface of Isidis Planitia than simply cones, sinuous ridges, impact craters and the surface manifestations of buried impacts and wrinkle ridges. Understanding the thermal, mineralogical, topographical, and textural properties of the surface of the basin can help illuminate the mechanisms that have led to the basin appearing the way it does now.

6.2 Thermal remote sensing

6.2.1 Thermal inertia

The thermal inertia, or the tendency of a material to resist changes in temperature, of a planetary surface is related to the thermal and physical nature of the top few centimetres of the surface, and reflects the ability of this upper surface layer to conduct and store heat during the day, and to lose it at night. Thermal inertia (I) relates the thermal conductivity (κ), bulk density (ρ) and specific heat capacity (c) of the material in question by the formula $I = (\kappa\rho c)^{1/2}$. Determination of thermal inertia from thermal observations of the martian surface requires knowledge of latitude, season, local time, dust opacity,

atmospheric pressure and albedo. The thermal inertia of a surface is strongly related to particle size, with dust having a lower thermal inertia than sand, with rocks and exposed bedrock having a higher thermal inertia still. Therefore, to some degree thermal inertia can be used to estimate particle size at a surface. However, the cementing of particles increases the efficiency of thermal conduction between them, and so cemented materials would have a higher thermal inertia than their unconsolidated equivalents (e.g. Christensen and Moore, 1992). Estimates of thermal inertia have already been used in this thesis to make inferences about particle size and therefore composition and the mechanism of formation of cones and cone chains and sinuous ridges (see Chapter 2, Subsections 2.5.1, and 2.5.3 respectively).

Although thermal observations of Mars were carried out by several of the Mariner and Soviet Mars missions, the first instrument to collect sufficient data to enable the production of global maps of thermophysical data (Christensen and Moore, 1992) was the Infrared Thematic Mapper (IRTM) (Kieffer et al., 1977) on board the two Viking Orbiters. Global thermal inertia maps derived from IRTM data and derived thermal models have a resolution of approximately 2 pixels per degree (Kieffer et al., 1977). The Thermal Emission Spectrometer (TES) (Christensen et al., 1992) aboard Mars Global Surveyor (MGS) was used to map thermal inertia (Jakosky et al., 2000) at a resolution of approximately 4 pixels per degree (Mellon et al., 2000) using data obtained during the early part of the primary mission of this orbiter, and which was increased to a resolution of 8 pixels per degree with the use of the entire primary mission data set (Mellon et al., 2002). The Thermal Emission Imaging System (THEMIS) (Christensen et al., 1999) aboard Mars Odyssey (MO), the latest instrument to map a large percentage of the martian surface using the thermal spectrum, has also provided data that are being used with newly developed thermal models to determine thermal inertia of the martian surface (e.g. Fergason and Christensen, 2003; Putzig et al., 2004), and results from these studies have resolutions of approximately 100 metres per pixel – considerably better than the TES results.

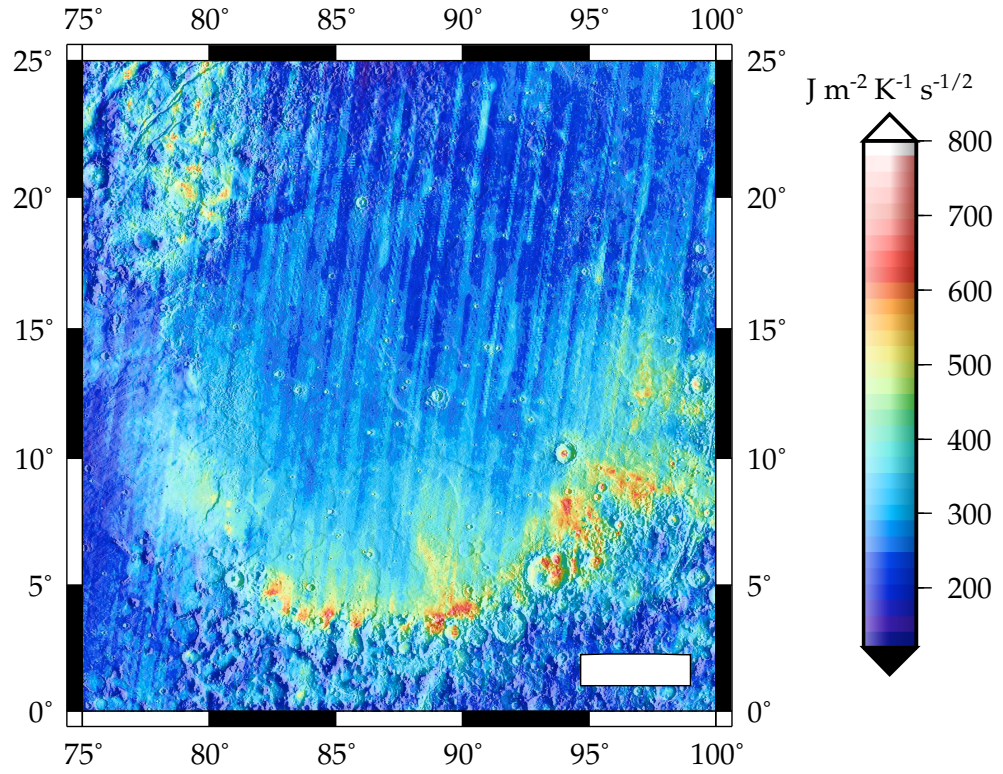
Figure 6.1 shows the results from the processing of TES thermal observations by researchers at the University of Colorado (Mellon et al., 2002) combined with illumination from topographic data by the author to enable easy comparison between thermal inertia

and topographic features. Figure 6.1(a) shows a plot I produced using the thermal inertia data for the Isidis Planitia basin, and clearly shows that the majority of the basin has a relatively low thermal inertia, with a general increase in thermal inertia towards the basin's rim in all directions apart from the north and northeast where the thermal inertia measured is similar to that found in the neighbouring lowland areas. Craters that can be seen in the image generally have higher thermal inertias than the surrounding terrain. Figure 6.1(b) shows detail from the basin's southern and southeastern rim. It can be clearly seen that the increased thermal inertia in these areas is not exclusively within the highland terrain south of the basin rim, but instead appears to extend into the lowland plains area of the basin, with no correlation with topography. In some areas these thermal inertia values are amongst the highest found on Mars.

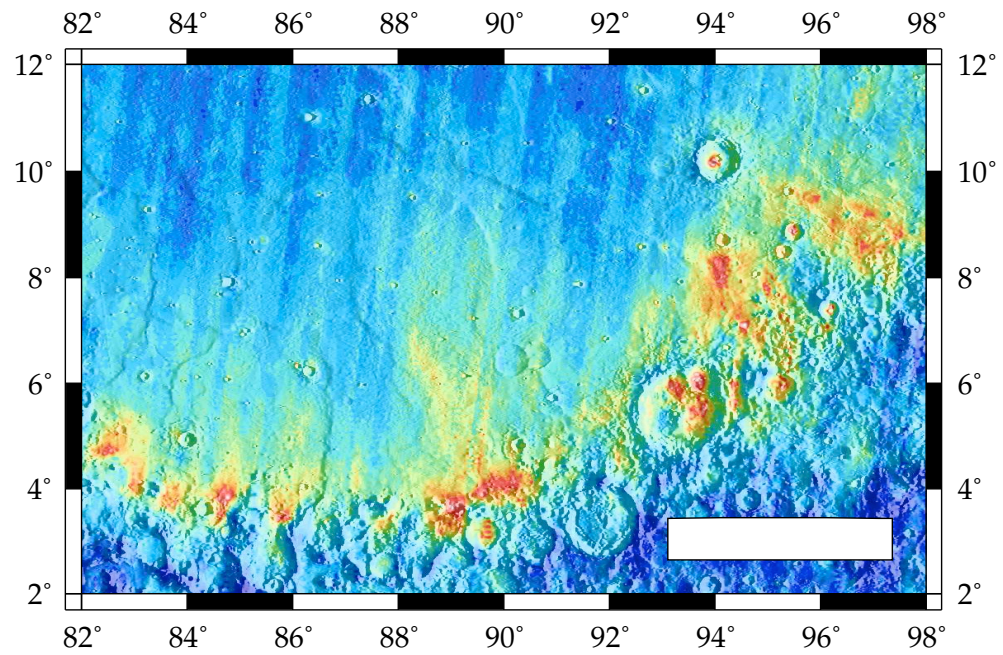
Combining thermal inertia and albedo datasets can be useful in determining possible surface properties. Analysis of early results from TES led to the division of martian thermal inertia/albedo regions into four distinct units (Mellon et al., 2002). This research placed the majority of Isidis Planitia into Unit C (moderate-to-high thermal inertia and intermediate albedo), along with the majority of the neighbouring lowland areas, and the highland region to the south of the basin. The high thermal inertia areas in the south and southeast of the basin were placed in Unit D, a category which simply combined areas that do not easily fall into the other three units. Mellon et al. (2002) believe that Unit C represents a distinct zone of cemented low thermal inertia particles, rather than a transition between dusty and rocky areas. Subsequent researchers have increased the number of units to seven (Putzig et al., 2003), retaining the Unit C of earlier studies, but recategorising Unit D into more specific replacement units. The high thermal inertia areas in Isidis Planitia are placed into Unit F (very high thermal inertia independent of albedo), and interpreted as having a high rock abundance and/or bedrock.

6.2.2 Particle size and rock abundance

Thermal inertia is strongly dependent on particle size and therefore thermal inertia measurements can be used to infer the average size of particles at a terrain surface. Presley (2002) presented a first order approximation of particle size based on thermal inertia under a standard martian atmospheric pressure, and for a given thermal conductivity, which,



(a)



(b)

Figure 6.1: Isidis Planitia thermal inertia. (a) shows the thermal inertia of the Isidis Planitia basin. (b) shows the thermal inertia of a selected region of the basin's southern and southeastern rim. Thermal inertia scale identical for both images. Thermal inertia data from the University of Colorado (Mellon et al., 2002). Illumination using topographical data added for clarity. Bars in both images are ~ 250 km.

under martian atmospheric pressures, is itself strongly dependent on particle size (Presley and Christensen, 1997). This model results in an approximate order of magnitude increase in particle size for an increase of $100 \text{ J m}^{-2} \text{ K}^{-1} \text{ s}^{-1/2}$ of thermal inertia. Figure 6.2 shows the results I obtained when applying this model to thermal inertia results from THEMIS derived by the University of Colorado (Mellon et al., 2002) (compare with Figure 6.1). It shows that the estimate for particle size in the majority of the basin is on the scale of millimetres, with the particle size increasing to centimetres towards the higher thermal inertia areas of the basin rim. Particle sizes of the order of a metre are also found in the most extreme areas of high thermal inertia, implying dense rock cover – probably bedrock. However, it must be considered that the model presented by Presley (2002) is only an approximation. Variation in thermal conductivity can be affected by particle shape, bulk density, sorting and porosity of sediments, as well as cementation. Thermal inertia data must be combined with other investigations, such as morphological interpretation of the surface, in order to determine the nature of surface materials.

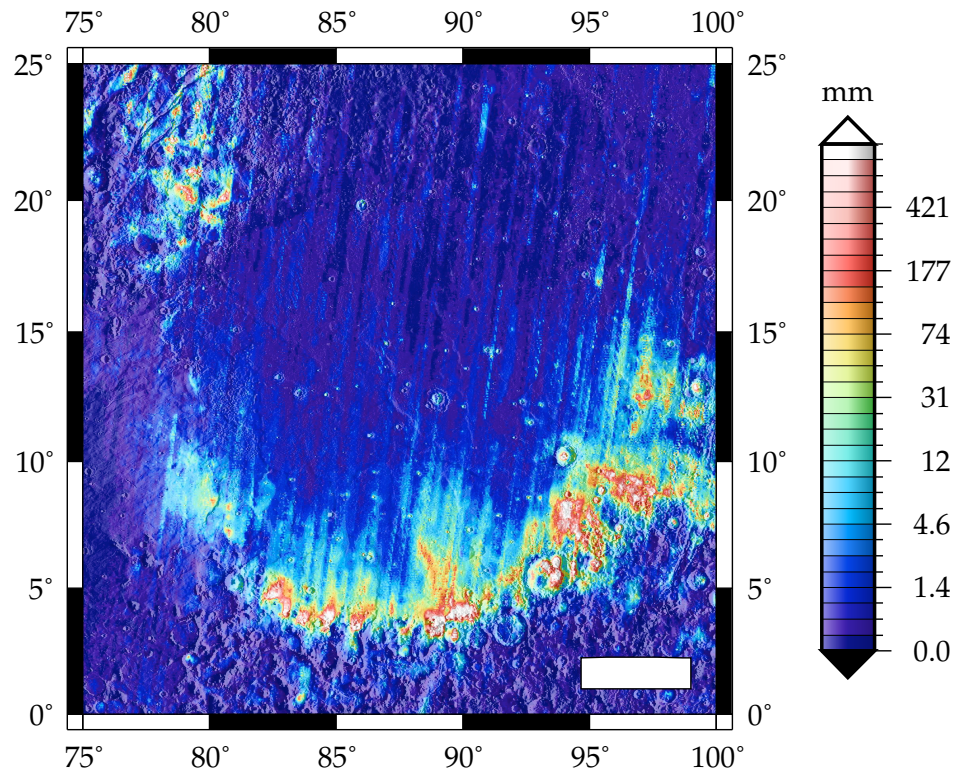


Figure 6.2: Isidis Planitia particle size, showing an approximation of particle size derived from thermal inertia using the model determined by Presley (2002) and thermal inertia data from the University of Colorado (Mellon et al., 2002). Illumination using topographical data added for clarity. Bar is ~ 250 km.

Thermal inertia data may also be used in determining rock abundance on the martian surface (e.g. Christensen, 1986; Golombek et al., 2003a). Multispectral thermal observations of a surface are used to derive a two-component thermal model with a high thermal inertia component (rocks) and a low thermal inertia component (fines) (Christensen, 1986; Christensen and Moore, 1992). This model, together with an estimate of the thermal inertia of the two components, can be used to identify the proportion of surface occupied by these two components. The rock component of this model represents rocks more than approximately 10 cm in diameter. This cut-off is used as at greater diameters rocks exhibit roughly the same temperature changes regardless of size, whereas smaller rocks show temperature changes that are strongly dependent on size (Christensen and Moore, 1992). Initially, IRTM data were used to produce rock abundance maps of the martian surface (Christensen, 1986), with higher resolution maps of rock abundance being subsequently produced using TES data (Nowicki and Christensen, 1999) with the same method. The accuracy of the thermal inertia observations and model was supported by the results from the Mars Pathfinder landing site, which had a rock abundance within 10% of that predicted (Golombek et al., 1999). Using this method, the rock abundance of Isidis Planitia ranges from 0 in parts of the centre and northwest of the basin, to a maximum of 0.43 (i.e. 43%) in the high thermal inertia areas at the southern rim of the basin.

Rock abundance for populations of rocks with a variety of thermal inertias has also been modelled using TES data (Golombek et al., 2003a,b). Results from this work have suggested a rock abundance of approximately 0.14 based upon the area of the proposed Mars Exploration Rover (MER) landing site in the southern part of the basin (Golombek et al., 2003a). Using the results from this model, and assuming that the thermal inertia of the central and northeastern part of the basin represents a ‘background’ level of thermal inertia that is represented by fines (although this itself is unlikely to have a zero rock abundance and be composed entirely of fines), and that this has a thermal inertia closest to the modelled thermal inertia value of $249 \text{ J m}^{-2} \text{ K}^{-1} \text{ s}^{-1/2}$, the higher thermal inertia areas at the basin rim suggest rock abundances of between approximately 0.08 and 0.38 based upon an effective rock inertia of $2500 \text{ J m}^{-2} \text{ K}^{-1} \text{ s}^{-1/2}$ and a range of bulk thermal inertias of $300\text{-}600 \text{ J m}^{-2} \text{ K}^{-1} \text{ s}^{-1/2}$ (in reality this is even higher in certain locations), and between approximately 0.1 and 0.45 based upon an effective rock inertia of $1300 \text{ J m}^{-2} \text{ K}^{-1} \text{ s}^{-1/2}$. This also implies that the increase in thermal inertia along the basin

rim is due to an increase in rock distribution rather than an increase in the induration of smaller particles. Work has also been done using THEMIS to support rock abundance estimates on Mars (Nowicki and Christensen, 2002), enabling both a higher resolution view of thermal inertia and corroboration of earlier rock abundance results.

There is a lack of correlation between topography and thermal inertia in the higher thermal inertia regions of Isidis Planitia. This perhaps suggests local modification by erosion or deposition to produce a surface that has a different thermal inertia from topographically similar areas elsewhere in the basin. This could be as a result of aeolian activity (e.g. Murphy et al., 2004), sedimentary deposition by a mechanism such as flooding (e.g. Kreslavsky and Head, 2002), or a combination of processes. The areas of particularly high thermal inertia at the southern basin rim correspond to points where valleys within Libya Montes enter the Isidis Planitia basin (Crumpler et al., 2002), suggesting that these features may be sediment fans with high rock abundances.

6.2.3 Mineralogy

Direct information on the mineralogy of the martian surface is limited to the experiments carried out by landers in relatively small areas of the surface, and later from meteorites that originated from Mars (e.g. Banin et al., 1992). A global view of the mineralogy of the martian surface comes from remotely sensed spectroscopic observations of the planet (e.g. Soderblom, 1992). Such information helps understand the physical and chemical processes that have occurred at or near the planet's surface. Current research into the global mineralogy of Mars mainly uses data from the TES instrument on Mars Global Surveyor (e.g. Bandfield et al., 2000; Hamilton et al., 2001; Bandfield, 2002).

Determination of surface composition using TES requires the removal of the atmospheric component of the emitted spectra, leaving the emission spectrum of the surface. Deconvolution techniques are then used to add and subtract the known spectra of a library of end member minerals to match the emission spectra of the surface. Results from processing the TES data showed that the surface of Mars is not compositionally diverse, and greater than 99% of the martian surface falls into one of three distinct emissivity groups (Bandfield, 2003). These are known as Surface Type 1 (ST1), which is primarily

found associated with areas in the southern highlands, Surface Type 2 (ST2), which is mainly found associated with areas of the northern lowlands, although with some mixing with ST1 in southern highlands areas, and a dust component, which obscures the mineralogy of the surface beneath it.

Bandfield et al. (2000) and Hamilton et al. (2001) suggested that ST1 represented basalt, and ST2 is similar to a terrestrial andesite or basaltic-andesite, probably being produced by the fractional crystallisation of basalt. However, Wyatt and McSween (2002) suggested that ST2 represents a weathered basalt, and that weathering of basalt by water in the northern lowlands may have been the method of formation. It is possible that both methods of formation are responsible for ST2 on Mars. Wyatt and Tanaka (2003) proposed that ST2 materials in the southern highlands may be andesitic and formed by the fractionation of ST1 basalts in hydrous conditions, reflecting the association of small amounts of ST2 with predominately ST1 in this area (Wyatt et al., 2003a), whereas ST2 found in the northern lowlands is more likely to be altered basalt formed by the interaction of sedimentary materials with surface or near-surface volatiles (Wyatt and Tanaka, 2003; Wyatt et al., 2003a).

Figures 6.3 and 6.4 show the surface mineralogy of Isidis Planitia using data from TES produced by Bandfield (2002), after separation of atmospheric effects using multiple emission angle observations. The figure shows the presence, or absence, of various end member minerals, along with distribution of surface dust, which obscures the detection of the mineral content of the surface beneath it. The large amounts of high calcium pyroxene and plagioclase found in Syrtis Major Planum are indicative of ST1, which is most likely basaltic. Isidis Planitia itself is characterised by a fairly strong dust signature, which appears stronger towards the north of the basin. There is little other evidence of specific end member minerals within Isidis Planitia. The strongest mineral return from the basin, and probably the only one at or near the detection limit of TES (given on the figures as 0.1, or 10%), is high silica glass, which is indicative of ST2 – and most likely indicates an altered basalt, particularly given other lines of evidence suggesting that the Isidis Planitia basin may have interacted with surface water at some time in its past. The dust end member return inversely correlates quite well with the high silica glass response in the north and west of the basin, suggesting that dust may obscure a surface generally

containing relatively large amounts of high silica glass across a wide area of the basin. However, this correlation is not as strong in the southern half of the basin, where the high silica glass response is patchy and relatively weak.

6.2.4 Discussion

The thermal remote sensing of Isidis Planitia has provided useful results that may help determine aspects of the basin's evolution. Thermal inertia data, along with associated particle size and rock abundance results, strongly suggest that the high thermal inertia material observed has been deposited as sediment fans at the mouths of valleys within Libya Montes (e.g. Crumpler et al., 2002). It is possible that this material could have been deposited as a result of a 'dry' gas-supported flow (e.g. Hoffman, 2000; Hoffman et al., 2001), but a more likely source is sediment deposited by water flowing through the valleys and into the basin. Water flow through the valleys would have been very turbulent, and therefore able to transport a relatively large amount of suspended material (e.g. Carr, 1996). On reaching the Isidis Planitia basin, turbulence would reduce, and the larger particles in the water would be deposited, with the largest material deposited closest to the valley mouth, and finer material being carried with the flood water further into the basin (e.g. Kreslavsky and Head, 2002). The suggestion by Kreslavsky and Head (2002) that the flood water may have been 'warm', generating intense convection within the ponded water in the basin which therefore maintained a sediment load for longer, is not strongly supported by the thermal inertia data as Figure 6.1(a) shows a noticeable pattern of thermal inertia decrease across the entire basin, roughly from south to north. However, the presence of buried craters in the north and northeastern parts of the basin (see Chapter 5, Section 5.4 for further discussion about the buried craters in Isidis Planitia) suggests that the water reaching this part of the basin retained a large enough sediment load to almost completely fill large (>5 km) craters. It is also possible that the visible thermal inertia pattern across the basin is the result of the most recent of what may have been a series of such flooding episodes (e.g. Fairén et al., 2003), and that the craters in the north and northeastern areas of the basin may have been filled by previous sedimentation episodes, possibly originating from a location other than Libya Montes. This is supported by the presence of small partially-buried stealth craters in the high thermal inertia areas

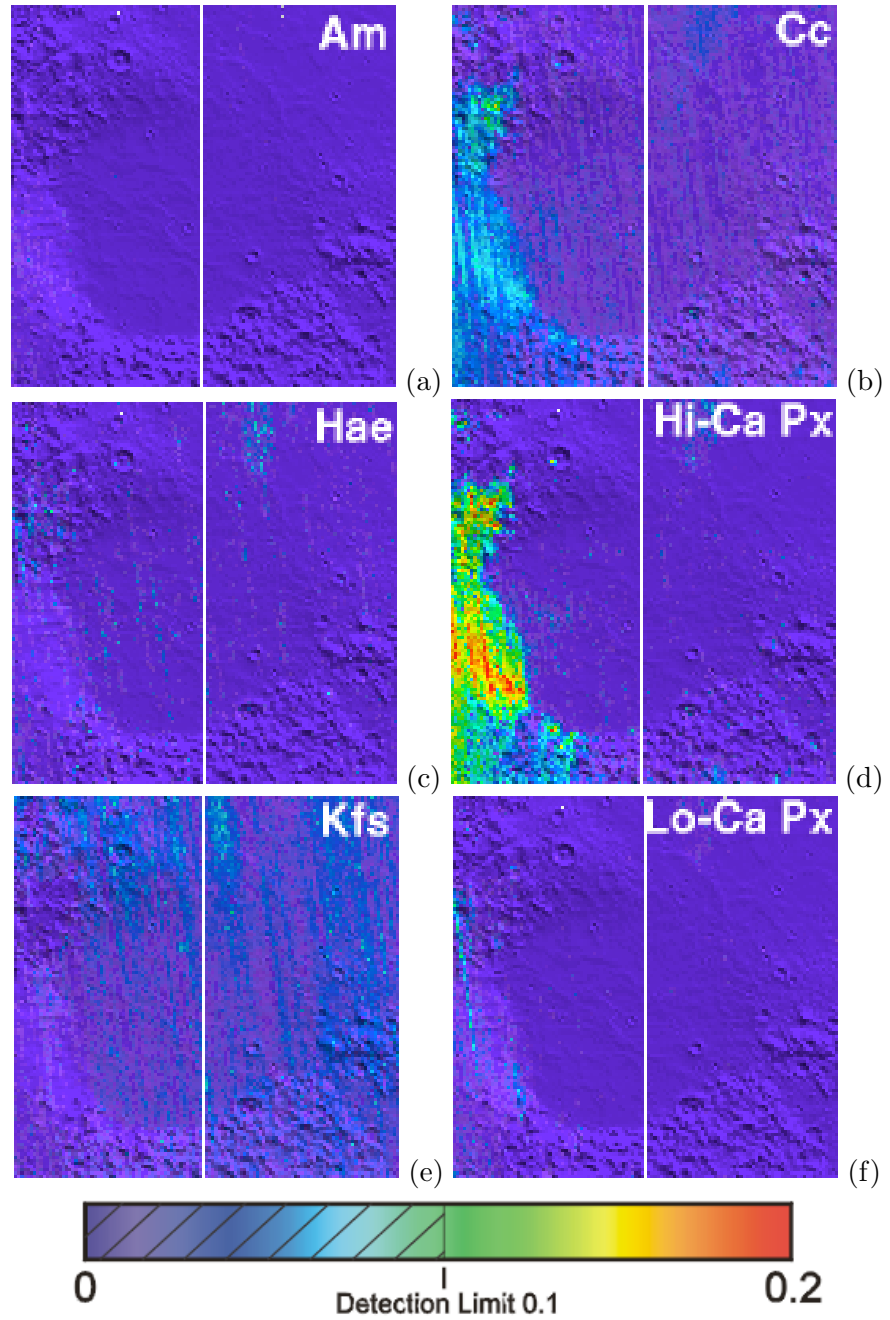


Figure 6.3: Isidis Planitia mineral maps. (a) shows amphibole, (b) carbonates, (c) haematite, (d) high calcium pyroxene, (e) potassium feldspar and (f) low calcium pyroxene. All maps use the same scale (75° to 105° E, 0° to 30° N) and key. Vertical line represents 90° E. All maps from global maps produced by Bandfield (2002) using TES data.

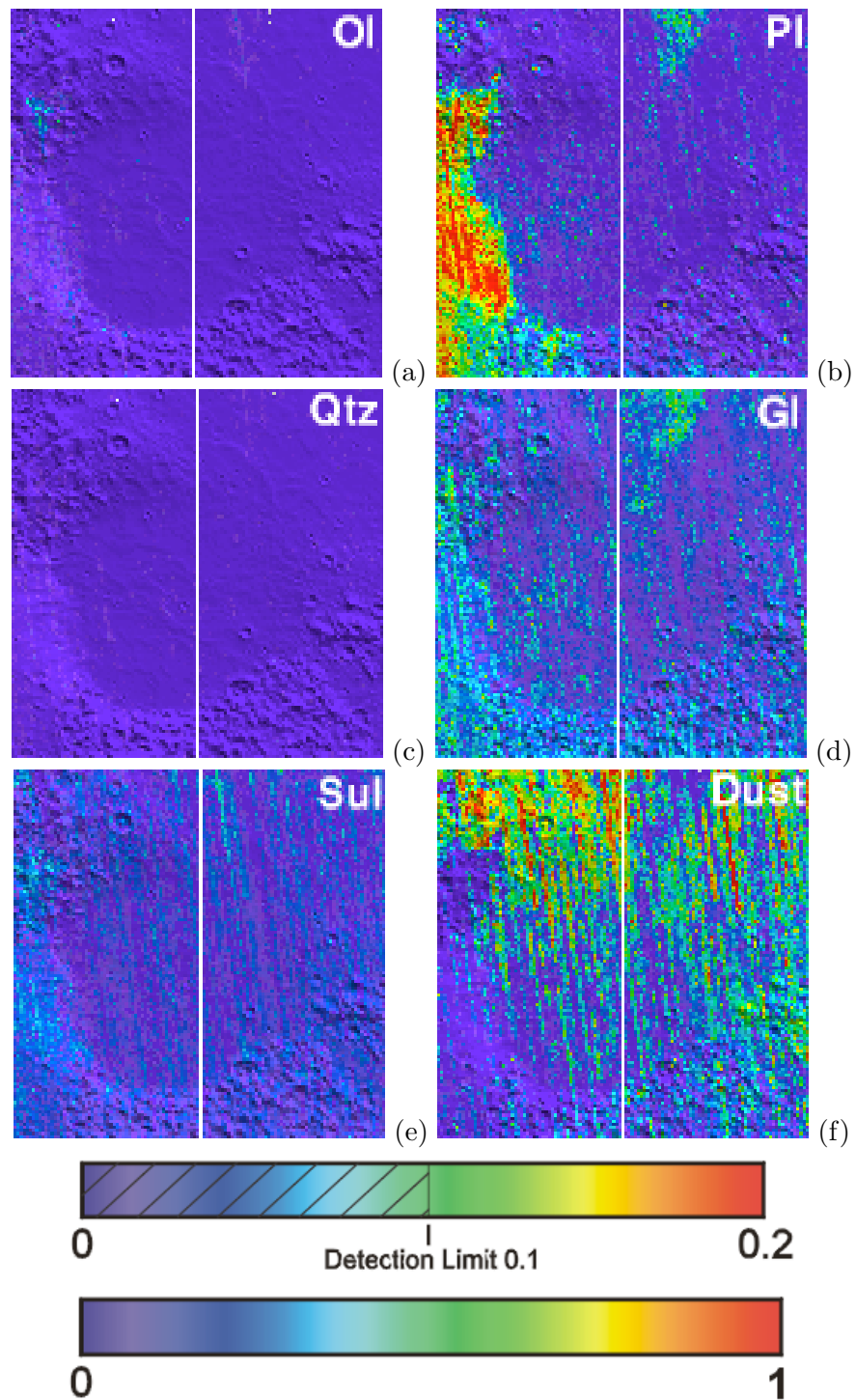


Figure 6.4: Isidis Planitia mineral maps. (a) shows olivine, (b) plagioclase, (c) quartz, (d) sheet high silica glass, (e) sulphate, and (f) surface dust. All maps use the same scale (75° to 105° E, 0° to 30° N) and use the upper key, except (f) which uses the lower key. Vertical line represents 90° E. All maps from global maps produced by Bandfield (2002) using TES data.

of the south eastern basin (see Chapter 5, Section 5.4, and Figure 5.20).

6.3 Surface roughness and slope

6.3.1 Introduction

The roughness and slope of a surface can give some indication of its history and composition, and its relationship to surrounding terrain. Radar measurements have been used since 1963 to investigate martian altimetry, surface roughness, surface reflectivity and surface structure (e.g. Simpson et al., 1992). Radar data from the Goldstone Solar System Radar (GSSR) were used to characterise slopes and roughness at a variety of scales within the basin as part of the selection of the landing site of Beagle 2 in Isidis Planitia (Bridges et al., 2003a). Laser altimetry can also be used to characterise surface roughness and slope (e.g. Garvin et al., 1998). The Mars Orbiter Laser Altimeter (MOLA) instrument aboard MGS has been used to determine these characteristics as an adjunct to its primary mission of determining surface topography.

6.3.2 Surface roughness from MOLA data

The MOLA instrument returns, along with other parameters, information about the width of the returned pulse of laser light. The spread of this pulse depends on a variety of factors, including the pointing angle of the instrument, the reflectivity of the surface, the slope of the surface, and the vertical roughness of the surface (e.g. Gardner, 1992; Abshire et al., 2000). This spread has been used to identify the roughness of the martian surface at a MOLA footprint scale (~ 150 m) (e.g. Garvin et al., 1999; Neumann et al., 2003a), which in turn can be used to infer other characteristics of the surface (e.g. Deal et al., 2003).

Figure 6.5 shows the RMS surface roughness of the Isidis Planitia basin and surrounding areas that I determined using MOLA received optical pulse width data. The data are corrected for filter characteristics and threshold settings, and data with high off-nadir pointing angles are not used. However, surface slopes and target reflectivity are not corrected for, and possible signal saturation (Garvin et al., 1999) is not accounted for. This

figure should therefore be used as indicative of general surface properties rather than quantitatively. It shows that the plains area of the Isidis Basin is relatively smooth at a sub-footprint scale, although not as smooth as Syrtis Major Planum which is formed from volcanic material that is smooth at this scale (e.g. Deal et al., 2003). Highland units surrounding the basin show that significantly rougher terrain is present, although this area also exhibits greater slopes. Generally, apart from the rougher terrain at crater rims and over crater ejecta, the Isidis Planitia basin has a relatively uniform roughness. However, there are areas in the northwest, northeast and south of the basin that appear to have slightly elevated roughness levels. These areas do not correlate with obvious topographic features.

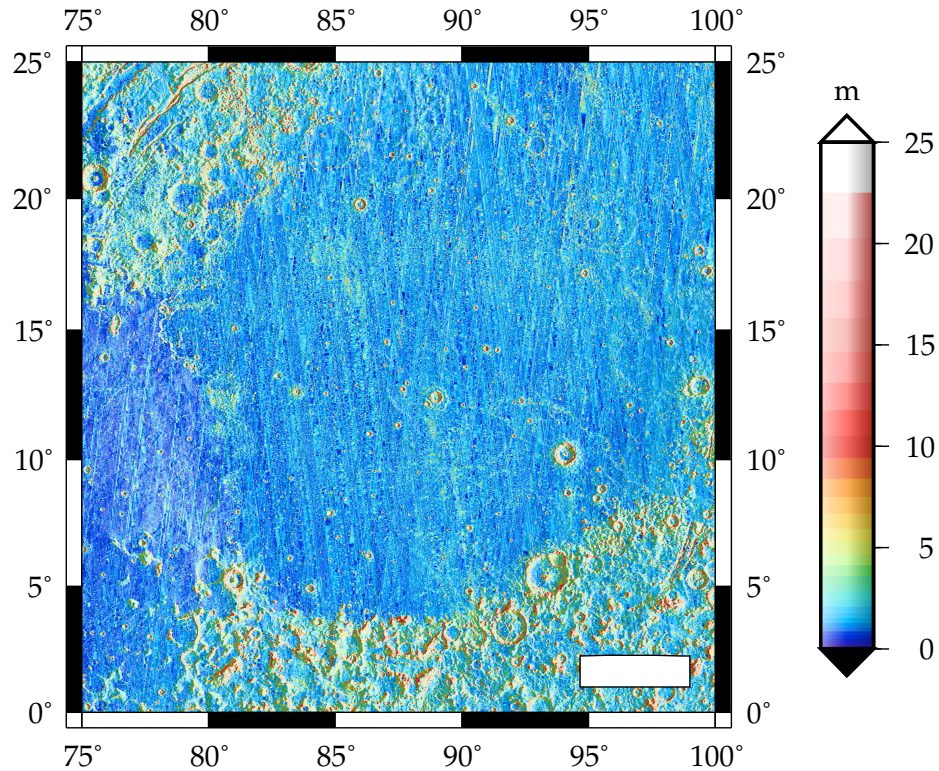


Figure 6.5: Surface roughness of Isidis Planitia. RMS surface roughness of the basin from MOLA received optical pulse width data. High off-nadir pointing angle data not used, and data corrected for filter characteristics and threshold settings, however the data is not corrected for footprint-scale slopes, target reflectivity, or sensor saturation. Illumination using topographical data added for clarity. Bar is ~ 250 km.

Kreslavsky and Head (2000) have also used the MOLA instrument to investigate the larger scale roughness of the martian surface by calculating the median differential slope of individual MOLA tracks using a variety of baselines from 0.6 to 19.2 kilometres. Re-

sults for Isidis Planitia indicate a smoothness characteristic of northern plains material in general, but with a noticeable increase in roughness at smaller baselines which may reflect the contribution of the ridged surface units' small-scale structure to surface roughness compared with the smoother geological units found elsewhere in the northern lowlands. Erosional processes involving water and aeolian action, as well as some types of glaciation, can also contribute to a higher surface roughness at this scale (Deal et al., 2003).

6.3.3 Slopes

Figure 6.6 shows the 1/64th degree (~ 0.924 kilometres) baseline gradient magnitude in metres per degree. At this baseline length the gradient map of Isidis Planitia basin is dominated by features such as wrinkle ridges (see Chapter 4) and impact craters (see Chapter 5), which are superimposed upon a generally very flat basin surface. The surrounding cratered highlands have extremely large gradients.

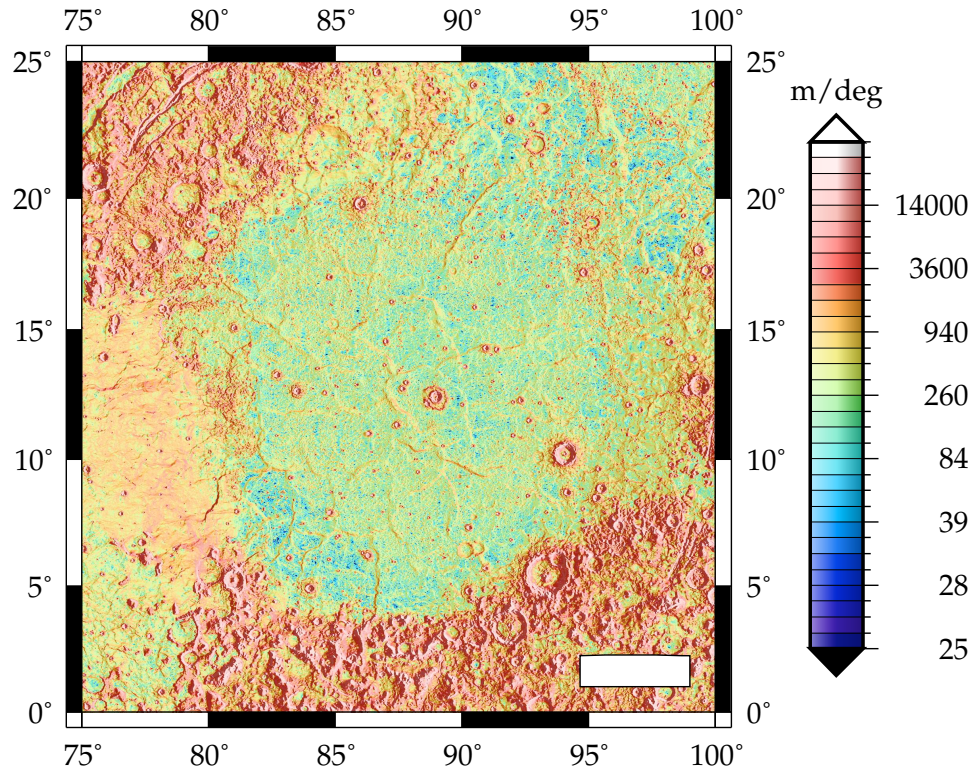


Figure 6.6: Gradients in Isidis Planitia. 1/64th degree baseline gradient magnitude (metres per degree) in Isidis Planitia from MOLA data. Illumination using topographical data added for clarity. Bar is ~ 250 km.

6.4 Geomorphology

6.4.1 Introduction

Availability of high-resolution images of the martian surface from instruments such as the Viking Orbiter Cameras (VOC), and particularly Mars Orbiter Camera (MOC), has provided another means of characterising areas of Mars. The latter instrument has a maximum resolution of approximately 1.4 metres per pixel, and despite having incomplete coverage of the martian globe at this resolution, is a useful tool in analysing features on Mars. An example of this can be found in Chapter 2, Section 2.4, where MOC data, along with other data, are used to characterise the sub-kilometre sized cones, sinuous ridges, and possible igneous features of Isidis Planitia. THEMIS images, at a higher resolution than the VOC global set, and with near global coverage at thermal infrared wavelengths, also provide a useful data set for surface characterisation.

Extensive characterisation of certain areas of Isidis Planitia has already been carried out in support of two missions. The Beagle 2 mission planned a landing in central Isidis Planitia (Bridges et al., 2003a,b), and the southern rim of Isidis Planitia was one of the candidate landing sites for the MER missions, although the final selection process decided upon Terra Meridiani and Gusev crater as landing targets (Golombek et al., 2003a). Targeting of the areas selected as potential landing sites has resulted in a large proportion of MOC images in Isidis Planitia being located near either the central Beagle 2 site, or the southern MER site.

6.4.2 General features

The area studied for potential MER operation is located at the southern rim of the basin, near the contact with Libya Montes. VOC and MOC images of the target sites in Isidis Planitia are described by Crumpler et al. (2001) as showing plains materials that are featureless at VOC Mars Digital Image Mosaic 2 (MDIM 2) resolutions (~ 231 metres), but show rolling moderate albedo plains with small secondary impacts spaced at ~ 100 metres, and small dune fields spaced at ~ 0.5 to 1 kilometres in high-resolution MOC images. Anderson and Parker (2002) described the area within the MER candidate landing

site in Isidis Planitia as having a bumpy topographic texture composed of hills and craters with an amplitude of 5-30 metres. The area around the proposed Beagle 2 landing site in central Isidis Planitia is also relatively featureless at Viking resolutions, and shows plains with often degraded small craters, high albedo streaks interpreted as dunes, and occasional small cones (see Chapter 2) (Bridges et al., 2001, 2003a). A few features identified in MOC images of both regions that may be related to igneous intrusion, such as exposed dykes and possible lava domes, have also been described in Chapter 2, Subsection 2.7.2. Here I will consider possible aeolian and lacustrine features.

Figures 6.7 and 6.8 compare high-resolution THEMIS visible images from four parts of the Isidis Planitia basin. These images all use Band 3 of the THEMIS visible detector, which has a wavelength of $0.65\ \mu\text{m}$, and have a high resolution for THEMIS images at 18 metres per pixel. Figures 6.7(a) and 6.7(b) show typical scenes from the central part of the basin. Small cones (see Chapter 2) are visible throughout the image. Between the cones the terrain is fairly smooth plains material with small impact craters. Figures 6.8(a) and 6.8(b) show images from the southern part of the Isidis Planitia basin, near the contact with Libya Montes, and within the high thermal inertia region of the basin. Neither of these images show small cones. Figure 6.8(a) shows smooth plains materials with what is likely to be a swarm of secondary impact craters to the east of the image. An interesting ridge-like feature bisects the image from south-west to north-east. It is much narrower than the wrinkle ridges discussed in Chapter 4, but could similarly be the result of compressive faulting on a more local scale. Another possibility is that it is an esker, similar to those discussed in Chapter 2, although it does not share all the morphological characteristics of these features. Figure 6.8(b) shows rougher topography, relatively few impact craters, a few knobs or hills, and an interesting feature at the western end of the image, which appears to be a channel oriented north-south. Although Libya Montes has very obvious channels that appear to empty into the southern Isidis Planitia basin, the presence of even small channels in the basin itself could have important implications for the mechanism of formation of the basin surface.

Figure 6.9 compares two high-resolution MOC images, located ~ 80 kilometres apart. Figure 6.9(a) is from a relatively low thermal inertia area of the basin, and Figure 6.9(b) is from a much higher thermal inertia area. Inferences from the comparison are limited

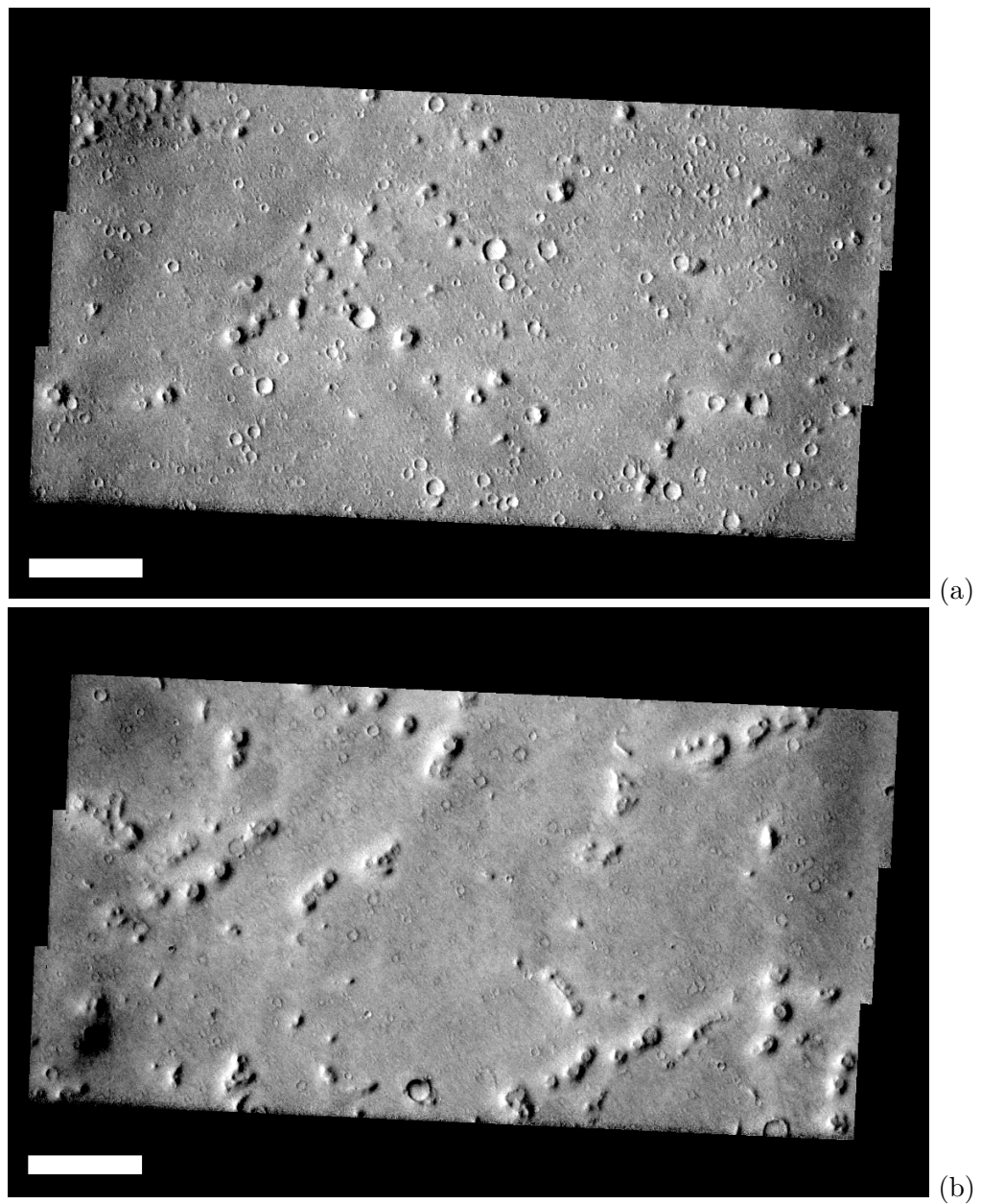


Figure 6.7: High resolution THEMIS visible images of central Isidis Planitia. (a) shows Band 3 of the THEMIS visible image V01994007. Image centred at 91.146° E 15.157° N, in the centre-east of the basin. (b) shows Band 3 of the THEMIS visible image V02119007. Image centred at 85.626° E 11.429° N, in the centre-west of the basin. Both images have a pixel size of 18 metres per pixel. Bars in both images are 2.5 kilometres.

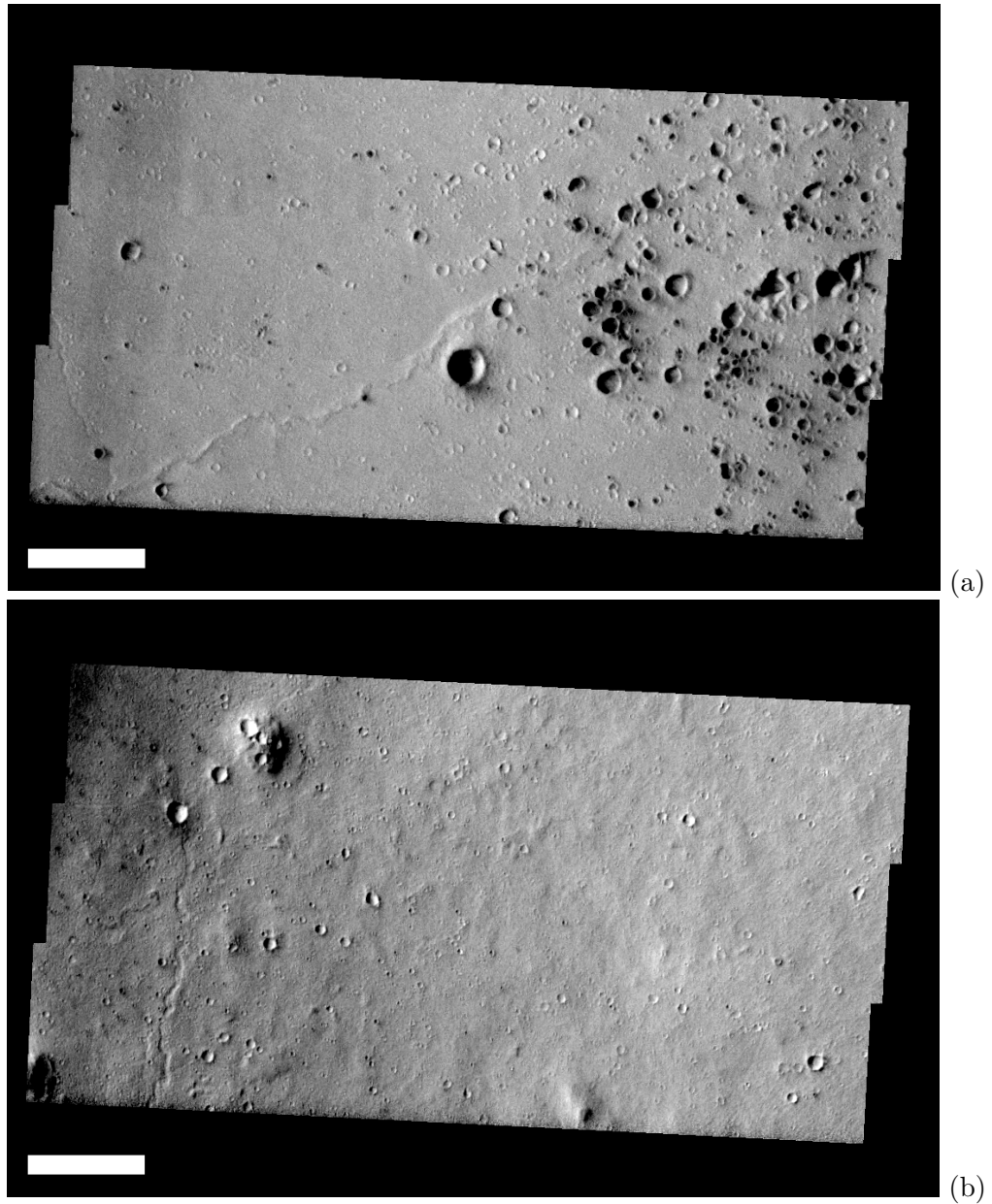


Figure 6.8: High resolution THEMIS visible images of southern Isidis Planitia. (a) shows Band 3 of the THEMIS visible image V01657007. Image centred at 88.733° E 4.285° N, in the south of the basin. (b) shows Band 3 of the THEMIS visible image V03904003. Image centred at 87.054° E 4.153° N, in the south of the basin. Both images have a pixel size of 18 metres per pixel. Bars in both images are 2.5 kilometres.

in scope because of the small area of each image. However, Figure 6.9(a) (low thermal inertia) appears smoother than Figure 6.9(b) (high thermal inertia). There are several larger craters in Figure 6.9(a) (low thermal inertia), but smaller craters appear modified by erosion or infill. The smallest crater sizes visible in Figure 6.9(b) (high thermal inertia) do not appear in Figure 6.9(a) (low thermal inertia). The high density of smaller craters in Figure 6.9(b) (high thermal inertia) is likely to be the result of secondary cratering from a source located beyond the extent of this image. It is possible that this higher density of cratering could be partly or wholly responsible for the greater thermal inertia that this area exhibits (see Figure 6.1), although the extent of the heavily cratered area, and whether it is contiguous with the area of higher thermal inertia, is unclear.

Rocks are identifiable in high-resolution images as light/dark pixel pairs (e.g. Schroeder and Golombek, 2003). The minimum practical size for rock identification is twice the pixel size. There is little evidence of large numbers of rocks larger than ~ 7 metres (twice the pixel size) in Figure 6.9(b) (high thermal inertia). This suggests that the higher thermal inertia in this area is not due to large numbers of rocks of this size or larger. Boulder fields identified in Isidis Planitia have always been associated with areas of crater ejecta (Schroeder and Golombek, 2003; Golombek et al., 2003a), rather than increased thermal inertia from a postulated deposition of material from Libya Montes. However, this does not necessarily rule out the increased thermal inertia in the basin being due to the presence of rocks smaller than are identifiable in MOC images at this resolution (the minimum reliable rock size identifiable in any MOC image would be ~ 3 metres), induration of smaller-grained surface materials, or a combination of the two.

Figures 6.10 and 6.11 show some of the features found in the southern part of Isidis Planitia, in and around the higher thermal inertia areas of the basin. Figure 6.10(a) shows an irregular ridge, possibly an igneous feature (see Chapter 2, Subsection 2.7.2 for further details of possible igneous features within the basin), although its higher irregular appearance perhaps argues against this origin. It could also be a feature generated during the glaciation of the basin, such as an esker or moraine, although it is not very similar in morphology to the features discussed in Chapter 2, Subsection ?? that are interpreted as eskers and moraines. Figure 6.10(b) shows a channel, of which there are several apparent in high-resolution MOC images of this part of the basin. This could be a lava channel, or

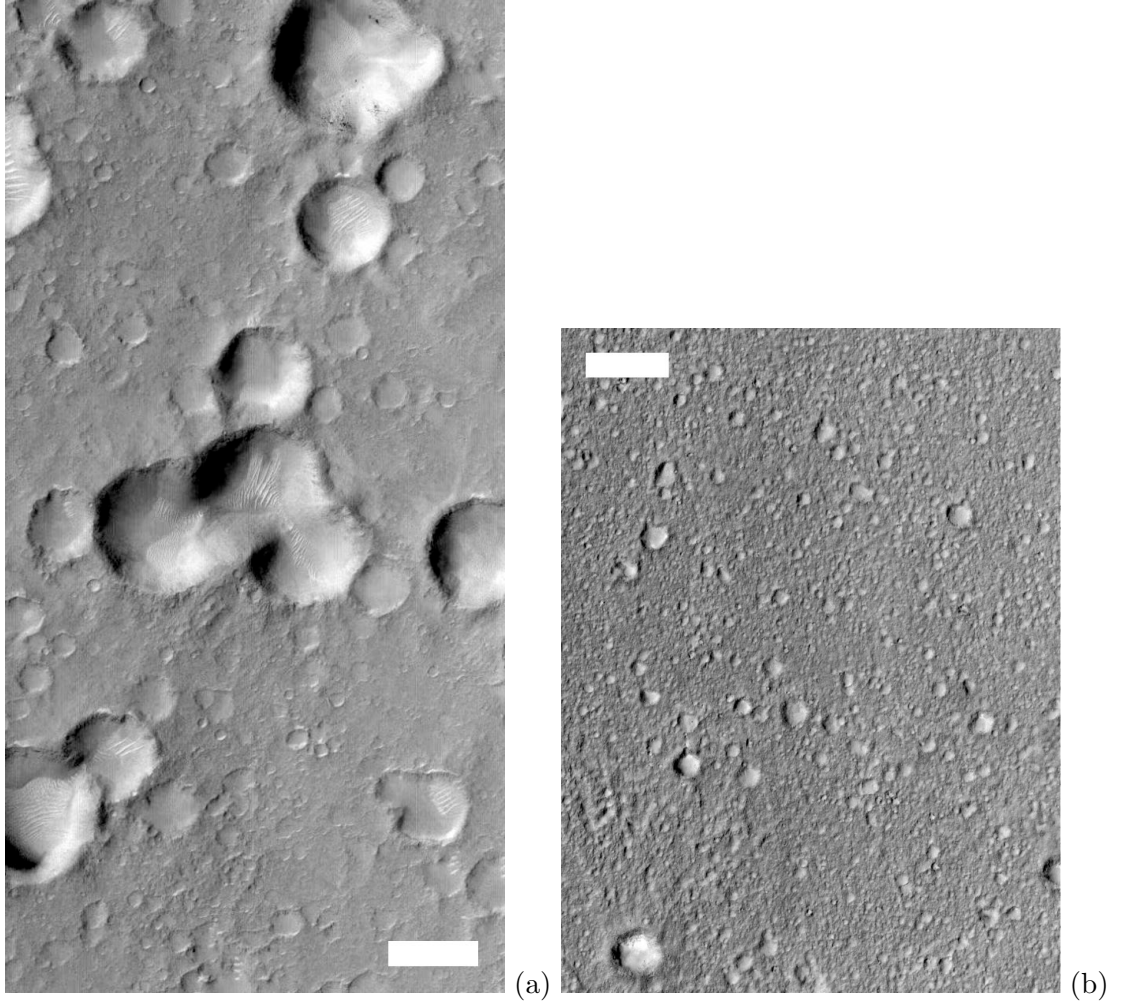


Figure 6.9: High resolution MOC images of southern Isidis Planitia. (a) shows part of MOC image m1800819. Complete image centred at 90.32° E 5.66° N, in the south of the basin, outside the highest thermal inertia area. Image has a pixel size of 4.40 metres per pixel. (b) shows part of MOC image e0402370. Complete image centred at 89.87° E 4.34° N, in the south of the basin, within a high thermal inertia area. Image has a pixel size of 3.53 metres per pixel. Bars in both images are 500 metres.

perhaps more plausibly, a fluvial channel. If the latter, it could have been formed after the subliming of the ice layer in the basin by water from the subsurface reaching the surface via fractures (e.g. Crumpler, 2003).

Figure 6.11(a) shows what appears to be the modification of the surface by aeolian, or possibly fluvial, processes. The streaks originating from the impact craters do not appear to be ejecta, and occur throughout the whole image (just a section is presented here) oriented in the same direction. The most likely formation mechanism is aeolian – wind streaks from the mobilisation of unconsolidated surface material. Larger-scale wind streaks associated with impact craters have been noted in earlier, lower resolution, images of the basin (e.g. Thomas et al., 1981; Greeley et al., 1992). If the features in Figure 6.11(a) are analogous to the larger-scale features then it appears that they comprise both bright depositional streaks, and dark erosional streaks (e.g. Thomas et al., 1981; Greeley et al., 1992). Study of the thermal inertia of the larger-scale wind streaks suggests that both types of streaks are formed from material forming a layer less than 1–3 millimetres thick (Pelkey et al., 2001). However, it is interesting to note that these streaks are parallel to the direction of suggested movement of material from the nearest channel. If it is assumed that the high thermal inertia areas are formed as the result of the movement of material over Isidis Planitia from channels in Libya Montes then an alternative to the aeolian mechanism could be that the streaks result from modification of a flow of debris from such an event ‘protecting’ the area behind the crater and forming a ‘backwash’ pattern. Figure 6.11(b) shows a large number of parallel streaks which I interpret as dunes. Dunes do not appear to be extensive in the southern area of the basin, although more obvious dunes are apparent in several MOC images of larger impact craters in the area, which presumably act as dust traps. Figures 6.9(a) and 6.10(a) (these are from the same parent MOC image) show dunes within dust or sand deposits within craters.

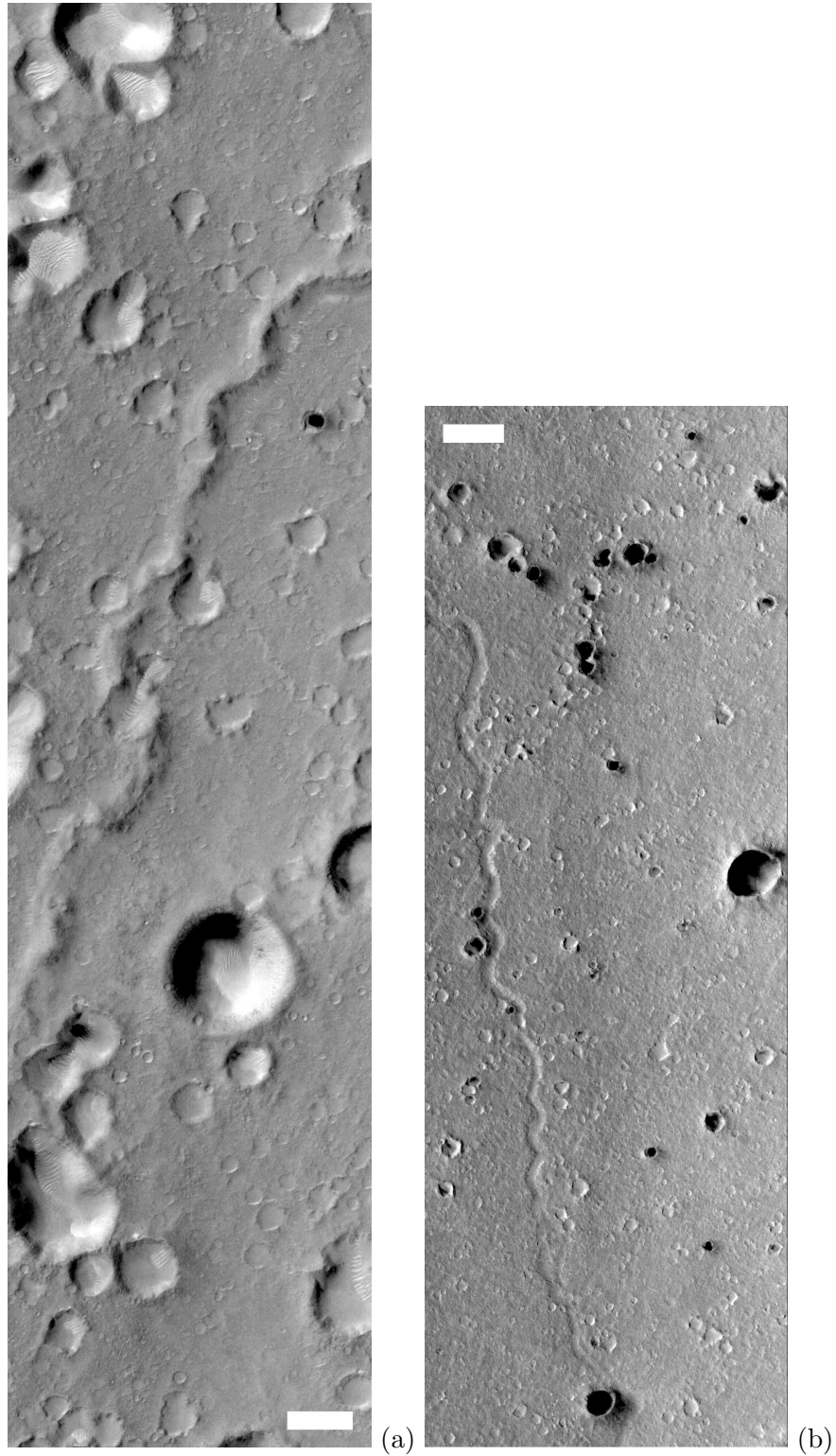


Figure 6.10: High resolution MOC images of southern Isidis Planitia. (a) shows part of MOC image m1800819. Complete image centred at 90.32° E 5.66° N, in the south of the basin. Image has a pixel size of 4.40 metres per pixel. (b) shows part of MOC image e0502100. Complete image centred at 88.28° E 4.48° N, in the south of the basin. Image has a pixel size of 3.52 metres per pixel. Bars in both images are 500 metres.

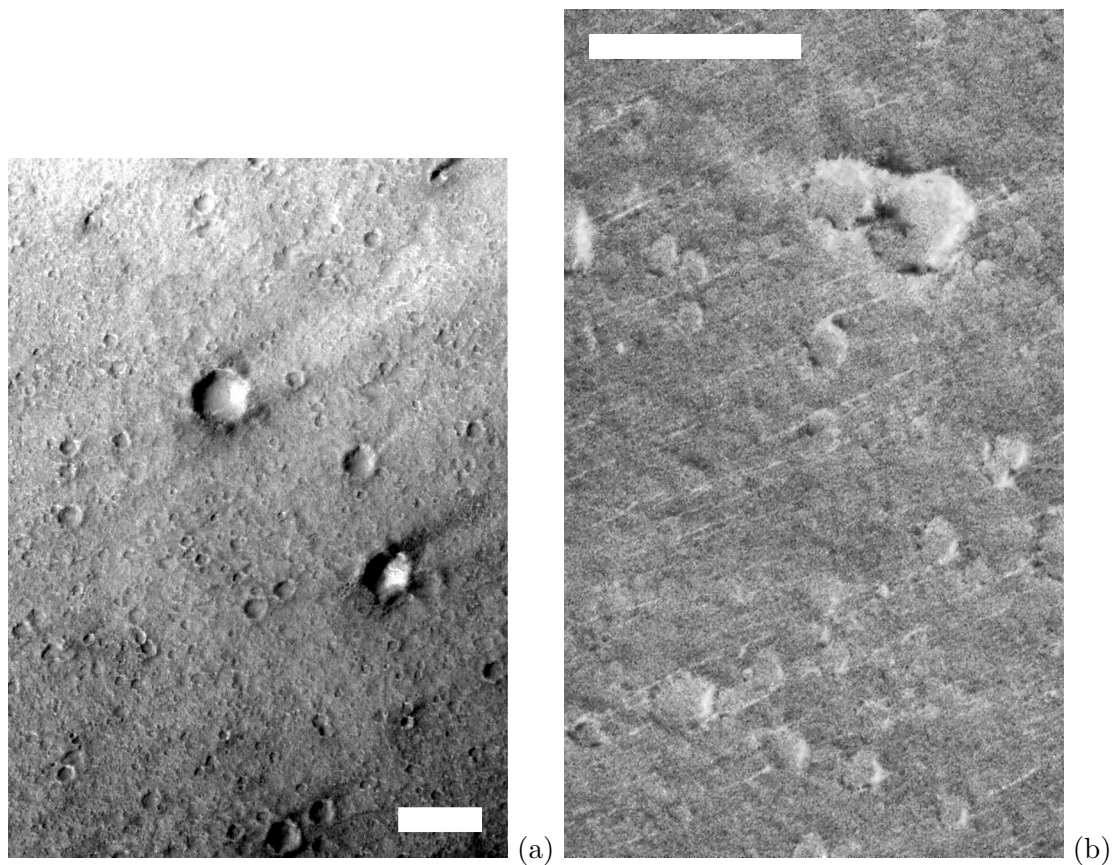


Figure 6.11: High resolution MOC images of southern Isidis Planitia. (a) shows part of MOC image e0100232. Complete image centred at 83.19° E 4.45° N, in the south of the basin. Image has a pixel size of 3.52 metres per pixel. Image has been contrast stretched to highlight information. (b) shows part of MOC image e1402034. Complete image centred at 87.99° E 4.36° N, in the south of the basin. Image has a pixel size of 1.51 metres per pixel. Image has been contrast stretched and despeckled to highlight information and reduce noise. Bars in both images are 500 metres.

Chapter 7

Conclusion

7.1 Summary of conclusions

In Chapter 2 I discussed various possible methods of formation for the numerous sub-kilometre cones, cone chains and sinuous ridges found throughout Isidis Planitia. Without appropriate in-situ data relating to these features, it is difficult to conclusively state which of the proposed hypotheses is the one responsible for cone formation in the basin, or indeed if it is a combination of formation methods, or even a process that has not been considered. However, I believe the most likely mechanisms involved in the formation of the cones and cone chains in the basin are the deposition of material from shrinking glaciers in a process analogous to terrestrial moraine formation, and the formation of pingos and/or mud- or cryovolcanoes most likely driven by the expansion of freezing fronts into areas containing liquid water or brine. The sinuous ridges in the basin are most likely formed in a process analogous to terrestrial eskers.

In Chapter 3 I described the Mars Orbiter Laser Altimeter (MOLA) instrument, its data set, and methods of data processing – chiefly the detrending of the data – which can provide further information on topographic features found in the basin. By detrending the MOLA topography data, features with a very small range of topographic variation can be identified. The methods shown in the chapter have been used in subsequent chapters in the processing of MOLA data to identify and analyse certain types of Isidis Planitia

landform that otherwise would be difficult or impossible to characterise.

In Chapter 4 I used detrended MOLA data to identify the extensive network of ridges found throughout the Isidis Planitia basin. I concluded that their origin was most likely tectonic faulting of the upper martian crust resulting from compressional forces generated by the loading of the Isidis Planitia basin. This process was also responsible for the development of the Isidis Planitia mascon.

In Chapter 5 I investigated the impact cratering record in Isidis Planitia, resulting in the calculation of relative and absolute ages of the basin surface using cratering chronology. I also identified a number of previously unknown circular features exhibiting subdued topography that are likely buried and/or eroded impact craters, to add to those that had already been recorded in the basin by previous researchers. Enough buried impact craters exist to calculate an approximate age for the buried unit in which they formed, which I estimated to be Lower to mid-Hesperian. I also identified evidence that supported the possibility that at least two episodes of sedimentation have occurred within the basin.

In Chapter 6 I analysed thermal and spectroscopic data of Isidis Planitia to attempt to identify the composition, grain size and rock abundance of the basin surface. The conclusion from these results is that the thermal inertia patterns seen in the basin are most likely the result of the deposition of material carried into the basin from Libya Montes. I also looked at some of the surface geomorphology of the basin, and considered aeolian activity in the basin, concluding that the layer of material modified by aeolian action is likely to be very thin.

7.2 Synthesis of ideas

The results of my investigations into the Isidis Planitia basin can be considered as a whole to form a relatively simple set of hypotheses about the basin's history, and why it looks the way it does today. The early history of the basin has not been considered in this thesis. Instead, I have concentrated on events which more directly shape the way the basin surface appears now. Isidis Planitia is an ancient large multiringed impact basin which formed in the Noachian. It is likely that the basin was subsequently infilled by volcanic material,

possibly from Syrtis Major Planum. This flooding by volcanic material may have occurred on more than one occasion, possibly interspersed with flooding by water and subsequent deposition of sedimentary material. Evidence of terracing in some larger crater walls, and the likelihood that a layer of relatively deeply buried volatiles has modified impact crater ejecta morphology (see Chapter 5, Section 5.2) may support a layered subsurface. It is this volcanic layer that formed the target for the impact craters that are now buried beneath sediment (see Chapter 5, Section 5.4) and which show only extremely subdued topography. It is also this layer that has been significantly tectonically altered, forming wrinkle ridges on its surface by compressional tectonism (see Chapter 4). Unlike many other such features on Mars, these are not controlled by Tharsis tectonism, and appear to have formed a pattern of ridges produced by concentric thrusts surrounded by ridges produced by radial thrusts. I believe that this loading and deformation took place in the Lower Hesperian as a result of infilling of the basin by volcanic material from Syrtis Major Planum, as described above.

This surface – cratered by impacts and wrinkled by tectonic loading – was then buried by a layer of sediments during the middle- to Upper Hesperian. This was deposited by water flooding into the basin, carrying a large suspended load of material, redistributing unconsolidated material already present within the basin, and probably eroding preexisting features to further increase its sediment load. At some stage extensive flooding was required in order to fill with sediment impact craters near the topographically high contact with Utopia Planitia. This event would have completely filled the basin with water and as turbulence within the water subsided finer suspended sediments were deposited and formed a layer several hundred metres thick across the basin (see Chapter 5, Subsection 5.4.3). This flooding may have taken place episodically – building up layers of sediments – or may have occurred in a single catastrophic event. Given the evidence from the small number of partially-buried stealth craters found in the high thermal inertia area in the south east of the basin (see Chapter 5, Section 5.4), it seems likely that there have been multiple sedimentation events within the basin. It appears that the most recent event deposited only a few tens of metres of sediment, and is unlikely to have been responsible for the sedimentation of the whole basin to depths of hundreds of metres. The thermal inertia evidence (see Chapter 6, Section 6.2) suggests that coarser sediment from the most recent event was quickly deposited nearer to the mouth of the valleys emptying into the basin

from Libya Montes as the turbulence of water decreased on entering the Isidis Planitia basin, but it is uncertain where previous flooding events originated. The sediment from the extensive basin-wide flooding event or events preferentially accumulated in impact craters, completely obscuring those smaller than a few kilometres across, and substantially filling those with larger diameters. Erosion by the water and its load of sediments may also have further subdued the topography of these larger craters by modifying their rims and ejecta. The ponded water in the basin would then have frozen over a timescale of probably hundreds to tens of thousands of years (Kreslavsky and Head, 2002).

The basin's ice cover would have been static, rather than mobile as in the case of glacial ice, and would therefore have had a limited erosional effect on the surface it covered. This explains the apparent absence of drumlins, which are depositional features and would be deprived of source material. The sinuous ridges in Isidis Planitia are interpreted as eskers – rivers of liquid water flowing beneath the ice which deposited suspended material to form ridges of sediment. Eventually, over a period of perhaps hundreds of thousands of years, the ice in the basin sublimed away. As this occurred, the ice fragmented, being preferentially concentrated in lower topography areas of the basin where the ice was thicker to start with. Ice retreat left behind features analogous to terrestrial terminal moraines – sedimentary material deposited at the edges of shrinking glaciers. This formed the features now identified as ‘cone chains’ in Isidis Planitia. The pits within these chains formed by the presence of ice amid the sedimentary debris. The ice sublimed, with resulting rim collapse in some instances. Expanding freezing fronts pressurised any remaining liquid water trapped in the subsurface. This water may have been rich in dissolved salts resulting from the concentration of salts in the lower regions of the ocean as freezing proceeded from the surface. It was also protected from sublimation by overlying layers of sediment, and even if still present today would be too deep for identification with instruments currently used for the detection of subsurface water. Eventually, overpressuring of this liquid water or brine layer results in the formation of pingos and/or sediment-rich mud- or cryovolcanoes. The subliming of ice cores within pingos resulted in the cones with summit pits seen in the basin today. The concentration and depth of ice in the topographically lower areas of the basin may be the cause of the differences in surface features between the western and eastern central areas of the basin (the cones and cone chains are more pronounced and more common in the topographically lower western central areas), and could explain the

relative lack of such features around the basin rim.

After the removal of the ice in the basin, there may have been further volcanic activity in Syrtis Major Planum, although this is far from conclusive as no evidence remains of lava flows within the basin itself. However, one plausible explanation for the chaotic terrain found at parts of the contact between Syrtis Major Planum and Isidis Planitia is volcanic material flowing over a volatile rich substrate, such as water-bearing near-surface layers of sedimentary material. The features within the basin were then modified by processes such as mass-wasting and erosion/deposition by aeolian activity forming dune deposits and similar features. The presence of dunes and wind streaks in the basin implies a covering of material deposited and modified by aeolian action, although this layer is likely to be relatively thin over most of the basin. This is also supported by the evidence that the thermal inertia variation within the basin is not obscured by low thermal inertia fine material, which would be the case if there were more than several centimetres of this fine material deposited by aeolian action, although dune formation would tend to suggest that thicker layers of material fine enough to be moved by martian winds exist.

7.3 Future research

There is plenty of opportunity for further research based upon the work in this thesis, in order to develop or further support the models presented. Even without the benefit of new data, further scientific progress could be made. With extra resources, further work could be carried out on several aspects of this research. The ever-increasing coverage of the basin by Mars Orbiter Camera (MOC), and both infrared and visible wavelength Thermal Emission Imaging System (THEMIS) images will provide more images of features such as cones and sinuous ridges. Coverage by the ~ 100 metre per pixel infrared THEMIS images is approaching the stage where they could be usefully used to map a large proportion of the basin for cones and sinuous ridges, as shown on a more limited scale in Chapter 2, Section 2.5.2. However, there is a wealth of new remotely sensed data being returned from current missions, and many exciting future orbiter missions are planned. Mars Global Surveyor (MGS) continues to exceed expectations with its greatly extended mission life. MOC images are still being returned, including images of the Mars Exploration Rover

(MER) operating sites during January 2005. Amongst the other major MGS instruments, and those also used in this thesis, Thermal Emission Spectrometer (TES) data are being returned more intermittently, and MOLA is restricted to operating as a passive radiometer after 2001, but is still returning scientifically useful data.

Since the start of my PhD research, two new orbiters have successfully returned remotely sensed data of the martian surface (and continue to do so) – Mars Odyssey (MO) and Mars Express (MEX). Data and results from MO have been extensively used in the research presented in this thesis, and the coverage of available data is constantly increasing. However, MEX only achieved a mapping orbit in early 2004, and so data from this mission has not been used in my research. The instruments aboard MEX will provide a very useful additional source of information about the martian surface which will help with future research into Isidis Planitia. Beagle 2 was sadly lost, but two landed missions were successful in 2004 – the MER landers in Terra Meridiani and Gusev Crater, which continue to provide a wealth of data, much of which may have implications for the study of Isidis Planitia when fully assessed. Further missions to Mars in the near future will again expand our knowledge of the planet, and I am sure answer some questions and most likely pose some new ones. Mars Reconnaissance Orbiter (MRO) will be launched in 2005, and should start returning data in mid-to-late 2007. Later missions should include the 2007 launch of Phoenix – a lander to study high latitudes, and the 2009 launch of the Mars Science Laboratory rover.

The research contained within this thesis is very much work in progress, with new data, models and analyses refining or replacing the old. Several lines of enquiry using current and future data would be of particular help in refining and developing the models herein. The morphological analysis of features such as the cones will be usefully aided by the High Resolution Stereoscopic Camera (HRSC) on MEX, and the High Resolution Imaging Science Experiment (HiRISE) instrument on MRO. Although MOC on MGS has a stereoscopic capability, a relatively limited number of stereo images were obtained. Both HiRISE and, particularly, HRSC have stereoscopic capability, and the availability of high-resolution stereoscopic images of Isidis Planitia will bring a great improvement to our understanding of many of the basin's features. After interpolation (see Chapter 3, Section 3.4) MOLA topography maps used in this thesis have a maximum pixel size of

1/128th degree (~ 0.5 km), whereas HRSC stereo images, although lacking the global coverage of MOLA, will have a pixel size of 10 metres. This will make it easier to determine the origin of features by analysing the background topography, to see, for example, the influence on local topography on the direction of flow of a channel. It may also be possible to identify characteristics about the former ice cover by analysing sinuous ridges and the topography of the terrain they lie upon. Eskers, which are the best terrestrial analogue to the sinuous ridges, may give an indication of the surface slope of the glacier under which they formed as they respond to the equipotential surface (Bennett and Glasser, 1996; Head and Hallet, 2001a). HiRISE will obtain images with a pixel size as small as 1 metre. This is a higher resolution than MOC, and will no doubt be valuable in analysing the morphology of many of the features described in this thesis.

Higher resolution global spectroscopic data will, at a relatively simple level, allow more accurate investigation of features such as the high thermal inertia areas at the basin rim (see Chapter 6, Section 6.2) and the cones, cone chains and sinuous ridges found within the basin (see Chapter 2). There is also the expectation of being able to derive much more accurate maps of mineralogical composition, with the hope that the influence of water will be more easily detectable. Higher data resolution will also enable the identification of any smaller-scale features, such as the cones and sinuous ridges, that may have interacted with water, and to identify any other small areas with hydrological potential, such as springs. To some extent this is already being realised with the development of models for using THEMIS data to determine thermal inertia (e.g. Fergason and Christensen, 2003; Putzig et al., 2004), with a resulting improvement in pixel size from TES with 3 km per pixel to 0.1 km per pixel in the THEMIS images. The Visible and Infrared Mineralogical Mapping Spectrometer, or OMEGA, aboard MEX, and the Compact Reconnaissance Imaging Spectrometer for Mars (CRISM) on MRO, will also provide comparable or higher resolutions. Although the MER landers are not operating in Isidis Planitia, nor in similar terrain, the geological and mineralogical results from these missions may be important in providing an in-situ reference for data retrieved from orbital instruments such as TES and THEMIS, and to investigate features that may be analogous to those found in Isidis Planitia itself.

The Gamma Ray Spectrometer (GRS) on MO has provided data that enables a map of global water content of the upper metre of the martian subsurface to be produced. MEX

AND MRO carry instruments which use different techniques to penetrate further into the surface to identify deeper concentrations of water and geologic structure. The Mars Advanced Radar for Subsurface and Ionosphere Sounding (MARSIS) instrument on MEX will be able to penetrate a few kilometers into the subsurface, and the Shallow Radar on MRO approximately a kilometre. These data will provide a first qualitative look into the deeper subsurface, and will penetrate deeply enough into the Isidis Planitia subsurface to image the entire sedimentary surface layer, quantify its depth, and determine whether its depth varies with location in the basin. Deeper layers will also be resolved, and the buried volcanic unit containing the wrinkle ridges and buried craters can be analysed, along with the structure of deeper volcanic or sedimentary layers. The subsurface structure of the wrinkle ridges may also be identifiable, confirming their nature, and enabling more complex and accurate models of their formation to be developed.

The Mars Radio Science Experiment (MaRS) on MEX, and the Gravity Field Investigation Package on MRO, will be used to determine the gravitational field of Mars, and refine the gravity model of the planet used in Chapter 4 to analyse the Isidis Planitia mascon and model its tectonic effects on surface layers.

7.4 Final thoughts

In this thesis I have presented some ideas and models for the origin and development of many of the surface and near-surface features that are characteristic of the Isidis Planitia basin as it is seen today. Investigation of the Isidis Planitia basin, and its relationship to neighboring regions of Mars, is important in understanding the dynamic evolution of this part of Mars, with implications that may stretch across the planet. With the loss of the Beagle 2 lander, and the rejection at the last hurdle of the candidate MER landing site, Isidis Planitia remains unexplored by a landed probe, a situation which, considering its wealth of scientific interest, I can not imagine being the case for long.

Appendix A

Location of images

Tables A.1 and A.2, and Figures A.1 and A.2 show the geographical location of the images used in this thesis. Images from outside Isidis Planitia are listed in the table, but their locations are not plotted on a map. Data from global data sets are not plotted (e.g. topography, gravity, spectroscopy), and these are generally shown annotated with geographical information within the thesis. However Viking Orbiter Camera mosaics are listed and plotted where appropriate.

Headings: Figure = Thesis figure number. Instr. = Instrument name. Type = Image type. Image No. = Image reference number. Pix. Size = Image pixel size*. Ref. = Reference letter for appropriate map – a capital letter denotes the location of more than one image. Images from outside Isidis Planitia do not have a reference letter.

Instrument names: VOC = Viking Orbiter Camera. MOC = Mars Orbiter Camera. THEMIS = Thermal Emission Imaging System. Apollo 17 = Apollo 17 Service Module Metric Camera.

Image types: MDIM 2 = Mars Digital Image Mosaic 2. NA = Narrow Angle. Day IR = Daytime Infrared. Visible = Daytime Visible. Night IR = Nighttime Infrared.

* Note that all image pixel sizes are given as the horizontal width of the pixel as in some cases the instruments have a slightly non-square aspect ratio.

A.1 Images from Chapter 2

Figure	Instr.	Type	Image No.	Pix. Size	Ref.
2.1	VOC	MDIM 2	-	231 m	a
2.2(a),(b)	MOC	NA	ab103405	2.95 m	B
2.3	THEMIS	Day IR	I01832002	100 m	c
2.4	THEMIS	Visible	V01807007	18 m	d
2.6	THEMIS	Visible	V06251019	18 m	e
2.7(a),(b)	see 2.2(a)				B
2.8(a),(b)	see 2.2(a)				B
2.9(a)	MOC	NA	m0302859	1.46 m	F
2.9(b)	MOC	NA	m0901055	2.94 m	g
2.10(a)	THEMIS	Day IR	I01807006	101 m	B
2.10(b)	THEMIS	Night IR	I06732011	99 m	B
2.11(a)	THEMIS	Day IR	I01782005	101 m	h
2.11(b)	see 2.11(a)				i
2.12	see 2.3, 2.10(a)				j
2.13	see 2.3, 2.10(a)				k
2.14	see 2.3, 2.10(a)				l
2.15(a)	THEMIS	Day IR	I05215009	101 m	M
2.15(b)	THEMIS	Night IR	I06757009	99 m	M
2.16(a)	THEMIS	Visible	V05215010	73 m	M
2.16(b)	MOC	NA	fha00994	1.49 m	M
2.18	see 2.2(a)				B
2.19(a)	see 2.9(a)				F
2.19(b),(c)	MOC	NA	e1004377	3.05 m	N
2.19(d)	MOC	NA	e0501865	7.31 m	o
2.20(a)	MOC	NA	m0203053	2.91 m	p
2.20(b)	see 2.19(d)				N
2.21	MOC	NA	m0303958	3.00 m	-

Table A.1: List of images used in figures from Chapter 2

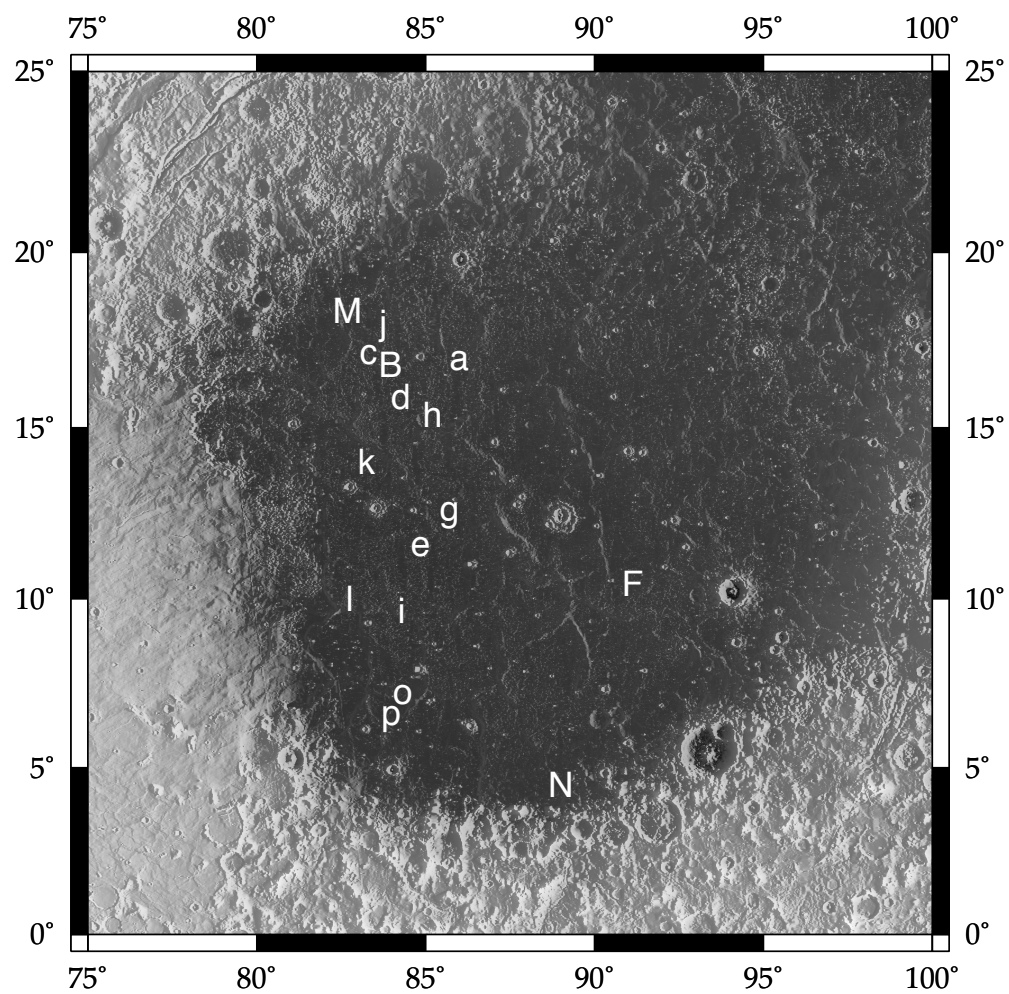


Figure A.1: Images from Chapter 2.

A.2 Images from Chapters 4, 5 and 6

Figure	Instr.	Type	Image No.	Pix. Size	Ref.
4.2(a)	VOC	MDIM 2	-	231 m	a
4.9	VOC	MDIM 2	-	231 m	-
4.14	Apollo 17	-	AS17-602	~20 m	-
5.1(a)	THEMIS	Visible	V09334009	18 m	b
5.1(b)	THEMIS	Visible	V01832003	18 m	C
	THEMIS	Visible	V06301020	18 m	C
5.4	THEMIS	Visible	V09933014	18 m	d
5.6	VOC		043A04	~71 m	-
5.18(a),(b)	THEMIS	Day IR	I01782005	101 m	E
5.19(a)	see 5.18(a)				E
5.20(a)	THEMIS	Day IR	I09808025	100 m	F
5.20(b)	THEMIS	Night IR	I02013005	100 m	F
5.20(c)	see 5.20(a)				g
5.21	MOC	NA	m2101624	2.92 m	h
6.7(a)	THEMIS	Visible	V01994007	18 m	i
6.7(b)	THEMIS	Visible	V02119007	18 m	j
6.8(a)	THEMIS	Visible	V01657007	18 m	k
6.8(b)	THEMIS	Visible	V03904003	18 m	l
6.9(a)	MOC	NA	m1800819	4.36 m	M
6.9(b)	MOC	NA	e0402370	2.93 m	n
6.10(a)	see 6.9(a)				M
6.10(b)	MOC	NA	e0502100	2.91 m	o

Table A.2: List of images used in figures in Chapters 4, 5 and 6.

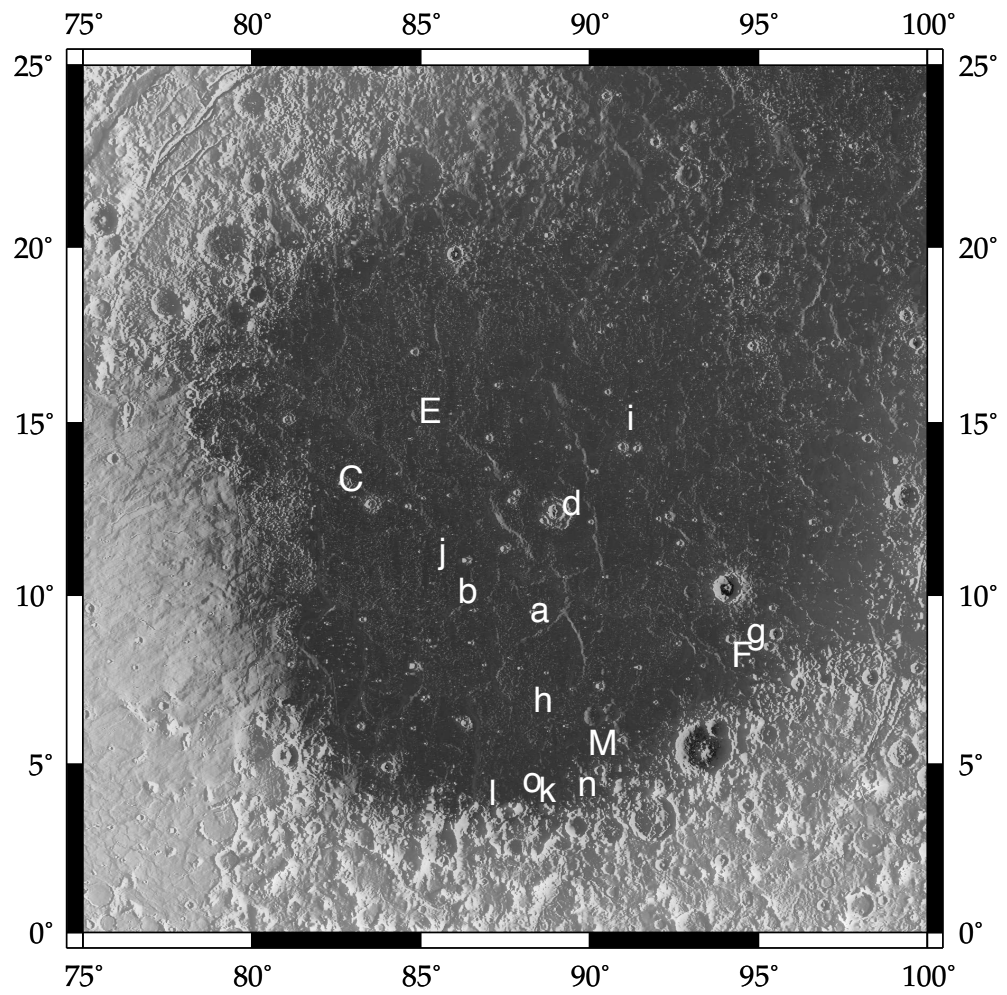


Figure A.2: Images from Chapters 4, 5 and 6.

Appendix B

Georectification of THEMIS data

The georectification of Thermal Emission Imaging System (THEMIS) infrared data and their superposition upon Mars Orbiter Laser Altimeter (MOLA) topographic data in order to undertake the comparison of cone chain orientation with underlying topography described in Chapter 2 was carried out using the powerful open source geographic information systems (GIS) package **GRASS** (Neteler and Mitasova, 2002). A pre-prepared interpolated MOLA topography map projected as a simple cylinder of the appropriate area of the basin was imported into **GRASS** and georectified. The latter is a simple process given the simple cylindrical projection of the MOLA data, combined with knowledge of the geographical extent of the MOLA data from the **GMT** script used to produce it. The georectified topography map produced therefore simply swaps pixel references for geographical references. The MOLA topography maps generated using the techniques outlined in Chapter 3 have a maximum resolution of 128 pixels per degree (approximately 460 metres per pixel), whereas the THEMIS infrared data has a resolution of approximately 100 metres per pixel. No further interpolation of the raw MOLA data to improve its resolution was realistically possible, therefore both data sets were combined at a resolution of 500 pixels per degree (approximately 120 metres per pixel) in order to ease the subsequent layering of the data sets while retaining detail in the THEMIS images.

Once the topographic data had been georectified, the THEMIS images were imported into **GRASS**. These were then georectified on to the topographic data by locating common ground control points (GCPs) in both images. This was problematic as the mismatch

in resolutions between the THEMIS and MOLA data sets, coupled with the interpolated nature of the latter producing a map that is not accurate to a pixel level, made finding the required minimum number of common GCPs – even for generating a first order transformation matrix – difficult. However, enough common points were found in the THEMIS images used to carry out the georectification, and the resulting RMS error from the predicted position calculated by the georectification transformation equation was significantly less than one pixel for all the images georectified. After the georectification process the THEMIS images could be overlaid upon the topographic map in GRASS or exported as image files and layered together using standard graphics software.

The latter route was chosen for files to be used in the analysis of the cone chains in Isidis Planitia. Subtle variation of topography over large areas is difficult to see in the THEMIS images, particularly in an area as flat as the Isidis basin, where features such as the wrinkle ridges (see Chapter 4) and buried craters (see Chapter 5) show only a few tens of metres of topography over tens of kilometers of the basin surface, although these features can be made more visible by the topographic detrending techniques discussed in Chapter 3. However, these topographical variations in a basin as flat as Isidis Planitia are significant, and it is important to assess any correlation between these features and the cones and cone chains. The best way to do this is to superimpose the cones and cone chains upon interpolated MOLA topography maps using the georectification techniques discussed earlier.

However, the THEMIS images contain too much detail to be easily combined with topography data, and in order to make this procedure work the data in the THEMIS images must be reduced from 8-bit to 1-bit – i.e. from a 256 greyscale detailed image of the surface to a black and white image showing solely the location and extent of the cones and cone chains. This was achieved by importing the original THEMIS infrared daytime images into a graphics package and performing several stages of image processing. Firstly, a standard edge-detection filter was used to pick out the edges of features in the basin. The Isidis Planitia basin is very smooth, and relatively lightly cratered at a resolution of approximately 100 metres per pixel, and so the majority of features identified within the basin in the images using this technique are cones or cone chains. The images were then colour-inverted in order to provide black cones on a white field. A standard blur filter was

then used to turn the detected edges into areas that more fully represented the features in their entirety. A threshold filter was then applied in order to remove the smaller non-black ‘noise’ elements in the images. The images were then edited by hand to remove non-cone and cone-chain features. This resulted in large areas of some images being blank due to the removal of large impact craters, their ejecta fields, and their fields of secondary impact craters. The resulting images were then imported into **GRASS**, georectified using the previously calculated transformation matrices for the unedited THEMIS images, exported as image files into a graphics package and then layered with the topography map.

Appendix C

MOLA PEDR volumes used

Volume	Date Posted	Orbits	Acquisition Dates	PEDR Version
MGSL_2010	17/7/00	1578-1690, 10012-10192	28/2/99-23/3/99	I
MGSL_2011	17/7/00	10183-10708	24/3/99-5/5/99	I
MGSL_2012	17/7/00	10709-10941	6/5/99-24/5/99	I
MGSL_2013	17/7/00	10942-11026	25/5/99-31/5/99	I
MGSL_2014	17/7/00	11027-11259	1/6/99-19/6/99	I
MGSL_2015	17/7/00	11260-11491	20/6/99-8/7/99	I
MGSL_2016	17/7/00	11492-11724	9/7/99-27/7/99	I
MGSL_2017	17/7/00	11725-11957	28/7/99-15/8/99	I
MGSL_2018	17/7/00	11958-12140	16/8/99-30/8/99	I
MGSL_2019	17/7/00	12141-12373	1/9/99-18/9/99	I
MGSL_2020	17/7/00	12374-12618	19/9/00-8/10/99	I
MGSL_2021	17/7/00	12619-12862	9/10/99-28/10/99	I
MGSL_2022	17/7/00	12863-13107	29/10/99-17/11/99	I
MGSL_2023	17/7/00	13108-13266	18/11/99-29/11/99	I

Table C.1: MOLA PEDR Primary Mission volumes used,
part 1.

Volume	Date Posted	Orbits	Acquisition Dates	PEDR Version
MGSL_2024	4/10/00	13267-13487	30/11/99-17/12/99	I
MGSL_2025	4/10/00	13488-13707	18/12/99-5/1/00	I
MGSL_2026	4/10/00	13708-13927	6/1/00-23/1/00	I
MGSL_2027	4/10/00	13928-14148	24/1/00-10/2/00	I
MGSL_2028	4/10/00	14149-14392	11/2/00-1/3/00	I
MGSL_2029	4/10/00	14393-14662	2/3/00-23/3/00	I
MGSL_2030	4/10/00	14663-14894	24/3/00-11/4/00	I
MGSL_2031	4/10/00	14895-15127	12/4/00-30/4/00	I
MGSL_2032	16/11/00	15128-15323	1/5/00-16/5/00	I
MGSL_2033	16/11/00	15324-15507	17/5/00-1/6/00	I

Table C.2: MOLA PEDR Primary Mission volumes used,
part 2.

Volume	Date Posted	Orbits	Acquisition Dates	PEDR Version
MGSL_2034	3/5/01	16259-16449	1/8/00-16/8/00	J
MGSL_2035	3/5/01	16450-16644	17/8/00-1/9/00	J
MGSL_2036	3/5/01	16645-16840	2/9/00-17/9/00	J
MGSL_2037	3/5/01	16841-17036	18/9/00-3/10/00	J
MGSL_2038	3/5/01	17037-17232	4/10/00-19/10/00	J
MGSL_2039	3/5/01	17233-17428	20/10/00-4/11/00	J
MGSL_2040	3/5/01	17429-17623	5/11/00-20/11/00	J
MGSL_2041	3/5/01	17624-17819	21/11/00-6/12/00	J
MGSL_2042	3/5/01	17820-18015	7/12/00-22/12/00	J
MGSL_2043	3/5/01	18016-18211	23/12/00-7/1/01	J
MGSL_2044	3/5/01	18212-18406	8/1/01-23/1/01	J
MGSL_2045	3/5/01	18407-18602	24/1/01-8/2/01	J
MGSL_2046	16/8/01	18603-18786	8/2/01-23/2/01	J
MGSL_2047	16/8/01	18787-18981	24/2/01-11/3/01	J
MGSL_2048	16/8/01	18982-19165	12/3/01-26/3/01	J
MGSL_2049	16/8/01	19166-19360	27/3/01-11/4/01	J
MGSL_2050	16/8/01	19361-19544	12/4/01-26/4/01	J
MGSL_2051	16/8/01	19545-19825	27/4/01-19/5/01	J
MGSL_2052	16/8/01	19826-20008	20/5/01-3/6/01	J
MGSL_2053	16/8/01	20009-20192	4/6/01-18/6/01	J
MGSL_2054	16/8/01	20193-20327	19/6/01-30/6/01	J

Table C.3: MOLA PEDR Extended Mission volumes used.

References

- Abramov, O. and McEwan, A. (2004). An evaluation of interpolation methods for Mars Orbiter Laser Altimeter (MOLA) data. *Int. J. Remote Sens.*, 25(3):669–676.
- Abshire, J. B., Sun, X., and Afzal, R. S. (2000). Mars Orbiter Laser Altimeter: receiver model and performance analysis. *Appl. Opt.*, 39:2440–2460.
- Afzal, R. S. (1994). Mars Orbiter Laser Altimeter: Laser transmitter. *Appl. Optics*, 33:3184–3188.
- Albin, E. F. and King, J. D. (2002). Exhumation of intrusive igneous complexes on the margins of martian impact basins. *Lunar Planet. Sci. XXXIII*, (1747).
- Anderson, E. M. (1951). *The dynamics of faulting*. Oliver and Boyd, 206 pp.
- Anderson, F. S. and Parker, T. J. (2002). Characterization of MER landing sites using MOC and MOLA. *Lunar Planet. Sci. XXXIII*, (2028).
- Arvidson, R., Guinness, E., and Slavney, S. (1999). Mars Global Surveyor project archive generation, validation and transfer plan. Technical report, Planetary Data System.
- Bandfield, J. L. (2002). Global mineral distributions on Mars. *J. Geophys. Res.*, 107(E6).
- Bandfield, J. L. (2003). Martian global surface mineralogy from the Thermal Emission Spectrometer: Surface emissivity, mineral map, and spectral endmember data products. In *6th Int. Conf. Mars*, number 3052.
- Bandfield, J. L., Hamilton, V. E., and Christensen, P. R. (2000). A global view of martian surface compositions. *Science*, 287:1626–1630.
- Banerdt, W. B. and Golombek, M. P. (1992). Stress and tectonics on Mars. In Kieffer,

- H. H., Jakosky, B. M., Snyder, C. W., and Matthews, M. S., editors, *Mars*, chapter 8, pages 249–297. The University of Arizona Press.
- Banerdt, W. B. and Golombek, M. P. (2000). Tectonics of the Tharsis region of Mars: Insights from MGS topography and gravity. *Lunar. Planet. Sci. XXXI*, (2038).
- Banin, A., Clark, B. C., and Wänke, H. (1992). Surface chemistry and mineralogy. In Kieffer, H. H., Jakosky, B. M., Snyder, C. W., and Matthews, M. S., editors, *Mars*, chapter 18, pages 626–651. The University of Arizona Press.
- Barlow, N. G., Boyce, J. M., Costard, F. M., Craddock, R. A., Garvin, J. B., Sakimoto, S. E. H., Kuzmin, R. O., Roddy, D. J., and Soderblom, L. A. (2000). Standardizing the nomenclature of martian impact crater ejecta morphologies. *J. Geophys. Res.*, 105(E11):26,733–26,738.
- Barlow, N. G. and Bradley, T. L. (1990). Martian impact craters – correlations of ejecta and interior morphologies with diameter, latitude, and terrain. *Icarus*, 87:156–179.
- Barlow, N. G., Koroshetz, J., and Dohm, J. M. (2001). Variations in the onset diameter for martian layered ejecta morphologies and their implications for subsurface volatile reservoirs. *Geophys. Res. Lett.*, 28(16):3,095–3,098.
- Barlow, N. G. and Perez, C. B. (2003). Martian impact crater ejecta morphologies as indicators of the distribution of subsurface volatiles. *J. Geophys. Res.*, 108(E8).
- Barnouin-Jha, O. S. and Schultz, P. H. (1998). Lobateness of impact ejecta deposits from atmospheric interactions. *J. Geophys. Res.*, 103(E11):25,739–25,756.
- Bennett, M. R. and Glasser, N. F. (1996). *Glacial Geology – Ice Sheets and Landforms*. John Wiley and Sons, 376 pp.
- Bishop, J. L., Pieters, C. M., Dyar, M. D., Hamilton, V. E., and Harloff, J. (2002). A spectral, chemical and mineralogical study of Mars analogue rocks. *Lunar Planet. Sci. XXXIII*, (1168).
- Bodnar, R. J. (2001). PTX phase equilibria in the H_2O - CO_2 -salt system at Mars near-surface conditions. *Lunar Planet. Sci. XXXII*, (1689).

- Boyce, J. M., Mouginis-Mark, P. J., and Garbeil, H. (2003a). Evidence for a thick, discontinuous mantle of volatile-rich materials in the northern high-latitudes of Mars based on crater depth/diameter measurements. In *6th Int. Conf. Mars*, number 3193.
- Boyce, J. M., Mouginis-Mark, P. J., and Garbeil, H. (2003b). Use of the IMPACT program for measurement of the depth to diameter relationships of craters in the high latitudes (70°-80°) of Mars: Implications for geologic history of those areas. In *Mars Crater Cons. Work. VI*, number 0603.
- Boyce, J. M. and Roddy, D. J. (1997). Martian crater ejecta, emplacement and implications for water in the subsurface. *Lunar Planet. Sci. XXVIII*, (1460).
- Boynton, W. V., Feldman, W. V., Squyres, S. W., Prettyman, T. H., Brückner, J., Evans, L. G., Reedy, R. C., Starr, R., Arnold, J. R., Drake, D. M., Englert, P. A. J., Metzger, A. E., Mitrofanov, I., Trombka, J. I., d'Uston, C., Wänke, H., Gasnault, O., Hamara, D. K., Janes, D. M., and Marcialis, R. L. (2002). Distribution of hydrogen in the near surface of Mars: Evidence for subsurface ice deposits. *Science*, 297:81.
- Bradak, B. and Kereszturi, A. (2003). Mud volcanism as model for various planetary surface processes. *Lunar Planet. Sci. XXXIV*, (1304).
- Bridges, J. C., Seabrook, A. M., Kim, J. R., Muller, J.-P., Rothery, D. A., Pillinger, C. T., Sims, M. R., Wright, I. P., Grady, M. M., Mitchell, K. L., and Morley, J. G. (2001). The Beagle 2 landing site in Isidis Planitia. *Lunar Planet. Sci. XXXII*, (1652).
- Bridges, J. C., Seabrook, A. M., Rothery, D. A., Kim, J. R., Pillinger, C. T., Sims, M. R., Golombek, M. P., Duxbury, T., Head, J. W., Haldemann, A. F. C., Mitchell, K. L., Muller, J.-P., Lewis, S. R., Moncrieff, C., Wright, I. P., Grady, M. M., and Morley, J. G. (2003a). Selection of the landing site in Isidis Planitia of Mars probe Beagle 2. *J. Geophys. Res.*, 108(E1).
- Bridges, J. C., Seabrook, A. M., Rothery, D. A., Pillinger, C. T., Sims, M. R., and Wright, I. P. (2003b). Revised target co-ordinates for the Beagle 2 lander. *Lunar Planet. Sci. XXXIV*, (1606).
- Bruno, B. C., Fagents, S. A., Thordarson, T., Baloga, S. M., and Pilger, E. (2004). Clustering within rootless cone groups on Iceland and Mars: Effect of nonrandom processes. *J. Geophys. Res.*, 109(E07009).

- Buczkowski, D. L. and Cooke, M. L. (2004). Formation of double-ring circular grabens due to volumetric compaction over buried impact craters: Implications for thickness and nature of cover material in Utopia Planitia, Mars. *J. Geophys. Res.*, 109(E02006).
- Buczkowski, D. L., Cooke, M. L., and McGill, G. E. (2003). Double-ringed circular grabens and thickness of cover material in Utopia Planitia, Mars. *Lunar Planet. Sci. XXXIV*, (1042).
- Buczkowski, D. L. and McGill, G. E. (2003). Utopia Planitia: Observations and models favoring thick water-deposited sediments. In *6th Int. Conf. Mars*, number 3031.
- Cabrol, N. A., Grin, E. A., and Pollard, W. H. (1997). Perennial frost mounds in Gusev crater (Mars). *Lunar. Planet. Sci. XXVIII*, (1027).
- Carr, M. H. (1981). *The Surface of Mars*. Yale University Press, 232 pp.
- Carr, M. H. (1996). *Water on Mars*. Oxford University Press, 229 pp.
- Carr, M. H., Crumpler, L. S., Cutts, J. A., Greeley, R., Guest, J. E., and Masursky, H. (1977). Martian impact craters and emplacement of ejecta by surface flow. *J. Geophys. Res.*, 82:4,055–4,065.
- Carr, M. H. and Head, J. W. (2003). Oceans on Mars: An assessment of the observational evidence and possible fate. *J. Geophys. Res.*, 108(E5).
- Chicarro, A., Schultz, P. H., and Masson, P. (1985). Global and regional ridge patterns on Mars. *Icarus*, 63:153–174.
- Christensen, P. R. (1986). The spatial distribution of rocks on Mars. *Icarus*, 68:217–238.
- Christensen, P. R., Anderson, D. L., Chase, S. C., Clark, R. N., Kieffer, H. H., Malin, M. C., Pearl, J. C., Carpenter, J., Bandiera, N., Brown, F. G., and Silverman, S. (1992). Thermal Emission Spectrometer Experiment: Mars Observer Mission. *J. Geophys. Res.*, 97(E5).
- Christensen, P. R., Jakosky, B. M., Kieffer, H. H., Malin, M. C., McSween, H. Y., Nealon, K., Mehall, G., Silverman, S., and Ferry, S. (1999). The Thermal Emission Imaging System (THEMIS) instrument for the Mars 2001 orbiter. *Lunar Planet. Sci. XXX*, (1470).

- Christensen, P. R. and Moore, H. J. (1992). The martian surface layer. In Kieffer, H. H., Jakosky, B. M., Snyder, C. W., and Matthews, M. S., editors, *Mars*, chapter 21, pages 686–729. The University of Arizona Press.
- Clifford, S. M. (1993). A model for the hydrologic and climatic behaviour of water of Mars. *J. Geophys. Res.*, 98:10,973–11,016.
- Comer, R. P., Solomon, S. C., and Head, J. W. (1985). Mars – thickness of the lithosphere from the tectonic response to volcanic loads. *Rev. Geophys.*, 23:61–92.
- Crumpler, L. S. (2003). Physical characteristics, geologic setting, and possible formation processes of spring deposits on Mars based on terrestrial analogs. In *6th Int. Conf. Mars*, number 3288.
- Crumpler, L. S. and Tanaka, K. L. (2003). Geology and MER target site characteristics along the southern rim of Isidis Planitia, Mars. *J. Geophys. Res.*, 108(E12).
- Crumpler, L. S., Tanaka, K. L., and Hare, T. M. (2001). Mars Exploration Rover target sites in southern Isidis. *Lunar Planet. Sci. XXXII*, (1977).
- Crumpler, L. S., Tanaka, K. L., and Hare, T. M. (2002). Final analysis of MER sites along the southern rim of Isidis Planitia. *Lunar Planet. Sci. XXXIII*, (1923).
- Davies, M. E., Batson, R. M., and Wu, S. S. C. (1992). Geodesy and cartography. In Kieffer, H. H., Jakosky, B. M., Snyder, C. W., and Matthews, M. S., editors, *Mars*, chapter 10, pages 321–342. The University of Arizona Press.
- Davis, P. A. and Tanaka, K. L. (1995). Curvilinear ridges in Isidis Planitia, Mars – the result of mud volcanism? *Abstracts of the Lunar Planet. Sci. Conf.*, 26:321–2.
- Deal, K. S., Arvidson, R. E., and Neumann, G. A. (2003). The surface roughness of terrains on Mars. In *6th Int. Conf. Mars*, number 3170.
- Duxbury, T. C., Kirk, R. L., Archinal, B. A., and Neumann, G. A. (2001). Mars geodesy/cartography working group recommendations on Mars cartographic constants and coordinate systems. In *ISPRS WG IV/9 Extraterrestrial Mapping Workshop*.
- Esposito, P. B., Banerdt, W. B., Lindal, G. F., Sjogren, W. L., and Slade, M. A. (1992). Gravity and topography. In Kieffer, H. H., Jakosky, B. M., Snyder, C. W., and

- Matthews, M. S., editors, *Mars*, chapter 7, pages 209–248. The Arizona University Press.
- Fagents, S. A., Pace, K., and Greeley, R. (2002). Origins of small volcanic cones on Mars. *Lunar Planet. Sci. XXXIII*, (1594).
- Fagents, S. A. and Wilson, L. (1996). Numerical modeling of ejecta dispersal from transient volcanic explosions on Mars. *Icarus*, 123:284–295.
- Fairén, A. G., Dohm, J. M., Baker, V. R., de Pablo, M. A., Ruiz, J., Ferris, J. C., and Anderson, R. C. (2003). Episodic flood inundations of the northern plains of Mars. *Icarus*, 165:53–67.
- Farrand, W. H. (2000). Remotely sensed signatures of hydrovolcanism: Examples from the Earth and preliminary results from Mars. *Lunar Planet. Sci. XXXI*, (1965).
- Farrand, W. H. and Gaddis, L. R. (2003). THEMIS observations of pitted cones in Acidalia Planitia and Cydonia Mensae. In *6th Int. Conf. Mars*, number 3094.
- Farrand, W. H., Gaddis, L. R., and Blundell, S. (2004). Variability in morphology and thermophysical properties of pitted cones in Acidalia Planitia and Cydonia Mensae. *Lunar Planet. Sci. XXXV*, (1928).
- Farrand, W. H. and Lane, M. D. (2002). Spectral differences between palagonite tuffs formed in sub-glacial versus liquid water environments: Relevance to Mars. *Lunar Planet. Sci. XXXIII*, (1804).
- Feldman, W. C., Prettyman, T. H., Boynton, W. V., Squyres, S. W., Bish, D. L., Elphic, R. C., Funsten, H. O., Lawrence, D. J., Maurice, S., Moore, K. R., Tokar, R. L., and Vaniman, D. T. (2003). The global distribution of near-surface hydrogen on Mars. In *6th Int. Conf. Mars*, number 3218.
- Ferguson, R. L. and Christensen, P. R. (2003). Thermal inertia using THEMIS infrared data. *Lunar Planet. Sci. XXXIV*, (1785).
- Freed, A. M., Melosh, H. J., and Solomon, S. C. (2001). Tectonics of mascon loading: Resolution of the strike-slip faulting paradox. *J. Geophys. Res.*, 106(E9):20,603–20,620.
- Frey, H. and Jarosewich, M. (1982). Subkilometer martian volcanoes: Properties and possible terrestrial analogs. *J. Geophys. Res.*, 97(B12):9867–9879.

- Frey, H., Jarosewich, M., and Partridge, K. (1981). Pseudocraters near Hellas? *Lunar Planet. Sci. XII*, pages 300–302.
- Frey, H., Lowry, B. L., and Chase, S. A. (1979). Pseudocraters on Mars. *J. Geophys. Res.*, 84(B14):8075–8086.
- Frey, H., Roark, J., and Sakimoto, S. (2000). Detailed topographic structure of the Isidis impact basin from MOLA data. *Lunar Planet. Sci. XXXI*, (1748).
- Frey, H. V. (2003). Large-diameter visible and buried impact basins on Mars: Implications for age of the highlands and (buried) lowlands and turn-off of the global magnetic field. *Lunar Planet. Sci. XXXIV*, (1838).
- Frey, H. V., Sakimoto, S. E. H., and Roark, J. H. (1998). MOLA topography and the Isidis Basin: Constraints on basin center and ring diameters. *Lunar Planet. Sci. XXIX*, (1631).
- Frigeri, A., Federico, C., Minelli, G., Pauselli, C., and Caldarella, C. (2002). Identifying wrinkle ridge structures from Mars MGS and Viking mission data: using Grass in planetary geology. In *Proc. Open Source GIS – GRASS Users Conf.*
- Gaidos, E. J. (2001). Cryovolcanism and the recent flow of liquid water on Mars. *Icarus*, 153:218–223.
- Gardner, C. S. (1992). Ranging performance of satellite laser altimeters. *IEEE T. Geosci. Remote*, 30(5):1061–1072.
- Garvin, J., Bufton, J., Blair, J., Harding, D., Luthcke, S., Frawley, J., and Rowlands, D. (1998). Observations of the Earth’s topography from the Shuttle Laser Altimeter (SLA): Laser-pulse echo-recovery measurements of terrestrial surfaces. *Phys. Chem. Earth*, 23(9-10):1053–1068.
- Garvin, J. B., Frawley, J. J., and Abshire, J. B. (1999). Vertical roughness of Mars from the Mars Orbiter Laser Altimeter. *Geophys. Res. Lett.*, 26(3):381–384.
- Garvin, J. B., Frawley, J. J., Sakimoto, S. E. H., and Schnetzler, C. (2000a). Global geometric properties of martian impact craters: an assessment from Mars Orbiter Laser Altimeter. *Lunar Planet. Sci. XXXI*, (1619).

- Garvin, J. B., Sakimoto, S. E. H., and Frawley, J. J. (2003). Craters on Mars: Global geometric properties from gridded MOLA topography. In *6th Int. Conf. Mars*, number 3277.
- Garvin, J. B., Sakimoto, S. E. H., Frawley, J. J., and Schnetzler, C. (2000b). North polar region craterforms on Mars: Geometric characteristics from the Mars Orbiter Laser Altimeter. *Icarus*, 144:329–352.
- Gilmore, M. S. and Tanaka, K. L. (2003). Sub-kilometre crater counts at the MER landing sites. *J. Geophys. Res.*, Submitted, November 2003.
- Golombek, M. P., Anderson, F. S., and Zuber, M. T. (2001). Martian wrinkle ridge topography: Evidence for subsurface faults from MOLA. *J. Geophys. Res.*, 106(E10):23,811–23,821.
- Golombek, M. P. and Banerdt, W. B. (1999). Recent advances in Mars tectonics. In *5th Int. Conf. Mars*, number 6020.
- Golombek, M. P., Grant, J. A., Parker, T. J., Kass, D. M., Crisp, J. A., Squyres, S. W., Haldemann, A. F. C., Adler, M., Lee, W., Bridges, N. T., Arvidson, R. E., Carr, M. H., Kirk, R. L., Knocke, P. C., Roncoli, R. B., Weitz, C. M., Schofield, J. T., Zurek, R. W., and Rice, J. W. (2003a). Selection of the Mars Exploration Rover landing sites. *J. Geophys. Res.*, 108(E12).
- Golombek, M. P., Haldemann, A. F. C., Forsberg-Taylor, N. K., DiMaggio, E. N., Schroeder, R. D., Jakosky, B. M., Mellon, M. T., and Matijevic, J. R. (2003b). Rock size-frequency distributions on mars and implications for Mars Exploration Rover landing safety and operations. *J. Geophys. Res.*, 108(E12).
- Golombek, M. P., Moore, H. J., Haldemann, A. F. C., Parker, T. J., and Schofield, J. T. (1999). Assessment of Mars Pathfinder landing site predictions. *J. Geophys. Res.*, 104(E4):8,585–8,594.
- Golombek, M. P., Plescia, J. B., and Franklin, B. J. (1991). Faulting and folding in the formation of planetary wrinkle ridges. *Proc. Lunar Planet. Sci. Conf. 21st*, pages 679–693.
- Greeley, R. and Fagents, S. A. (2001). Icelandic pseudocraters as analogs to some volcanic cones on Mars. *J. Geophys. Res.*, 106(E9):20527–20546.

- Greeley, R. and Guest, J. E. (1987). Geologic map of the eastern equatorial region of Mars. (USGS I-Map 1802-B).
- Greeley, R., Lancaster, N., Lee, S., and Thomas, P. (1992). Martian aeolian processes, sediments, and features. In Kieffer, H. H., Jakosky, B. M., Snyder, C. W., and Matthews, M. S., editors, *Mars*, chapter 22, pages 730–766. The University of Arizona Press.
- Greeley, R. and Theilig, E. (1978). Small volcanic constructs in the Chryse Planitia region of Mars. Technical Report TM-79729, NASA.
- Grizzaffi, P. and Schultz, P. H. (1989). Isidis Basin: Site of ancient volatile-rich debris layer. *Icarus*, 77:358–381.
- Hall, J. L., Solomon, S. C., and Head, J. W. (1986). Elysium region, Mars – tests of lithospheric loading models for the formation of tectonic features. *J. Geophys. Res.*, 91:11,377–11,392.
- Hamilton, V. E., Wyatt, M. B., McSween, H. Y., and Christensen, P. R. (2001). Analysis of terrestrial and martian volcanic compositions using thermal emission spectroscopy: II. application to martian surface spectra from the Mars Global Surveyor Thermal Emission Spectrometer. *J. Geophys. Res.*, 106(7):14,733–14,746.
- Hartmann, W. K. (1977). Relative crater production rates on planets. *Icarus*, 31:260–276.
- Hartmann, W. K. and Neukum, G. (2001). Cratering chronology and the evolution of Mars. *Space Sci. Rev.*, 96:165–194.
- Hauck, S. A., Solomon, S. C., and Phillips, R. J. (2003). Potential sources of Hesperian contractional tectonics on Mars. *Lunar Planet. Sci. XXXIV*, (1667).
- Head, J. W. (2000). Tests for ancient polar deposits on Mars: Morphology and topographic relationships of esker-like sinuous ridges (Dorsa Argenta) using MOLA data. *Lunar Planet. Sci XXXI*, (1117).
- Head, J. W. and Bridges, J. C. (2001). Beagle 2 landing site: Regional characteristics of Isidis Planitia from MOLA data. *Lunar Planet. Sci. XXXII*, (1236).
- Head, J. W. and Hallet, B. (2001a). Origin of sinuous ridges in the Dorsa Argentea Formation: Additional criteria for tests of the esker hypothesis. *Lunar Planet. Sci XXXII*, (1366).

- Head, J. W. and Hallet, B. (2001b). Origin of sinuous ridges in the Dorsa Argentea Formation: New observations and tests of the esker hypothesis. *Lunar Planet. Sci. XXXII*, (1373).
- Head, J. W., Kreslavsky, M. A., and Pratt, S. (2002). Northern lowlands of Mars: Evidence for widespread volcanic flooding and tectonic deformation in the Hesperian Period. *J. Geophys. Res.*, 107(E1).
- Helbert, J. and Benkhoff, J. (2003). Thermal modeling of the near surface layer at the Beagle 2 landing site in the Isidis Planitia region. *Lunar Planet. Sci. XXXIV*, (1819).
- Hiesinger, H. and Head, J. W. (2003). Geology of the Syrtis Major/Isidis region of Mars: New results from MOLA, MOC, and THEMIS. In *6th Int. Conf. Mars*, number 3061.
- Hoffman, N. (2000). White Mars: A new model for Mars' surface and atmosphere based on CO₂. *Icarus*, 146:326–342.
- Hoffman, N., Kargel, J. S., and Tanaka, K. L. (2001). Isidis Basin – a potential focus of cryovolcanic activity on Mars. *Lunar Planet. Sci. XXXII*, (1493).
- Hurst, M., Golombek, M. P., and Kirk, R. (2004). Small crater morphometry within Gusev crater and Isidis Planitia: Evidence for widespread secondaries on Mars. *Lunar Planet. Sci. XXXV*, (2068).
- Ivanov, B. A. (2001). Mars/Moon cratering rate ratio estimates. *Space Sci. Rev.*, 96:87–104.
- Ivanov, M. A. and Head, J. W. (2003). Syrtis Major and Isidis Basin contact: Morphological and topographic characteristics of Syrtis Major lava flows and material of the Vastitas Borealis Formation. *J. Geophys. Res.*, 108(E6).
- Jakosky, B. M., Mellon, M. T., Kieffer, H. H., Christensen, P. R., Stacy, V. E., and Lee, S. W. (2000). The thermal inertia of Mars from the Mars Global Surveyor Thermal Emission Spectrometer. *J. Geophys. Res.*, 105(E4):9643–9652.
- Janhunen, P. (2002). Are the northern plains of Mars a frozen ocean? *J. Geophys. Res.*, 107(E11).
- Jöns, H. P. (1987). Large fossil mud lakes or giant mud sheet flows in Syrtis Major (Isidis Planitia) and Mare Australe, Mars. *Abstracts of the Lunar Planet. Sci. Conf.*, 18:470.

- Kargel, J. S., Baker, V. R., Begét, J. E., Lockwood, J. F., Péwé, T. L., Shaw, J. S., and Strom, R. G. (1995). Evidence of ancient continental glaciation in the martian northern plains. *J. Geophys. Res.*, 100(E3):5351–5368.
- Kargel, J. S. and Marion, G. M. (2004). Mars as a salt-, acid-, and gas-hydrate world. *Lunar Planet. Sci. XXXV*, (1965).
- Kargel, J. S. and Strom, R. G. (1991). Terrestrial glacial eskers: Analogs for martian sinuous ridges. *Abstracts of the Lunar Planet. Sci. Conf.*, 22:683–684.
- Kargel, J. S., Tanaka, K. L., Baker, V. R., Komatsu, G., and MacAyeal, D. R. (2000). Formation and dissociation of clathrate hydrates on Mars: polar caps, northern plains and highlands. *Lunar Planet. Sci. XXXI*, (1891).
- Kiefer, W. S. (1999). Lunar gravity models: Large, near side impact basins. *Lunar Planet. Sci. XXX*, (1995).
- Kieffer, H. H., Jakosky, B. M., and Snyder, C. W. (1992). The planet Mars: From antiquity to the present. In Kieffer, H. H., Jakosky, B. M., Snyder, C. W., and Matthews, M. S., editors, *Mars*, chapter 1, pages 1–33. The University of Arizona Press.
- Kieffer, H. H., Martin, T. Z., Peterfreund, A. R., Jakosky, B. M., Miner, E. D., and Palluconi, F. D. (1977). Thermal and albedo mapping of Mars during the Viking primary mission. *J. Geophys. Res.*, 82:4249–4291.
- Kopf, A. J. (2002). Significance of mud volcanism. *Rev. Geophys.*, 40(2):1–52.
- Kortz, B. E. and Head, J. W. (2001). Comparisons of volcanic fields on Venus, Earth, and Mars. *Lunar Planet. Sci. XXXII*, (1422).
- Kreslavsky, M. A. and Head, J. W. (2000). Kilometer-scale roughness of Mars: Results from MOLA data analysis. *J. Geophys. Res.*, 105(E11):26,695–26,711.
- Kreslavsky, M. A. and Head, J. W. (2001). Stealth craters in the northern lowlands of Mars: Evidence for a buried early-Hesperian-aged unit. *Lunar Planet. Sci. XXXII*, (1001).
- Kreslavsky, M. A. and Head, J. W. (2002). Fate of outflow channel effluents in the northern lowlands of Mars: The Vastitas Borealis Formation as a sublimation residue from frozen ponded bodies of water. *J. Geophys. Res.*, 107(E12).

- Lanagan, P. D., McEwen, A. S., Keszthelyi, L. P., and Thordarson, T. (2001). Rootless cones on Mars indicating the presence of shallow equatorial ground ice in recent times. *Geophys. Res. Lett.*, 28:2365–2367.
- Lee, P. (2000). Cold-based glaciations on Mars: Landscapes of glacial selective linear erosion on Devon Island, Nunavut, arctic Canada, as a possible analog. In *Mars Polar Sci.*, number 4108, pages 105–6.
- Lockwood, J. F. and Kargel, J. S. (1994). Thumbprint terrain in Isidis Planitia: Formed in a glacial paleolake environment? *Abstracts of the Lunar. Planet. Sci. Conf.*, 25:799–800.
- Lucchita, B. K. (1978). Geologic map of the Ismenius Lacus quadrangle, Mars, scale 1:5,000,000. Technical Report Map I-1065, USGS.
- Madden, M. E. E. and Bodnar, R. J. (2002). Geochemical modeling of basalt-brine interactions as an analog for Mars near-surface processes. *Lunar Planet. Sci. XXXIII*, (1211).
- Malin, M. C., Danielson, G. E., Ingersol, A. P., Masursky, H., Veverka, J., Ravine, M. A., and Soulanille, T. A. (1992). The Mars Orbiter Camera. *J. Geophys. Res.*, 97(E5):7699–7718.
- Malin, M. C., Danielson, G. E., Ravine, M. A., and Soulanille, T. A. (1991). Design and development of the Mars Orbiter Camera. *Int. J. Imag. Syst. Tech.*, 3:76–91.
- Mangold, N. (2000). Giant paleo-eskers of Mauritania: analogs for martian esker-like landforms. In *Mars Polar Sci.*, number 4031, page 120.
- Mangold, N., Allemand, P., and Thomas, P. G. (1998). Wrinkle ridges of Mars: Structural analysis and evidence for shallow deformation controlled by ice-rich décollements. *Planet. Space Sci.*, 46(4):345–356.
- Marchant, D. R. and Head, J. W. (2003). Cold-based glaciers in the western dry valleys of Antarctica: Terrestrial landforms and martian analogs. *Lunar Planet. Sci. XXXIV*, (1245).
- McEwen, A. S. (2003). Secondary cratering on Mars: Implications for age dating and surface properties. In *6th Int. Conf. Mars*, number 3268.
- Mellon, M. T. (2001). Thermal inertia and rock abundance. In *TES data workshop*.

- Mellon, M. T., Jakosky, B. M., Kieffer, H. H., and Christensen, P. R. (2000). High resolution thermal inertia mapping from the Mars Global Surveyor Thermal Emission Spectrometer. *Icarus*, 148:437–455.
- Mellon, M. T., Kretke, K. A., Smith, M. D., and Pelkey, S. M. (2002). A global map of thermal inertia from Mars Global Surveyor of mapping-mission data. *Lunar Planet. Sci XXXIII*, (1416).
- Mellon, M. T. and Phillips, R. J. (2001). Recent gullies on Mars and the source of liquid water. *J. Geophys. Res.*, 106(E10):23,165–23,180.
- Melosh, H. J. (1978). The tectonics of mascon loading. *Proc. Lunar. Planet. Sci. Conf. 9th*, pages 3513–3525.
- Mest, S. C. and Crown, D. A. (1996). Relationships between wrinkle ridges and craters in Hesperia Planum: Constraints on the timing of ridge formation. *Lunar Planet. Sci. XXVII*.
- Metzger, S. M. (1995). Martian sinuous ridges: exploring their paleoclimate significance. *Abstracts of the Lunar and Planet. Sci. Conf.*, 26:959–960.
- Metzger, S. M. (2001). Re-exploring the formation of martian sinuous ridges. *Lunar Planet. Sci. XXXII*, (1911).
- Mitchell, D. E., Sakimoto, S. E. H., and Garvin, J. B. (2002). MOLA topography and morphometry of rampart and pedestal craters, Mars. *Lunar Planet. Sci. XXXIII*, (1805).
- Mitchell, K. L. (2001). Explosive volcanic eruptions in Mars: an improved numerical model. *Lunar Planet. Sci XXXII*, (1189).
- Mitchell, K. L. and Wilson, L. (1998). Implications of the apparent absence of maars in Viking Orbiter imagery. *Lunar Planet. Sci. XXIX*, (1589).
- Mitchell, K. L. and Wilson, L. (2001). Explosive volcanic eruptions on Mars: misconceptions and new insights. *Lunar Planet. Sci XXXII*, (1190).
- Mitchell, K. L. and Wilson, L. (2002). Influence of climate on martian magmatic eruptions. *Lunar Planet. Sci. XXXIII*, (1734).

- Mitchell, K. L., Wilson, L., and Wilson, C. J. N. (1999). Consequences of adiabatic cooling within volcanic conduits on Earth and Mars. *Lunar Planet. Sci. XXX*, (1716).
- Montési, L. G. J. and Zuber, M. T. (2003). Clues to the lithospheric structure of Mars from wrinkle ridge sets and localization instability. *J. Geophys. Res.*, 108(E6).
- Moore, J. M., Clow, G. D., Davis, W. L., Gulick, V. C., Janke, D. R., McKay, C. P., Stoker, C. R., and Zent, A. P. (1995). The circum-Chryse region as a possible example of a hydrologic cycle on Mars: Geologic observations and theoretical evaluation. *J. Geophys. Res.*, 100(E3):5,433–5,447.
- Mouginis-Mark, P. (1979). Martian fluidized crater morphology – variations with crater size, latitude, altitude, and target material. *J. Geophys. Res.*, 84:8,011–8,022.
- Mouginis-Mark, P. J. (1985). Volcano/ground ice interactions in Elysium Planitia, Mars. *Icarus*, 64:265–284.
- Mouginis-Mark, P. J., Garbeil, H., Boyce, J. M., Ui, C. S. E., and Baloga, S. (2004). The geometry of martian impact craters: First results from an interactive software package. *J. Geophys. Res.*, 109(E08006).
- Mueller, K. and Golombek, M. (2004). Compressional structures on Mars. *Ann. Rev. Earth Pl. Sc.*, 32:435–464.
- Murphy, N., Hynek, B. M., Jakosky, B. M., Martinez-Alonzo, S., Putzig, N. E., Mellon, M. T., and Pelkey, S. (2004). Thermophysical properties of Isidis impact basin, Mars. *Lunar Planet. Sci. XXXV*, (1797).
- Murray, K. C., Christensen, P. R., Mehall, G. L., Gorelick, N. S., Harris, J. C., Bender, K. C., and Cherednik, L. L. (2003). 2001 Mars Odyssey THEMIS data archive. *Lunar Planet. Sci. XXXIV*, (1363).
- Mustard, J. F. (2003). First look at the thermophysical properties of the dissected mantle. *Lunar Planet. Sci. XXXIV*, (2005).
- Neteler, M. and Mitasova, H. (2002). *Open Source GIS: A GRASS GIS Approach*. Kluwer Academic Publishers, 464 pp.
- Neukum, G., Ivanoc, B., and Hartmann, W. K. (2001). Cratering records in the inner Solar System in relation to the Lunar Reference System. *Space Sci. Rev.*, 96:55–86.

- Neukum, G. and Wise, D. U. (1976). A standard crater curve and possible new time scale. *Science*, 194:1381–1387.
- Neumann, G. A., Abshire, J. B., Aharonson, O., Garvin, J. B., Sun, X., and Zuber, M. T. (2003a). Mars Orbiter Laser Altimeter pulse width measurements and footprint-scale roughness. *Geophys. Res. Lett.*, 30(11).
- Neumann, G. A., Lemoine, F. G., Smith, D. E., and Zuber, M. T. (2003b). The Mars Orbiter Laser Altimeter archive: Final Precision Experiment Data Record release status and status of radiometry. *Lunar Planet. Sci. XXXIV*, (1978).
- Neumann, G. A., Zuber, M. T., and Smith, D. E. (2000). Mola Precision Experiment Data Record Software Interface Specification. Technical Report Version 2.8, NASA Goddard Space Flight Centre.
- Nowicki, S. A. and Christensen, P. R. (1999). Mars surface rock abundance from Thermal Emission Spectrometer (TES) mapping data. In *5th Int. Conf. Mars*, number 6191.
- Nowicki, S. A. and Christensen, P. R. (2002). THEMIS corroboration of TES rock abundance observations on Mars. In *American Geophysical Union, Spring Meeting*, number P31A-05.
- Nyquist, L. E., Bogard, D., Shih, C.-Y., Greshake, A., Stöffler, D., and Eugster, O. (2001). Ages and geologic histories of martian meteorites. *Space Sci. Rev.*, 96:105–164.
- Okubo, C. H. and Schultz, R. A. (2002). Fault geometry below wrinkle ridges based on slope asymmetry and implications for mechanical stratigraphy. *Lunar Planet. Sci. XXXIII*, (1708).
- Okubo, C. H., Schultz, R. A., and Stefanelli, G. S. (2004). Gridding Mars Orbiter Laser Altimeter data with GMT: effects of pixel size and interpolation methods on DEM integrity. *Comput. Geosci.*, 30:59–72.
- Okubo, C. H., Schultz, R. A., and Tanaka, K. L. (2003). Fault-controlled fluid seep potential and surface strength at the Isidis & Elysium Planitia MER sites based on numerical modeling of wrinkle ridge topography. *Lunar Planet. Sci. XXXIV*, (1484).
- Ori, G. G., Komatsu, G., Ormo, J., and Marinangeli, L. (2001). Subsurface models for the formation of mound-like morphologies on Mars. *Lunar Planet. Sci. XXXII*, (1539).

- Ori, G. G., Marinangeli, L., and Komatsu, G. (2000). Gas (methane?)-related features on the surface of Mars and subsurface reservoirs. *Lunar Planet. Sci. XXXI*, (1550).
- Pelkey, S. M., Jakosky, B. M., and Mellon, M. T. (2001). Thermal inertia of crater-related wind streaks on Mars. *J. Geophys. Res.*, 106(E10):23,909–23,920.
- Plescia, J. B. (1980). Cinder cones of Isidis and Elysium. In *Reports of Planetary Geology Program*, volume NASA TM-82385, pages 263–265.
- Plescia, J. B. and Golombek, M. P. (1986). Origin of planetary wrinkle ridges based on the study of terrestrial analogs. *Geol. Soc. Am. Bull.*, 97:1289–1299.
- Pomerantz, W. J. and Head, J. W. (2003). Thumbprint terrain and sinuous troughs with medial ridges in the northern lowlands of Mars: Assessment of the glacial hypothesis using new spacecraft data. *Lunar Planet. Sci. XXXIV*, (1277).
- Presley, M. A. (2002). What can thermal inertia do for you? *Lunar Planet. Sci. XXXIII*, (1144).
- Presley, M. A. and Christensen, P. R. (1997). Thermal conductivity measurements of particulate materials 2: results. *J. Geophys. Res.*, 102(E3):6551–6566.
- Priest, S. S., Duffield, W. A., Malis-Clark, K., Hendley, J. W., and Stauffer, P. H. (2001). The San Francisco volcanic field, Arizona. Technical Report Fact Sheet 017-01, U. S. G. S.
- Putzig, N. E., Mellon, M. T., Arvidson, R. E., and Kretke, K. A. (2003). Thermal inertia analysis of the martian globe, south polar region, and past landing sites. *Lunar Planet. Sci. XXXIV*, (1429).
- Putzig, N. E., Mellon, M. T., Jakosky, B. M., Pelkey, S. M., Martinez-Alonso, S., Hynek, B. M., and Murphy, N. W. (2004). Mars thermal inertia from THEMIS data. *Lunar Planet. Sci. XXXV*, (1863).
- Quaide, W. (1965). Rilles, ridges and domes – clues to maria history. *Icarus*, 4:390–395.
- Raitala, J. and Kauhanen, K. (1992). Ridge systems related to martian impact craters. *Earth Moon Planets*, 58:65–78.

- Rossbacher, L. A. and Judson, S. (1981). Ground ice on Mars: Inventory, distribution and resulting landforms. *Icarus*, 45:39–59.
- Rothery, D. A., Seabrook, A. M., Bridges, J. C., and Wright, I. P. (2001). Possible tuff rings in the Beagle 2 landing area and implications for sub-surface volatiles. In *Eos, AGU Fall Mtg. Suppl.*, number F709.
- Ruff, S. W. (1992). Dorsa Argentea type sinuous ridges, Mars: evidence for linear dune hypothesis. In *Workshop on the martian surface and atmosphere*, pages 126–7. Lunar and Planetary Institute.
- Ruff, S. W. (1994). Comparison of Mars sinuous ridges with terrestrial linear dunes: observations from the field. *Abstracts of the 25th Lunar Planet Sci. Conf.*, (1171).
- Salamunićar, G. and Selar-Glavočić, D. (2003). Image processing algorithms for visualization of quasi-circular-depressions: A step toward the automatic process of detection and classification of martian buried impact craters. In *6th Int. Conf. Mars*, number 3202.
- Schroeder, R. D. and Golombek, M. P. (2003). Mars Exploration Rover landing site boulder fields. *Lunar Planet. Sci. XXXIV*, (1975).
- Schultz, P. H. (2002). Uncovering Mars. *Lunar Planet. Sci. XXXIII*, (1790).
- Schultz, P. H. and Gault, D. E. (1979). Atmospheric effects on martian ejecta emplacement. *J. Geophys. Res.*, 84:7,669–7,687.
- Schultz, R. A. (2000a). Localization of bedding plane slip and backthrust faults above blind thrust faults: Keys to wrinkle ridge structure. *J. Geophys. Res.*, 105(E5):12,035–12,052.
- Schultz, R. A. (2000b). Toward a comprehensive structural model for planetary wrinkle ridges. *Lunar Planet. Sci. XXXI*, (1171).
- Schultz, R. A. and Frey, H. V. (1990). A new survey of large multiring impact basins on Mars. *J. Geophys. Res.*, 95:14,175–14,189.
- Sheridan, M. F. and Wohletz, K. H. (1983). Hydrovolcanism: Basic considerations and review. *J. Volcanol. Geoth. Res.*, 17:1–29.

- Simpson, R. A., Harmon, J. K., Zisk, S. H., Thompson, T. W., and Muhleman, D. O. (1992). Radar determination of Mars surface properties. In Kieffer, H. H., Jakosky, B. M., Snyder, C. W., and Matthews, M. S., editors, *Mars*, chapter 20, pages 652–685. The University of Arizona Press.
- Smith, D. E., Zuber, M. T., Frey, H. V., Garvin, J. B., Head, J. W., Muhleman, D. O., Pettengill, G. H., Phillips, R. J., Solomon, S. C., Zwally, H. J., Banerdt, W. B., Duxbury, T. C., Golombek, M. P., Lemoine, F. G., Neumann, G. A., Rowlands, D. D., Aharonson, O., Ford, P. G., Ivanov, A. B., Johnson, C. L., McGovern, P. J., Abshire, J. B., Afzal, R. S., and Sun, X. (2001). Mars Orbiter Laser Altimeter: Experiment summary after the first year of global mapping Mars. *J. Geophys. Res.*, 106:23,689–23,722.
- Smith, W. H. F. and Wessel, P. (1990). Gridding with continuous curvature splines in tension. *Geophysics*, 55 (3):293–305.
- Soare, R. J. and Peloquin, C. (2003). Crater-based evidence of periglacial processes in northwest Utopia Planitia. In *Eos Trans. AGU*, 84(46), *Fall Meet. Suppl.*, number C21C-0825.
- Soderblom, L. A. (1992). The composition and mineralogy of the martian surface from spectroscopic observations: 0.3 μm to 50 μm . In Kieffer, H. H., Jakosky, B. M., Snyder, C. W., and Matthews, M. S., editors, *Mars*, chapter 17, pages 557–593. The University of Arizona Press.
- Sohn, Y. K. (1996). Hydrovolcanic processes forming basaltic tuff rings and cones on Cheju Island, Korea. *Geol. Soc. Am. Bull.*, 108:1199–1211.
- Solomon, S. C. and Head, J. W. (1980). Lunar mascon basins – lava filling, tectonics, and evolution of the lithosphere. *Rev. Geophys. Space GE*, 18:107–141.
- Solomon, S. C., Johnson, C. L., McGovern, P. J., Aharonson, O., Banerdt, W. B., Head, J. W., Phillips, R. J., Smith, D. E., and Zuber, M. T. (1998). An overview of lithospheric flexure on Mars: Implications of initial MOLA observations. *Lunar Planet. Sci. XXIX*, (1389).
- Solomon, S. C., Sjogren, W. L., and Bratt, S. R. (1983). The structure of the Isidis Basin, Mars, from gravity anomalies. *Lunar Planet. Sci. XIV*, pages 725–726.

- Strom, R. G., Croft, S. K., and Barlow, N. G. (1992). The martian impact cratering record. In Kieffer, H. H., Jakosky, B. M., Snyder, C. W., and Matthews, M. S., editors, *Mars*, chapter 12, pages 383–423. The University of Arizona Press.
- Sueyoshi, T. and Hamano, Y. (2002). Possible mechanism for formation of martian ground ice. In *Eos. Trans. AGU, 83(47), Fall Meet. Suppl.*, number P72C-05.
- Sun, X., Abshire, J. B., Neumann, G. A., and Zuber, M. T. (2001). Radiometry measurements of Mars at $1064\mu\text{m}$ using the Mars Orbiter Laser Altimeter. In *Eos Trans. AGU, 82*, number P42A-0557.
- Tanaka, K. L. (1986). The stratigraphy of Mars. *J. Geophys. Res.*, 91(B13):E139–E158.
- Tanaka, K. L. (1997). Geologic mapping of sedimentary materials in the northern plains of Mars. *Lunar Planet. Sci. XXVIII*, (1180).
- Tanaka, K. L., Joyal, T., and Wenker, A. (2000). The Isidis plains unit, Mars: Possible catastrophic origin, tectonic tilting, and sediment loading. *Lunar Planet. Sci. XXXI*, (2023).
- Tanaka, K. L. and Skinner, J. A. (2003). Volatile-driven, deformational and resurfacing origin for the Vastitas Borealis Formation on Mars. *Lunar Planet. Sci. XXXIV*, (1924).
- Tanaka, K. L., Skinner, J. A., Hare, T. M., Joyal, T., and Wenker, A. (2002). Resurfacing of the northern plains of Mars by shallow subsurface volatile-driven activity. *Lunar Planet. Sci. XXXIII*, (1406).
- Tanaka, K. L., Skinner, J. A., Hare, T. M., Joyal, T., and Wenker, A. (2003). Resurfacing history of the northern plains of Mars based on geologic mapping of Mars Global Surveyor data. *J. Geophys. Res.*, 108(E4).
- Thomas, P., Veverka, J., Lee, S., and Bloom, A. (1981). Classification of wind streaks on Mars. *Icarus*, 45:124–153.
- Thomson, B. J. and Head, J. W. (2001). Utopia Basin, Mars: Characterization of topography and morphology and assessment of the origin and evolution of the basin internal structure. *J. Geophys. Res.*, 106(10):23,209–23,230.
- Thorarinsson, S. (1953). Crater groups in Iceland. *B. Volcanol.*, 14:1–44.

- Tyler, G. L., Balmino, G., Hinson, D. P., Sjogren, W. L., Smith, D. E., Woo, R., Armstrong, J. W., Flasar, F. M., Simpson, R. A., and Priest, P. (2000). NASA Planetary Data System, MGS RST science data products.
- Watters, T. R. (1988). Wrinkle ridge assemblages on the terrestrial planets. *J. Geophys. Res.*, 93:10236–10254.
- Watters, T. R. (2001). Studies of martian wrinkle ridges using MOLA topographic data: The nature of elevation offsets. *Lunar Planet. Sci. XXXII*, (1414).
- Watters, T. R. (2003). Lithospheric flexure and the origin of the dichotomy boundary on Mars. *Geology*, 31(3):271–274.
- Watters, T. R. and Robinson, M. S. (1997). Radar and photoclinometric studies of wrinkle ridges on Mars. *J. Geophys. Res.*, 102(E5):10889–10904.
- Watters, T. R. and Robinson, M. S. (2000). Topographic studies of wrinkle ridges: The significance of elevation offsets. *Lunar Planet. Sci. XXXI*, (1879).
- Werner, C. and Loper, D. E. (2000). On the origin of lunar mascons. *Lunar Planet. Sci. XXXI*, (1752).
- Wessel, P. and Smith, W. H. F. (1991). Free software helps map and display data. *EOS Trans. Amer. Geophys. U.*, 72 (41):441, 445–446.
- Wessel, P. and Smith, W. H. F. (1995). New version of the Generic Mapping Tools released. *EOS Trans. Amer. Geophys. U.*, 76 (33):329.
- Wessel, P. and Smith, W. H. F. (1998). New, improved version of Generic Mapping Tools released. *EOS Trans. Amer. Geophys. U.*, 79 (47):579.
- Wilhelms, D. E. (1973). Comparison of martian and lunar multiringed circular basins. *J. Geophys. Res.*, 78:4,084–4,095.
- Wilson, L. and Head, J. W. (1994). Mars: Review and analysis of volcanic eruption theory and relationships to observed landforms. *Rev. Geophys.*, 32(3):221–263.
- Withers, P. and Neumann, G. A. (2001). Enigmatic northern plains of Mars. *Nature*, 410:652.

- Wohletz, K. H. (1986). Explosive magma-water interactions: Thermodynamics, explosion mechanisms and field studies. *B. Volcanol.*, 48:245–264.
- Wood, C. A. (1979). Monogenetic volcanoes of the terrestrial planets. *Proc. Lunar Planet. Sci. Conf. 10th*, pages 2815–2840.
- Wood, C. A. (1980). Morphometric evolution of cinder cones. *J. Volcanol. Geotherm. Res.*, 7:387–413.
- Wood, C. A. (1982). Pingos, gervigiars and martian mysteries. *Lunar Planet. Sci. XIII*, pages 875–6.
- Wyatt, M. B. and McSween, H. Y. (2002). Spectral evidence for weathered basalt as an alternative to andesite in the northern lowlands of Mars. *Nature*, 417:263–266.
- Wyatt, M. B., McSween, H. Y., Christensen, P. R., and Head, J. W. (2003a). Basalt, altered basalt, and andesite on the martian surface: observations, interpretations and outstanding questions. In *6th Int. Conf. Mars*, number 3271.
- Wyatt, M. B., McSween, H. Y., Moersch, J. E., Gorelick, N. S., and Christensen, P. R. (2003b). THEMIS observations of low-albedo intracrater materials and wind streaks in Western Arabia Terra. *Lunar Planet. Sci. XXXIV*, (2009).
- Wyatt, M. B. and Tanaka, K. L. (2003). Origin of MGS-TES surface compositions in the northern plains and polar regions of Mars. In *3rd Mars Polar Sci. Conf.*, number 8118.
- Zuber, M. T. (1995). Wrinkle ridges, reverse faulting, and the depth penetration of lithospheric strain in Lunae Planum, Mars. *Icarus*, 114:80–92.
- Zuber, M. T., Smith, D. E., Solomon, S. C., Muhleman, D. O., Head, J. W., Garvin, J. B., Abshire, J. B., and Bufton, J. L. (1992). The Mars Orbiter Laser Altimeter investigation. *J. Geophys. Res.*, 97(E5):7781–7797.
- Zuber, M. T., Solomon, S. C., Phillips, R. J., Smith, D. E., Tyler, G. L., Aharonson, I., Balmino, G., Banerdt, W. B., Head, J. W., Johnson, C. L., Lemoine, F. G., McGovern, P. J., Neumann, G. A., Rowlands, D. D., and Zhong, S. (2000). Internal structure and early thermal evolution of Mars from Mars Global Surveyor topography and gravity. *Science*, 287:1788–1793.

Production and Software Notes

This thesis was produced using the L^AT_EX document preparation system – specifically the teTeX distribution in combination with the TeXShop previewer and editor running under OS X on an Apple Macintosh computer. Bibliography duties were handled by BibDesk, the B_IB_TE_X bibliography manager.